

AFRPL-TR-71-130

AD 738622

**MATERIAL PERFORMANCE OF CARBON PHENOLIC
ABLATORS AND PYROLYTIC GRAPHITE COATINGS IN
NOZZLES SUBJECTED TO MULTIPLE PULSE DUTY CYCLES**

by

M. R. Wool
D. L. Baker
A. J. Murphy

Aerotherm Corporation

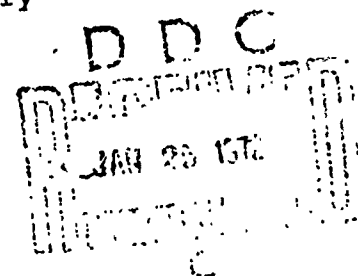
Technical Report AFRPL-TR-71-130

Aerotherm Final Report No. 71-43

October 1971

Air Force Rocket Propulsion Laboratory
Air Force Systems Command
United States Air Force
Edwards, California

THIS DOCUMENT APPROVED
FOR
FULL RELEASE
& UNLIMITED DISTRIBUTION



~~This document is subject to special export controls
and each transmittal to foreign governments or foreign
nationals may be made only with prior approval of AFRPL
(RPOR-STINFO), Edwards, California 93523~~

Reproduced by
NATIONAL TECHNICAL
INFORMATION SERVICE
Springfield, VA 221

NOTICE

When U. S. Government drawings, specifications, or other data are used for any purpose other than a definitely related Government procurement operation, the fact that the Government may have formulated, furnished, or in any way supplied the said drawings, specifications, or other data, is not to be licensing the holder or any other person or corporation, or conveying any rights or permission to manufacture, use, or sell any patented invention that may be in any way be related thereto.

✓

SECTION/AVAILABILITY CODE	
DISC.	AVAIL. AND AC. DESIGN.
A	

AFRPL-TR-71-130

MATERIAL PERFORMANCE OF CARBON PHENOLIC
ABLATORS AND PYROLYTIC GRAPHITE COATINGS IN
NOZZLES SUBJECTED TO MULTIPLE PULSE DUTY CYCLES

M. R. Wool
D. L. Baker
A. J. Murphy

THIS DOCUMENT APPROVED
FOR
PUBLIC RELEASE
& UNLIMITED DISTRIBUTION

October 1971

~~This document is subject to special export controls and each transmittal to foreign governments or foreign nations may be made only with prior approval of AFRPL (RDOR STINPO), Edwards, California 93523~~



485 CLYDE AVE MOUNTAIN VIEW CALIFORNIA 94040

FORWARD

This report was prepared by the Aerotherm Division of Acurex Corporation under USAF Contract FO4611-70-C-0019 and presents the post-test measurements and analysis results for five nozzles which were subjected to multiple pulse duty cycles. The work was administered under the direction of the Air Force Rocket Propulsion Laboratory with Captain David R. Zorich as the Project Officer.

Mr. Duane L. Baker was the Aerotherm Corporation overall program manager. Mr. Mitchell R. Wool was the principal investigator in performing the thermochemical analysis predictions and in correlating these predictions with the post-test measurements. He was provided support by Mr. Andrew J. Murphy.

The authors wish to acknowledge the contribution of Mr. T. Imai, of the Stanford Research Institute, for his support in performing the x-ray diffraction and x-ray transmission measurements.

This technical report has been reviewed and is approved.

Charles R. Cooke
Chief, Solid Rocket Division

ERRATA

AFRPL-TR-71-130

Aerotherm Final Report 71-43

On cover page, title page, and distribution statement
of DD Form 1473

delete

This document is subject to special export
controls and each transmittal to foreign
governments or foreign nationals may be
made only with prior approval of AFRPL
(RPOR-STINFO), Edwards, California 93523

add

Approved for public release: distribution
unlimited

Aerotherm Division
ACUREX Corporation
485 Clyde Avenue
Mountain View, Ca. 94040

ABSTRACT

Measurement and analyses of the thermal response of five identical rocket nozzles were performed. The nozzles were fired on the Philco-Ford Axonutronic Division, TMSO-EM simulator between April 15, 1971 and May 4, 1971 under Air Force Contract F04611-69-C-0039. The simulated solid propellant, designated ANB-3066, contained approximately 16 percent aluminum. The five nozzles were exposed to various multiple pulse duty cycles with individual pulse times ranging from 10 to 20 seconds. Nominal chamber pressure for each pulse was 750 psia. Each nozzle was instrumented with thermocoupled plugs at two locations in the exit cone and with two spring loaded thermocouple probes at the backwall of the graphite throat package parts.

Post-test measurements of surface recession, char penetration, density versus depth, and in-depth crystallization were made. Predictions of the thermal and ablative responses of the throat package and the exit cone material at an area ratio of approximately 4.0 were performed for each nozzle and pulse. Agreement between throat package backwall temperature response data and the predicted 2-D response was excellent. One-dimensional conduction solutions at the throat plane were less accurate, although surface temperature and recession predictions agreed favorably with the 2-D conduction results. Recession of the PG coated throat surface was underpredicted using the kinetically controlled surface response model developed under Air Force Contract F04611-69-C-0031. The probable reason for the underprediction is the inability to accurately evaluate the severe heating at the boundary layer reattachment point on the throat insert.

Temperature response predictions for the FM 5055A carbon cloth phenolic exit cone thermocoupled plug location agreed favorably with data, although conduction along the char layer during nozzle cooldowns was not modeled. Carbon phenolic recession comparisons were confounded by char swell phenomenon. Agreement was obtained by utilizing a physically reasonable semi-empirical char swell correction relation. Density profile predictions were also in agreement with X-ray transmission measurements and shave and weigh measurements. X-ray diffraction measurements indicated the anticipated increase graphite crystallization with charring, independent of the type of duty cycle.

The general conclusion of these studies is that current thermal analysis techniques are suitable for the evaluation of multiple pulse duty cycle ablative response phenomena, and that no extraordinary material response phenomena occur during multiple pulse nozzle exposures.

TABLE OF CONTENTS

Section	Page
1 INTRODUCTION	1-1
2 MULTIPLE PULSE DUTY CYCLE ROCKET MOTOR TESTS	2-1
2.1 Nozzle	2-1
2.2 Test Facility	2-3
2.3 Propellant	2-4
2.4 Chamber Pressure Histories	2-7
2.5 Measured In-Depth Temperatures	2-10
3 POST-TEST MEASURED MATERIAL PERFORMANCE	3-1
3.1 Surface Recession and Char Thickness Measurements	3-1
3.2 In-Depth Density Profile Measurements	3-25
3.3 X-Ray Diffraction Measurements	3-29
4 EVALUATION OF MATERIAL PERFORMANCE DATA	4-1
4.1 Summary of Analysis Methods	4-1
4.2 Intermediate Analysis Results and Material Properties	4-7
4.2.1 Time Dependent Non-Blowing Surface Boundary Conditions	4-7
4.2.2 Ablating Surface Thermochemical Response Solutions	4-16
4.2.3 Thermal Properties	4-20
4.3 Comparison of Computed & Measured Material Performance Data	4-26
4.3.1 Throat Package Response Analysis Results	4-27
4.3.2 Carbon Cloth Phenolic Exit Cone Response Analysis	4-37
5 CONCLUSIONS AND RECOMMENDATIONS	5-1
REFERENCES	R-1
APPENDIX A - MEASURED CHAMBER PRESSURE HISTORIES	A-1
APPENDIX B - MEASURED TRANSIENT IN-DEPTH TEMPERATURE HISTORIES	B-1
APPENDIX C - DESCRIPTION OF AEROTHERM COMPUTER PROGRAMS	C-1
APPENDIX D - DISTRIBUTION LIST	D-1

LIST OF TABLES

<u>Table</u>		<u>Page</u>
2-1	Pre-Test Nozzle Quality Control Record	2-3
2-2	Simulator Propellant Ingredients	2-5
2-3	Simulator Propellant Elemental Concentrations	2-5
2-4	Properties and Combustion Products of the Simulator Propellant	2-6
2-5	Measured Propellant Flowrates	2-6
2-6	Description of Multiple Pulse Duty Cycles	2-7
2-7	Summary of Measured Temperatures	2-10
3-1	Summary of Nozzle Throat Recession Measurements	3-24
3-2	Summary of Char Thickness and Surface Measurements	3-24
4-1	Summary of Major Features of Computer Programs	4-4
4-2	Typical Procedure for Analyzing Rocket Motor Nozzles	4-5
4-3	Kinetically Controlled Reaction Rate Expressions Used For PG Layer and ATJ Graphite Surface Thermochemistry Solutions	4-17
4-4	Chemical Elemental Compositions for Throat and Exit Cone Surface Thermochemistry Solutions	4-18
4-5	Summary of Throat and Exit Cone Conditions for which Surface Thermochemistry Solutions were Obtained	4-18
4-6	Physical and Chemical Properties for FM 5055A Carbon Cloth Phenolic	4-22
4-7	Specific Heat and Densities for Pyrolytic Graphite, ATJ Graphite, AGSR Graphite, and GA Carbon	4-26
4-8	Thermal Properties used for RPD 150 Asbestos Phenolic	4-26
4-9	Multiple Pulse Nozzle Throat Response Summary	4-36
4-10	Comparison of Predicted and Measured FM 5055A Carbon Cloth Phenolic Thermal Performance at $A/A^* = 4.2$	4-43

LIST OF FIGURES

<u>Figure</u>		<u>Page</u>
2-1	Schematic of Restart Nozzle	2-2
2-2	Schematic Drawing of Thermocoupled Plug	2-2
2-3	Chamber Pressure Histories for Multiple Pulse Duty Cycle Rocket Motor Tests	
3-1	Pre, Post, and Char Line Contours for Nozzle No. 4	3-2
3-2	Pre, Post, and Char Line Contours for Nozzle No. 5	3-6
3-3	Pre, Post, and Char Line Contours for Nozzle No. 6	3-10
3-4	Pre, Post, and Char Line Contours for Nozzle No. 7	3-14
3-5	Pre, Post, and Char Line Contours for Nozzle No. 8	3-18
3-6	Typical Multiple Pulse Nozzle Post Test Surface Characteristics, Nozzle No. 8	3-22
3-7	Correlation of Local Nozzle Throat Surface Recession with Circumferential Location	3-23
3-8	Comparison of Predicted and Measured In-Depth Density Profiles in FM 5055A Carbon Cloth Phenolic at an Area Ratio of 4.2	3-26
3-9	Schematic of X-Ray Transmission System	3-27
3-10	Location for X-Ray Transmission Sample (Nozzle No. 9)	3-28
3-11	Measured X-Ray Transmission for Density Profile Sample	3-29
3-12	Material Density Profile Determined from X-Ray Transmission Measurements	3-30
3-13	Cross Section of X-Ray Transmission Sample	3-30
3-14	Locations for X-Ray Diffraction Samples	3-31
3-15	Lattice Structure of Graphite Crystal	3-31
3-16	X-Ray Diffraction Measurements in FM 5055A Carbon Cloth Phenolic at an Area Ratio of 4.0	3-33
4-1	Characterization of the Solid Propellant Rocket Environment and the Response of a Charring Ablator	4-2
4-2	Flow Chart for Aerothermodynamic Analysis	4-6
4-3	Isentropic Expansion Temperature Ratios for Ideal and Actual Propellant Combustion Efficiencies	4-8
4-4	Free Stream Isentropic Expansion Properties as Computed for 97 Percent Combustion Efficiency	4-9
4-5	Nominal Nozzle Geometry as a Function of Streamwise Boundary Layer Length	4-10
4-6	ARGEIBL Heat Transfer Coefficient Distribution for Multiple Pulse Nozzle Configuration. ANB3066 Simulator Propellant	4-11

LIST OF FIGURES (CONTINUED)

<u>Figure</u>		<u>Page</u>
4-7	Variation of Effective Emissivity with Streamwise Length	4-14
4-8	Effect of Cooldown Radiation Interchange Model on In-Depth Temperature Predictions During Cooldown	4-16
4-9	Kinetically Controlled Response of Pyrolytic and ATJ Graphites to ANB 3066 Propellant Simulation	4-19
4-10	Diffusion Controlled Surface Response of FM5055A Carbon Phenolic to ANB3066 Propellant Simulation for Various Non-Dimensional Pyrolysis Gas Rates.	4-20
4-11	Thermal Conductivity of FM 5055A and MX 4926 Carbon Cloth Phenolics	4-21
4-12	Comparison of Measured and Predicted Temperatures for Different Carbon Cloth Phenolic Thermal Properties	4-22
4-13	Modified Thermal Conductivity for FM 5055A - 0 Degree Layup	4-23
4-14	Comparison of Predicted and Measured In-Depth Temperature Using Option 2 CMA	4-24
4-15	Thermal Conductivities for Pyrolytic Graphite, ATJ Graphite, GA Carbon, and AGSR Graphite	4-25
4-16	Throat Package Nodal Layout for 2-D Analysis	4-27
4-17	Comparison of Predicted and Measured In-Depth Temperature Histories at the Throat - Nozzle No. 8	4-29
4-18	Comparison of Predicted and Measured In-Depth Temperature Histories at the ATJ Backwall - Nozzle No. 8	4-30
4-19	One-Dimensional Analysis Temperature Correction Increment	4-32
4-20	Comparison of Predicted and Measured In-Depth Temperature Histories at the Throat - Nozzle No. 4	4-33
4-21	Comparison of Predicted and Measured In-Depth Temperature Histories at the Throat - Nozzle No. 5	4-33
4-22	Comparison of Predicted and Measured In-Depth Temperature Histories at the Throat - Nozzle No. 6	4-34
4-23	Comparison of Predicted and Measured In-Depth Temperature Histories at the Throat - Nozzle No. 7	4-34
4-24	One-Dimensional Nodal Grid for Exit Cone Carbon Phenolic Thermal Analysis	4-38
4-25	Comparison of Predicted and Measured In-Depth Temperatures for FM5055A Carbon Cloth Phenolic at an Area Ratio of 4.2 - Nozzle No. 4	4-38
4-26	Comparison of Predicted and Measured In-Depth Temperatures for FM5055A Carbon Cloth Phenolic at an Area Ratio of 4.2 - Nozzle No. 5	4-39
4-27	Comparison of Predicted and Measured In-Depth Temperatures for FM5055A Carbon Cloth Phenolic at an Area Ratio of 4.2 - Nozzle No. 6	4-39

LIST OF FIGURES (CONCLUDED)

<u>Figure</u>		<u>Page</u>
4-28	Comparison of Predicted and Measured In-Depth Temperatures for FM5055A Carbon Cloth Phenolic at an Area Ratio of 4.2 - Nozzle No. 7	4-40
4-29	Comparison of Predicted and Measured In-Depth Temperatures for FM5055A Carbon Cloth Phenolic at an Area Ratio of 4.2 - Nozzle No. 8	4-40

LIST OF SYMBOLS

A	area
A/A*	area ratio
B	pre-exponent factor
B' _c	non-dimensional char erosion rate $\dot{m}_c / \rho_e u_e C_M$
B' _g	non-dimensional pyrolysis gas rate $\dot{m}_g / \rho_e u_e C_M$
C	experimentally determined constant (used in equation 4-6)
C _H	Stanton number
C/A	Chromel/Alumel thermocouple
d	spacing between adjacent crystal planes
D	local beam length
E	activation energy
F	view factor
h, H	enthalpy
H _{GAS} , H _{STATIC}	static edge gas enthalpy
I	transmitted x-ray intensity
I ₀	x-ray incident beam intensity
K	correlation factor (used in equation 4-1)
k	thermal conductivity
k _{0°} , k _{90°}	thermal conductivity for the 0° and 90° layup angles, respectively

k_s	proportionality factor used in char swell correlation
\dot{m}	mass flux
n	percent of aluminum propellant loading by mass
O/F	mass ratio of oxidizer to fuel
p	partial pressure
P	pressure
PG	pyrolytic graphite
Pr	Prandtl number
$\dot{q}_{chem\ prod}$	rate of chemical energy into material
\dot{q}_{conv}	rate of energy convection into material
\dot{q}_{cond}	rate of energy conduction into material
q_{diff}	diffusion energy flux
$\dot{q}_{inc\ rad}$	rate of radiant energy arriving at surface
$\dot{q}_{net\ rad}$	rate of net radiant energy into material ($\dot{q}_{rad\ in} - \dot{q}_{rad\ out}$)
$\dot{q}_{rad\ in}$	rate of radiant energy absorption by material
$\dot{q}_{rad\ out}$	rate of radiant energy emission from material
R	nozzle radius, universal gas constant
\dot{s}	surface recession rate
T	temperature
T_{1D}, T_{2D}	temperature obtained from a one- and two-dimensional analysis, respectively

T_A, T_B	thermocouple locations in throat package
TC	thermocouple
u, v	velocity
\dot{W}	mass flowrate
x	thickness of absorbing material
X	moles of reduction per unit area per unit time
XSC	oxidation ratio
α	absorptivity
Γ	volume fraction of resin in a composite material
δ	depth below original surface
δ_{swell}	additional material thickness due to char swell
ΔT	temperature correction increment
ϵ	emissivity
η_{C*}	combustion efficiency
θ	angle of incidence, layup angle, time
λ	wavelength, streamwise length
μ/ρ	mass absorption coefficient
ρ	density
ρ_i	dens. ty of material component i
ρ_{o_i}	original density of material component i

ρ_{r_i}	residual (terminal) density of material component i
$\overline{\rho u^*}$	throat mass flux
$\rho_e u_e C_H$	convective heat transfer coefficient
$\rho_e u_e C_M$	mass transfer coefficient
σ	Stefan-Boltzmann constant
τ_{char}	predicted char thickness in the absence of char swell
ϕ	local boundary layer energy thickness
ψ_i	decomposition reaction order for i^{th} component

SUBSCRIPT

A	backside of AGSR graphite substrate
ARGEIBL	obtained from ARGEIBL computer program
B	backside of ATJ graphite
c	char
e	edge, environment
eff	effective
g	gas
o	chamber condition, non-blowing condition
s	stream
w	wall

SUPERScript

.	rate derivative
*	throat condition

SECTION 1

INTRODUCTION

The Solid Rocket Division of AFRPL recently conducted an in-house program to provide design information for multiple pulse duty cycle nozzles in solid rocket motor applications. During the course of this program, five instrumented nozzles were fabricated and tested. The material components for these nozzles included a MXC 313 carbon phenolic throat entrance section, a pyrolytic graphite coated nozzle throat, an ATJ graphite throat exit section, and a FM 5055A carbon cloth phenolic exit cone. The nozzles were tested in the Aeronutronic Simulator by Philco-Ford under Contract F04611-69-C-0039. In this simulator, a propellant slurry containing approximately 16 percent aluminum was used to simulate the flame temperature and combustion products of ANB-3066 solid propellant. The test variables included in the multiple pulse duty cycles were the number of pulses which varied from two to four, the length of each pulse which varied from 10 to 20 seconds, and the type of restart which included both hot and cold. The nominal chamber pressure for each pulse was approximately 750 psia.

After completing the test firings, the nozzles and reduced test data were delivered to Aerotherm for post-test analysis under Contract F04611-70-C-0019. This analysis included

- surface recession and char regression measurements
- in-depth density profile measurements for the carbon cloth phenolic in the exit cone at an area ratio of approximately 4.0
- in-depth crystallographic measurements for the carbon cloth phenolic in the exit cone at an area ratio of approximately 4.0
- prediction of transient in-depth temperatures in the nozzle throat insert, a comparison of predicted and measured temperatures at the backside of the AGSR substrate and the ATJ exit section and a comparison of predicted and measured nozzle throat recessions
- comparison of predicted and measured in-depth transient temperature distributions, of measured and predicted char regressions, and of measured and predicted surface recessions for the carbon cloth phenolic located in the exit cone at an area ratio of approximately 4.0

The objectives of this extensive post-test analysis were to characterize the degradation of the charring ablating exit cone material when subjected to

multiple pulse duty cycles, to obtain material thermal performance data which can be effectively used by the nozzle designer, and to correlate the material thermal performance data using conventional analytical techniques. The analytical techniques used in correlating the data were those included in the following computer programs:

- Aerotherm Chemical Equilibrium (ACE) Computer Program
- Aerotherm Real Gas Energy Integral Boundary (ARGEIBL) Computer Program
- Charring Material Ablation (CMA) Computer Program
- Axisymmetric Transient Heating and Material Ablation (ASTHMA) Computer Program

These analytical techniques were chosen

- because they have been used extensively for the thermal analysis of rocket nozzles and reentry nose cones
- because they have been validated for charring ablating and carbon/carbon composite materials for chamber pressures which range from 200 psia to 3000 psia (References 1-5)
- because they are currently being validated for pyrolytic graphites under Air Force Contract F04611-69-C-0081
- because they are or shortly will become available to the rocket motor community

The nozzle configuration used in the multiple pulse duty cycle tests, the test facility configuration, and a summary of the test results including chamber pressure and temperature histories are presented in Section 2.0. A description of the measured material performance which includes the surface recession, char regression, in-depth density profiles, and x-ray diffraction measurements are presented in Section 3. A description of the analytical techniques together with a comparison of measured and predicted material thermal performance is presented in Section 4. Finally, conclusions and recommendations are made in Section 5.

SECTION 2

MULTIPLE PULSE DUTY ROCKET MOTOR TESTS

The five instrumented nozzles which were tested in the Aeronutronic Solid Rocket Motor Simulator are described in Section 2.1, and the simulator test facility is described in Section 2.2. The propellant slurry used to simulate the solid rocket motor propellant is defined in Section 2.3. The duty cycles including the chamber pressure histories for each test are presented in Section 2.4. The thermocouple data from the spring loaded thermocouples behind the nozzle insert and from the plugs in the nozzle exit cone are presented in Section 2.5.

2.1 NOZZLE

The five nozzles used for the multiple pulse duty cycle and the geometry and materials of each nozzle were identical. A schematic drawing including the average nozzle dimensions is shown in Figure 2-1, and the detailed pre-test quality control records for each nozzle are summarized in Table 2-1. As shown in Figure 2-1, the throat entrance consisted of MXC 313 carbon phenolic which overlaps the pyrolytic graphite (PG) coating at the entrance to the nozzle throat. The PG coating which has a nominal thickness of 0.049 mils is supported by an AGSR graphite substrate, and the throat insert is insulated from the steel shell by the 150 RPD asbestos phenolic. The throat extensor consists of ATJ graphite backed by GA carbon. The taper on the backside of the ATJ graphite together with a corresponding taper on the backside of the GA carbon provided the axial structural support for the PG coating throat insert. The exit cone is composed of FM 5055A carbon cloth phenolic wrapped parallel to the nozzle centerline.

The thermal instrumentation for each nozzle consisted of two spring loaded Chromel/Alumel thermocouples and two thermocoupled plugs. The pre-test quality control records showed that all of the thermocoupled plugs had identical dimensions and that the locations of the thermocouples were identical for all of the plugs. The dimensions of the plug and the location of the three in-depth thermocouples are shown in Figure 2-2. As shown by this figure, the thermocouple nearest the surface is tungsten 5 percent rhenium/tungsten 26 percent rhenium with the other two being Chromel/Alumel.

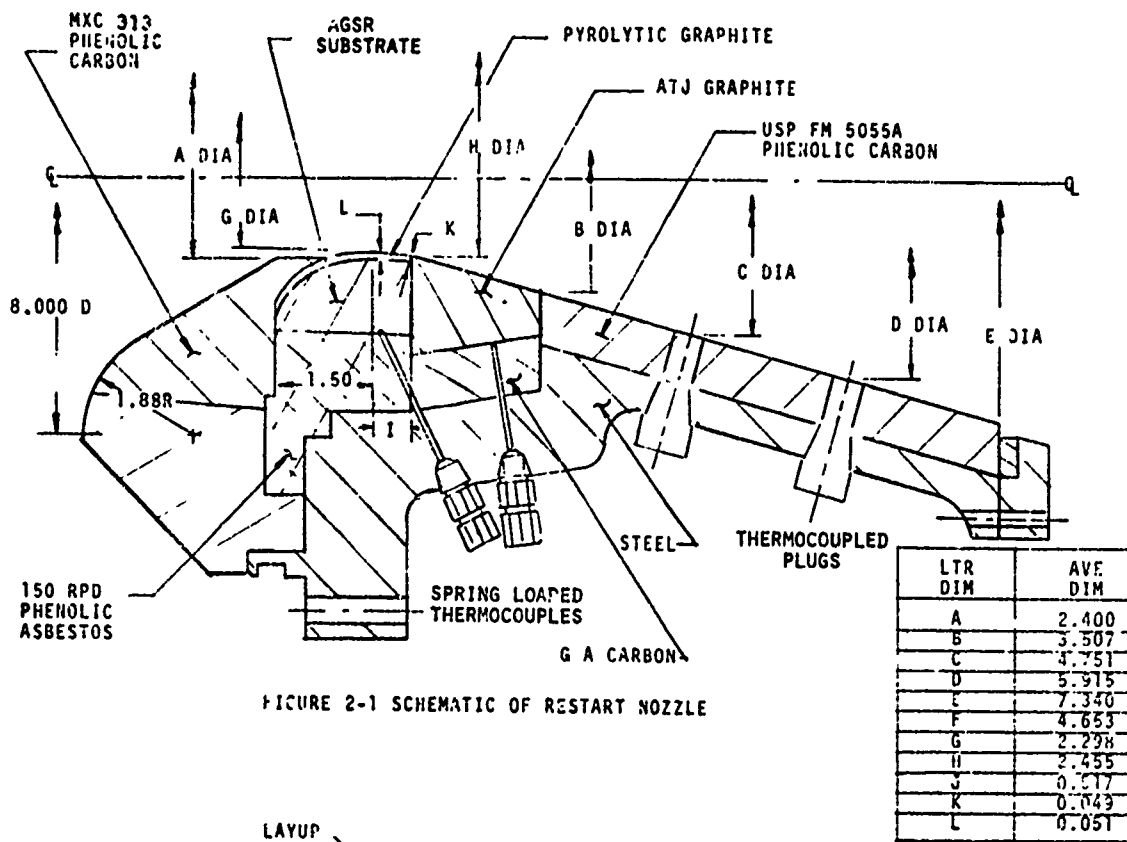


FIGURE 2-1 SCHEMATIC OF RESTART NOZZLE

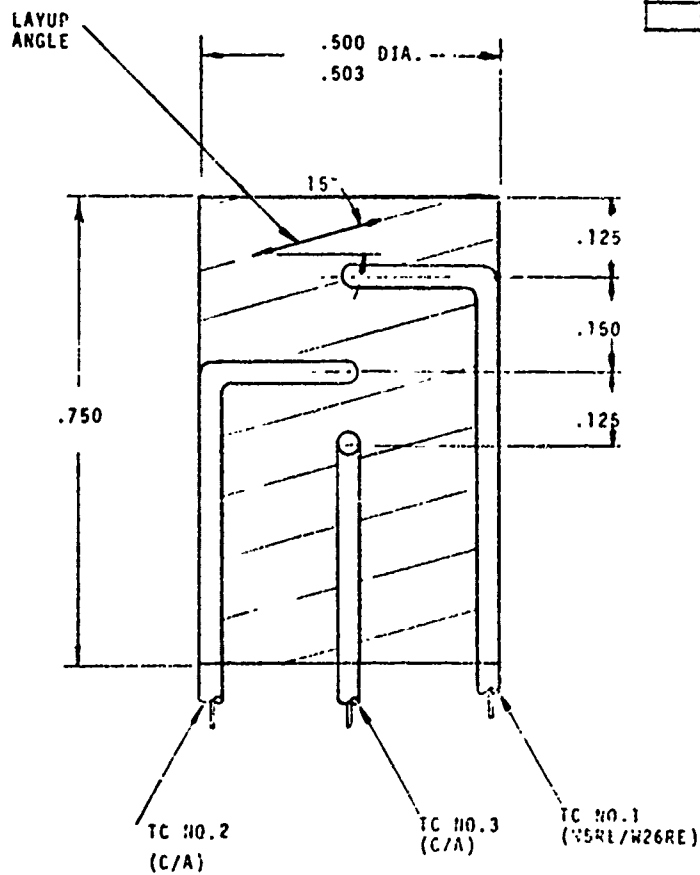


FIGURE 2-2 SCHEMATIC DRAWING OF THERMOCOUPLED PLUG

TABLE 2-1

PRE-TEST NOZZLE QUALITY CONTROL RECORD

Ltr. Dim.	-- Dimensions -- (in)					
	Nozzle Number*					
	4	5	6	7	8	Average
A	2.396	2.402	2.402	2.400	2.401	2.400
B	3.507	3.509	3.509	3.504	3.507	3.507
C	4.754	4.740	4.755	4.754	4.755	4.751
D	5.920	5.926	5.907	5.910	5.915	5.915
E	7.336	7.350	7.336	7.344	7.338	7.340
F	4.668	4.662	4.663	4.663	4.663	4.663
G	2.294	2.300	2.304	2.297	2.296	2.298
H	2.455	2.457	2.457	2.452	2.455	2.455
J	0.510	0.518	0.520	0.516	0.521	0.517
K	0.050	0.049	0.046	0.049	0.051	0.049
L	0.053	0.049	0.049	0.053	0.055	0.051

*The nozzle numbering system coincides with that used by the fabricator to designate the nozzles and that used by the test facility to designate the tests.

2.2 TEST FACILITY

The tests of the five instrumented nozzles were conducted in the Aeronutronic EME Solid Propellant Simulator which is a slurry gaseous rocket engine system. By proper selection of the propellant ingredients, it can be used to duplicate the combustion products and flame temperature of aluminized solid rocket propellants. The ingredients in the simulation propellant for the multiple pulse duty cycle firings consisted of oxygen, hydrogen, nitrogen, and a slurry mixture of 5 micron particles of aluminum and aluminum oxide mixed with RP-1 fuel and a small quantity of napalm. These propellant ingredients were injected into a 9.5 inch diameter combustion chamber which was lined with a one-inch thick hollow cylinder of silica phenolic. Because of surface recession during the simulator operation, this liner was replaced after conducting tests for nozzles 4, 5, and 6. The surface recession on the new liner was approximately 0.5 inches at the

conclusion of tests for nozzles no. 7 and 8. Attached to the simulator combustion chamber was a small rocket motor which was used to assist the startup operation of the simulator. The start sequence was as follows:

- ignition of a fuel rich mixture of oxygen and hydrogen in the start motor (The combustion products were injected through a sonic nozzle into the simulator combustion chamber.)
- after approximately 0.75 seconds, the oxygen and hydrogen propellant simulation ingredients were injected into the combustion chamber
- after approximately 0.25 seconds, nitrogen and the slurry mixture were also injected into the chamber
- after approximately 1.0 second, the start motor was shut down

During each test, both the ballistic and thermochemical performance of the simulator were monitored. The ballistic performance was determined by pressure measurements made in the simulator combustion chamber and in the start motor. The thermochemical performance was monitored by measuring the flowrates of each of the propellant ingredients which were then compared with pre-selected values. The thermochemical performance of the simulator in terms of the flame temperature and combustion products were determined from theoretical analysis using the pre-selected flow rates. This information is presented in the following section.

2.3 PROPELLANT

As mentioned previously, the propellant used in the rocket motor simulator consisted of the following ingredients: RP-1, napalm, five micron aluminum and aluminum oxide particles, oxygen, hydrogen and nitrogen. The chemical formula and nominal relative amounts of each ingredient are shown in Table 2-2, and the resulting chemical elemental concentrations are given in Table 2-3. The flame temperature and the major combustion products for this propellant at a chamber pressure of 700 psia are given in Table 2-4.

The propellant formulation given in Table 2-2 has an O/F ratio of 0.573 where the O/F ratio is defined as

$$O/F = \frac{\dot{W}_{\text{oxygen}}}{(\dot{W}_{\text{slurry}} + \dot{W}_{\text{hydrogen}})} \quad (2-1)$$

The flowrates and O/F ratio for each test are defined in Table 2-5. As shown by this table, the O/F ratio varied by only 2 percent (0.572 to 0.581).

TABLE 2-2
SIMULATOR PROPELLANT INGREDIENTS

Ingredient	Chemical Formula	Relative Amount by Mass Percent
RP-1/Tri-Chloro-Ethylene	$C_{1.642}H_{2.580}O_{0.115}N_{0.009}Cl_{2.135}$	30.4
Napalm	$CH_{1.9532}$	5.13
Aluminum	Al	11.31
Aluminum Oxide	Al_2O_3	8.24
	$Al_{1.0}H_{35.0}O_{5.0}C_{13.0}$	0.74
Oxygen	O_2	33.50
Nitrogen	N_2	8.70
Hydrogen	H_2	1.90

TABLE 2-3
SIMULATOR PROPELLANT ELEMENTAL CONCENTRATIONS

Element	Concentration gr atom/100 gr
Carbon	0.9047
Hydrogen	3.4605
Oxygen	2.3816
Nitrogen	0.6238
Chlorine	0.6508
Aluminum	0.5829

TABLE 2-4
 PROPERTIES AND COMBUSTION PRODUCTS
 OF THE SIMULATOR PROPELLANT

Properties	
Flame Temperature, °R	6210
Pressure, psia	700
Ratio of Specific Heats	1.19
Combustion Products	
Species	mol/100 gr
AlCl	0.156×10^{-1}
AlCl ₂	0.158×10^{-1}
CO	0.836×10^0
CO ₂	0.677×10^{-1}
Cl	0.562×10^{-1}
HCl	0.545×10^0
H	0.129×10^0
HO	0.384×10^{-1}
H ₂	0.837×10^0
H ₂ O	0.537×10^0
N ₂	0.310×10^0
O	0.343×10^{-1}
Al ₂ O ₃ (condensed)	0.275×10^0

TABLE 2-5
 MEASURED PROPELLANT FLOWRATES

Nozzle No.	Pulse No.	Flowrates (lb/sec)					O/F
		Slurry	Oxygen	Nitrogen	Hydrogen	Total	
4	1	11.298	6.787	1.769	0.385	20.239	0.580
	2	11.394	6.800	1.780	0.385	20.359	0.577
	3	11.410	6.800	1.769	0.385	20.364	0.577
5	1	11.300	6.780	1.777	0.385	20.242	0.580
	2	11.290	6.760	1.812	0.391	20.253	0.579
6	1	11.380	6.720	1.780	0.385	20.265	0.572
	2	11.380	6.760	1.780	0.390	20.310	0.574
	3	11.377	6.740	1.780	0.390	20.287	0.572
7	1	11.377	6.787	1.780	0.385	20.329	0.577
	2	11.377	6.840	1.770	0.391	20.378	0.581
	3	11.377	6.840	1.770	0.391	20.378	0.581
8	1	11.410	6.760	1.780	0.380	20.330	0.573
	2	11.410	6.830	1.770	0.385	20.395	0.579
	3	11.410	6.830	1.770	0.385	20.395	0.579
	4	11.410	6.830	1.770	0.385	20.395	0.579

Another parameter often used to characterize a solid rocket propellant is the oxidation ratio (XSO) which is defined by

$$XSO = \frac{\text{elemental concentration of oxygen}}{(\text{elemental concentration of oxygen in CO} + \text{AL}_2\text{O}_3)} \quad (2-2)$$

Applying this formula to the simulator propellant gives an oxidation ratio of 1.34 which is typical of solid rocket propellants with an aluminum loading of 16 percent.

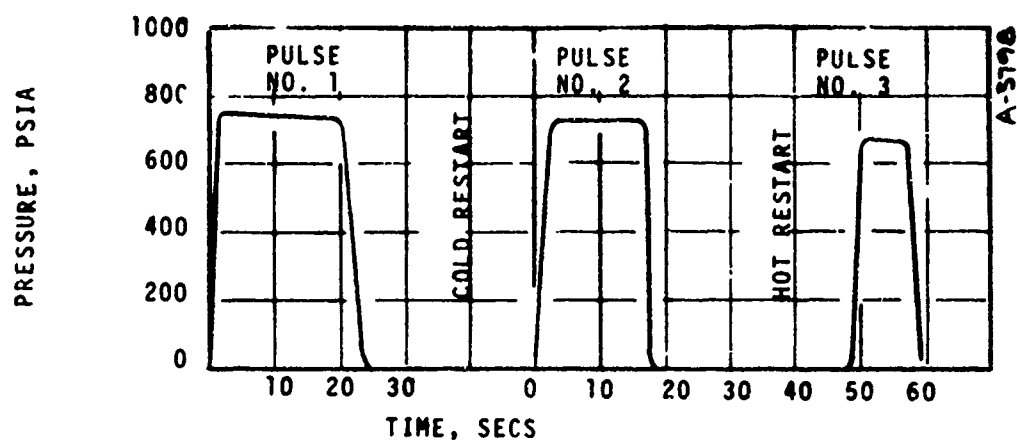
2.4 CHAMBER PRESSURE HISTORIES

The chamber pressure histories for the five multiple pulse duty cycle rocket nozzle tests are described in Table 2-6 and are shown graphically in Figure 2-3. More exact details of the chamber pressure histories are given in Appendix A. As shown by this figure, the number of pulses per test varied from

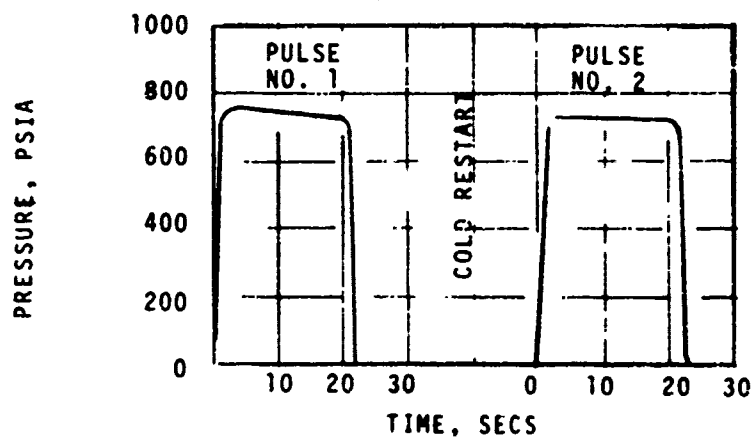
TABLE 2-6

DESCRIPTION OF MULTIPLE PULSE DUTY CYCLES

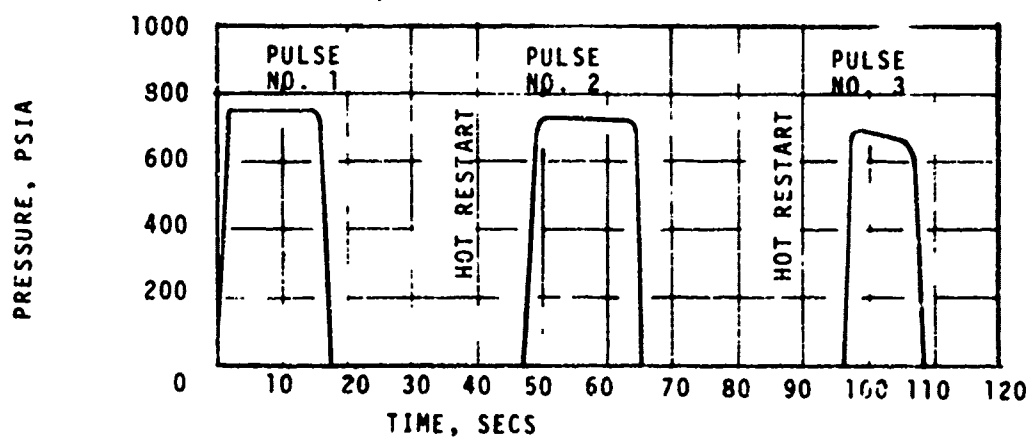
Nozzle Number	No. Of Pulse	Pulse Description			
		No.	Type of Restart	Nominal Duration (sec)	Nominal Chamber Pressure (psia)
4	3	1	-	20	750
		2	cold	16	725
		3	hot	8	675
5	2	1	-	20	740
		2	cold	20	725
6	3	1	-	15	750
		2	hot	15	730
		3	hot	10	680
7	3	1	-	15	750
		2	hot	15	725
		3	hot	10	680
8	4	1	-	11	750
		2	hot	11	740
		3	hot	11	720
		4	hot	11	680



a) NOZZLE NO. 4

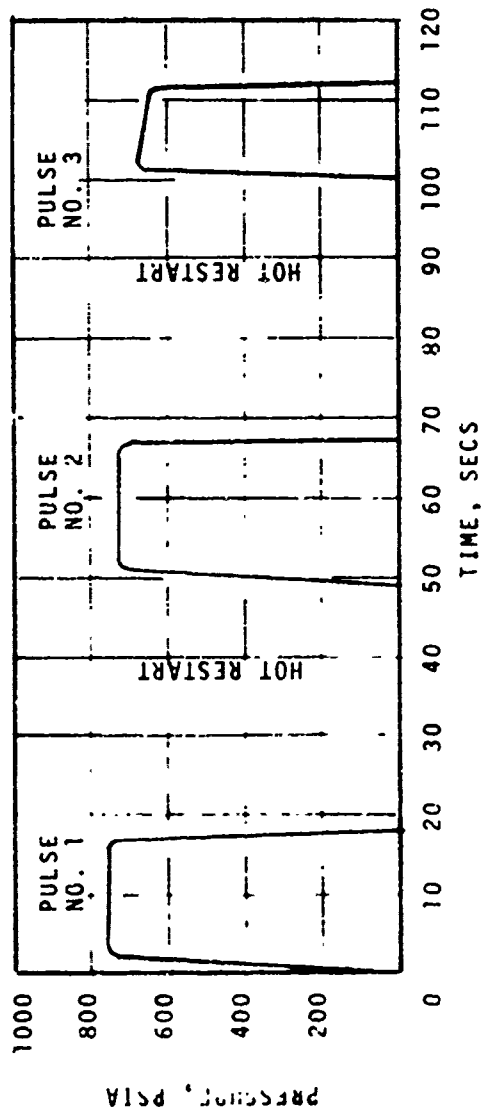


b) NOZZLE NO. 5

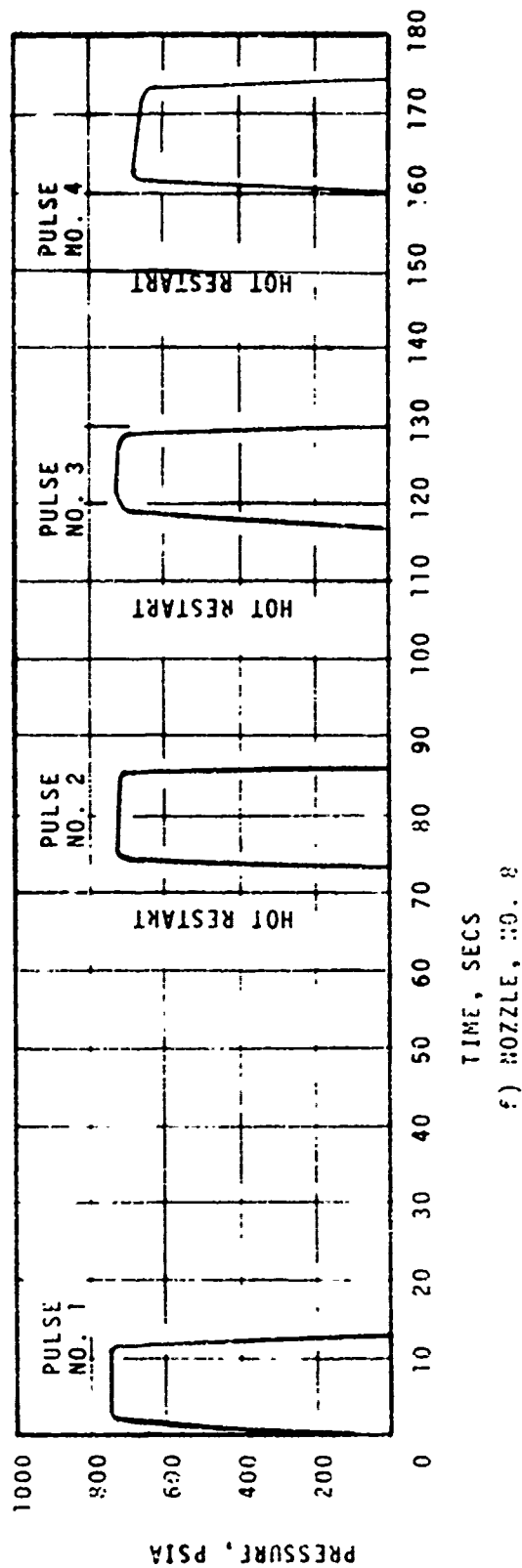


c) NOZZLE NO. 6

FIGURE 2-3 CHAMBER PRESSURE HISTORIES FOR MULTIPLE PULSE DUTY CYCLE ROCKET MOTOR TESTS.



d) NOZZLE, NO. 7



e) NOZZLE, NO. 8

FIGURE 2-3 (CONCLUDED)

two for nozzle no. 5 to four for nozzle no. 8, the pulse duration varied from 8 to 20 seconds, and both cold and hot restarts were performed. The nominal chamber pressure for all the pulses remained relatively constant as it varied only from 680 to 750 psia. In addition, the total test time was approximately 40 seconds for each of the five nozzles.

2.5 MEASURED IN-DEPTH TEMPERATURES

As described in Section 2.1 and shown by the schematic nozzle drawing (refer to Figure 2-1), the nozzles tested during this program had 1) two spring loaded thermocouples measuring temperatures at the backside of the AGSR and ATJ graphites in the nozzle throat assembly and 2) two thermocoupled plugs in the nozzle exit cone with three thermocouples in each plug. The maximum temperatures measured during a pulse motor burn by the spring loaded thermocouples and by the thermocouples in the upstream plug are summarized in Table 2-7. Detailed transient temperature histories for all of the thermocouples are presented in Appendix B.

TABLE 2-7
SUMMARY OF MEASURED TEMPERATURES

Nozzle No.	Pulse No.	Max. Burn Time (sec)	Measured Temperatures at Motor Burnout				
			Backside of AGSR (°F)	Backside of ATJ (°F)	Upstream Thermocoupled Plug		
					TC1 (°F)	TC2 (°F)	TC3 (°F)
4	1	22	900	1500	2200	400	150
	2	18	1000	1330	3000	450	100
	3	9	1880	1840	3260	1200	500
5	1	22	1070	1560	2480	450	150
	2	22	1550	1600	2400	1250	230
6	1	17	600	1150	2430	320	120
	2	18	1350	1820	3170	1360	520
	3	11	1830	1860	3240	1670	790
7	1	17	860	1350	1580	250	80
	2	17	1630	1860	2980	860	400
	3	11	2090	2180	3120	1500	700
8	1	12	630	1230	930	150	---
	2	12	1150	1570	2850	1350	---
	3	12	1620	2030	2380	650	---
	4	13	2090	2300	3070	1860	---

By comparing measured temperatures presented in Table 2-7 for similar pulse durations and for identical restart conditions, an estimate can be made of the accuracy of the temperature measurement. Similar environmental conditions exist at the surface of the nozzle for pulse no. 1 for nozzles no. 4 and 5 and

and for pulse no. 1 for nozzles no. 6 and 7. For nozzles no. 4 and 5, pulse no. 1 has a duration of 22 seconds while for nozzles no. 6 and 7, pulse no. 1 has a duration of 17 seconds. For the first two nozzles, the measured temperatures are 900 and 1070°F at the backside of the AGSR and 1500°F at the backside of the ATJ. These variations in the measured temperatures give an accuracy of approximately $\pm 100^\circ\text{F}$ for the spring loaded C/A thermocouples. Making a similar comparison for the upstream thermocoupled plug shows that essentially identical temperatures are measured for pulse no. 1 for nozzles no. 4 and 5. However, a large discrepancy exists in the measured temperatures for nozzles no. 6 and 7. This discrepancy which is approximately 850°F for TC no. 1 is probably a result of an error in defining the thermocouple depth. Based on this comparison, the accuracy of the temperature measurement is approximately $\pm 400^\circ\text{F}$ for TC no. 1. Because of the lower temperature gradients, the magnitude of the temperature variation would be less at the other two thermocouple locations in the thermocoupled plug.

SECTION 3

POST-TEST MEASURED MATERIAL PERFORMANCE

The post-test analyses to define the material thermal response of the multiple pulse duty cycle nozzles included:

- measurement of surface recession and char regression profiles (Section 3.1)
- measurement of in-depth material density profiles for the FM 5055A carbon cloth phenolic at a supersonic area ratio of approximately 4.0 (Section 3.2)
- measurements of in-depth crystal structure profiles for the FM 5055A carbon cloth phenolic at a supersonic area ratio of approximately 4.0 (Section 3.3)

3.1 SURFACE RECESSION AND CHAR THICKNESS MEASUREMENTS

Surface recession and char thickness data were obtained at several locations along each of eight circumferential planes in the five multiple pulse nozzles. The measurement planes were spaced evenly at every 45° of rotation about the nozzle centerline with the 0 degree reference plane passing through the thermocoupled plugs. Diameter measurements were taken by AFRPL personnel at one circumferential location but at several nozzle axial locations to confirm the pre-test surface geometry. In defining the post test surface recession, the assumption was made that the initial internal nozzle shape was axisymmetric and that the initial radius was half the measured diameter in all circumferential planes. The surface recessions were determined by subtracting the post-test measurements of surface radius from the corresponding pre-test dimension.

The post-test radii were defined using the technique described in Reference 6. The technique consisted of chucking the entire nozzle assembly in a machine shop lathe so that the lathe tool position indicator could be used to define the distance from the lathe (and nozzle) centerline to the surface point of interest (i.e. the local radius). Measurements of nozzle radius at several discrete surface points in one plane defined the post-test surface contours and enabled the evaluation of the local surface recession. The uncertainty in radius measurements taken in this manner was estimated to be ± 0.002 inches. The post-test nozzle surface contours determined using this measurement technique are compared to pre-test contours in Figures 3-1 through 3-5. Photographs showing typical surface characteristics are shown in Figure 3-6.

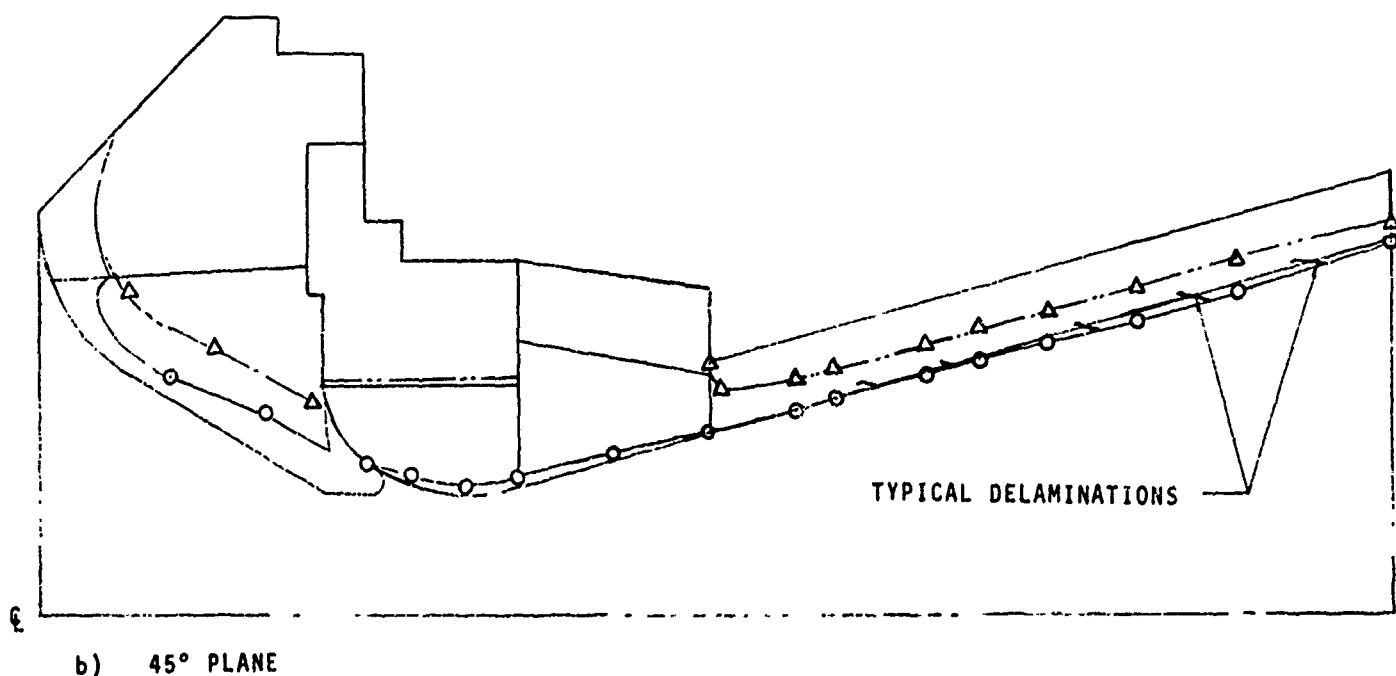
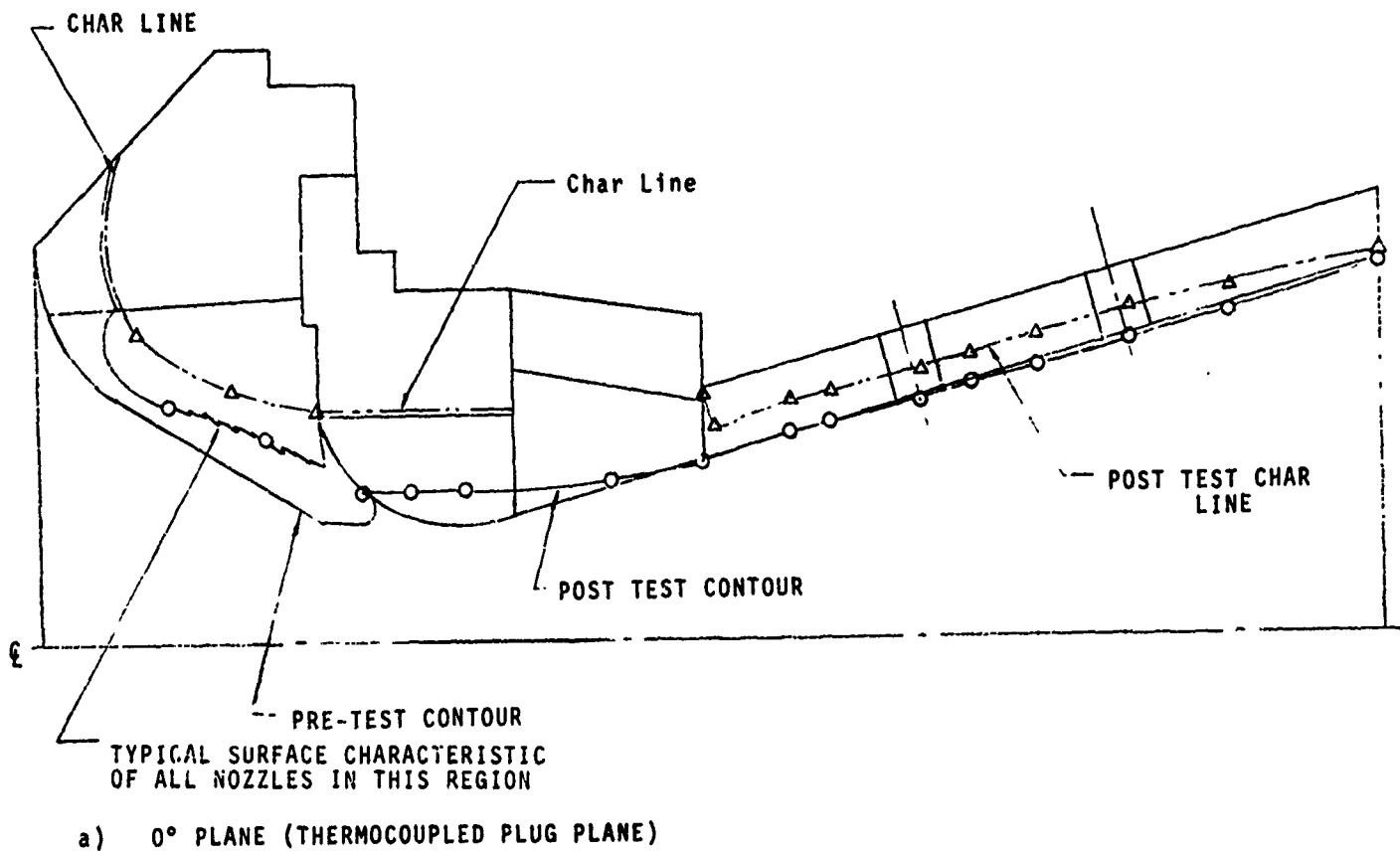
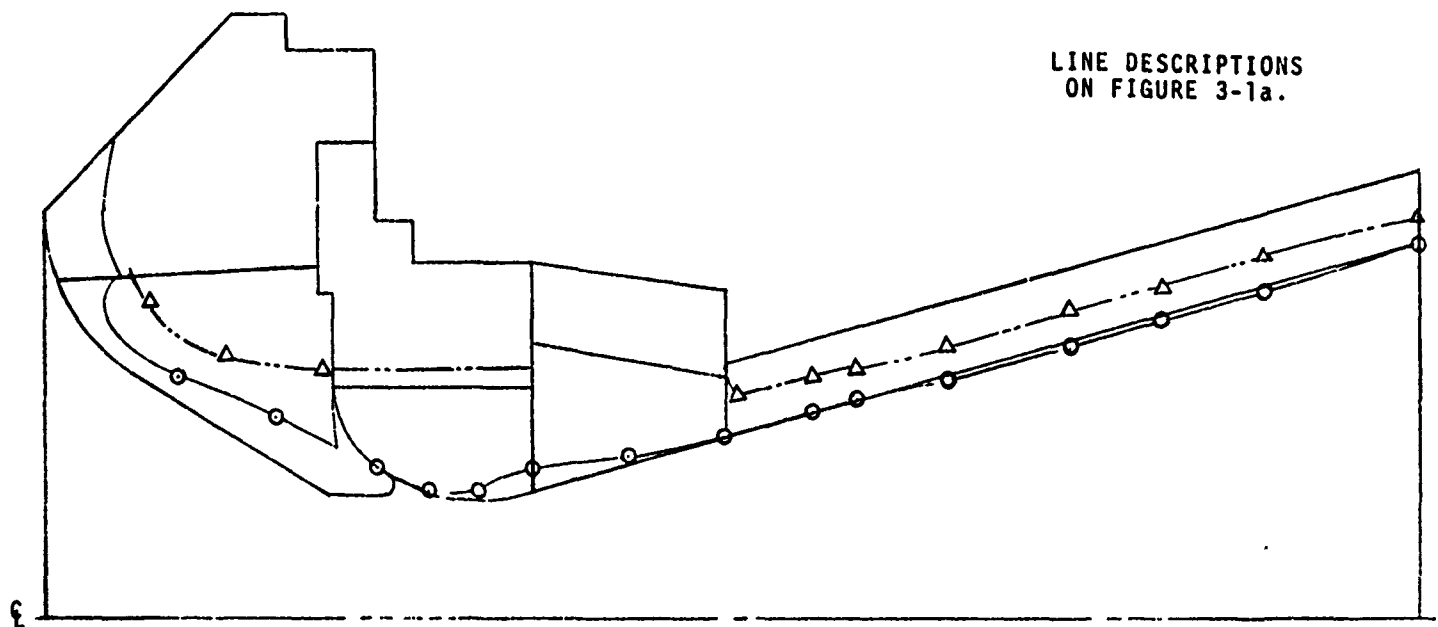
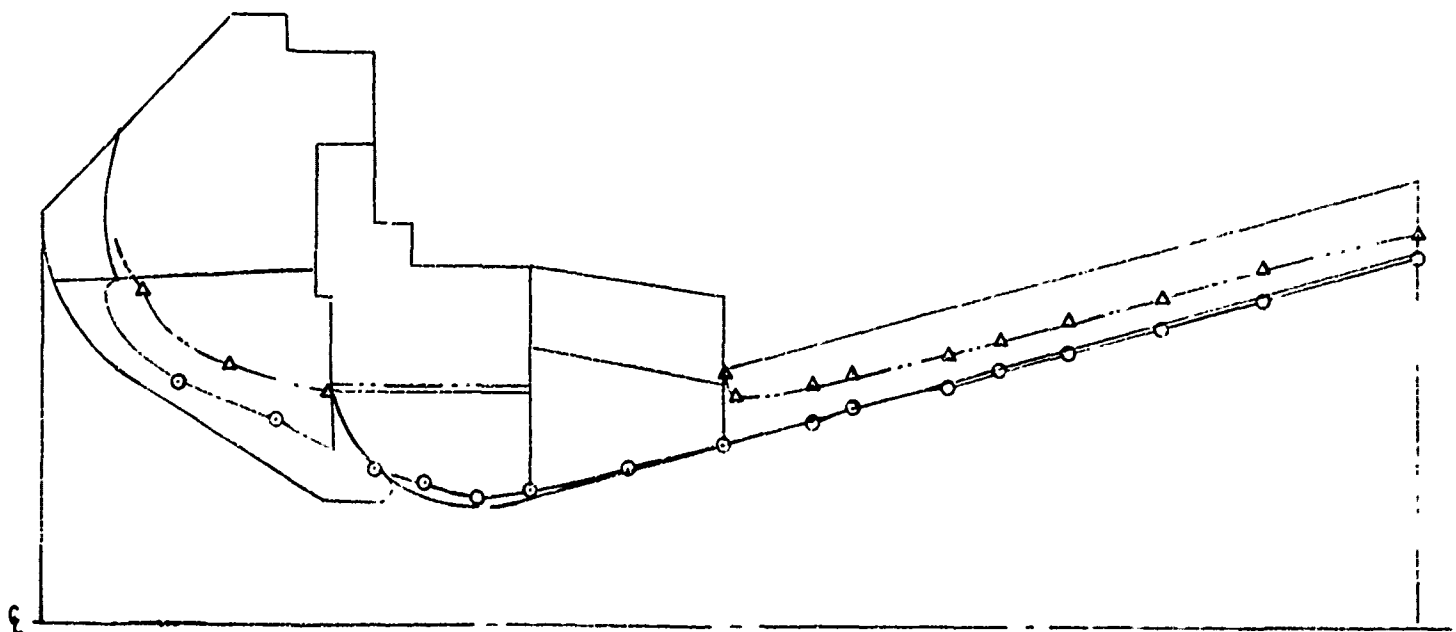


FIGURE 3-1 PRE, POST, AND CHAR LINE CONTOURS FOR NOZZLE NO. 4

LINE DESCRIPTIONS
ON FIGURE 3-1a.



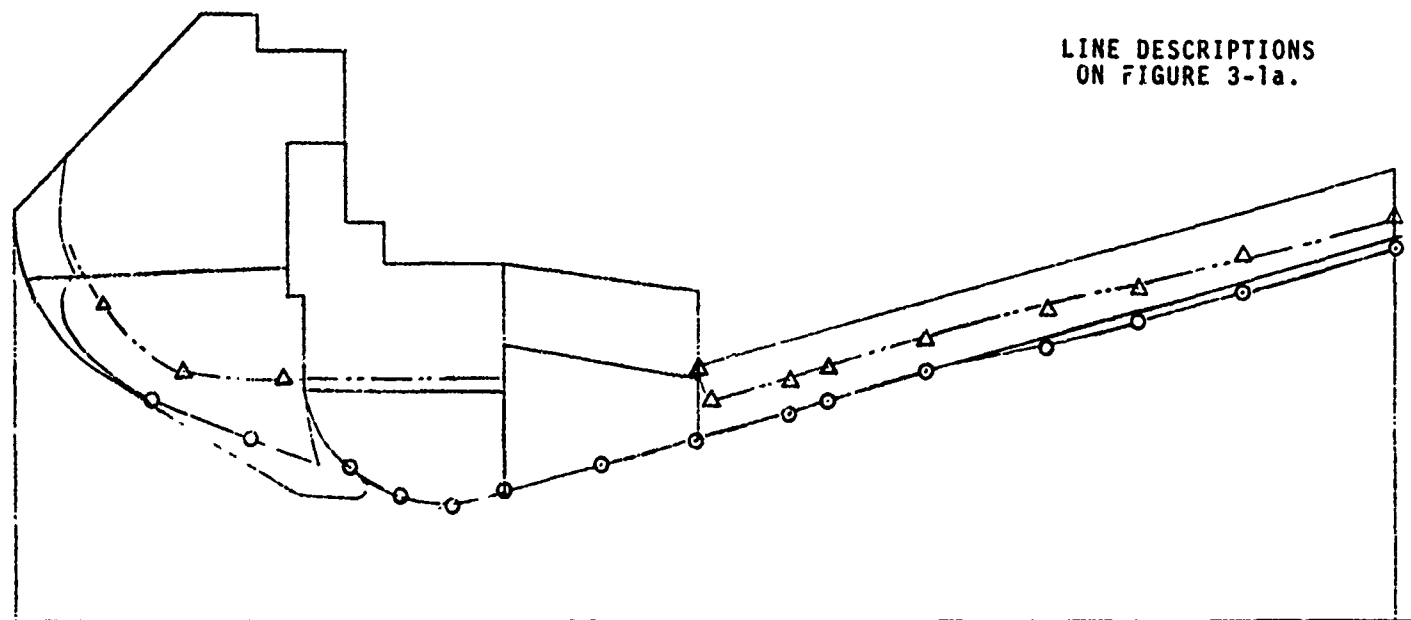
c) 90° PLANE



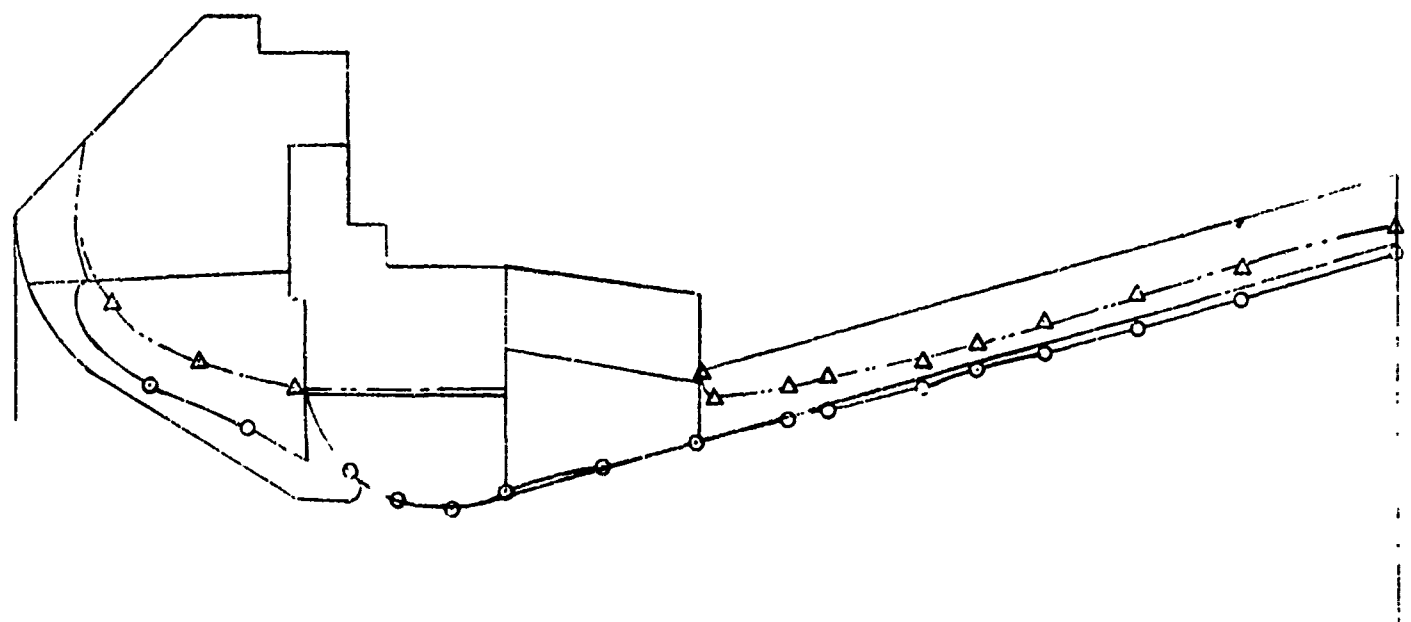
d) 135° PLANE

FIGURE 3-1 (CONTINUED)

LINE DESCRIPTIONS
ON FIGURE 3-1a.



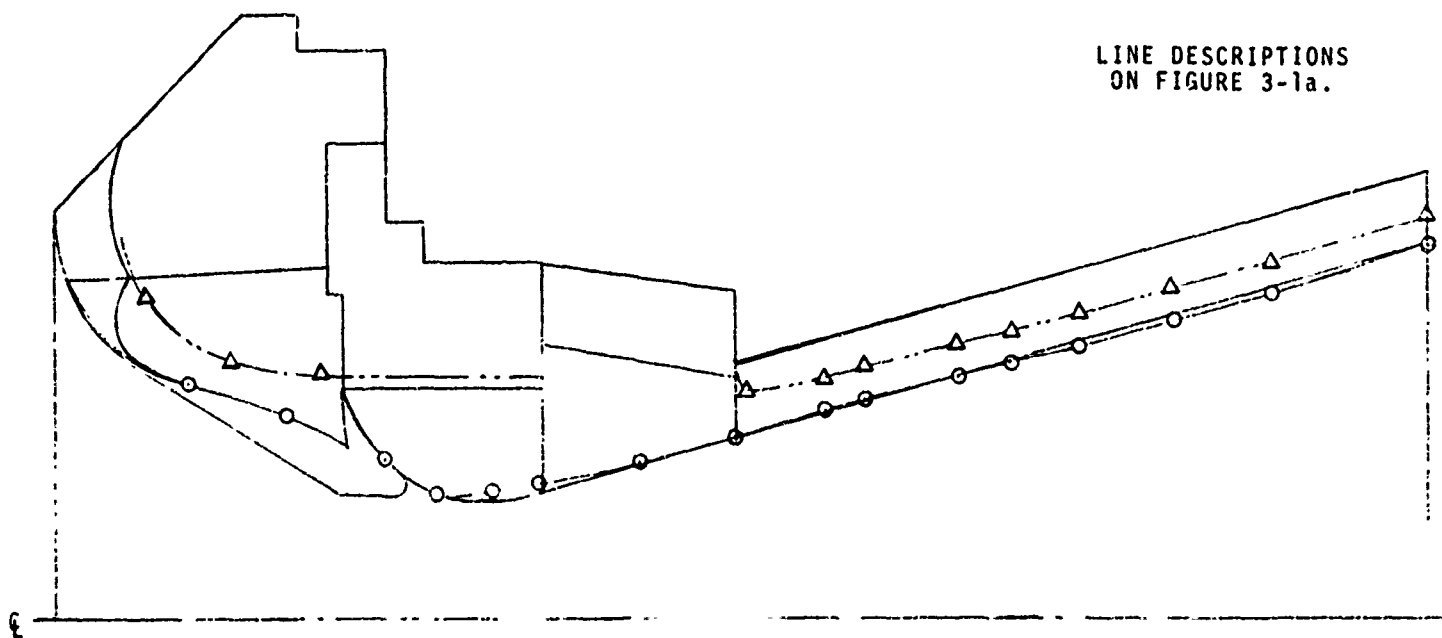
e) 180° PLANE



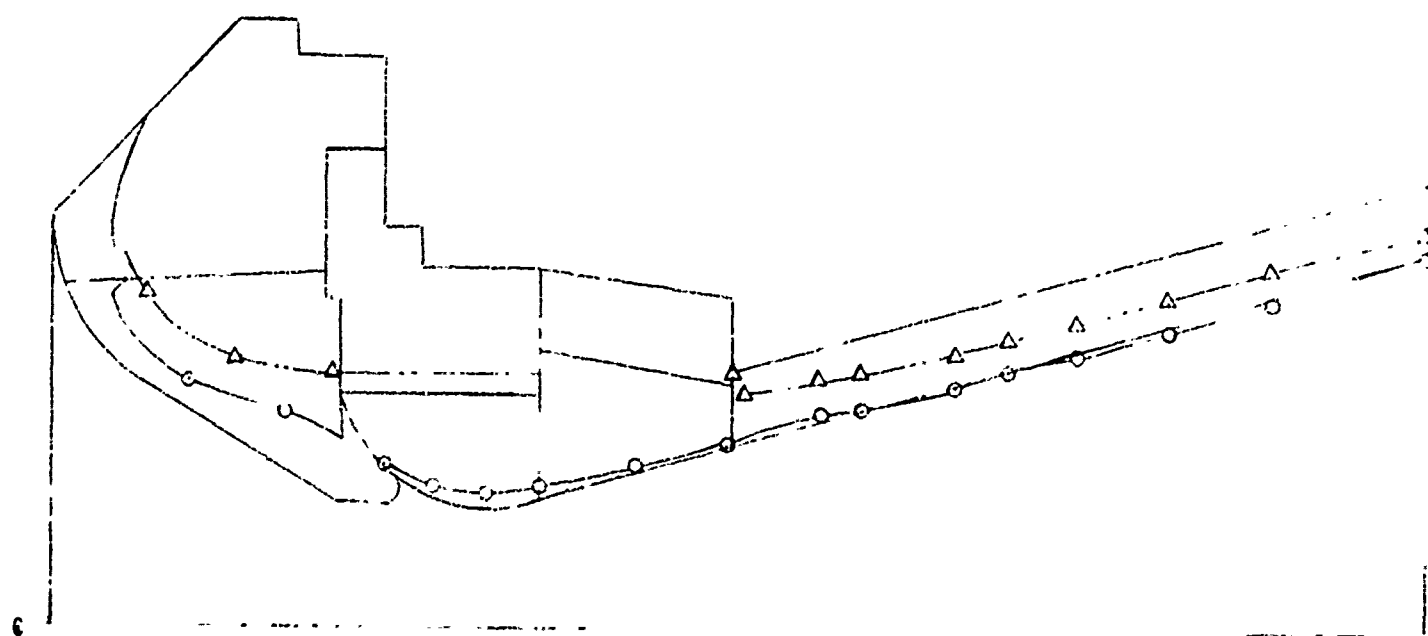
f) 225° PLANE

FIGURE 3-1 (CONTINUED)

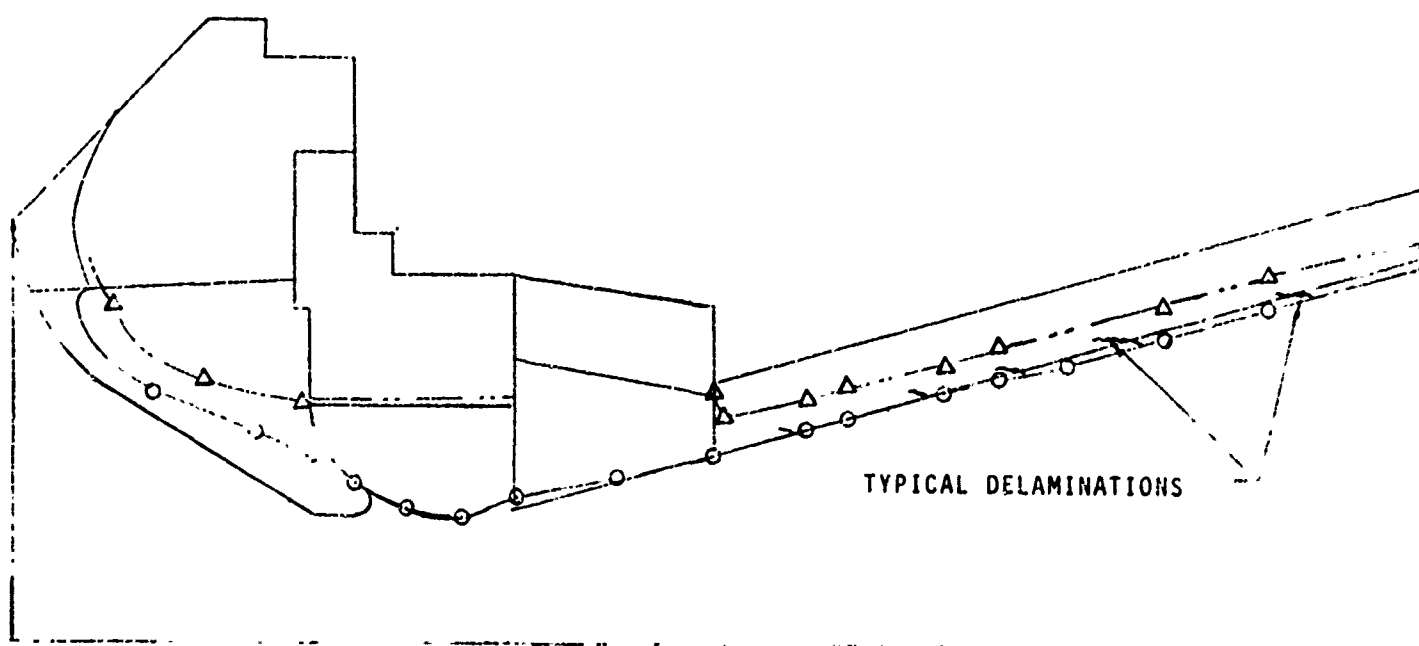
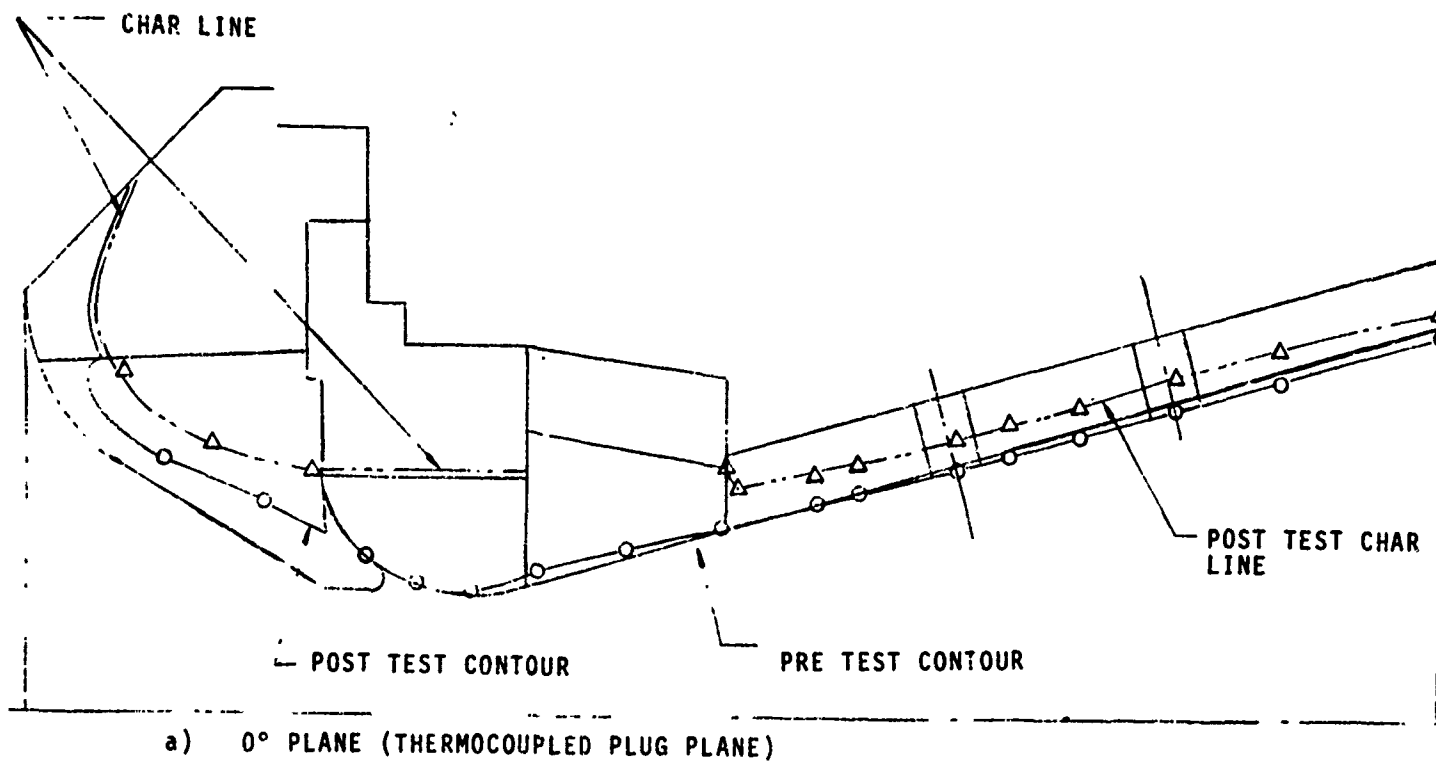
LINE DESCRIPTIONS
ON FIGURE 3-1a.



g) 270° PLANE



h) 315° PLANE
FIGURE 3-1 (CONCLUDED)



b) 45° PLANE

FIGURE 3-2 PRE, POST, AND CHAR LINE CONTOURS FOR NOZZLE NO. 5

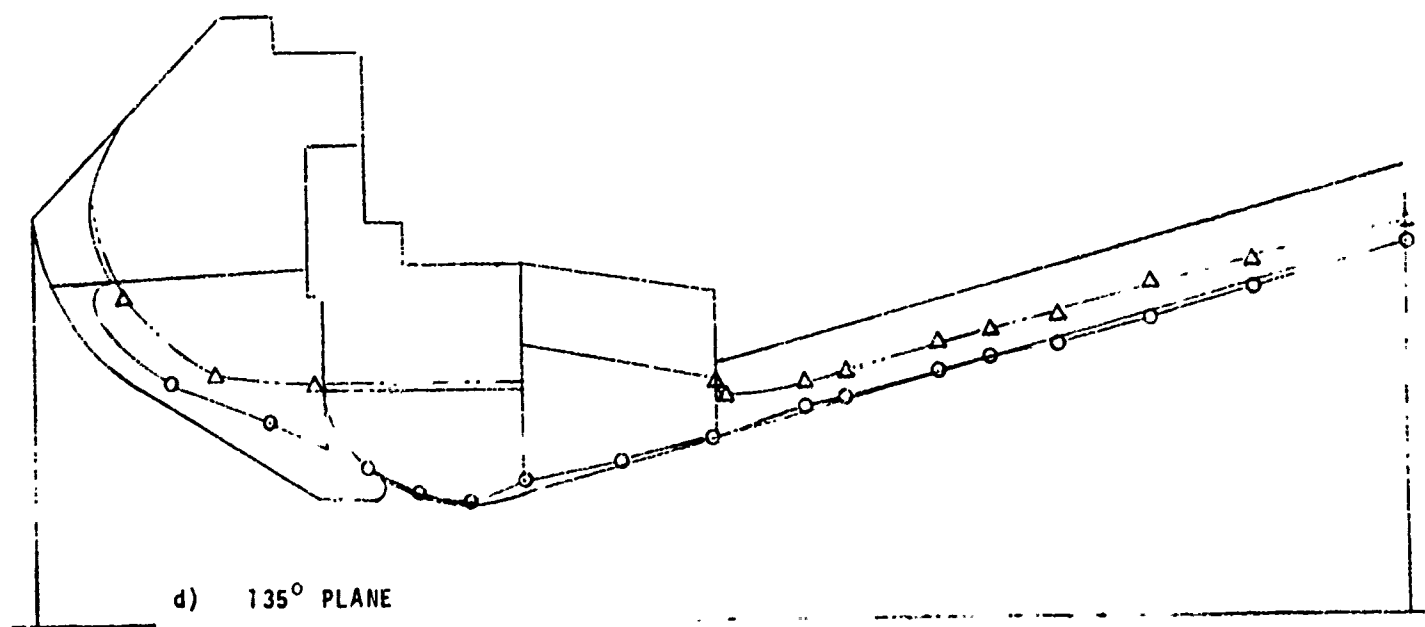
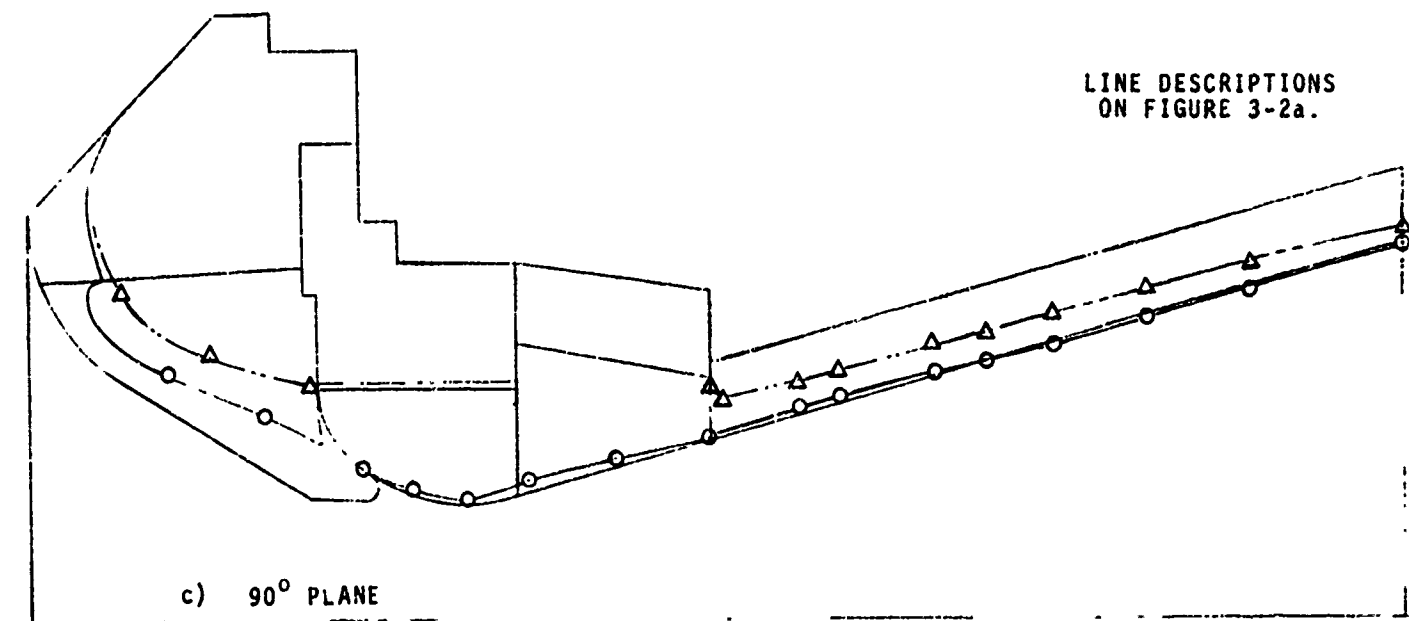


FIGURE 3-2 (CONTINUED)

LINE DESCRIPTIONS
ON FIGURE 3-2a.

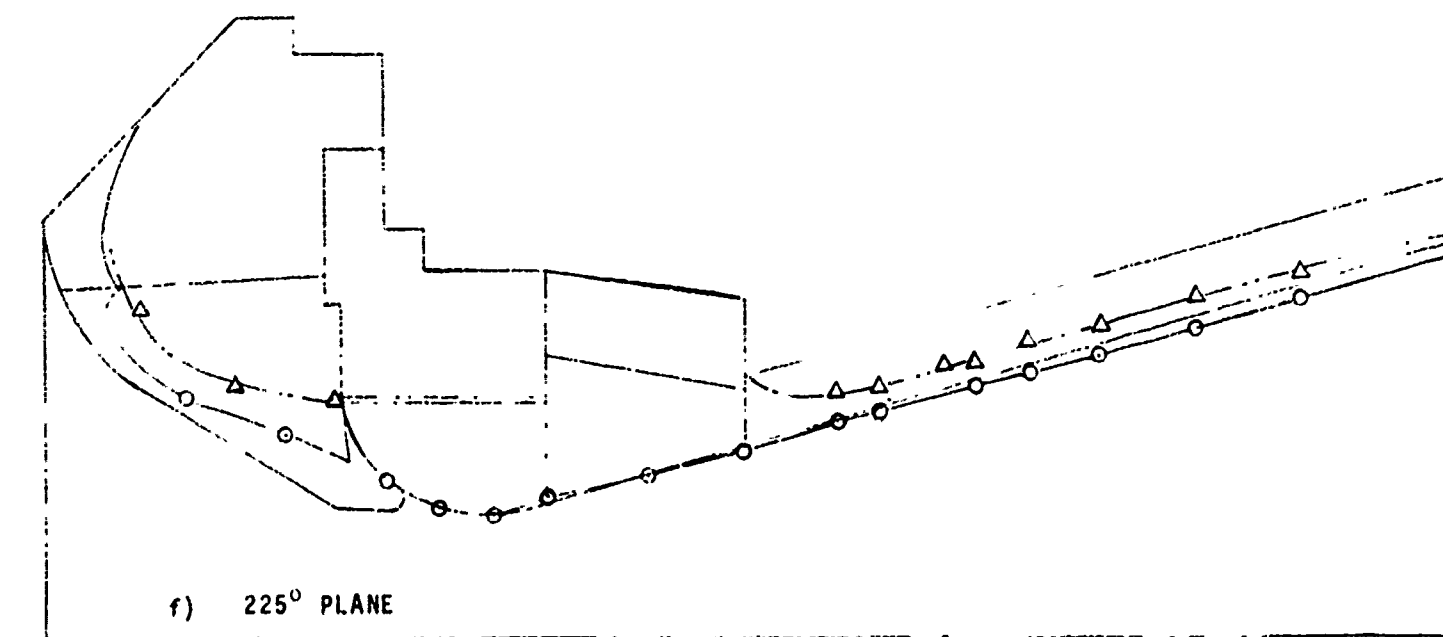
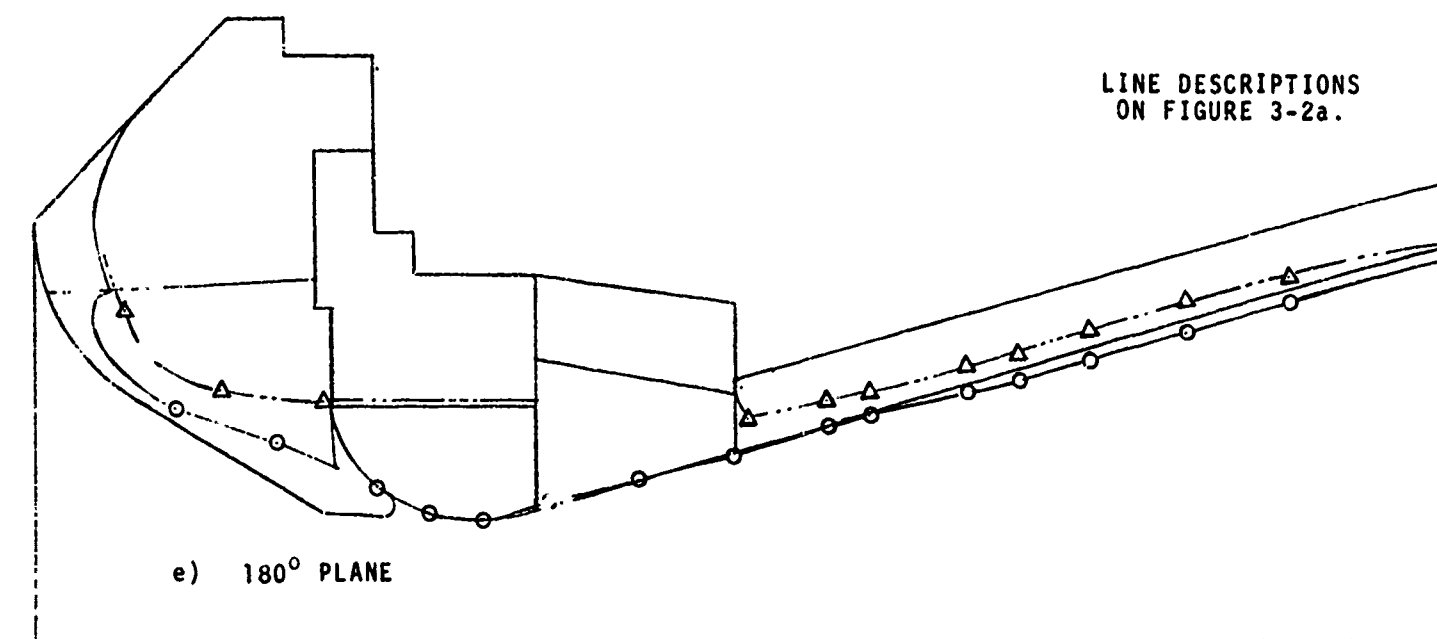


FIGURE 3-2 (CONTINUED)

LINE DESCRIPTIONS
ON FIGURE 3-2a.

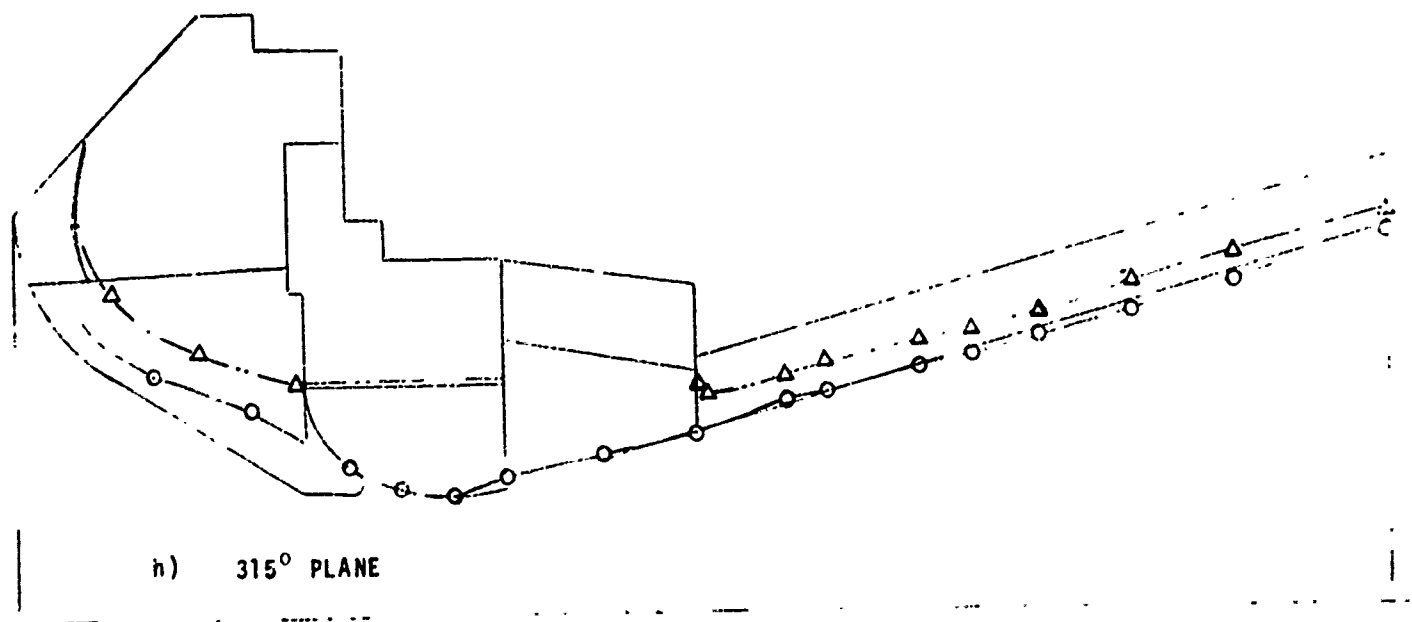
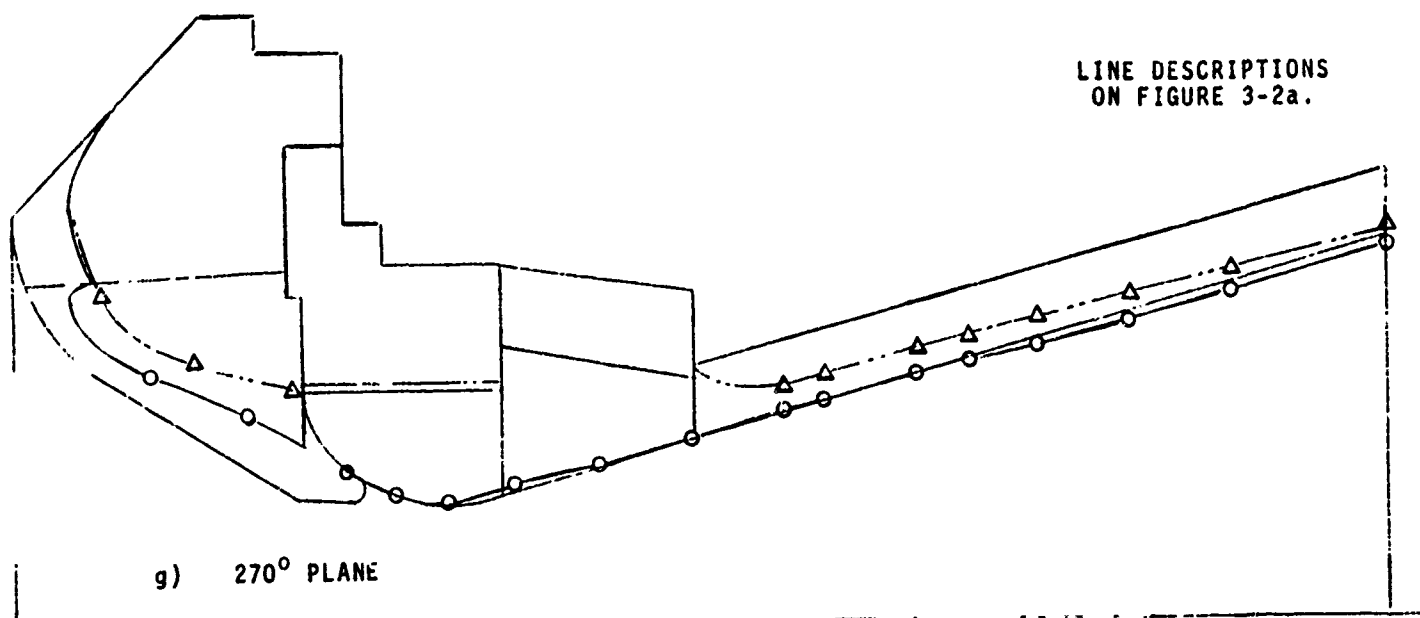
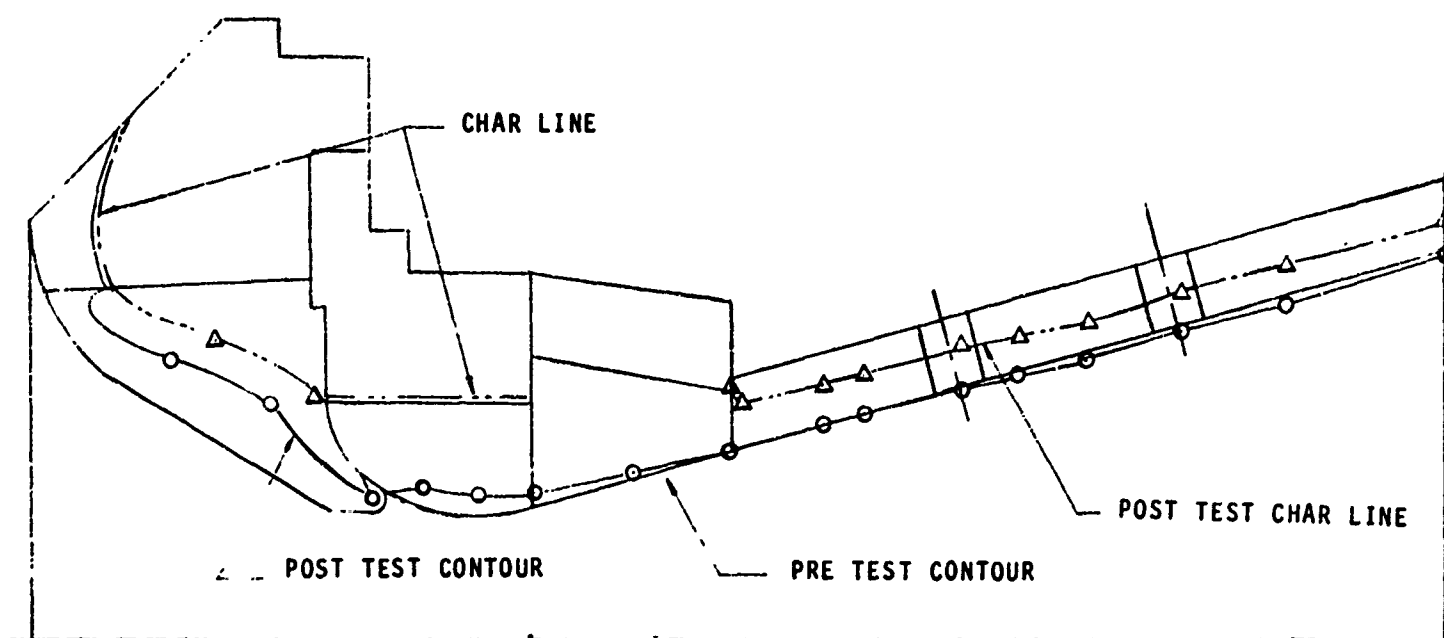
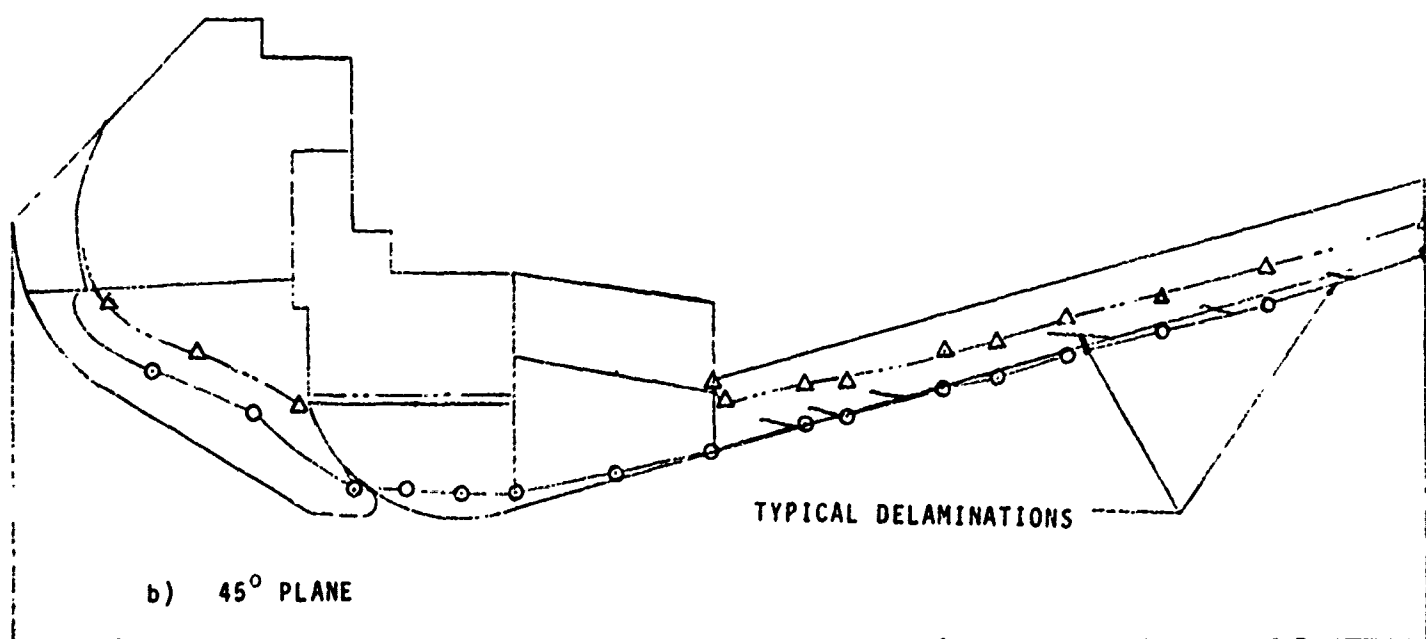


FIGURE 3-2 (CONCLUDED)



a) 0° PLANE (THERMOCOUPLED PLUG PLANE)



b) 45° PLANE

FIGURE 3-3 PRE, POST, AND CHAR LINE CONTOURS FOR NOZZLE NO. 6

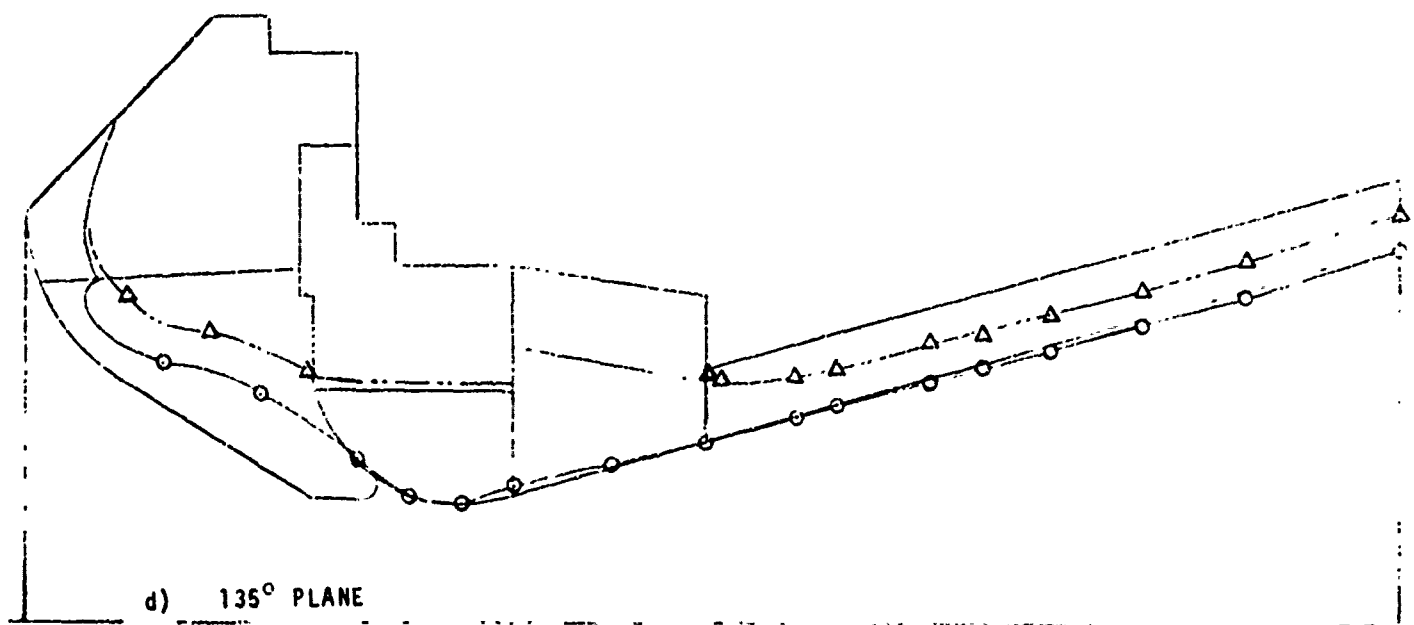
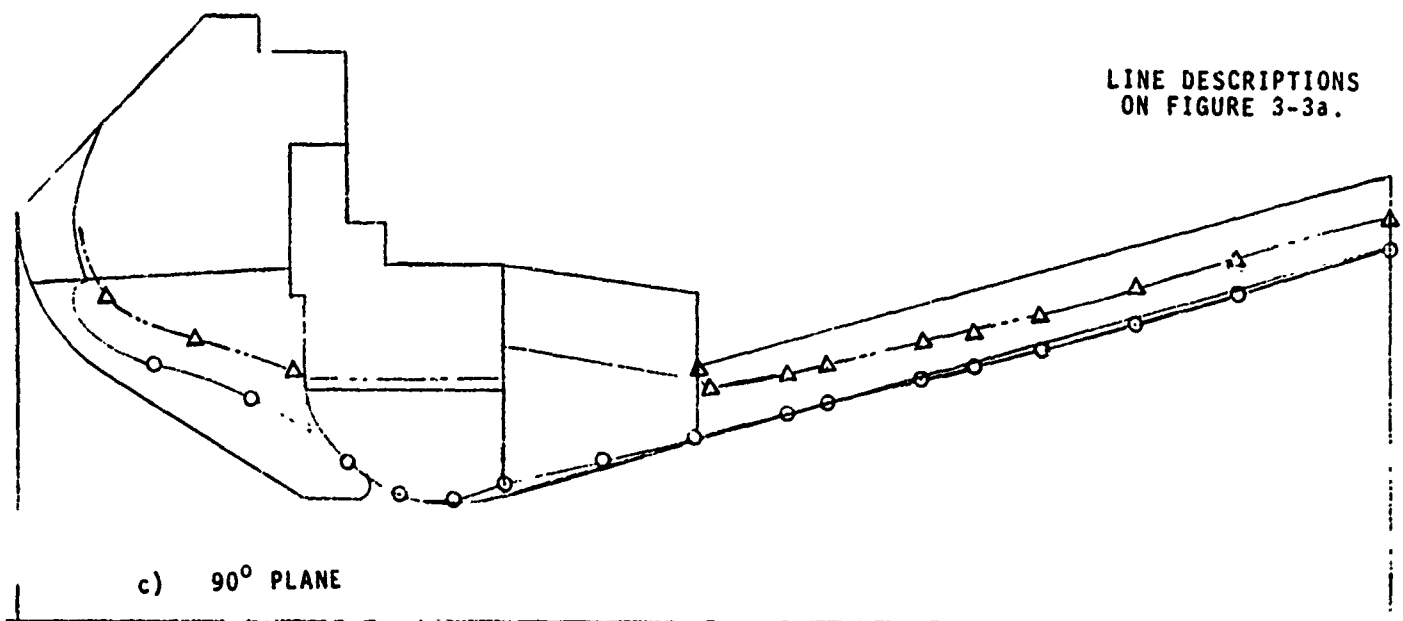
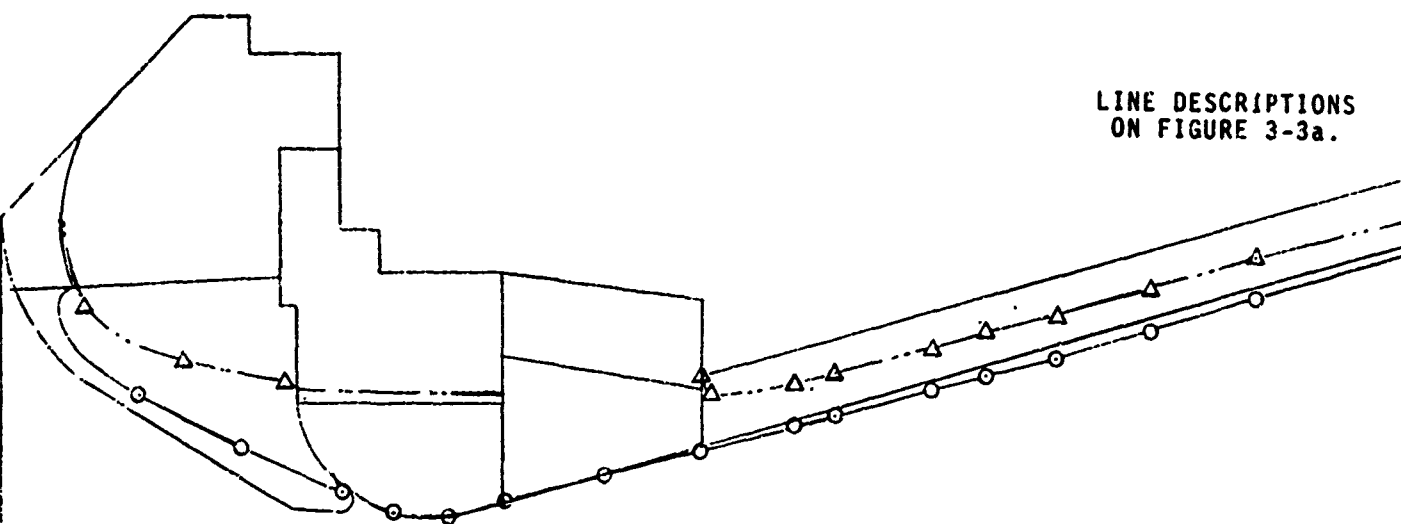
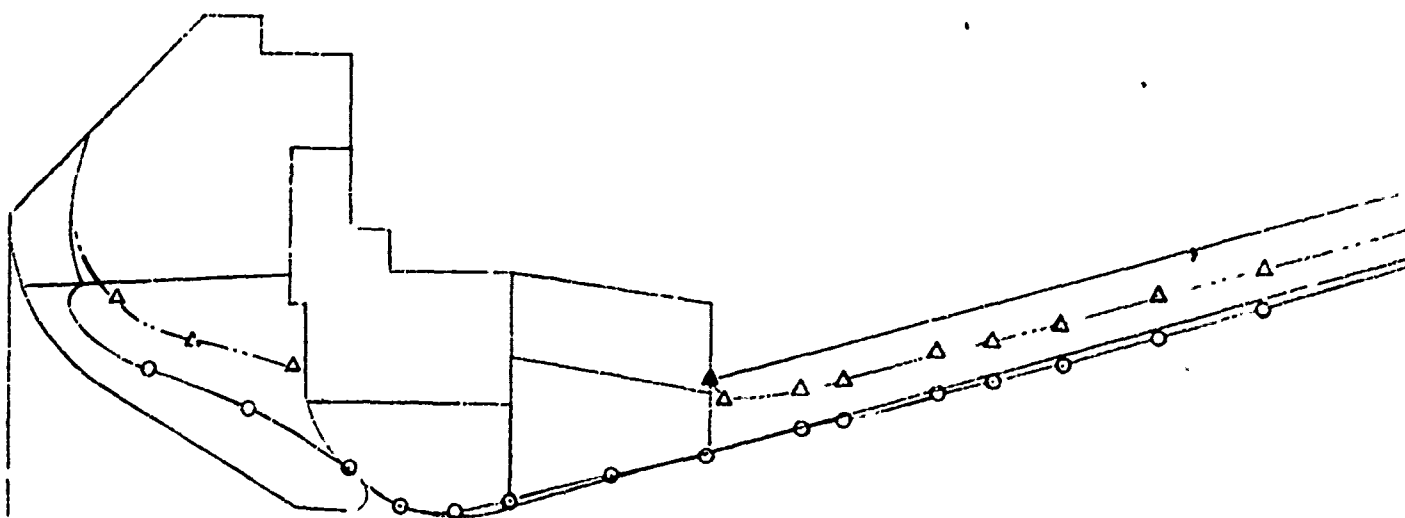


FIGURE 3-3 (CONTINUED)

LINE DESCRIPTIONS
ON FIGURE 3-3a.



e) 180° PLANE



f) 225° PLANE

FIGURE 3-3 (CONTINUED)

LINE DESCRIPTIONS
ON FIGURE 3-3a.

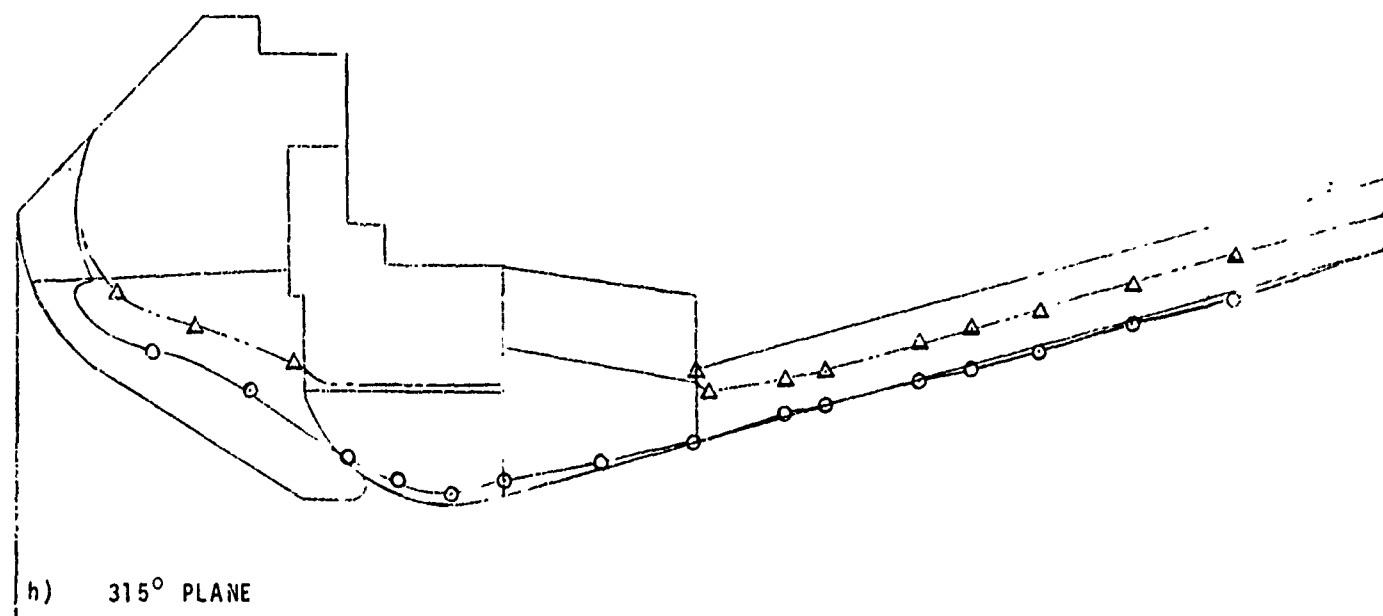
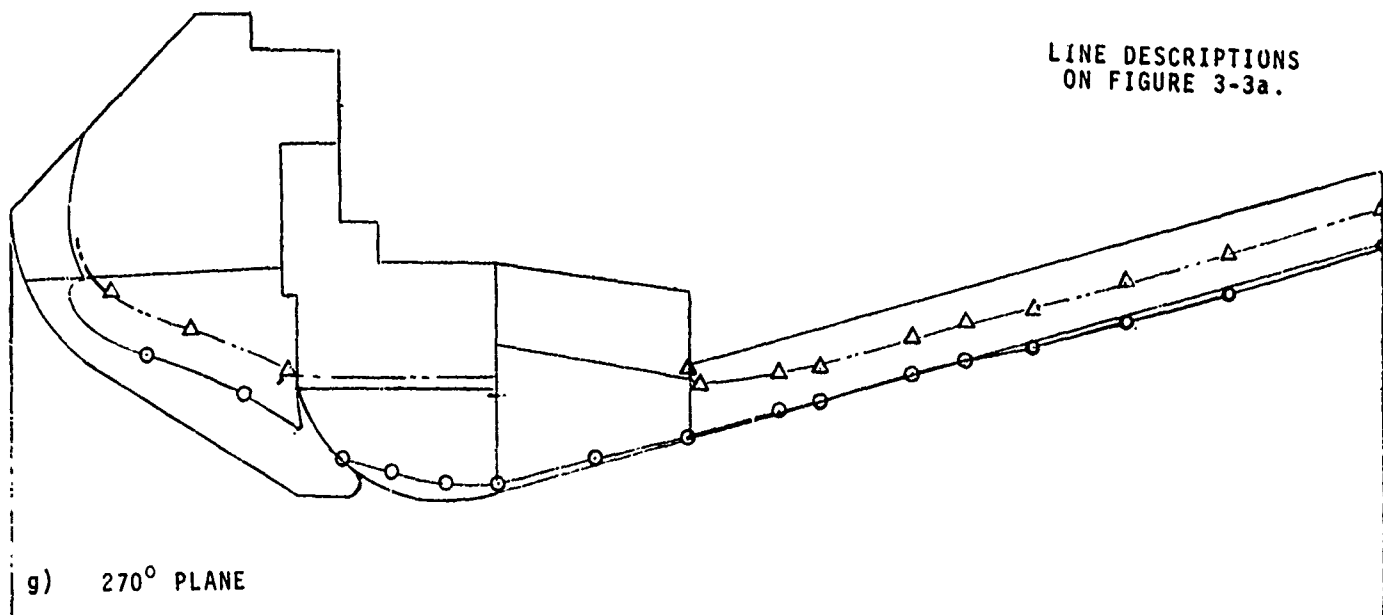
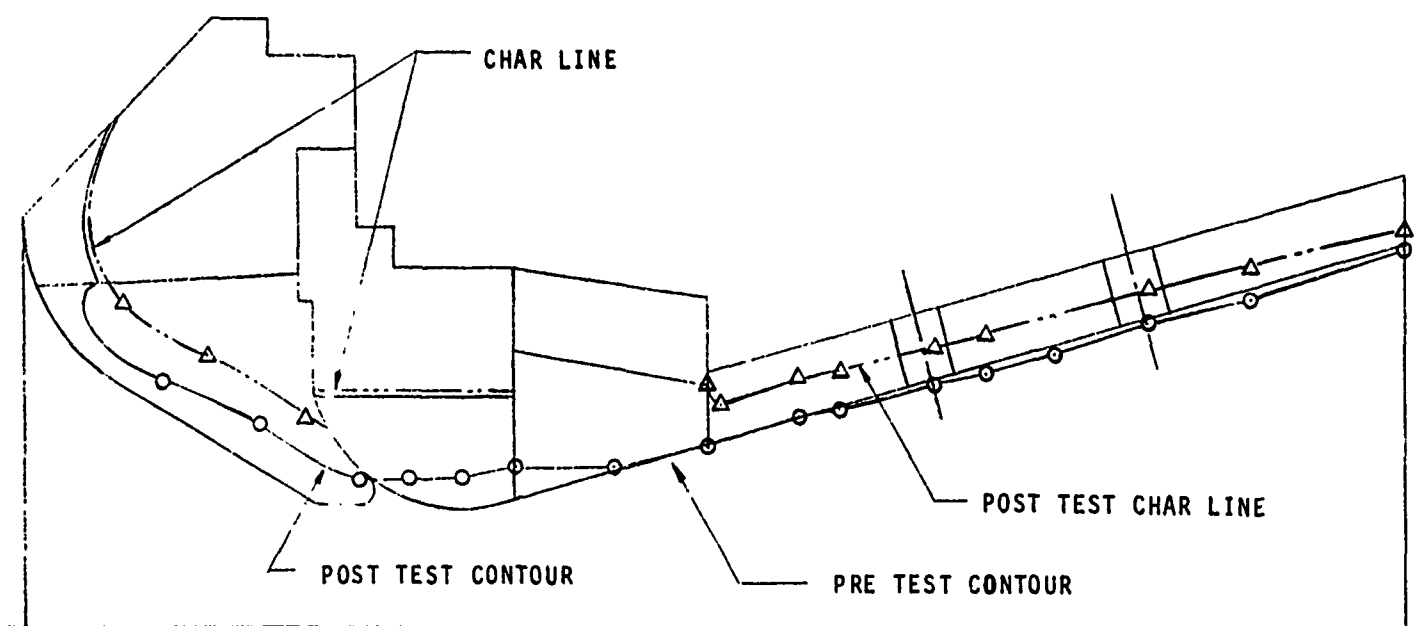
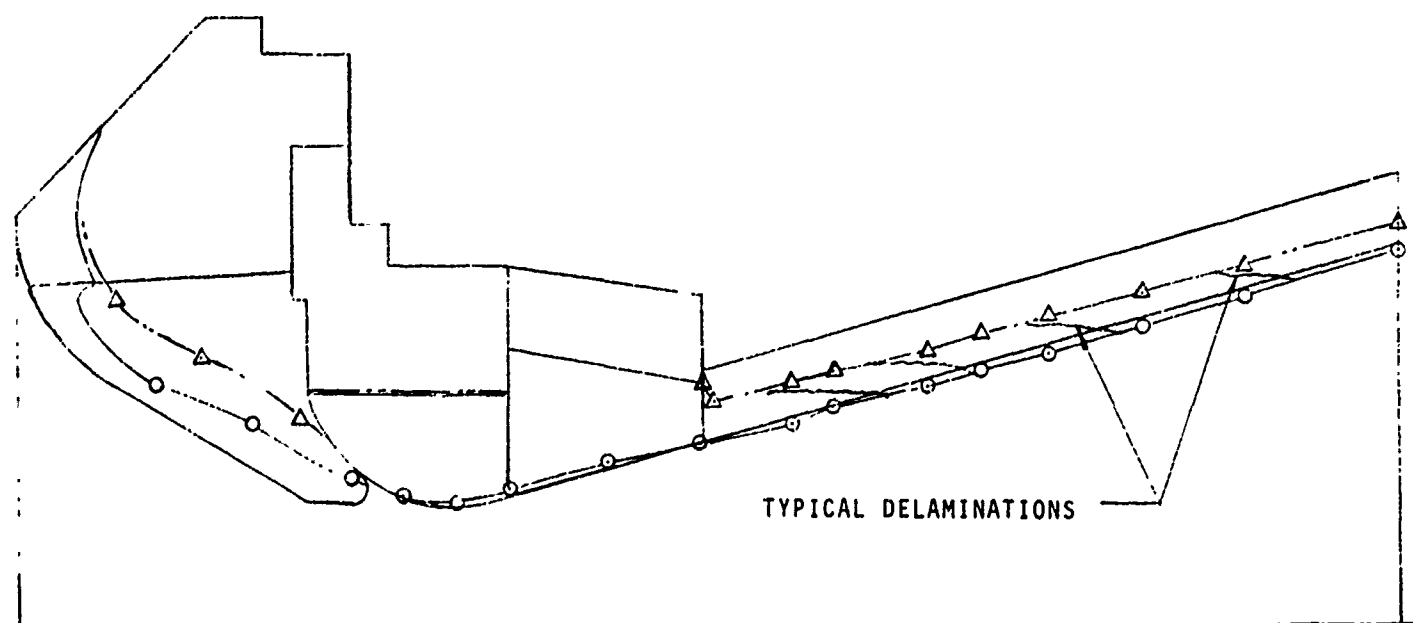


FIGURE 3-3 (CONCLUDED)



a) 0° PLANE (THERMOCOUPLED PLUG PLANE)



b) 45° PLANE

FIGURE 3-4 PRE, POST, AND CHAR LINE CONTOURS FOR NOZZLE NO. 7

LINE DESCRIPTIONS
ON FIGURE 3-4a.

c) 90° PLANE

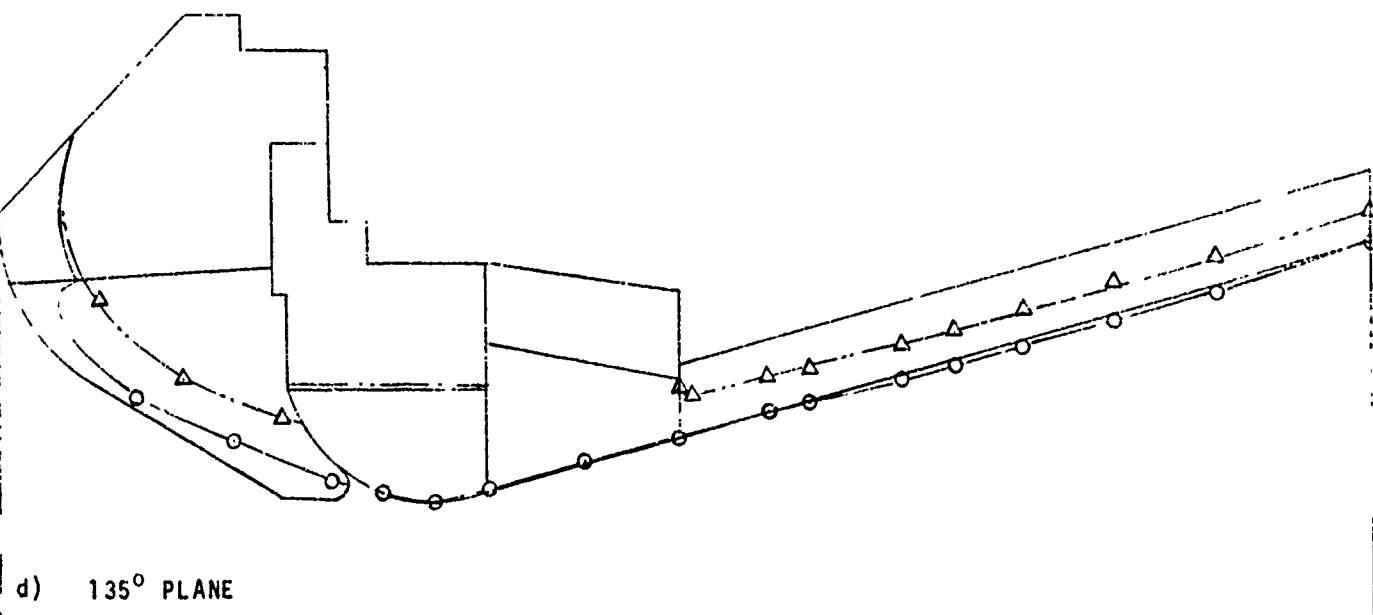
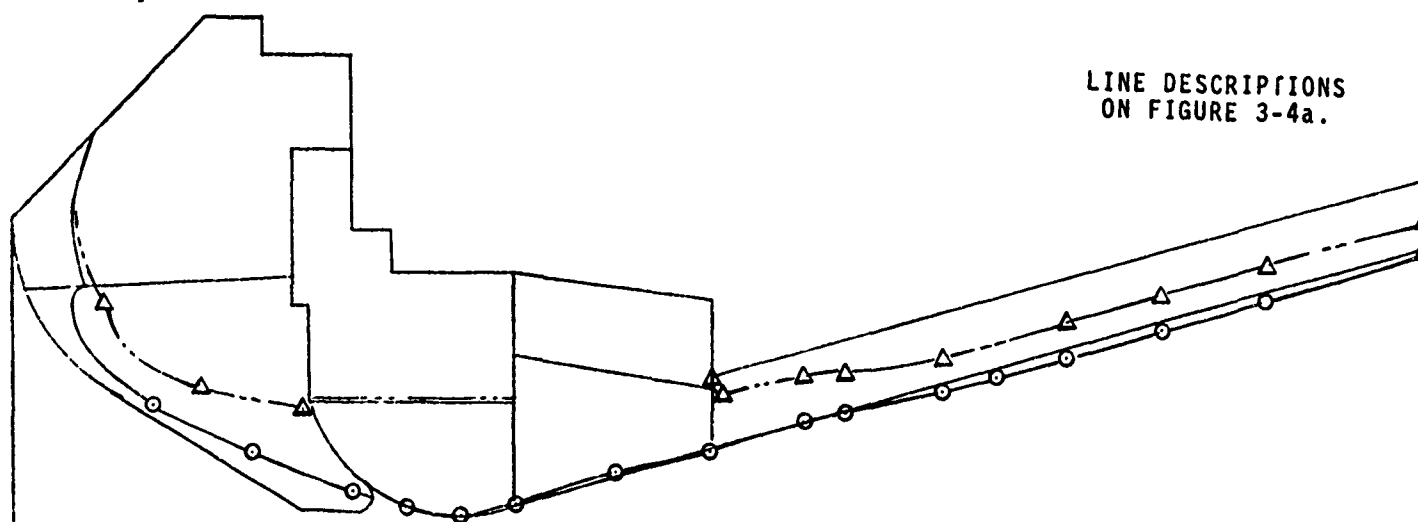
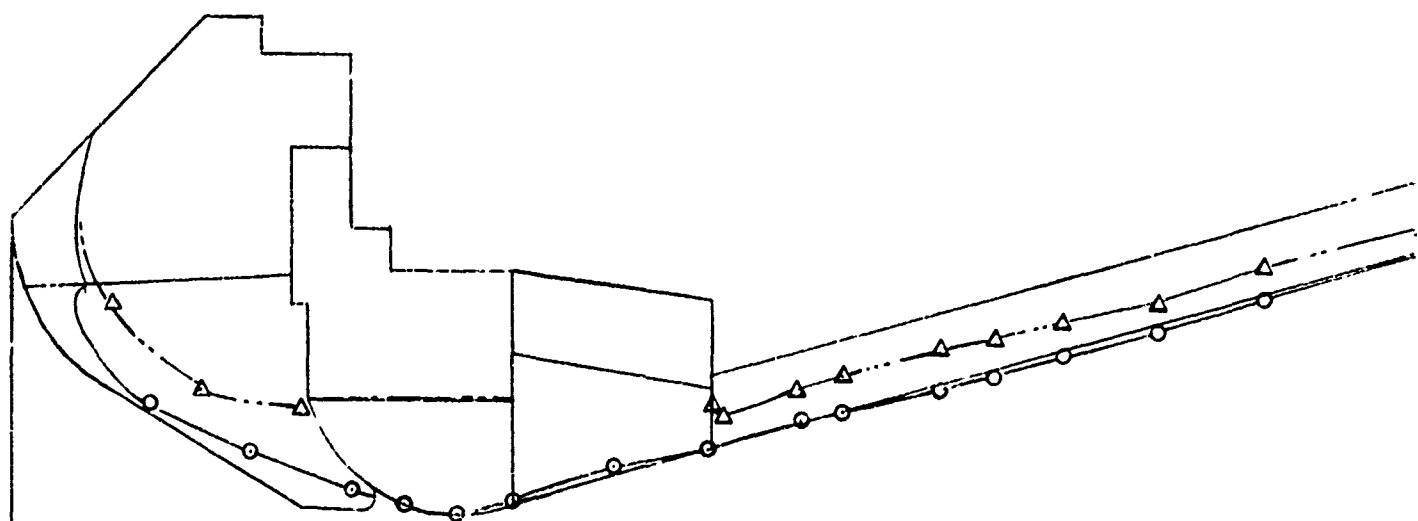


FIGURE 3-4 (CONTINUED)

LINE DESCRIPTIONS
ON FIGURE 3-4a.



e) 180° PLANE



f) 225° PLANE

FIGURE 3-4 (CONTINUED)

LINE DESCRIPTIONS
ON FIGURE 3-4a.

CHAR PATTERN IRREGULAR
WITH NO DEFINITION

g) 270° PLANE

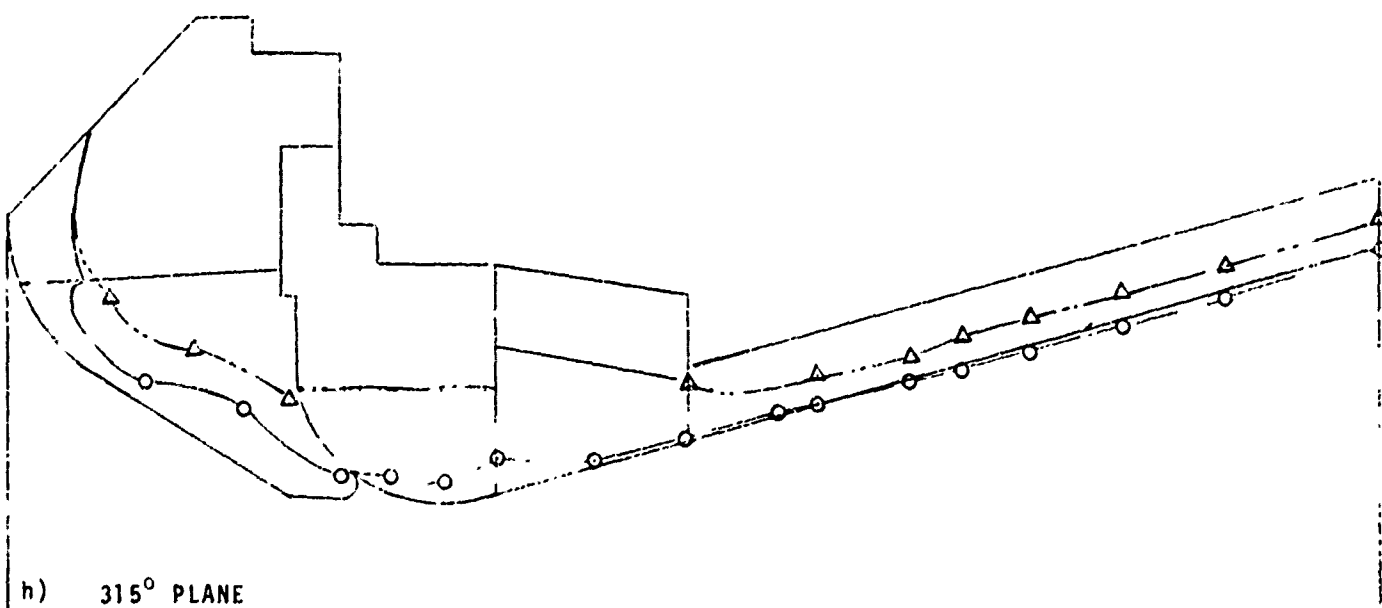
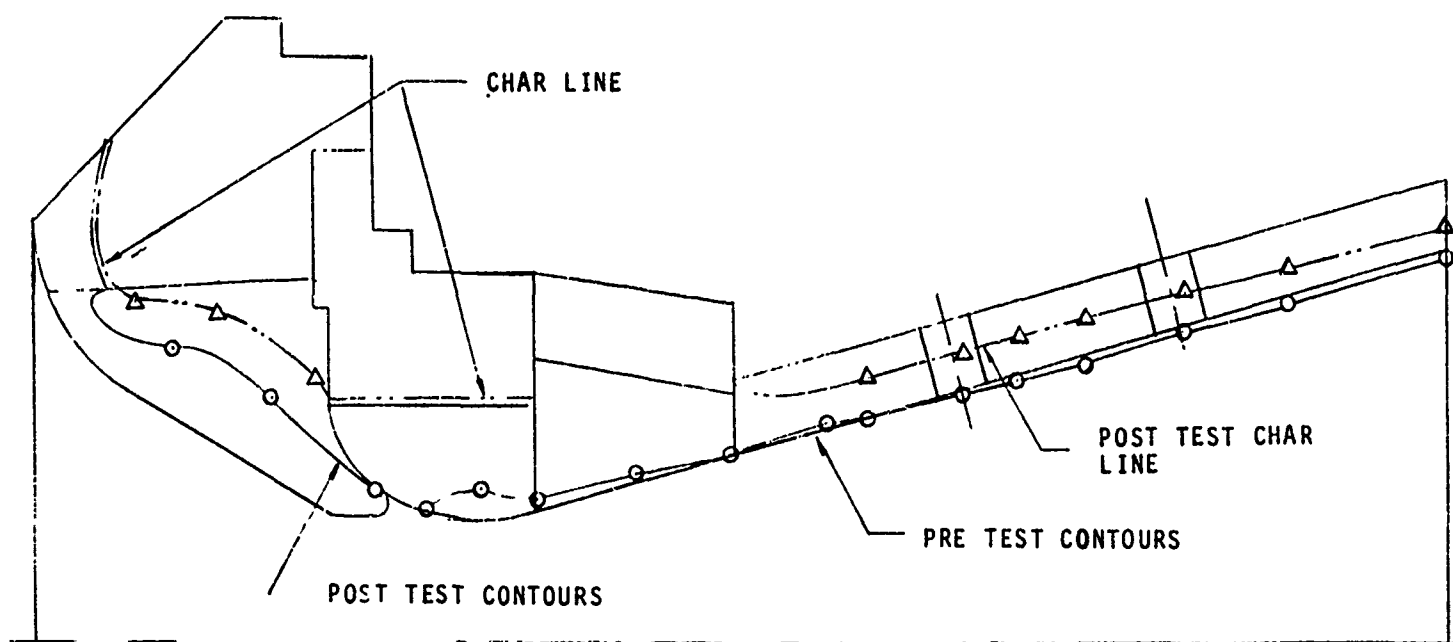
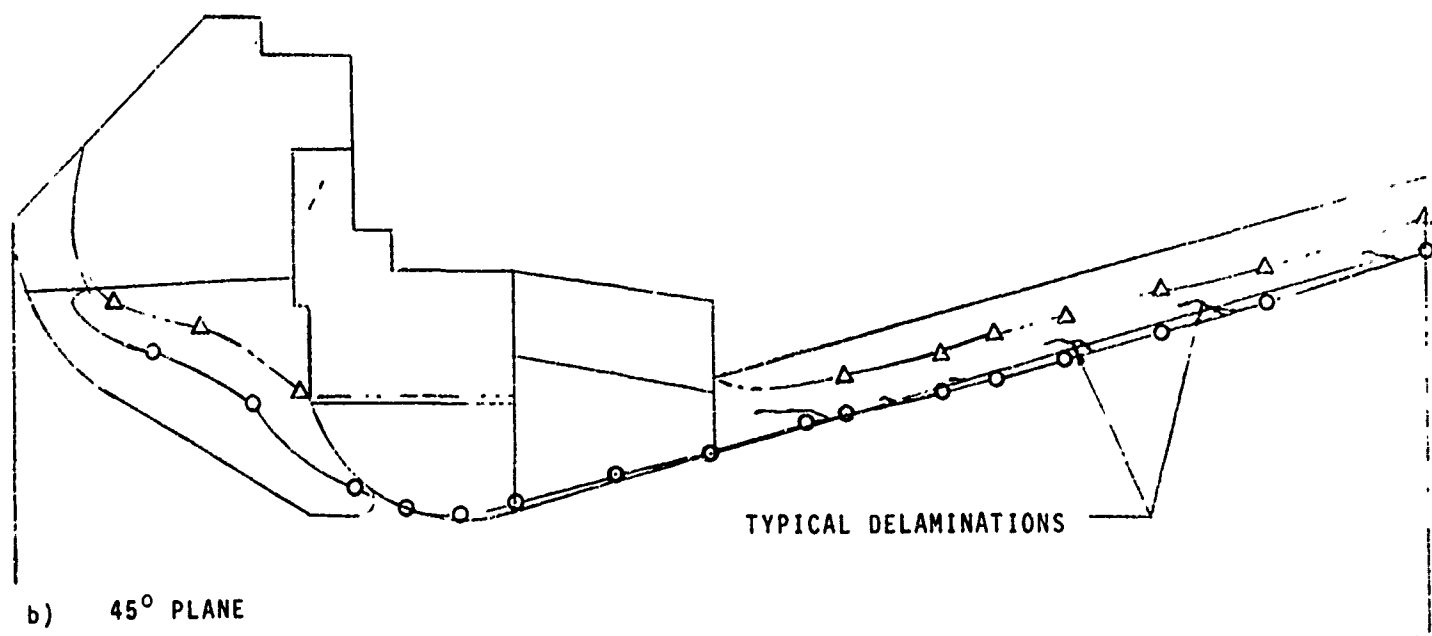


FIGURE 3-4 (CONCLUDED)



a) 0° PLANE (THERMOCOUPLED PLUG PLANE)



b) 45° PLANE

FIGURE 3-5 PRE, POST, AND CHAR LINE CONTOURS FOR NOZZLE NO. 8

LINE DESCRIPTIONS
ON FIGURE 3-5a.

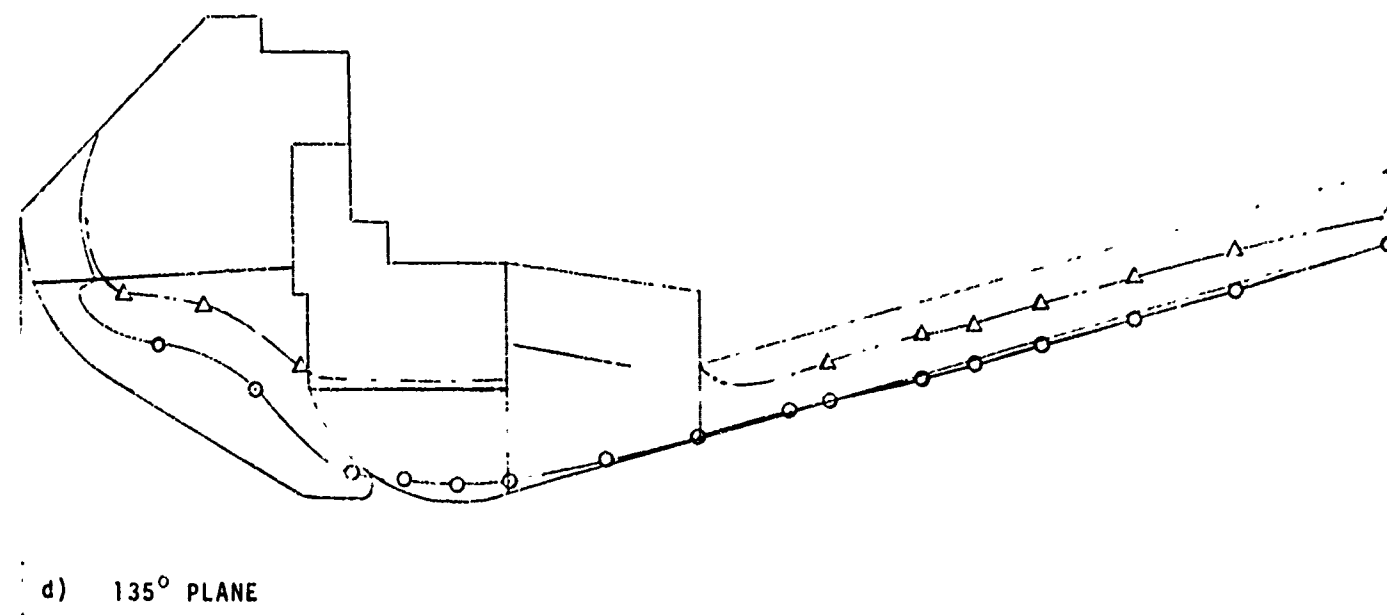
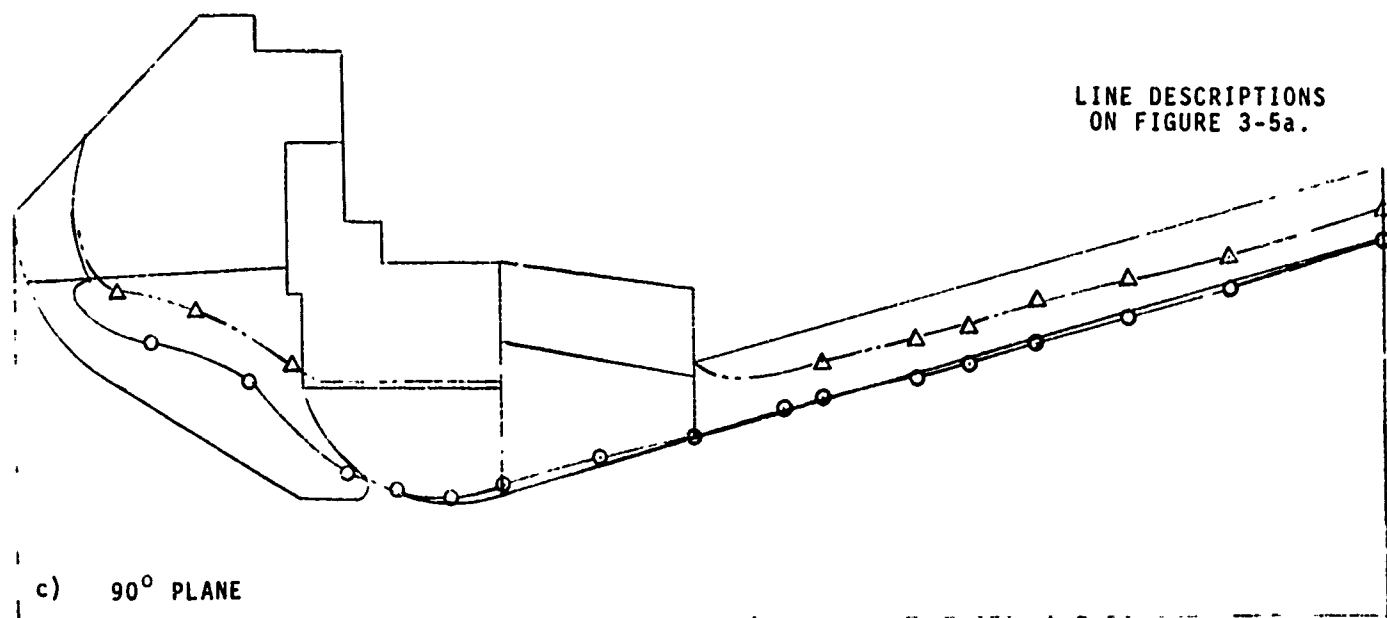
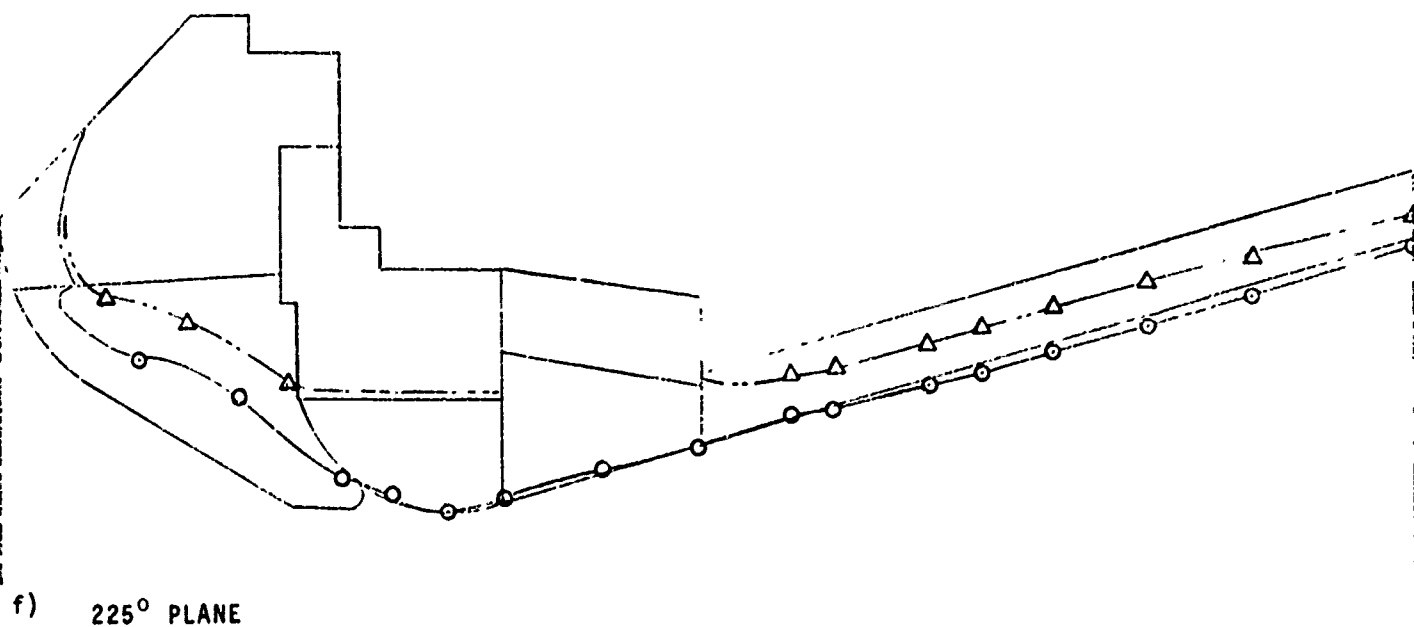


FIGURE 3-5 (CONTINUED)

LINE DESCRIPTIONS
ON FIGURE 3-5a.

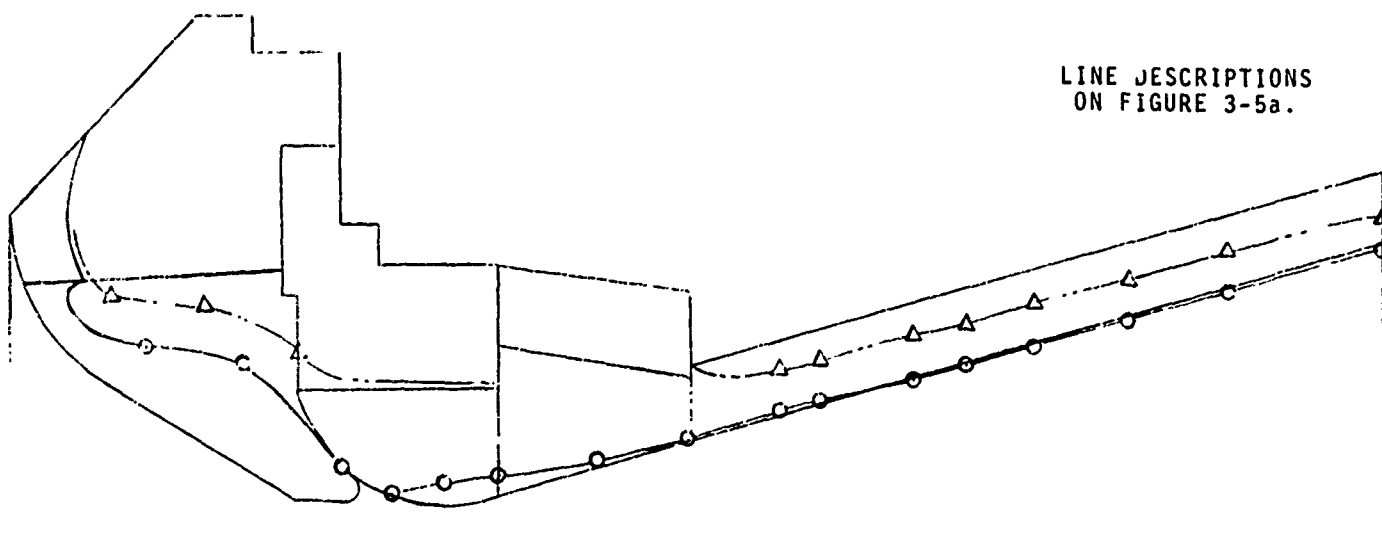
e) 180° PLANE



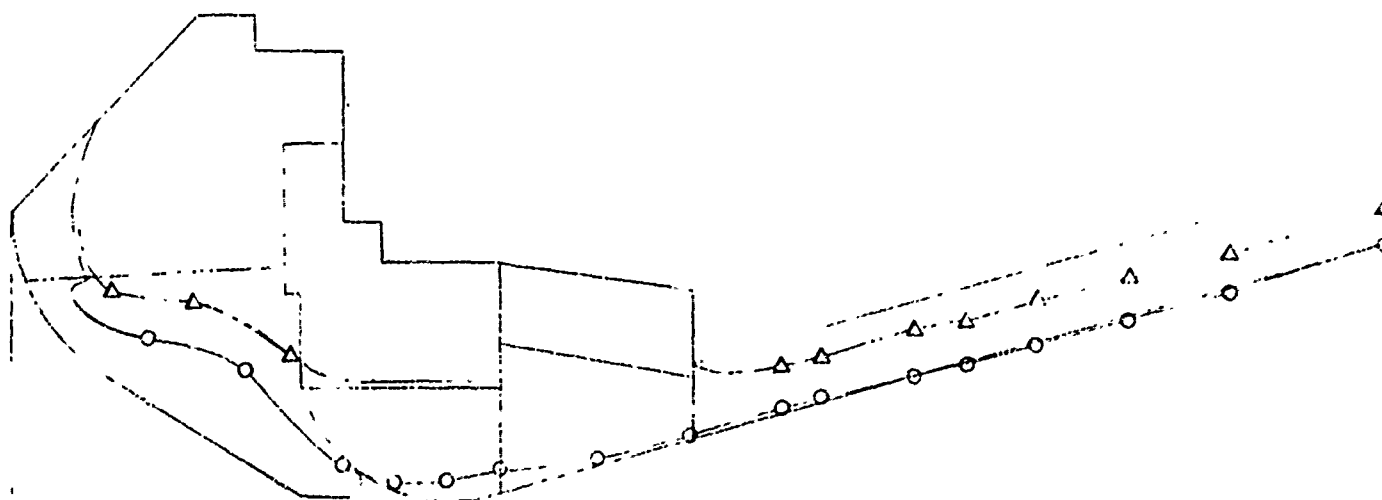
f) 225° PLANE

FIGURE 3-5 (CONTINUED)

LINE DESCRIPTIONS
ON FIGURE 3-5a.



g) 270° PLANE



h) 315° PLANE

FIGURE 3-5 (CONCLUDED)



a) Throat Insert

Reproduced from
best available copy.



b) Exit Cone Section

Figure 3-6 Typical Multiple Pulse Nozzle Post Test Surface Characteristics, Nozzle No. 8.

Pre- and post-test radii and net surface recession at the two axial locations (nozzle throat and upstream thermocouple plug) for which analysis efforts were performed are given in Tables 3-1 and 3-2. The throat recession data presented in Table 3-1 are plotted as a function of circumferential location in Figure 3-7. Also included in Table 3-1 are average throat recession rate values per pulse which have been inferred from chamber pressure versus time data.

Both the surface contours and the nozzle radius tabulations show that for all nozzles, except nozzle number 5, the carbon cloth phenolic in the exit cone exhibited some amount of surface growth (negative recession). To verify that these data were not grossly in error due to inaccurate post-test radius measurements, the recessions were evaluated by an alternate procedure. After the nozzle radius measurements were completed, the ablative components were separated from the steel shells and sectioned along the eight circumferential planes. Measurements of the final exit cone material thickness at several locations in nozzles no. 5 and 8 were made, and net surface movements were computed. The results obtained using these measurements were within 0.010 inches of those obtained from the lathe data. Possible explanations for the surface growth phenomena are presented in Section 4.

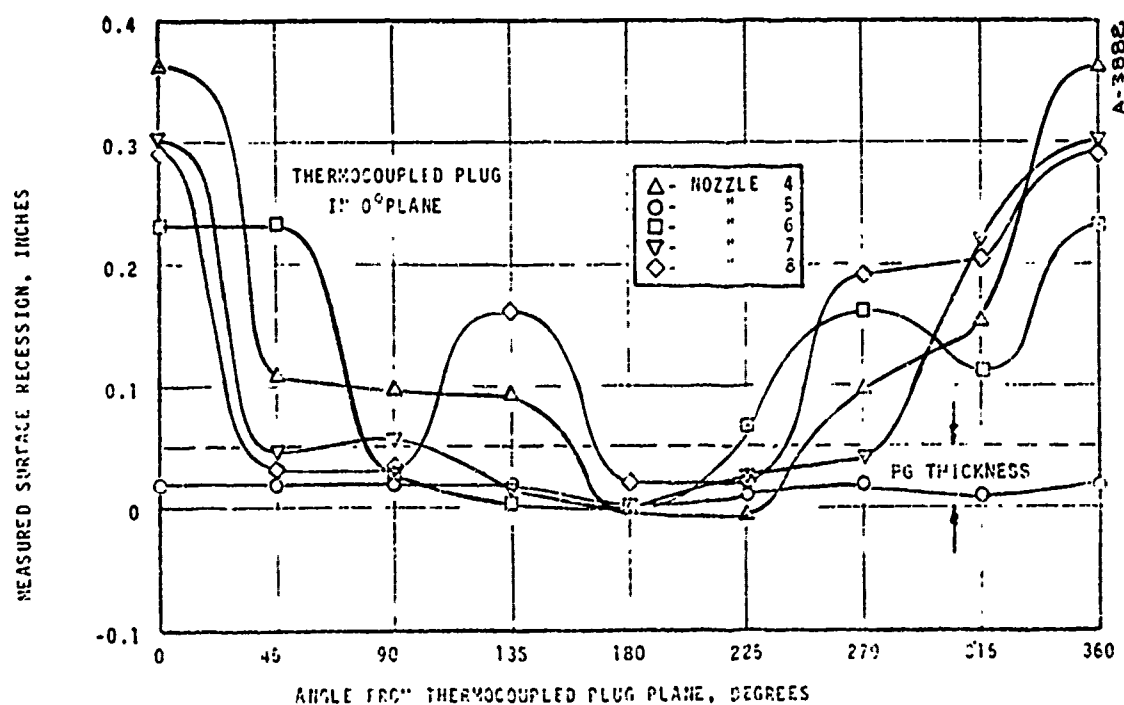


FIGURE 3-7 CORRELATION OF LOCAL NOZZLE THROAT SURFACE RECESSION WITH CIRCUMFERENTIAL LOCATION

TABLE 3-1

SUMMARY OF NOZZLE THROAT RESSION MEASUREMENTS

Nozzle Number		Circumferential Plane Measurements (inches) ^b								Average Recession ^c	Firing Pulse	Recession Data Inferred From Pressure Data (mile/sec)
		0° ^a	45°	90°	135°	180°	225°	270°	315°			
4	Post-Test Radius, Inches	1.510	1.255	1.245	1.240	1.145	1.140	1.245	1.300		1	2.0
	Pre-Test Radius, Inches	<u>1.147</u>	<u>1.147</u>	<u>1.147</u>	<u>1.147</u>	<u>1.147</u>	<u>1.147</u>	<u>1.147</u>	<u>1.147</u>		2	2.1
	Surface Recession	(.363)	(.108)	(.098)	(.093)	-.002	-.007	(.098)	(.153)	.037 ± .050	3	3.7
5		1.170	1.170	1.170	1.170	1.155	1.162	1.170	1.168		1	1.9
		<u>1.150</u>	<u>1.150</u>	<u>1.150</u>	<u>1.150</u>	<u>1.150</u>	<u>1.150</u>	<u>1.150</u>	<u>1.150</u>		2	0.6
		.020	.020	.020	.020	.005	.012	.020	.012	.016 ± .010		
6		1.385	1.385	1.180	1.155	1.150	1.220	1.315	1.265		1	1.6
		<u>1.152</u>	<u>1.152</u>	<u>1.152</u>	<u>1.152</u>	<u>1.152</u>	<u>1.152</u>	<u>1.152</u>	<u>1.152</u>		2	2.0
		(.233)	(.233)	.028	.003	-.002	(.058)	(.163)	(.113)	.035 ± .030	3	6.9
7		1.445	1.190	1.200	1.160	1.150	1.170	1.185	1.365		1	2.3
		<u>1.143</u>	<u>1.143</u>	<u>1.143</u>	<u>1.143</u>	<u>1.143</u>	<u>1.143</u>	<u>1.143</u>	<u>1.143</u>		2	2.3
		(.302)	.047	(.057)	.017	.007	.027	.042	(.222)	.036 ± .030	3	7.7
8		1.440	1.180	1.180	1.310	1.170	1.170	1.340	1.355		1	2.3
		<u>1.148</u>	<u>1.148</u>	<u>1.148</u>	<u>1.148</u>	<u>1.148</u>	<u>1.148</u>	<u>1.148</u>	<u>1.148</u>		2	2.5
		(.292)	.032	.032	(.162)	.022	.022	(.192)	(.207)	.038 ± .020	3	2.5
											4	6.4

^a 0 degrees is the thermocoupled plug plane.

^b number in parentheses indicate P.G. coating burn through.

^c burn through recessions taken as 0.050 inches (P. G. thickness) for averaging.

TABLE 3-2

SUMMARY OF CHAR THICKNESS AND SURFACE MEASUREMENTS

 $\lambda/A^\circ = 4.0$

Nozzle Number		Circumferential Plane Measurements (Inches) ^b								Average Recession ^c
		0° ^a	45°	90°	135°	180°	225°	270°	315°	
4	Char Thickness, Inches	.325	.310	.305	.330	.310	.260	.305	.320	0.31 ± 0.04
	Post-Test Radius, Inches	2.355	2.360	2.360	2.355	2.342	2.345	2.352	2.360	
	Pre-Test Radius, Inches	<u>2.377</u>	<u>2.377</u>	<u>2.377</u>	<u>2.377</u>	<u>2.377</u>	<u>2.377</u>	<u>2.377</u>	<u>2.377</u>	(0.026) ± 0.010
5		(0.022)	(0.016)	(0.037)	(0.022)	(0.035)	(0.032)	(0.025)	(0.017)	
		.300	.235	.290	.275	.230	.235	.230	.245	0.26 ± 0.04
		2.355	2.390	2.395	2.410	2.375	2.390	2.390	2.385	
6		<u>2.370</u>	<u>2.370</u>	<u>2.370</u>	<u>2.370</u>	<u>2.370</u>	<u>2.370</u>	<u>2.370</u>	<u>2.370</u>	
		(0.015)	(0.020)	(0.025)	(0.040)	(0.005)	(0.020)	(0.020)	(0.015)	0.016 ± 0.025
		.430	.355	.345	.290	.375	.380	.325	.370	0.37 ± 0.06
7		2.370	2.375	2.380	2.375	2.352	2.385	2.405	2.375	
		<u>2.377</u>	<u>2.377</u>	<u>2.377</u>	<u>2.377</u>	<u>2.377</u>	<u>2.377</u>	<u>2.377</u>	<u>2.377</u>	
		(0.007)	(0.002)	(0.003)	(0.002)	(0.025)	(0.008)	(0.028)	(0.002)	0.0 ± 0.025
8		.370	.350	.300	.330	.315	.370	.345	.360	0.34 ± 0.04
		2.370	2.335	2.335	2.337	2.345	2.350	2.335	2.345	
		<u>2.377</u>	<u>2.377</u>	<u>2.377</u>	<u>2.377</u>	<u>2.377</u>	<u>2.377</u>	<u>2.377</u>	<u>2.377</u>	(.032) ± 0.010
8		(0.007)	(0.042)	(0.042)	(0.040)	(0.032)	(0.027)	(0.042)	(0.032)	
		.395	.365	.350	.420	.420	.395	.430	.430	0.40 ± 0.04
		2.365	2.350	2.345	2.350	2.345	2.365	2.345	2.380	
		<u>2.377</u>	<u>2.377</u>	<u>2.377</u>	<u>2.377</u>	<u>2.377</u>	<u>2.377</u>	<u>2.377</u>	<u>2.377</u>	(0.021) ± 0.010
		(0.012)	(0.027)	(0.032)	(0.027)	(0.032)	(0.012)	(0.032)	(0.003)	

^a 0 degrees is the thermocoupled plug plane.

^b Numbers in parentheses indicate a net surface growth (Negative Recession)

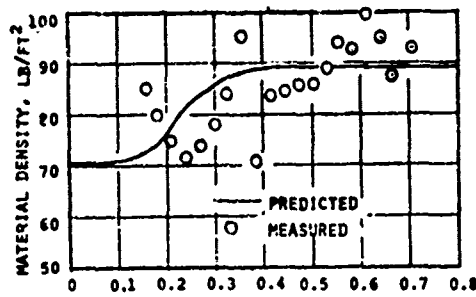
^c Estimated char thickness uncertainties based on 1) random measurement errors, ± .020 inches, and 2) response asymmetries; recession (or growth) uncertainties are due to response asymmetries.

Char thickness measurements were taken from the sectioned pieces of the ablative exit cone with the char thickness defined as the distance from the internal surface to the midpoint of the char/virgin material interface. Uncertainty in this measurement is due primarily to the difficulty in visually picking out the interface since both the virgin material and the char are black. The uncertainty in these data points is estimated to be ± 0.020 inches. Sufficient char thickness measurements were acquired to define a char line contour for each circumferential plane of the five nozzles. These contours are shown along with pre- and post-test surface contours in Figures 3-1 through 3-5; in addition, the thickness measurements at the $A/A^* = 4.2$ prediction location are given in Table 3-1.

3.2 IN-DEPTH DENSITY PROFILE MEASUREMENTS

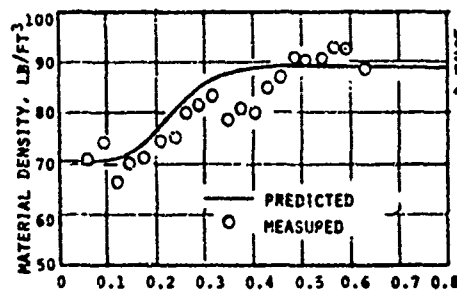
The in-depth material density profiles were measured for the FM 5055A carbon cloth phenolic at a supersonic area ratio of 4.2. This area ratio corresponds to the location of the upstream thermocoupled plug. The two techniques used for measuring the density profiles were the shave and weigh technique and the x-ray transmission technique. For the shave and weigh determination of density profiles, two samples were machined from the exit cone material of each nozzle. Samples were taken from the 0 and 180 degree circumferential locations at the area ratio of 4.2. Each sample was 0.5 inches square in the plane corresponding to the exposed surface and extended approximately 0.75 inches in the direction normal to the surface (i.e. to the steel shell). Density as a function of depth was evaluated by a differencing technique. Overall material density was accurately obtained from dimension and weight measurements. Then, approximately 25 mils of the sample was removed starting from the fully charred, 0.5 inch square end; and the sample was re-measured. The change in weight and volume defined the density of the removed material. This process was repeated until the sample was consumed. The density profiles resulting from these measurements are represented by the symbols in Figure 3-8. The curve shown on each of these figures is the analytical prediction, and it, as well as the comparison between the measured and predicted profiles, is discussed in Section 4.3.3.

The second method used to define the density profile was the x-ray transmission technique. The experimental portion of this technique is performed by directing a narrow x-ray beam of known intensity normal to one surface of the material sample and detecting the intensity of the beam which is transmitted through the material and out the opposite surface. The configuration of this apparatus is shown schematically in Figure 3-9. The x-ray source generates a 1 mm wide beam of $K\alpha$ radiation which is passed through a $K\beta$ nickel filter and then through a collimator which directs it at the sample being tested. The



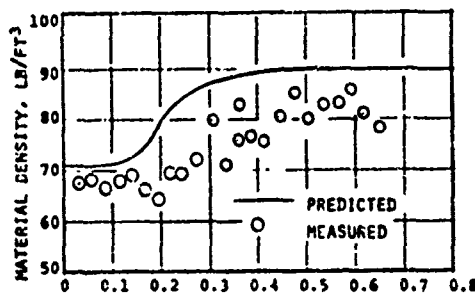
DISTANCE FROM NOZZLE SURFACE, IN.

a) NOZZLE NO. 4, 0 DEGREE



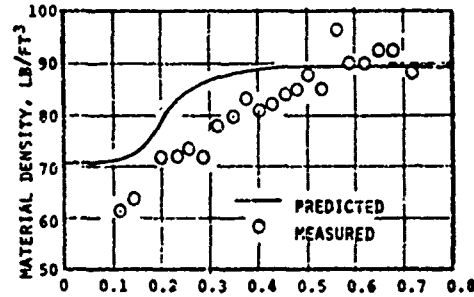
DISTANCE FROM NOZZLE SURFACE, IN.

b) NOZZLE NO. 4, 180 DEGREES



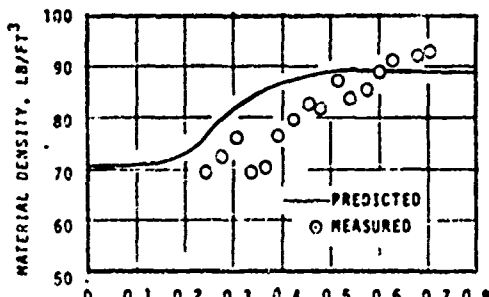
DISTANCE FROM NOZZLE SURFACE, IN.

c) NOZZLE NO. 5, 0 DEGREE



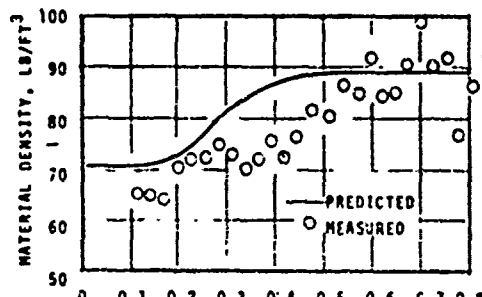
DISTANCE FROM NOZZLE SURFACE, IN.

d) NOZZLE NO. 5, 180 DEGREES



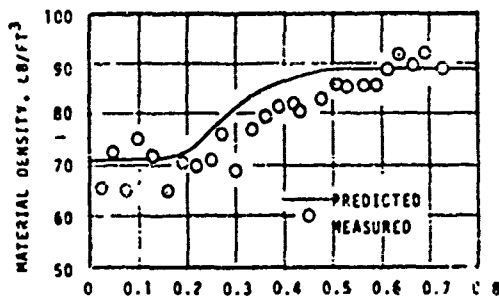
DISTANCE FROM NOZZLE SURFACE, IN.

e) NOZZLE NO. 6, 0 DEGREES



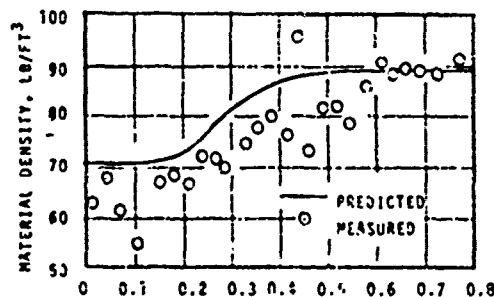
DISTANCE FROM NOZZLE SURFACE, IN.

f) NOZZLE NO. 6, 180 DEGREES



DISTANCE FROM NOZZLE SURFACE, IN.

g) NOZZLE NO. 7, 0 DEGREES



DISTANCE FROM NOZZLE SURFACE, IN.

h) NOZZLE NO. 7, 180 DEGREES

FIGURE 3-8 COMPARISON OF PREDICTED AND MEASURED IN-DEPTH DENSITY PROFILES IN FM 5055A CARBON CLOTH PHENOLIC AT AN AREA RATIO OF 4.2

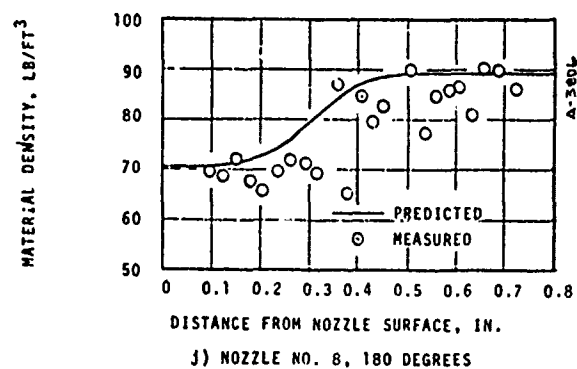
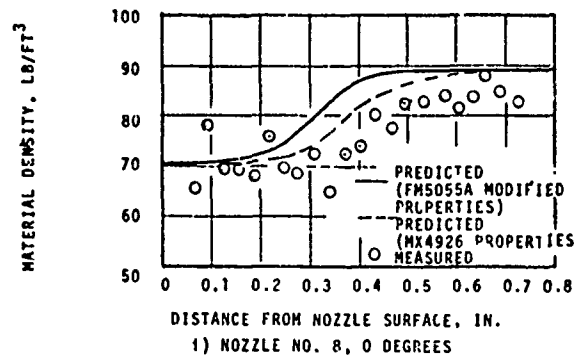


FIGURE 3-8 (Concluded)

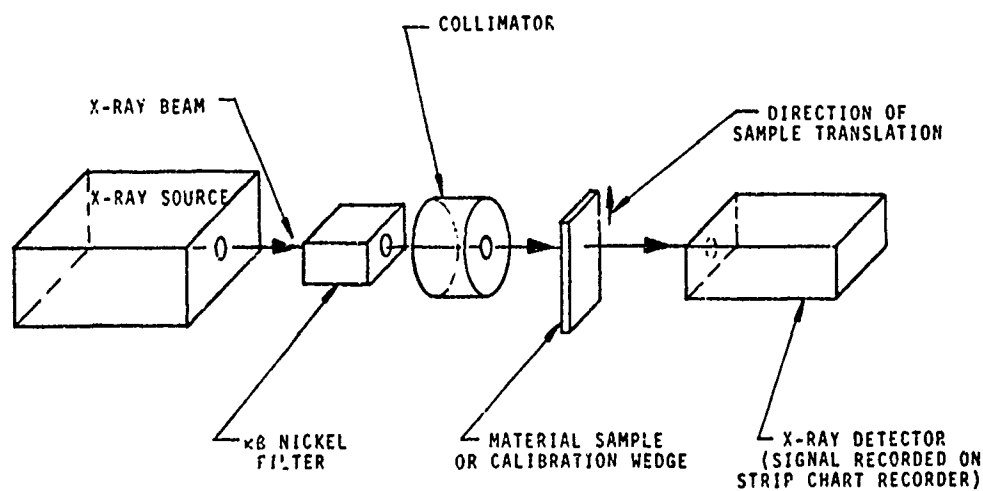


FIGURE 3-9 SCHEMATIC OF X-RAY TRANSMISSION SYSTEM

portion of the beam which passes through the sample is measured by the detector and recorded on a strip chart recorder. The sample was positioned in the x-ray beam at discrete 1 mm steps. The procedure for making the measurement was to 1) locate the sample, 2) turn on the strip chart recorder which had a speed of 1/2 inch/minute, 3) turn on the x-ray source, 4) record data for 2 minutes. The x-ray source and recorder were then stopped and the sample was repositioned. Measurements were taken at 1 mm intervals which also corresponded to the diameter of the x-ray source.

The material sample was taken from nozzle number 8 at the location shown in Figure 3-10. The nominal dimensions of the sample are also shown.

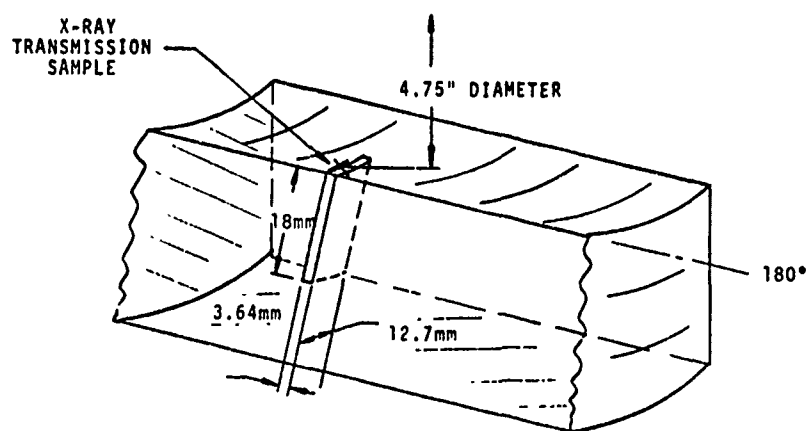


FIGURE 3-10 LOCATION FOR X-RAY TRANSMISSION SAMPLE (NOZZLE NO. 8)

The relative transmission measurements of the x-ray beam through this sample are shown in Figure 3-11 for the various discrete locations. The abscissa on this figure is distance from the surface which corresponds to the center of the x-ray source; thus, at a distance corresponding to zero, half of the beam is passing through air and half through the sample. The data shown in Figure 3-11 were reduced to material density using the following equation:

$$\frac{I}{I_0} = \exp \left[- \left(\frac{\mu}{\rho} \right) \rho x \right] \quad (3-1)$$

where

- I - the transmitted x-ray intensity
- I_0 - the x-ray incident beam intensity
- $\frac{\mu}{\rho}$ - the mass absorption coefficient
- ρ - local material density
- x - the thickness of the absorbing material

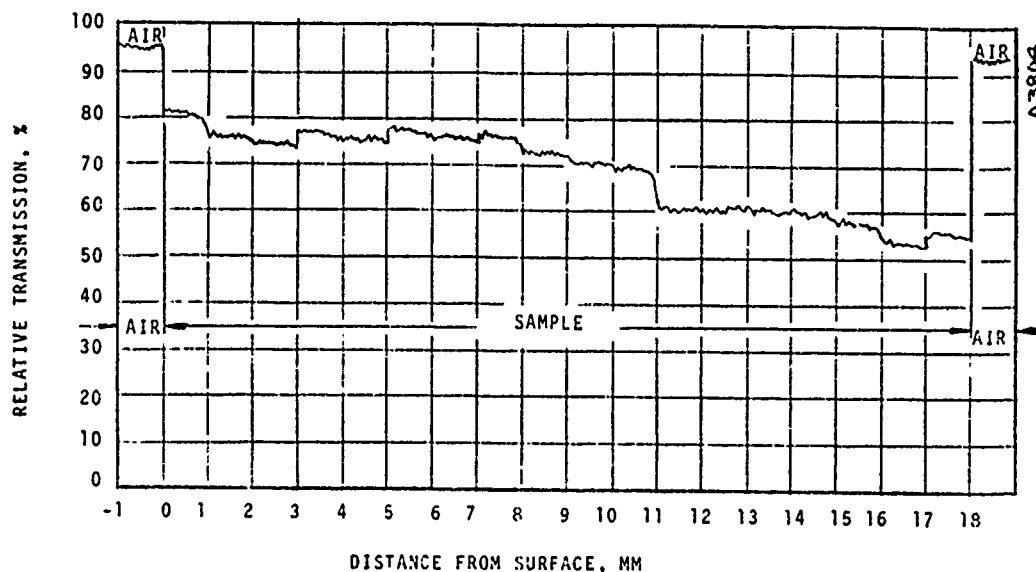


FIGURE 3-11 MEASURED X-RAY TRANSMISSION
FOR DENSITY PROFILE SAMPLE

A mass absorption coefficient of $1.15 \text{ cm}^2/\text{gr}$ was evaluated based on the transmission intensity through the virgin material. The virgin material density used for this evaluation was 1.37 gr/cm^3 . This value was obtained from a small sample of virgin material which was taken from the nozzle in the vicinity of the x-ray sample. The mass absorption coefficient for the virgin material carbon cloth phenolic compares favorably with the value ($1.18 \text{ cm}^2/\text{gr}$) obtained from a sample of pure graphite for the x-ray transmission results presented in Reference 1.

The densities calculated using the above equation are shown in Figure 3-12. The amount of scatter in the data is a result of the porous nature of the sample which is shown by the photograph presented in Figure 3-13. In addition, the porosity in the char region probably explains the low value of char density determined from the x-ray measurements in the char zone.

3.3 X-RAY DIFFRACTION MEASUREMENTS

X-ray diffraction measurements were made for three samples of carbon cloth phenolic in each of the five nozzles. As shown in Figure 3-14 the three samples in each of the nozzles were one-eighth inch thick and one-half inch on a side and were taken at an area ratio of 4.2 and at the 180 degree circumferential location. The three samples were machined from the exit cone at depths corresponding to the fully charred zone, the partially charred zone, and the virgin material zone.

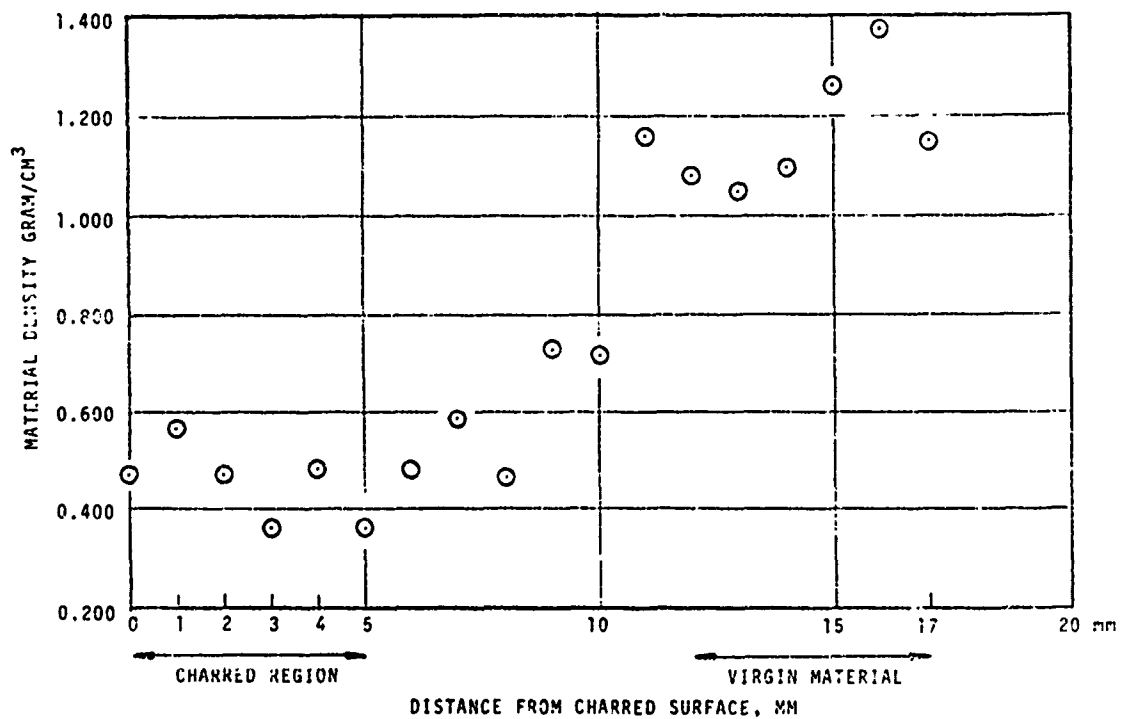


FIGURE 3-12 MATERIAL DENSITY PROFILE DETERMINED FROM X-RAY TRANSMISSION MEASUREMENTS

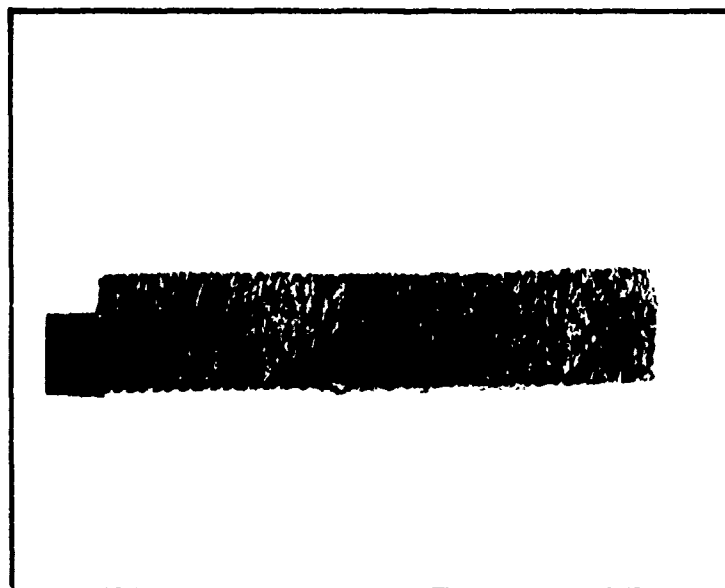


FIGURE 3-13 CROSS SECTION OF X-RAY TRANSMISSION SAMPLE

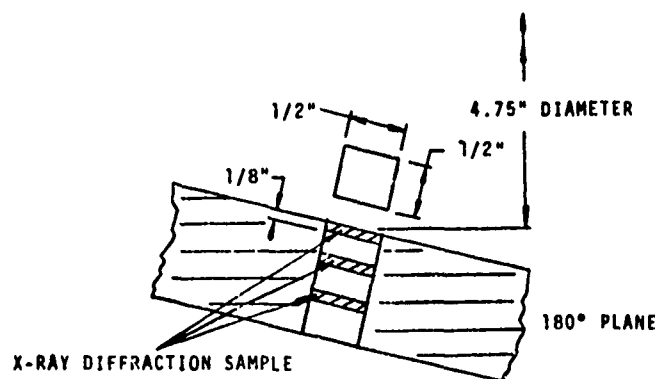


FIGURE 3-14 LOCATIONS FOR X-RAY DIFFRACTION SAMPLES

The reason for making the x-ray diffraction measurements was to determine whether any significant changes occurred in the crystal structure of the material as a result of subjecting the material to multiple pulse duty cycles. The type of material changes which would be expected is an increase in the graphitic carbon content in the char. This increase in graphitic carbon can be measured by x-ray diffraction because graphitic carbon (or graphite) has a uniformity of structure which can be represented by the graphite crystal lattice shown in Figure 3-15.

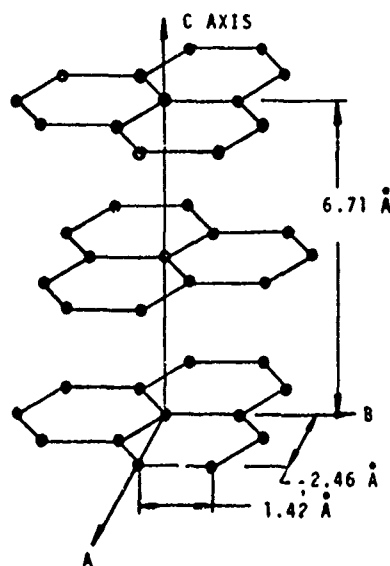


FIGURE 3-15 LATTICE STRUCTURE OF GRAPHITE CRYSTAL

As this type of crystal structure becomes more prevalent, the x-ray diffraction measurement will begin to show a sharp peak at an incidence angle defined by Bragg's Law

$$\sin \theta = \frac{\lambda}{2d} \quad (3-2)$$

where

- θ - angle of incidence
- λ - wavelength of x-ray source
- d - spacing between adjacent crystal planes

For the x-ray diffraction measurements made under this program, a copper $k\alpha$ x-ray source was used which has a wavelength of 1.54 \AA . When this value for λ is used in the above equation together with a value of 3.355 \AA for the spacing between adjacent planes of carbon atoms in the graphite crystal lattice, the angle of x-ray incidence which gives the maximum strength of the diffracted x-ray beam is 13.3 degrees.

The results from the x-ray diffraction measurements for the nozzle material samples are shown in Figure 3-16. The ordinate for each of these figures represents on a relative basis the strength of the diffracted x-ray beam. The abscissa represents the angle 2θ (two times the incidence angle defined in Equation (3-2)). The samples for nozzle no. 8 (Figure 3-16e) were tested first. The incident angle of the x-ray beam was varied from 45 (or $2\theta = 90^\circ$) to 5 degrees to determine the range of interest for this angle. As shown by this figure, the x-ray diffraction measurements were of primary interest for 2θ angles between 10 and 40° , and, therefore, sample sets for the other nozzles were only tested over this range. For all of the sample sets, the x-ray diffraction measurements for the virgin material sample gave a low magnitude increase over a broad angle spectrum from between 10 and 30 degrees. For the partially charred samples, very little change, except for nozzle no. 5, was noted between the virgin and partially charred x-ray diffraction measurements. However, for the fully charred sample, the intensity of the diffracted beam increased for 2θ angles between 22 and 28 degrees with the peak occurring at a 2θ incident angle of approximately 26 degrees. These changes in the x-ray diffraction measurements for the fully charred samples indicate that crystallization and ordering of the (00.2) layer plane of the hexagonal graphite crystal has taken place. The most pronounced peaks occurred for samples from nozzles No. 4 and 6 (Figures 3-16a and 3-16c).

Since the amount of graphitic carbon content is a function of the maximum temperature and of the time at this temperature, the trends shown by the x-ray diffraction measurements for nozzles no. 4 and 6 were compared with the predicted surface temperatures and with the temperatures measured by TC no. 1. This comparison showed that

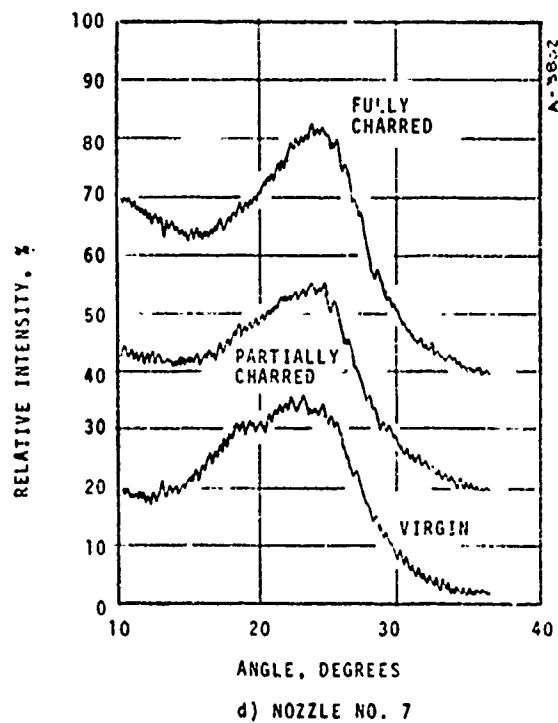
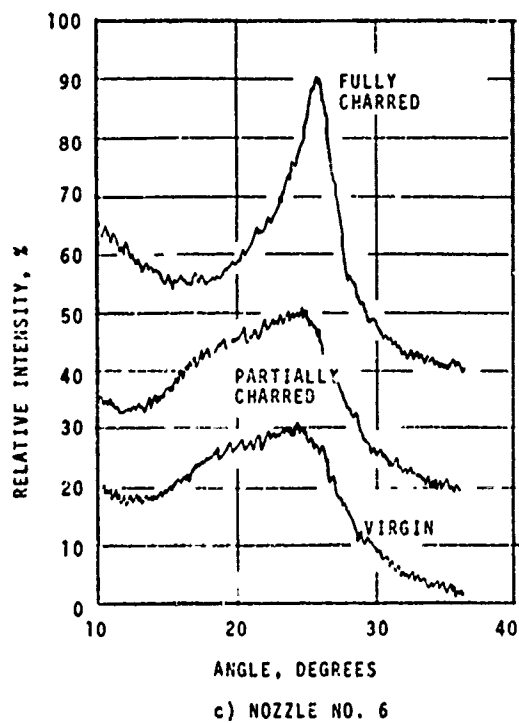
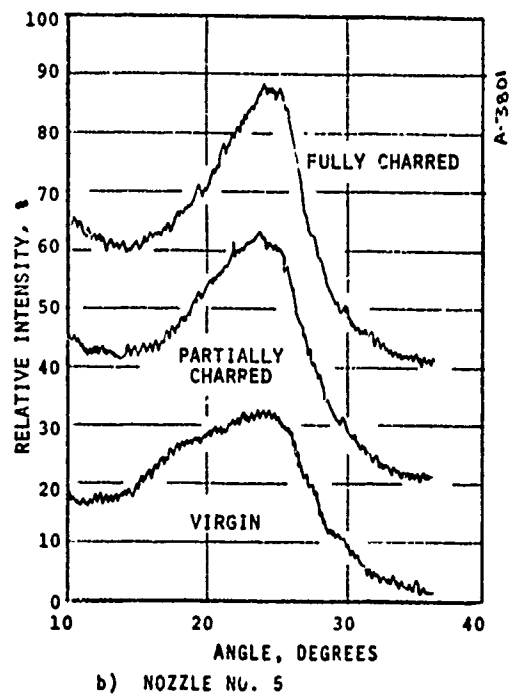
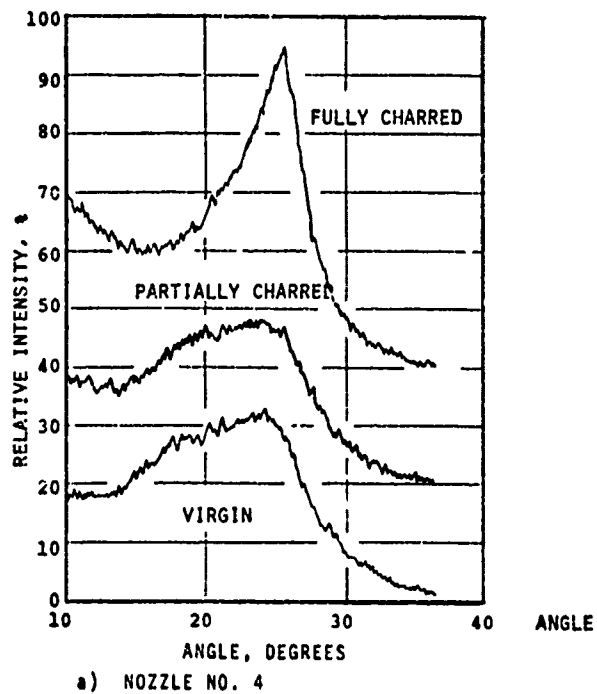
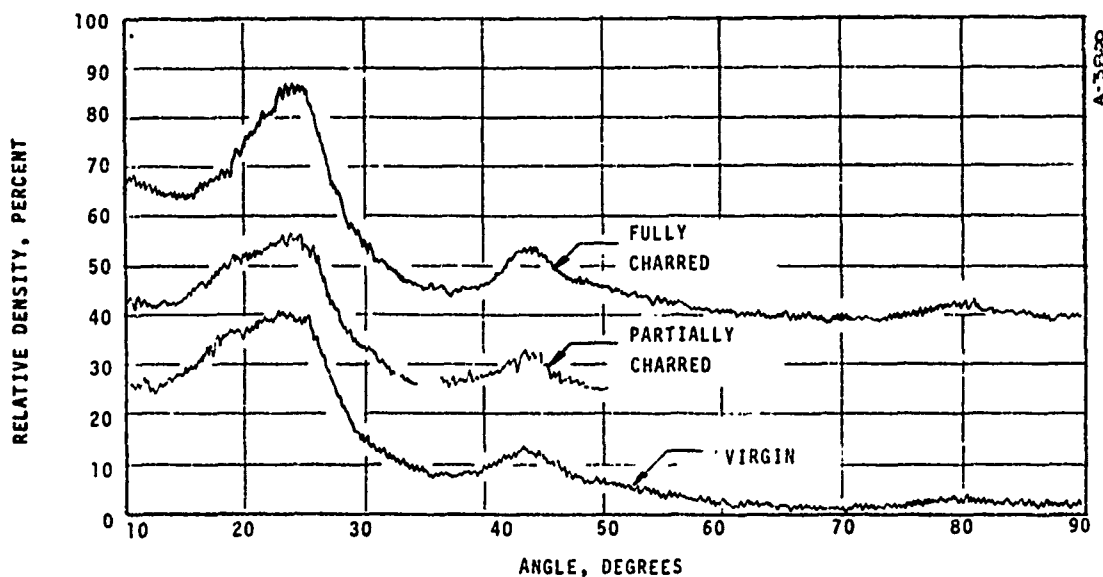


FIGURE 3-16 X-RAY DIFFRACTION MEASUREMENTS IN FM 5055A CARBON CLOTH PHENOLIC AT AN AREA RATIO OF 4.0



e) NOZZLE NO. 8

FIGURE 3-16 (Concluded)

- the maximum temperatures recorded by TC no. 1 were for nozzles no. 4 and 6 (Table 2-7) which is consistent with the x-ray diffraction measurements
- the maximum predicted surface temperatures and the duration at this temperature are not significantly different for the five duty cycles (Figures 4-25 through 4-29) which is inconsistent with the x-ray diffraction measurements

Because the magnitude of the measured temperatures in the thermocoupled plug is a strong function of the thermocouple depth and because small variations in this depth would result in significant changes in the measured temperature, the apparent correlation between the x-ray diffraction and the thermocouple measurements should be viewed with caution. This is particularly true because of the discrepancies in the measured temperatures noted in Section 2.5 and because the predicted temperatures do not substantiate this same correlation.

SECTION 4

EVALUATION OF MATERIAL PERFORMANCE DATA

The simulator firings of the five nozzles provide information for the design of multiple pulse duty cycle rocket motors. In this section, the multiple pulse firing data are used to verify the adequacy of current analysis procedures. Once substantiated, these analysis tools should facilitate a more efficient design process by minimizing the amount of experimentation required. Also in this section the material response predictions are used to identify the relative significance of observed trends in the firing data. Any material response characteristics peculiar to multiple pulse duty cycles would be exposed by the correlation effort. Results of response analyses are compared to material performance data for each of the five multiple pulse nozzles.

The methods utilized to perform these analyses are summarized in Section 4.1. The important boundary layer, surface thermochemistry, and material property information which are needed for the material response calculations are described in Section 4.2. Results of the response analyses are compared to the test data in Section 4.3.

4.1 SUMMARY OF ANALYSIS METHODS

The analysis of material response to rocket nozzle environment encompasses both the determination of surface recession due to chemical corrosion and mechanical erosion and the evaluation of in-depth heat conduction and material decomposition. The events occurring at and below the surface of a charring ablator which is being exposed to a solid propellant rocket environment are characterized in Figure 4-1. Except for the material decomposition and pyrolysis gas flow, the figure applies equally to noncharring materials such as pyrolytic graphite. A set of comprehensive computerized analysis tools have been developed to define the thermochemical performance of these types of materials. These computer codes are used to evaluate thermal ablation phenomena, and they have been designed to be applicable for arbitrary material and propellant compositions and for any general environmental duty cycle specification.

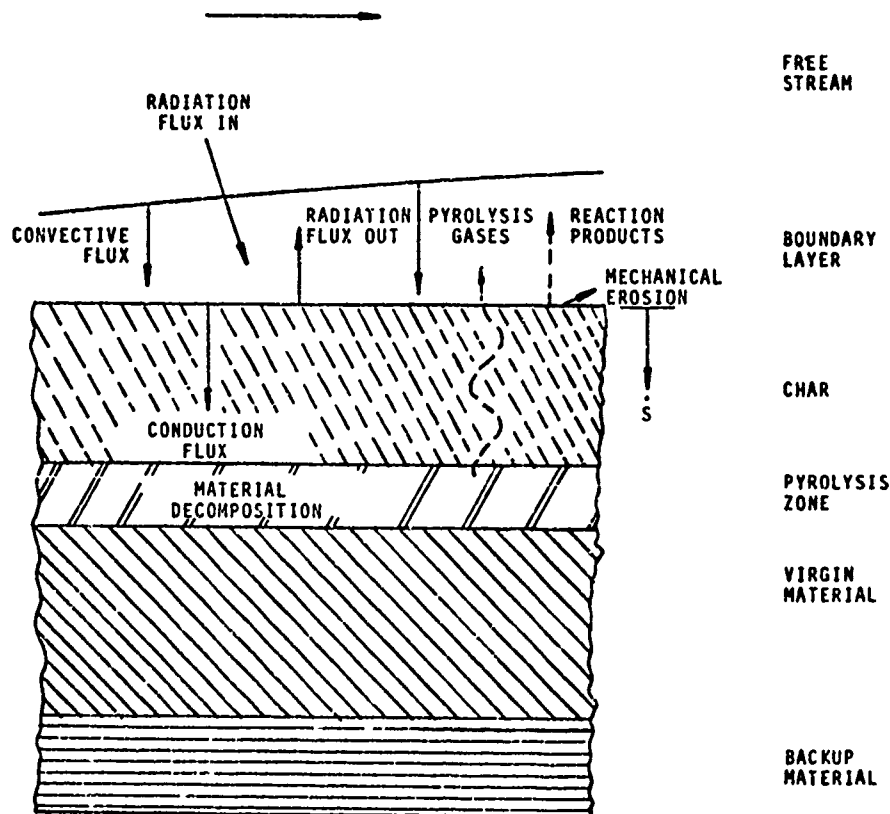


FIGURE 4-1 CHARACTERIZATION OF THE SOLID PROPELLANT ROCKET ENVIRONMENT AND THE RESPONSE OF A CHARRING ABLATOR

The ablation analysis computer codes utilized for the multiple pulse nozzle calculations are as follows:

- Aerotherm Chemical Equilibrium (ACE) Program*
- Aerotherm Real Gas Energy Integral Boundary Layer (ARGEIBL) Program
- Charring Material Ablation (CMA) Program
- Axi-Symmetric Transient Heating and Material Ablation (ASTHMA) Program

The first program computes the thermochemical state of any set of chemical elemental quantities. For ablative rocket nozzle considerations, the code assists

* The ACE program combines all the features of the Equilibrium Surface Thermochemistry, Version 3 (EST3) code (currently available to the rocket technology community) and the graphite response code developed under Contract F04611-69-C-0081 to account for surface kinetics.

in the computations of nozzle expansion properties, gas phase transport and thermodynamic state properties, pyrolysis gas enthalpy-temperature relationships, and thermochemical behavior of a surface material in contact with the hyperthermal boundary layer flow. The surface removal mechanisms considered by the code are chemical corrosion, surface vaporization, and liquid layer removal.

The ARGEIBL program calculates bulk film transfer coefficients for non-ablating laminar and/or turbulent boundary layers of axisymmetric or flat plate geometries using an energy integral method. The solution procedure allows any real gas chemical system because it accepts generalized thermodynamic property information which are obtained from ACE code computations. Variations in axial surface temperature and free stream properties are accounted for in the integral procedure. The convective heat transfer coefficient distributions computed using the ARGEIBL technique have been confirmed by solutions generated with the more sophisticated Boundary Layer Integral Matrix Procedure (BLIMP) computer code (Ref. 5).

Both the ACE and ARGEIBL codes are utilized to provide information needed by the CMA or the ASTHMA material response codes. The CMA code computes the transient thermal response of a material which is receding due to chemical or mechanical surface removal and which is decomposing in depth via specified rate controlled phase change reactions. Heat conduction is modeled along a one-dimensional nodal column of arbitrarily varying cross-sectional area and is implicitly tied to ablating or nonablating surface boundary conditions. The ASTHMA code is used to evaluate the transient response of nondecomposing materials such as graphite within which two-dimensional heat conduction effects are important. The same generalized surface boundary condition options used by CMA are available in ASTHMA.

The major features of the four computer codes are described further in Table 4-1 and the procedure for using these codes to perform an ablation and thermal response analysis is diagrammed in Figure 4-2. The sequence of events in the analysis procedure is also outlined in Table 4-2. The major result of each analysis step in the procedure is defined along with how this result is used to obtain the desired analysis predictions. The analysis starts by defining the boundary layer edge properties from the flow field and ACE expansion analyses and concludes with the definition of the thermal performance parameters, namely, char depth, surface recession, and in-depth temperature distributions. Additional details of the computerized analysis techniques utilized in the program are included in Appendix C.

TABLE 4-1
SUMMARY OF MAJOR FEATURES OF COMPUTER PROGRAMS

Computer Program	Major Features	Typical Use
ACE	1. Calculation of thermodynamic state for isentropic or isenthalpic process for a closed system including condensed phases.	Nozzle equilibrium isentropic expansion.
	2. Calculation of transport properties (viscosity, thermal conductivity, and mass diffusion coefficients).	Evaluation of transport coefficients for use in boundary layer analysis.
	3. Calculation of surface state of any material exposed to an environment considering all possible chemical reactions between the material and the environment. Surface reactions may be kinetically controlled. Mechanical removal of surface melt layer may also be considered.	Generate Mollier charts for any gas system.
	4. Considers unequal diffusion coefficients.	Generation of thermochemical data for use with CMA and ASTHMA computer programs.
CMA	1. Calculation of transient thermal response of a composite slab or cylinder containing up to five in-depth charring (or noncharring) materials.	Thermal analysis of ablative materials in liquid and solid rocket motors.
	2. Calculation of surface recession rate resulting from diffusion or kinetically controlled surface chemical reactions and/or mechanical melt removal.	Thermal analysis of reentry nose tips.
	3. Considers variable thermal properties with a flexible physical model of thermal conductivity which permits the treatment of partially charred values less than the virgin material value.	
	4. Considers in-depth and surface thermochemical effects of the pyrolysis gases being generated by both the surface and backup materials.	
ASTHMA	1. Calculation of transient thermal response of a two-dimensional body.	Thermal analysis of heat sink materials in liquid and solid rocket motors and reentry nose tips.
	2. Considers surface recession.	
	3. General thermochemical surface boundary conditions.	
	4. Considers anisotropic temperature dependent thermal properties.	
ARGEIBL	1. Calculation of laminar or turbulent convective heat transfer coefficients for nonablating wall.	Transfer coefficient analysis of solid and liquid rocket motors.
	2. Considers any real gas system and axial variations in wall temperature and free stream properties.	
	3. Solves the energy integral equation.	
BLIMP	1. Calculation of laminar or turbulent convective heat transfer coefficients for ablating or nonablating wall.	Transfer coefficient analysis of solid and liquid rocket motors and reentry nose cones.
	2. Considers any real gas system and axial variations in wall temperature, free stream properties, and surface recession.	
	3. Considers chemical and thermal diffusion in the boundary layer.	
	4. Solves nonsimilar laminar and turbulent boundary layer equations.	

TABLE 4-2

TYPICAL PROCEDURE FOR ANALYZING ROCKET MOTOR NOZZLES

Sequence	Purpose	Applicable Computer Program	Result	Use of Results
1	Flow field	--	Boundary layer edge mass flow rate/unit area as a function of distance	Combined with results from Item 2 to define boundary layer edge properties as a function of distance
2	Equilibrium nozzle expansion analysis	ACE	Boundary layer edge properties as a function of mass flow rate/unit area	Combined with results from Item 1 as mentioned above. Information from Items 1 and 2 are input into ARGEIBL
3	Define Mollier diagram and transport properties for real gas system	ACE	Thermodynamic and transport property maps	Input to ARGEIBL and CMA or ASTHMA computer programs
4	Define convective heat transfer coefficient	ARGEIBL or BLIMP	Convective heat transfer coefficient as a function of distance for desired wall temperature.	Input to CMA or ASTHMA computer program
5	Define radiative heat flux	--	Radiative flux as a function of distance	Input to CMA or ASTHMA computer program
6	Generation of surface and in-depth thermochemical data	ACE	Frozen edge enthalpy as a function of temperature, surface enthalpy as a function of surface temperature and nondimensionalized pyrolysis gas and char removal rates including the effect of mechanical melt removal if applicable, and pyrolysis gas enthalpy as a function of temperature	Input to CMA or ASTHMA computer program. Note that the data requirements resulting from in-depth charring are not appropriate to ASTHMA
7	Thermal response predictions	CMA or ASTHMA	In-depth temperature distribution and surface recession rates as functions of time	Define insulation thickness requirements, refine ballistic predictions, and used as input to structural analysis

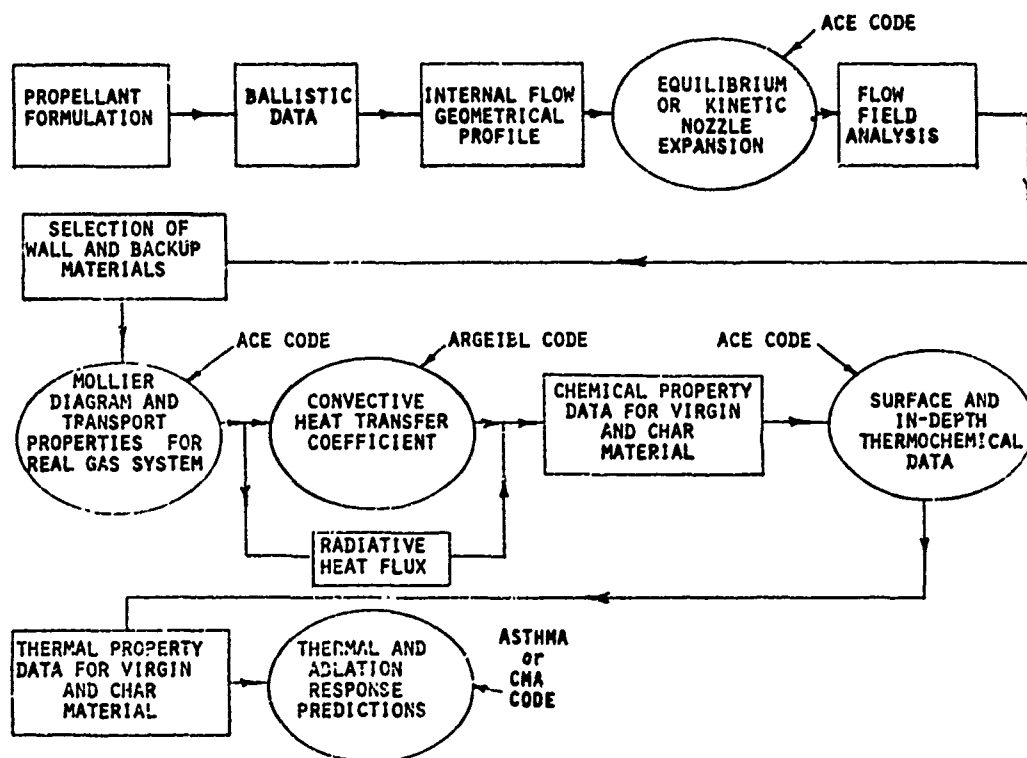


FIGURE 4-2 FLOW CHART FOR AEROTHERMODYNAMIC ANALYSIS

Those quantities which must be specified to perform the thermal analysis using the procedures described above are as follows:

- Propellant (or simulator) elemental composition
- Either propellant initial composition or theoretical flame temperature
- Combustion chamber operating conditions (e.g., pressure)
- Combustion product radiation properties
- Surface material elemental chemical compositions and constituent makeup, if applicable
- Material virgin and char densities
- Material thermophysical properties

Specific heat	}	Virgin and Char
Thermal conductivity		
Surface emissivity		
Heat of formation		
Decomposition kinetic constants for constituents, if applicable		

Simulator operating conditions and combustion product compositions have been presented for the five multiple pulse duty cycles in Section 3. Material dependent properties including surface thermochemical response data are given along with the computed surface boundary conditions in Section 4.2.

4.2 INTERMEDIATE ANALYSIS RESULTS AND MATERIAL PROPERTIES

Analysis of material thermal response in hyperthermal combustion product environments requires the evaluation of convective and radiative boundary condition information and the specification of material thermophysical properties. The results of studies performed to obtain these quantities are reviewed in this section.

The analysis of the nozzle flow, boundary layer transport, and radiative energy interchange phenomena are covered in Section 4.2.1. These calculations define the non-blowing (i.e., non-ablating) surface time dependent heating condition for the five duty cycles. The ablating surface thermochemical response calculations for both the graphitic throat package and the exit cone material at $A/A^* = 4.2$ are described in Section 4.2.2. Material thermophysical properties are given in Section 4.2.3.

4.2.1 Time Dependent Non-Blowing Surface Boundary Conditions

The time dependent non-blowing surface boundary condition specifications may be conveniently divided into the following categories:

- Convective heating during simulator firings
- Radiative heating during simulator firings
- Exposed surface boundary conditions during cooldowns

These categories are discussed in Sections 4.2.1.1, 4.2.1.2, and 4.2.1.3, respectively.

4.2.1.1 Convective Heating During Firings

The evaluation of the turbulent convective, non-blowing heating during firing pulses was done utilizing the Aerotherm Real Gas Energy Integral Boundary Layer (ARGEIBL) computer code. The uncertainty in heat transfer coefficient using this or any other turbulent boundary layer prediction procedure has been estimated to be on the order of ± 25 percent (e.g., Reference 7).

The ARGEIBL procedure requires the specification of boundary layer edge properties as a function of streamwise boundary layer length. These quantities were obtained from real gas, two-phase flow isentropic nozzle expansion solutions which were computed using the Aerotherm Chemical Equilibrium (ACE) computer code.

The expansion solutions were generated for the nominal simulator propellant composition given in Section 2. One solution corresponded to ideal combustion at 700 psia chamber pressure ($T_o = 6210^\circ\text{R}$), and one corresponded to 97 percent combustion efficiency* at 700 psia ($T_o = 5830^\circ\text{R}$). The 97 percent combustion efficiency was simulated by doing equilibrium solutions at a lower total temperature. A comparison of the boundary layer edge static temperature ratios for the two combustion efficiencies is given in Figure 4-3. As the figure indicates, the effect of the non-ideal combustion on the expansion characteristics is noticeable. The difference between the two temperature ratio curves is due to the greater condensed alumina formation at the lower temperature. The lower total temperature also means that the alumina solidifies earlier in the expansion. Although Figure 4-3 indicates that the effect of incomplete simulator fluid combustion should be accounted for, errors in the expansion properties attributable to instantaneous fluctuations in combustion efficiency or, equivalently, in combustion product composition are small relative to the 25 percent uncertainty in the overall boundary layer analysis results.

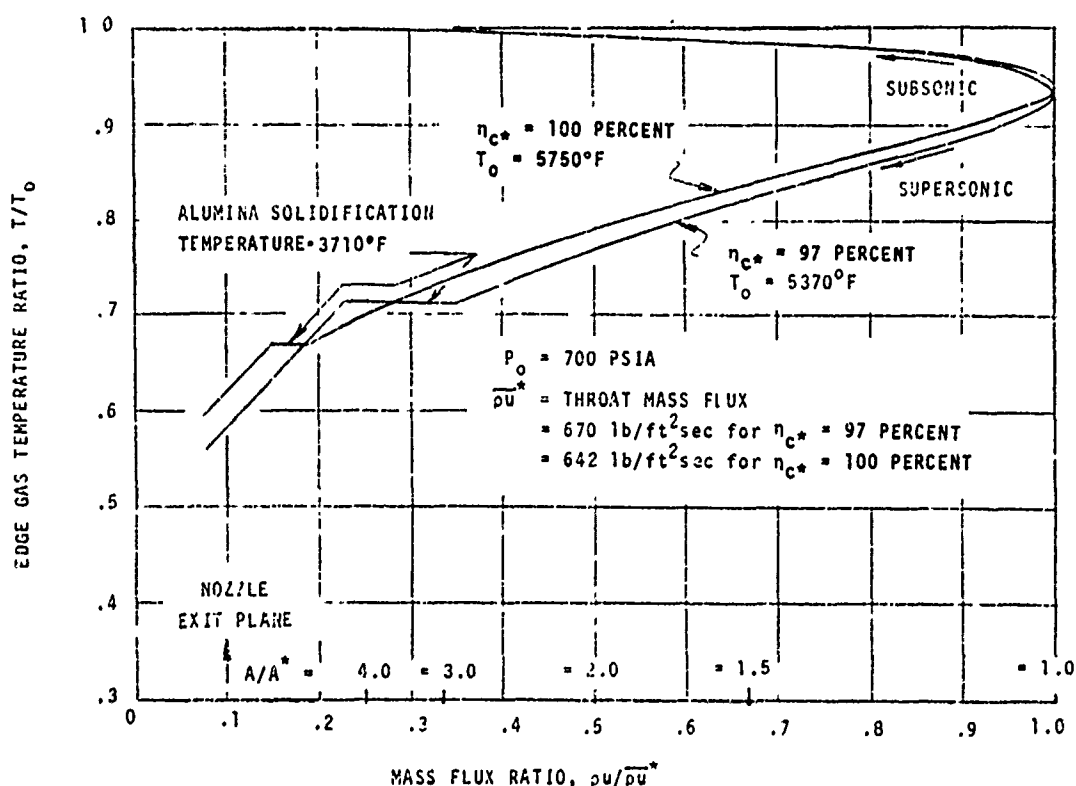


FIGURE 4-3 ISENTROPIC EXPANSION TEMPERATURE RATIOS FOR IDEAL AND ACTUAL PROPELLANT COMBUSTION EFFICIENCIES

*As used here, the combustion efficiency is defined as the ratio of the actual to the ideal characteristic exhaust velocity which varies approximately as the chamber temperature to the one-half power.

The 97 percent efficiency solution was felt to best characterize the simulator combustion product flow and was used to define boundary layer edge properties for the ARGEIBL convective heating distribution computation. These properties are shown as a function of non-dimensional mass flux in Figure 4-4.

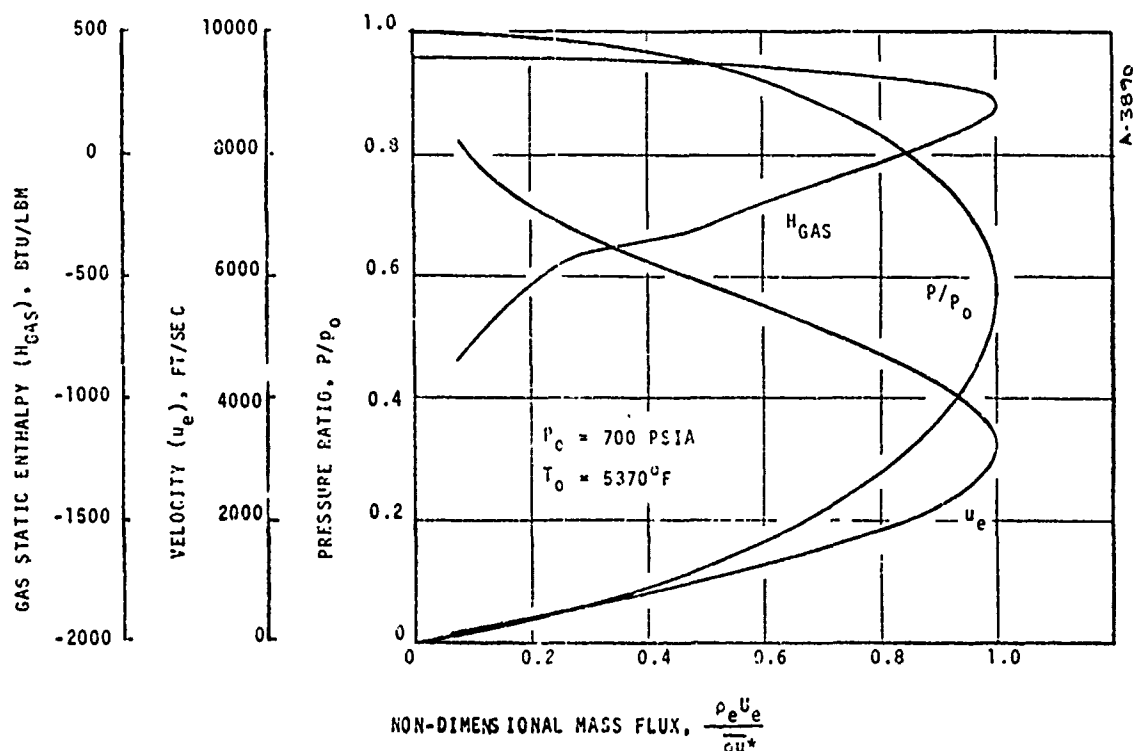


FIGURE 4-4 FREE STREAM ISENTROPIC EXPANSION PROPERTIES AS COMPUTED FOR 97 PERCENT COMBUSTION EFFICIENCY

The enthalpy values correspond to the gaseous component of the two phase flow. As discussed in Section 4.1, the relationship between the expansion results and the streamwise boundary layer length coordinate is defined by a nozzle flow field analysis. For the multiple pulse rocket nozzle analysis, the flow was assumed to be one-dimensional. Thus the ratio of local edge mass flux to throat flux is directly related to local area ratio by mass conservation, i.e.,

$$\frac{\rho_e u_e}{\rho u^*} = A^*/A = \text{inverse of area ratio}$$

where A^*/A is defined as a function of streamwise length from the nozzle geometry. The radius and inverse area ratio for the nominal nozzle geometry shown in Figure 2-1 are shown as a function of boundary layer length in Figure 4-5. An assumption about the flow over the lip of the throat entrance cap was required

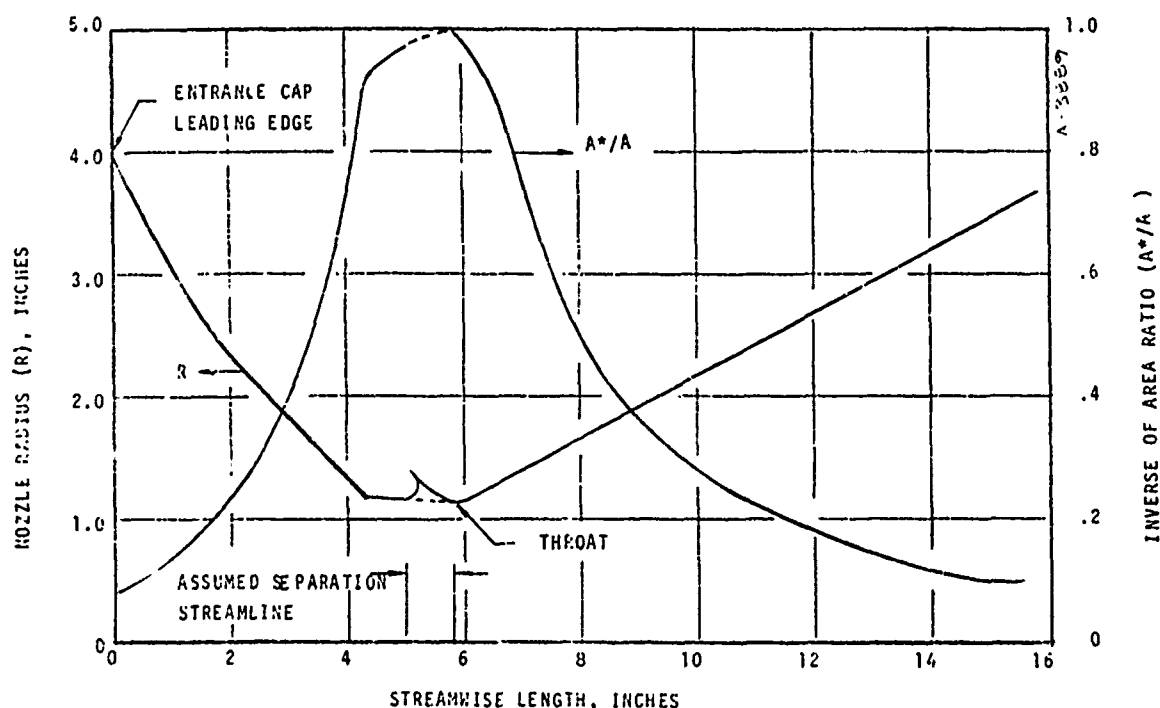


FIGURE 4-5 NOMINAL NOZZLE GEOMETRY AS A FUNCTION OF
STREAMWISE BOUNDARY LAYER LENGTH

to define edge conditions in the throat region. A separation-recirculation region aft of the throat entrance ring was expected but was difficult to quantify. For simplicity, the separation streamline shown in Figure 4-5 was assumed. Based on this assumption, streamwise variations of pressure, velocity, and edge gas enthalpy were obtained from Figures 4-4 and 4-5.

The other information needed to perform an ARGEIBL prediction are

- 1) Mollier-type thermodynamic property tables including Prantl number and
- 2) specification of the streamwise variation of gas phase enthalpy at the surface temperature. As explained in Section 4.1, the Mollier tables are generated by parametric ACE code thermodynamic state solutions. Surface temperature variation is estimated based on the anticipated material ablative response.

For the multiple pulse nozzle analysis, ARGEIBL predictions were performed for the anticipated surface temperature (5000°R isothermal surface) and for a cold (900°R) surface to assess the sensitivity of the heat transfer coefficient for a wide range in surface temperature. The two transfer coefficient distributions are shown in Figure 4-6. Based upon the nozzle throat values of the convective heat transfer coefficient, the two solutions indicate that the coefficient varies as temperature to the -0.22 power. This means that a 20 percent error in estimating surface temperature (1000°R) amounts to only a 4 percent error in heat transfer coefficient.

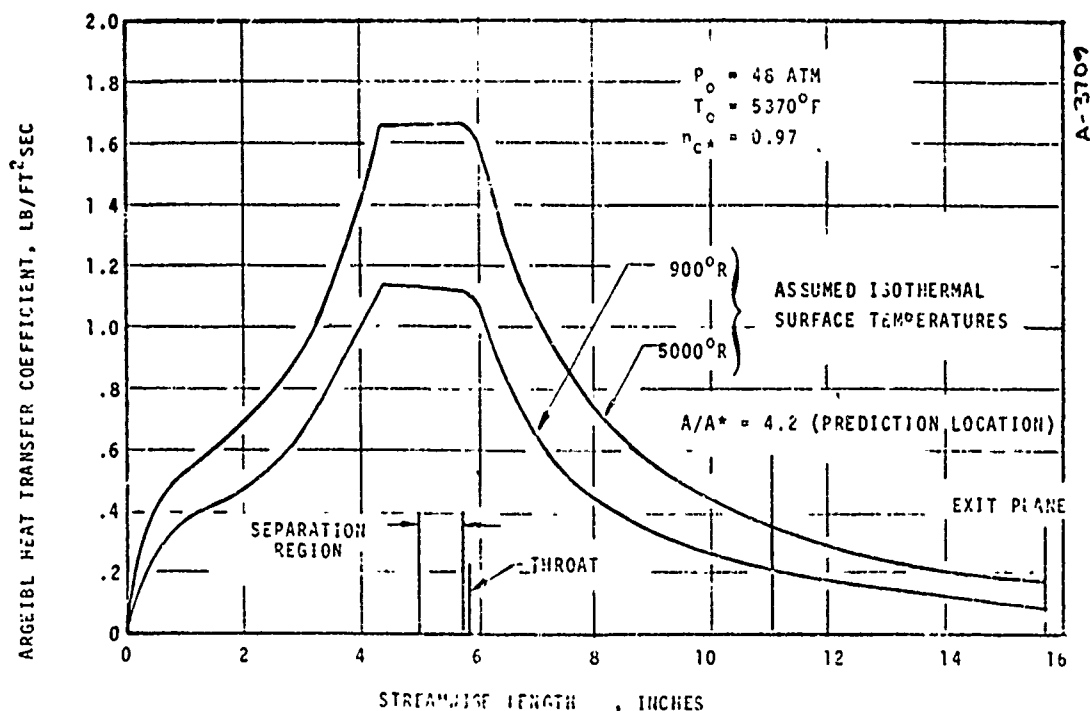


FIGURE 4-6 ARGEIBL HEAT TRANSFER COEFFICIENT DISTRIBUTION FOR MULTIPLE PULSE NOZZLE CONFIGURATION. ANB3066 SIMULATOR PROPELLANT

To this point, the convective heating evaluation was performed for the nominal rocket simulator operating conditions (propellant composition from Table 2-3 and a combustion chamber pressure of 700 psia). Turbulent heating considerations (Reference 8) indicate that in a rocket nozzle, the heat transfer coefficient varies as the 0.8 power of chamber pressure. To account for pressure changes during the various firing pulses, the following relationship was used:

$$\rho_e u_e C_{H_O} = (K) \left(\frac{P_O}{700} \right)^{0.8} \rho_e u_e C_{H_{ARGEIBL}} \quad (4-1)$$

where

- $\rho_e u_e C_{H_O}$ - non-blowing convective heat transfer coefficient applicable to a recovery enthalpy driving potential
- P_O - instantaneous measured chamber pressure in psia units (see Section 2 and Appendix A)
- $\rho_e u_e C_{H_{ARGEIBL}}$ - predicted ARGEIBL heat transfer coefficient at the nozzle location of interest
- K - correlation factor (evaluated in Reference 9 as 0.75)

The variation of heat transfer coefficient with time, plus the applicable local recovery enthalpy, defines the convective, time dependent boundary condition during the firing pulses.

In applying the convective heating boundary condition as a function of time to the PG coated nozzle throat, consideration had to be given to the protection of the upstream section of the coating by the overlapping portion of the MXC 313 carbon phenolic. This protection of the PG coating was taken into account by assuming zero convective heating to that portion of the coating which was covered by the MXC 313 carbon phenolic until such time as the phenolic carbon had recessed and exposed the coating. In addition, convective heating in the separation region, which is shown in Figure 4-5 for the initial configuration, was assumed to be negligible. As the MXC 313 carbon phenolic recedes, the axial length of this separation region decreases.

4.2.1.2 Radiation Heating During Simulator Firings

In both the CMA and the ASTHMA codes, the surface energy balance takes the following form:

$$\dot{q}_{\text{conv}} + \dot{q}_{\text{chem prod}} + \dot{q}_{\text{rad in}} - \dot{q}_{\text{rad out}} - \dot{q}_{\text{cond}} = 0 \quad (4-2)$$

These flux terms account for the energy transport phenomena shown in Figure 4-1. This section is concerned with the two radiation terms. The radiant flux absorbed by the surface ($\dot{q}_{\text{rad in}}$) is defined as the incident radiation multiplied by the absorptance of the wall. The radiant flux emitted by the surface ($\dot{q}_{\text{rad out}}$) is defined as that emitted by a black body multiplied by an emittance factor and by a view factor. Therefore the net radiation to the surface ($\dot{q}_{\text{net rad}}$) is defined by

$$\dot{q}_{\text{net rad}} = \alpha_w \dot{q}_{\text{inc rad}} - F \epsilon_w \sigma T_w^4 \quad (4-3)$$

where

α_w, ϵ_w - absorptivity and emissivity, respectively, of wall material
(α_w and ϵ_w are equal by Kirchoff's Law for a gray body)

σ - Stefan-Boltzmann constant

T_w - wall temperature

F - view factor

In order to model the radiation transport between a particle laden stream and the nozzle surface, it was assumed that the stream was optically thick and that the particles and wall exchange radiant energy as if they were two parallel plates. In this way multiple reflections between the wall and stream were taken into account. In addition, it was assumed that both the stream and wall behave

as gray bodies and that they emit and reflect radiant energy diffusely. Based on the above assumption, the net radiant heat flux relation is given in as:

$$\dot{q}_{\text{net rad}} = \epsilon_{\text{eff}} (\sigma T_s^4 - \sigma T_w^4) \quad (4-4)$$

where

$$\epsilon_{\text{eff}} \text{ (effective emissivity)} = \left(\frac{1}{\frac{1}{\epsilon_w} + \frac{1}{\epsilon_s} - 1} \right) \quad (4-5)$$

ϵ_s - particle laden stream emissivity

T_s - local stream static temperature

To define the net radiation heat flux using Equation (4-4) the local static stream temperature and the effective emissivity had to be evaluated. The stream temperature was obtained from the isentropic expansion data presented previously in Figure 4-3. At the nozzle throat and upstream thermocoupled plug analysis prediction locations, the stream temperatures are 5000 and 3710°F, respectively. The effective emissivity was evaluated from Equation (4-5) using a value of 0.9 for the wall emissivity and using the following relationship (Reference 8) for the emissivity of the particle laden combustion products.

$$\epsilon_s = 1 - \exp \left(-C \frac{n}{16} \rho D \right) \quad (4-6)$$

where

- C - experimentally determined constant (0.808 for the propellant being considered in this analysis)
- n - percentage of aluminum loading (= 15.5 for ANB 3066 simulation propellant)
- ρ - local density of propellant combustion species (lb/ft³)
- D - local beam length, usually taken as the diameter (in.)

At the nozzle throat and exit cone analysis prediction locations, the effective emissivities calculated from Equation (4-5) were 0.30 and 0.09, respectively, for a nominal chamber pressure of 700 psia. However, a distribution of the effective emissivity with streamwise length was required for the two-dimensional analysis of the nozzle throat insert for nozzle no. 8. This distribution is shown in Figure 4-7 for each of the four pulses which comprised the multiple pulse duty cycle for this nozzle. This figure shows the increase in effective

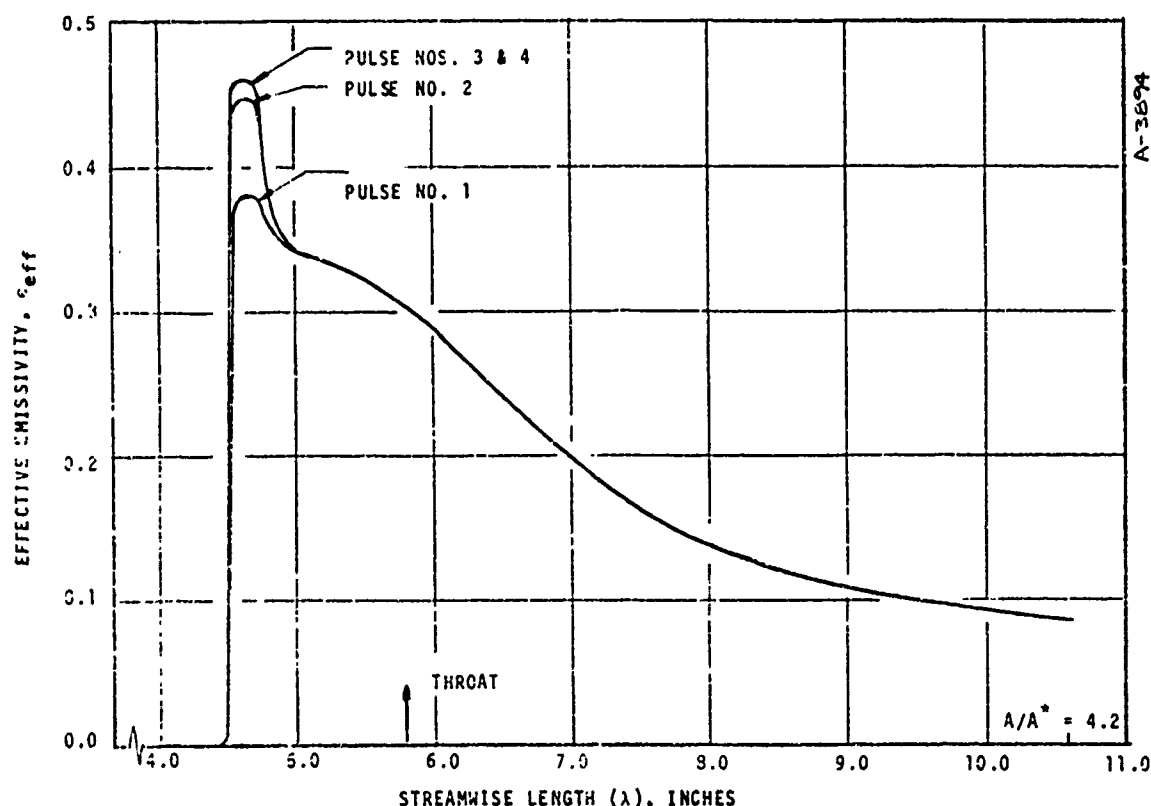


FIGURE 4-7, VARIATION OF EFFECTIVE EMISSIVITY WITH STREAMWISE LENGTH

emissivity with the recession of the MXC 313 carbon phenolic entrance cap. Average values of local pressure (or area ratio) during a particular pulse were used for predicting the effective emissivity as the accuracy of the stream emissivity correlation (Equation (4-6)) did not warrant a detailed analysis.

In conclusion, the overall effect of radiation as compared to convective heat transfer during the firing pulses is small. For example, during the first pulse of the nozzle no. 8 firing, the net radiation at an exit cone area ratio of 4.2 amounted to only 4 percent of the total energy transferred to the nozzle surface.

4.2.1.3 Exposed Surface Boundary Condition During Cooldown

At motor burnout, convective heating of the nozzle surface is eliminated which simplifies the surface energy balance given by Equation (4-2) to the following form:

$$q_{\text{rad in}} - q_{\text{rad out}} - q_{\text{cond}} = 0 \quad (4-7)$$

In applying this equation during cooldown, it was assumed that the nozzle surface was an isothermal gray body. This assumption implies there is no net radiant heat transfer between the surface under consideration and the rest of the nozzle interior. The only net transfer of radiant energy occurs between the section of wall being analyzed and the environment beyond the exit plane of the nozzle exit cone. This flux is given by

$$\dot{q}_{\text{net rad}} = F\epsilon_w\sigma (T_e^4 - T_w^4) \quad (4-8)$$

where

T_e = environment temperature exterior to the exit cone

Neglecting T_e^4 in comparison to T_w^4 , this equation becomes

$$\dot{q}_{\text{net rad}} = - F\epsilon_w\sigma T_w^4 \quad (4-9)$$

Equation (4-9) was used to model the radiative heat flux during cooldown.

In evaluating $\dot{q}_{\text{net rad}}$ at the nozzle throat and exit cone analysis locations from Equation (4-9) a value of 0.9 was used for the wall emissivity and values of 0.011 and 0.310 were used for the view factor at the nozzle throat and exit cone locations respectively. The view factors were calculated using the procedures presented in References 9 and 10.

A brief analysis was performed to study the sensitivity of the predicted cooldown temperatures on the magnitude of the view factor for the upstream thermocoupled plug. For this sensitivity analysis, one prediction was made using the view factor mentioned above (0.310) and one was made assuming a view factor of zero. The temperatures were predicted for the cooldown following pulse no. 1 for nozzle no. 8, and these temperatures are shown in Figure 4-8. Based on these results two conclusions are apparent, namely

- the predicted temperatures during cooldown are a weak function of the radiation view factor
- the predicted temperatures during cooldown at the TC no. 1 location for either value of the radiation view factors are considerably below the measured temperatures

Even though the finite value for the radiation view factor causes the cooldown temperatures to be under predicted, it best represents the radiation phenomena during cooldown, and, thus, it was used for all of the multiple pulse nozzle analyses. The reason for the temperatures being under predicted during cooldown is presented in Section 4.3.

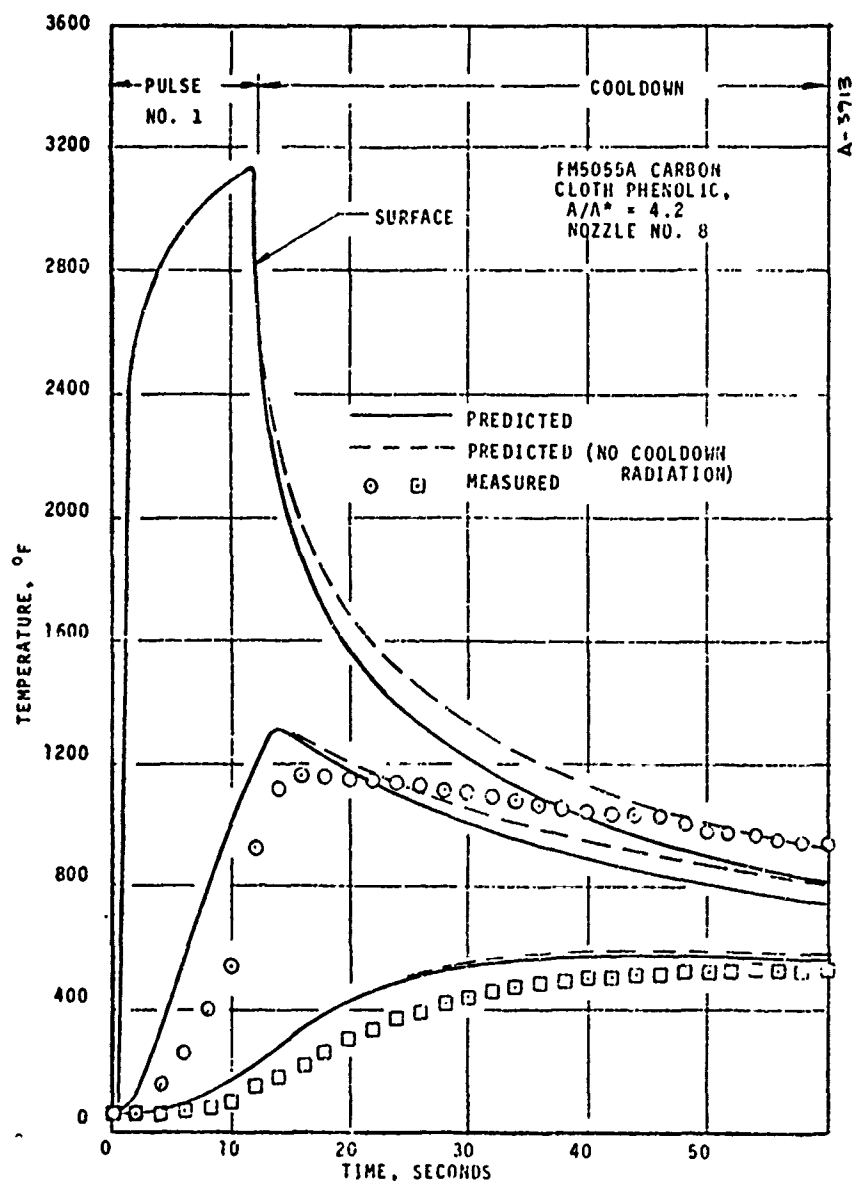


FIGURE 4-8 EFFECT OF COOLDOWN RADIATION INTERCHANGE MODEL
ON IN-DEPTH TEMPERATURE PREDICTIONS DURING COOLDOWN

4.2.2 Ablating Surface Thermochemical Response Solutions

During the firing pulses, the nozzles were exposed to a high temperature chemically reacting environment which caused chemical corrosion at the surface of all of the components and caused in-depth material degradation and off-gassing for the charring ablating components. In order to account for the complicated boundary layer thermochemical phenomena occurring at the nozzle surface in such an environment, the ACE code described in Section 4.1 was utilized to generate parametric sets of surface thermochemical solutions suitable for input to the CMA or ASTHMA thermal response analysis procedures. The surface thermochemistry results computed for the throat package are presented in Section 4.2.2.1 and those for the exit cone location are presented in Section 4.2.2.2.

4.2.2.1 Graphite Surface Thermochemistry Solutions

The surface thermochemical response of graphitic materials such as ATJ and pyrolytic graphite (PG) is controlled by the finite (as opposed to equilibrium) reaction rates of the surface carbon atoms with the H_2O , CO_2 and H_2 components of the solid propellant simulator combustion products. The kinetically controlled reaction rate models developed under Air Force Contract F04611-69-C-0081 were utilized to compute the surface response of the graphite components in the multiple pulse nozzle throat package. The solutions were performed using the ACE code.

The kinetic response model incorporates a Langmuir type surface reaction inhibition expression into an Arrhenius temperature dependent rate relation. The rate expression and reaction kinetic rate constants are given in Table 4-3.

TABLE 4-3
KINETICALLY CONTROLLED REACTION RATE EXPRESSIONS USED FOR PG LAYER
AND ATJ GRAPHITE SURFACE THERMOCHEMISTRY SOLUTIONS^a

Material	Pre-Exponent Factors (units to give X_{C^*} below)		Activation Energies (cal/mole)	
	B_1	B_2	E_1	E_2
Layer PG	12.5	0.77	46,000	55,500
Edge PG ^b	4.12×10^3	1.03×10^6	65,500	129,500
ATJ (Bulk) Graphite	1.98×10^3	4.94×10^7		

^a

$$X_{C^*} = \frac{B_1 \exp(-E_1/RT_w)}{(1 + P_{H_2O} + P_{H_2} + P_{CO_2} + P_{CO})(1 + 3P_{HCl})} \left[\left(P_{H_2O} - \frac{P_{CO}P_{H_2}}{K_{H_2O}} \right) + \left(P_{CO_2} - \frac{P_{CO}^2}{K_{CO_2}} \right) \right]$$

$$+ \frac{B_2 \exp(-E_2/RT_w)}{(1 + P_{H_2O} + P_{CO_2} + P_{CO})} \left[\left(P_{H_2} - \frac{P_{C_2H_2}}{K_{H_2}} \right) \right], \text{ moles of reaction/ft}^2\text{sec}$$

^bNo edge PG solutions were performed; constants included for completeness.

The partial pressure quantities were evaluated in the ACE code using the film coefficient, multicomponent unequal diffusion boundary layer model. Gaseous species adjacent to the graphite surface were allowed to be in chemical equilibrium with each other but not with the surface. In order to allow diffusion of only the gaseous components of the freestream fluids, an effective boundary layer edge gas composition was defined by removing those elemental amounts tied to the condensed alumina from the ANB 3066 composition. The relative elemental composition with and without alumina are given in Table 4-4.

TABLE 4-4
CHEMICAL ELEMENTAL COMPOSITIONS FOR THROAT AND EXIT CONE
SURFACE THERMOCHEMISTRY SOLUTIONS^a

Element	Boundary Layer Edge		PG & ATJ Surface	FM5055A Carbon Phenolic	
	Including Condensed Al ₂ O ₃ ^a	No Al ₂ O ₃ ^a Allowed ^b		Pyrolysis Gas	Char
Hydrogen	3.460	3.460	---	10.597	---
Carbon	0.905	0.905	8.326	5.083	8.326
Nitrogen	0.624	0.624	---	---	---
Oxygen	2.382	1.534	---	1.767	---
Aluminum	0.583	0.018	---	---	---
Chlorine	0.651	0.551	---	---	---

^aAll quantities in gr atoms/100 gr of mixture

^bMass of Al₂O₃^a removed per mass of gas phase remaining = 0.404

Surface maps were generated for two locations for both the ATJ throat retainer ring and the layer oriented pyrolytic graphite throat insert. One of the pyrolytic graphite maps was generated for the throat plane conditions and used for all one-dimensional throat response calculations. The conditions for the other three maps were defined so that streamwise variations in surface thermochemical response could be accounted for in the two-dimensional throat package response calculation (nozzle no. 8 only). The area ratio, local static pressure and temperature, local edge gas recovery enthalpy, and the local mass transfer coefficient values for which the kinetically controlled response calculations were performed are given in Table 4-5. The non-dimensional ablation rate maps

TABLE 4-5
SUMMARY OF THROAT AND EXIT CONE CONDITIONS FOR WHICH
SURFACE THERMOCHEMISTRY SOLUTIONS WERE OBTAINED

Area Ratio ^a	Material	Edge Static Conditions		Nominal Transfer Coefficient		Recovery Enthalpy ^d (Btu/lbm)
		Pressure (atm)	Temperature (°R)	Heat ^b (lb/ft ² sec)	Mass ^c (lb/ft ² sec)	
-1.7	PG	44.0	3208.	0.67	0.53	287.
Throat	PG	27.6	3029.	0.82	0.65	361.
1.4	ATJ	13.5	2786.	0.53	0.42	324.
2.0	ATJ	6.5	2521.	0.36	0.29	263.
4.2	FM5055A	2.4	2319.	0.17	0.14	327.

^aNegative number indicates subsonic area ratio
^bHeat transfer coefficient equals 0.75 times ARGENT result
^cRatio of mass to heat coefficient equals 0.734
^dRecovery enthalpy equals $h_{\text{STATIC}} + Pr^{1/3}(u_{\infty}^2/2)$; $Pr = 0.504$

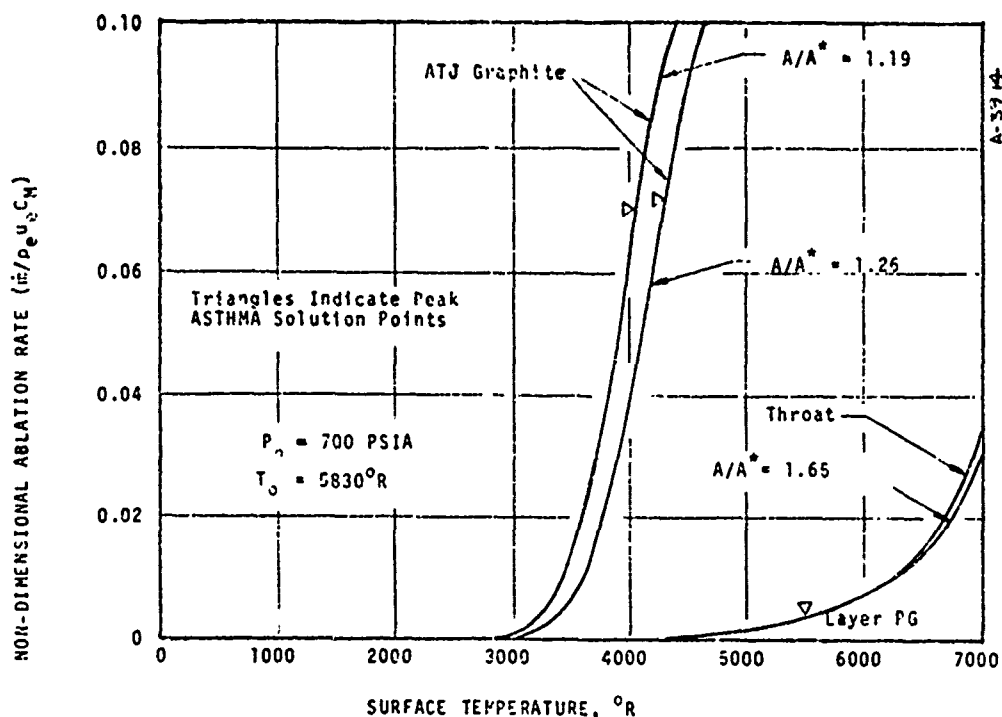


FIGURE 4-9 KINETICALLY CONTROLLED RESPONSE OF PYROLYTIC AND ATJ GRAPHITES TO ANB 3066 PROPELLANT SIMULATION

for each location are shown in Figure 4-9. Also shown in Figure 4-9 are the peak surface temperature points attained during the ASTHMA throat package thermal analysis.

4.2.2.2 Carbon Cloth Phenolic Exit Cone Thermochemistry Solution

Diffusion controlled surface thermochemistry state solutions were computed using the ACE computer code for conditions corresponding to an area ratio of 4.2 in the exit cone of the multiple pulse nozzles. These solutions parametrically defined the surface response analysis. The surface thermochemistry solutions utilized 1) the same multicomponent, unequal diffusion coefficient boundary layer model that was used for the kinetically controlled throat response analyses (Section 4.2.2.1), 2) the effective edge gas composition given in Table 4-3 as the change in the freestream alumina between the throat and the $A/A^* = 4.2$ locations was negligible, and 3) the boundary layer edge conditions given in Table 4-4. Furthermore, since the carbon cloth phenolic depolymerizes in depth at varying rates, the effect of different relative amounts of pyrolysis gas on the surface thermochemical response was evaluated. The computed non-dimensional ablation rates for parametrically changing values of non-dimensional pyrolysis off gas rate are shown in Figure 4-10.

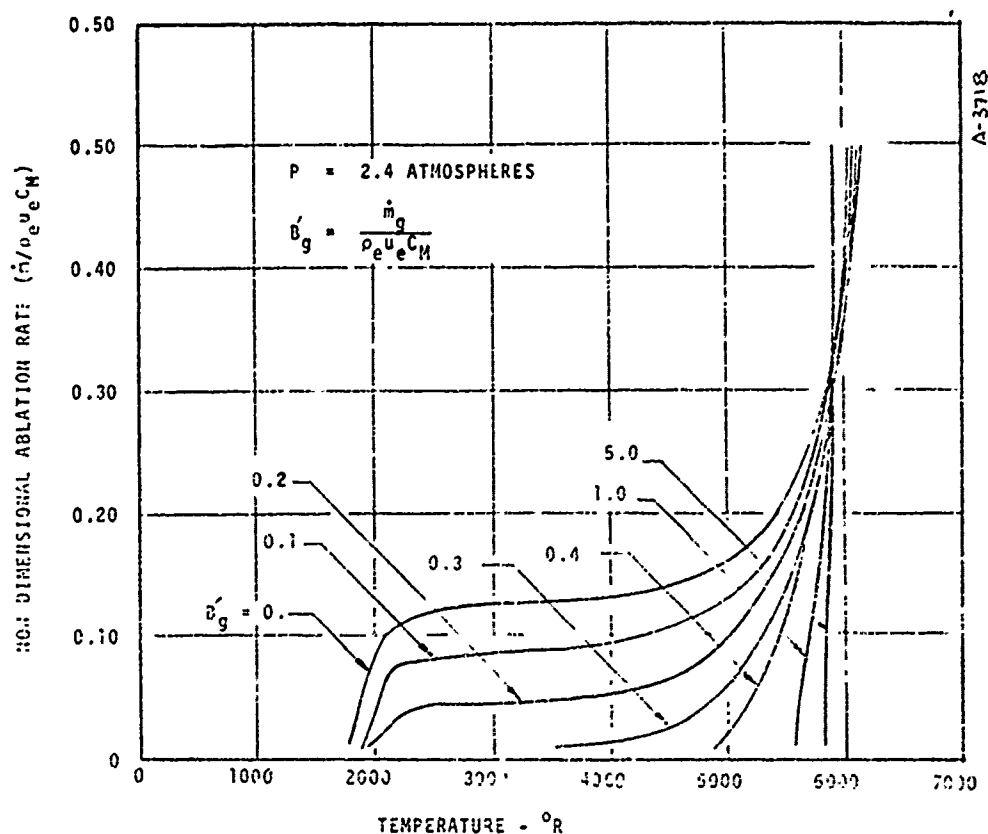


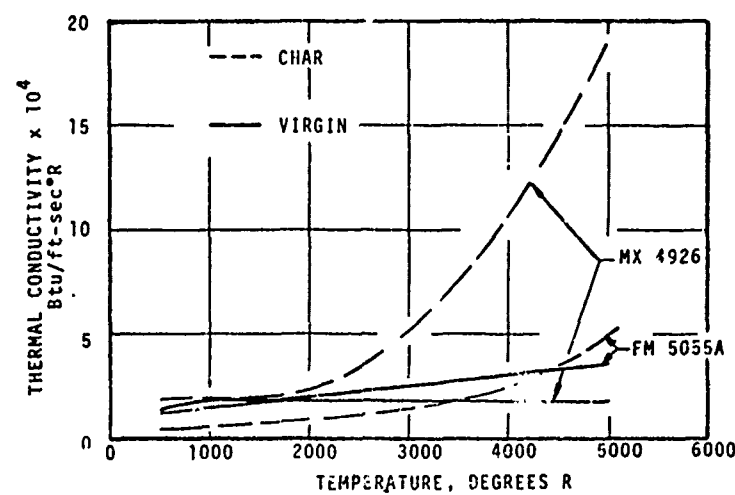
FIGURE 4-10 DIFFUSION CONTROLLED SURFACE RESPONSE OF FM5055A CARBON PHENOLIC TO ANB3065 PROPELLANT SIMULATION FOR VARIOUS NON-DIMENSIONAL PYROLYSIS GAS RATES.

4.2.3 Thermal Properties

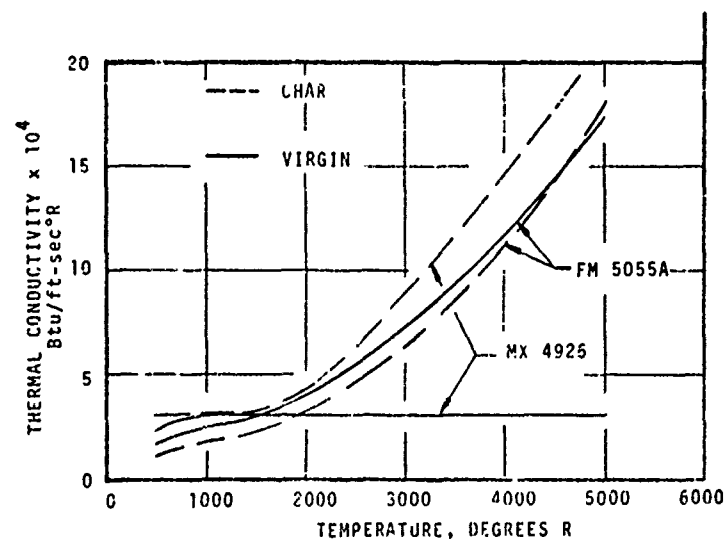
A brief literature survey was conducted to define the most applicable thermal properties to be used in predicting the thermal performance of the FM 5055A carbon cloth phenolic. This survey revealed that the desired data could be obtained from either Reference 2 or Reference 11. The major discrepancy between the data presented in these references is for the virgin and char thermal conductivities. In Reference 2, virgin and char thermal conductivities are presented for MX 4926* while in Reference 11, a model is presented for calculating the virgin and char thermal conductivities for either MX 4926 or FM 5055A. The thermal conductivity results from these references are shown in Figure 4-11 with the properties labeled MX 4926 obtained from Reference 2 and with the properties labeled FM 5055A obtained from Reference 11. Since virgin material thermal conductivity above 2000°R has very little significance because the material is generally approaching the fully charred state at this temperature, the virgin and char thermal conductivities from the two references for a 90 degree layup angle are in close agreement. In addition the virgin material properties from

* MX 4926 and FM 5055A are similar materials which are fabricated by different manufacturers.

the two sources are in close agreement for the 0 degree layup angle material. However, Figure 4-11a shows that a major discrepancy exists for the char thermal conductivity from the two references for the 0 degree layup material. Since the layup angle for the FM 5055A exit cone under consideration is 15 degrees,



a) 0 DEGREE LAYUP



b) 90 DEGREE LAYUP

FIGURE 4-11 THERMAL CONDUCTIVITY OF FM 5055A AND MX 4926 CARBON CLOTH PHENOLICS

the discrepancy in the char thermal conductivities at a 0 degree layup angle had to be resolved. As a first step, CMA analyses were performed for pulse no. 1 of nozzle no. 4 using both sets of thermal conductivity properties, and the predicted temperatures from the analyses are compared with the measured in-depth temperatures in Figure 4-12. In performing these analyses, the input information (Section 4.1) other than the virgin and char thermal conductivities was obtained

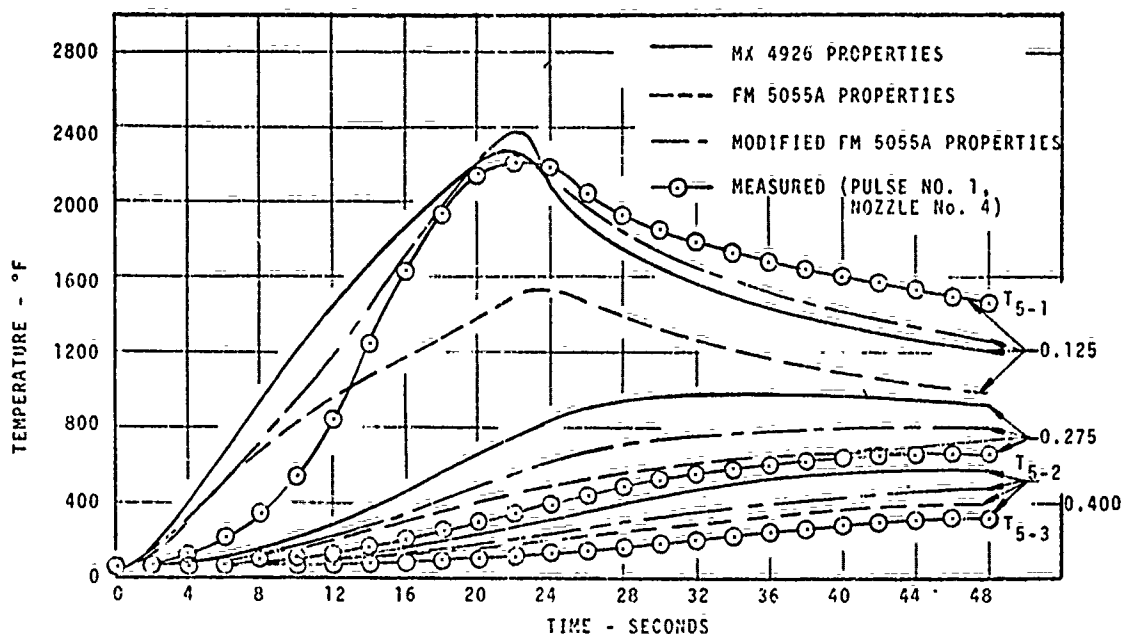


FIGURE 4-12 COMPARISON OF MEASURED AND PREDICTED TEMPERATURES FOR DIFFERENT CARBON CLOTH PHENOLIC THERMAL PROPERTIES

from Reference 2 and a portion of this information is summarized in Table 4-6.

TABLE 4-6

PHYSICAL AND CHEMICAL PROPERTIES
FOR FM 5055A CARBON CLOTH PHENOLIC

Nominal Density, lb/ft ³	89.4
Nominal Resin Fraction	0.345
Resin Residual	0.40
Virgin Material Heat of Formation, Btu/lb	-379
Assumed Resin Elemental Formula	C ₆ H ₆ O
Reinforcement Elemental Formula	C

In addition, the effect of material layup angle on the thermal conductivity was accounted for by using the following relationship:

$$k = k_{0^\circ} \left[1 + \left(\frac{k_{90^\circ}}{k_{0^\circ}} - 1 \right) \sin \theta \right] \quad (4-9)$$

where

k_{0° , k_{90° - thermal conductivity for the 0° and 90° layup angles, respectively

θ - layup angle

Careful examination of Figure 4-12 shows that the predicted temperatures using the MX 4926 properties are in good agreement with the measured temperatures for temperatures above 1200°R but that the predicted temperatures using FM 5055A properties provide better agreement for temperatures below 1200°R. A review of the comparisons between the measured and predicted temperatures presented in Reference 2, which were for MX 4926 thermal properties, also showed that the material temperatures were overpredicted for temperatures less than 1200°R. Based on the temperature comparisons presented in Figure 4-12 and Reference 2, a set of modified FM 5055A thermal conductivities were defined for a 0 degree layup angle. These properties which combine the best features from the MX 4926 and FM 5055A properties are presented in Figure 4-13.

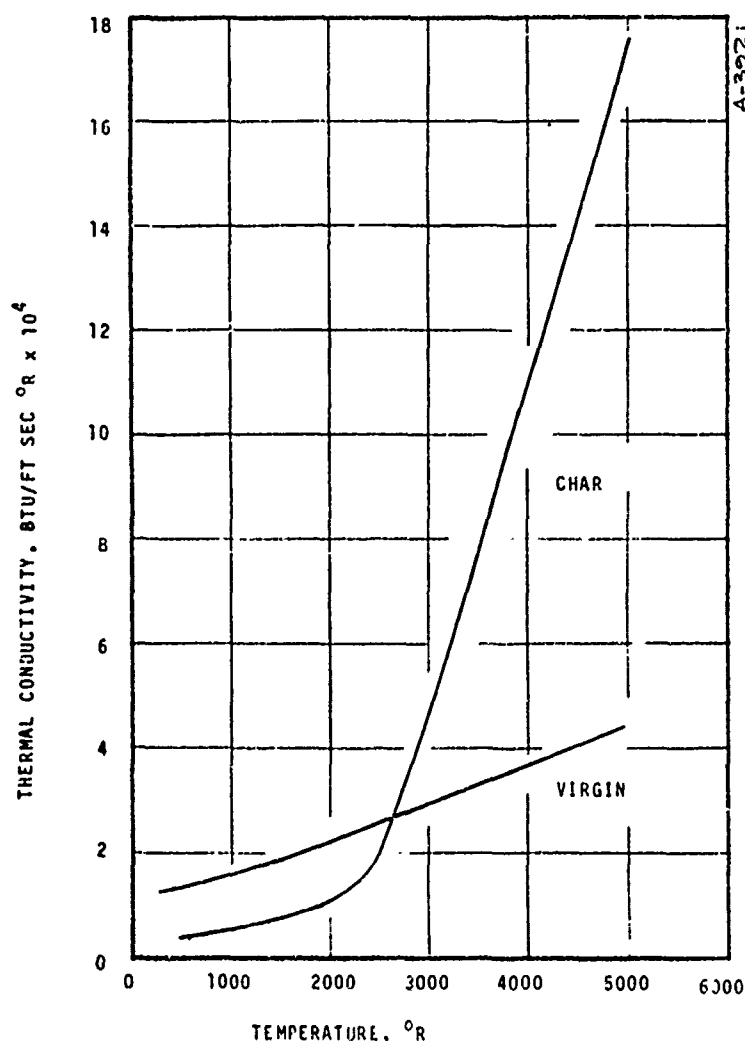


FIGURE 4-13 MODIFIED THERMAL CONDUCTIVITY FOR FM 5055A-0 DEGREE LAYUP

The predicted temperatures using these modified properties are also presented in Figure 4-12 and, as expected, provide better overall agreement with the measured temperatures. As a further check on the modified FM 5055A thermal properties, option 2 CMA analyses were performed using TC no. 2 of pulses no. 1 and 2 for nozzle no. 8 as an impressed boundary condition. For the MX 4926, FM 5055A, and modified FM 5055A thermal properties, the predicted in-depth temperatures at the TC no. 3 location are compared with the measured temperatures in Figure 4-14.

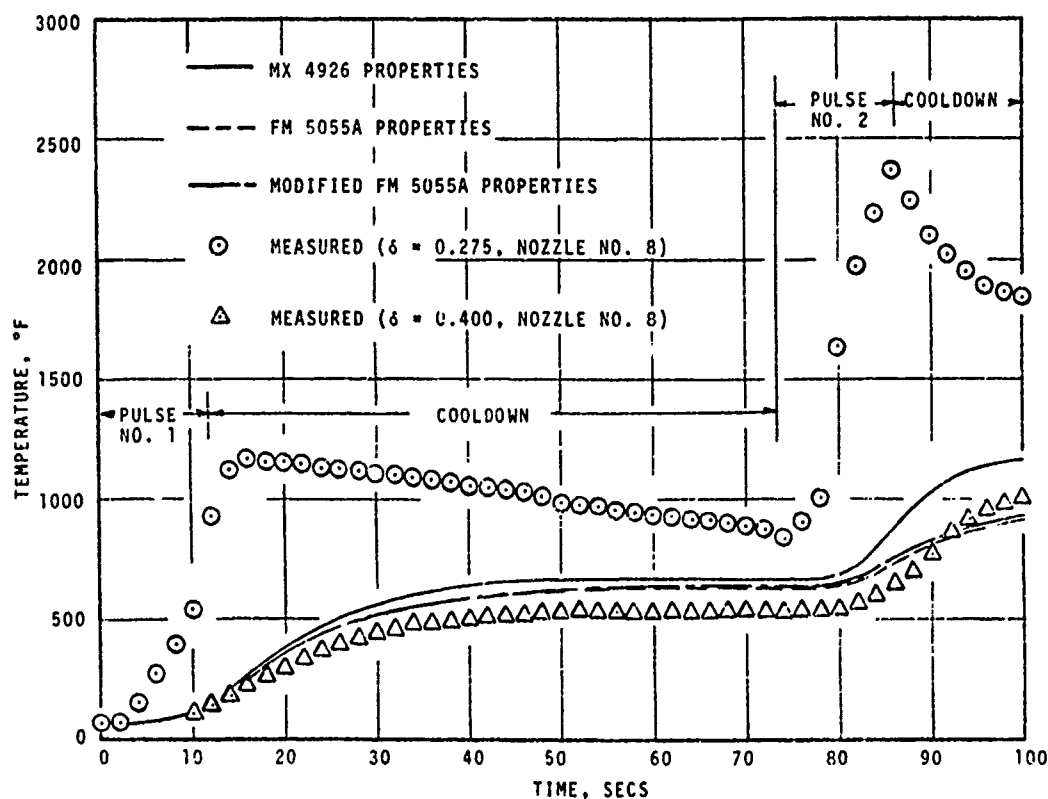


FIGURE 4-14 COMPARISON OF PREDICTED AND MEASURED IN-DEPTH TEMPERATURE USING OPTION 2 CMA

The temperatures predicted using the modified FM 5055A properties are in better agreement with the measured data than those using the MX 4926 properties. However, the slope of the measured temperatures for pulse no. 2 and the subsequent cooldown was predicted better by the temperatures using the MX 4926 thermal conductivities.

Based on the above analyses, the modified FM 5055A thermal conductivities were considered the most realistic and were used in predicting the thermal performance of the FM 5055A carbon cloth phenolic at a supersonic area ratio of 4.2. The thermal properties used for the PG coating, the ATJ and AGSR graphites, the GA carbon, and the RPD 150 asbestos phenolic materials in the nozzle throat analysis are presented in Figure 4-5 and Tables 4-7 and 4-8.

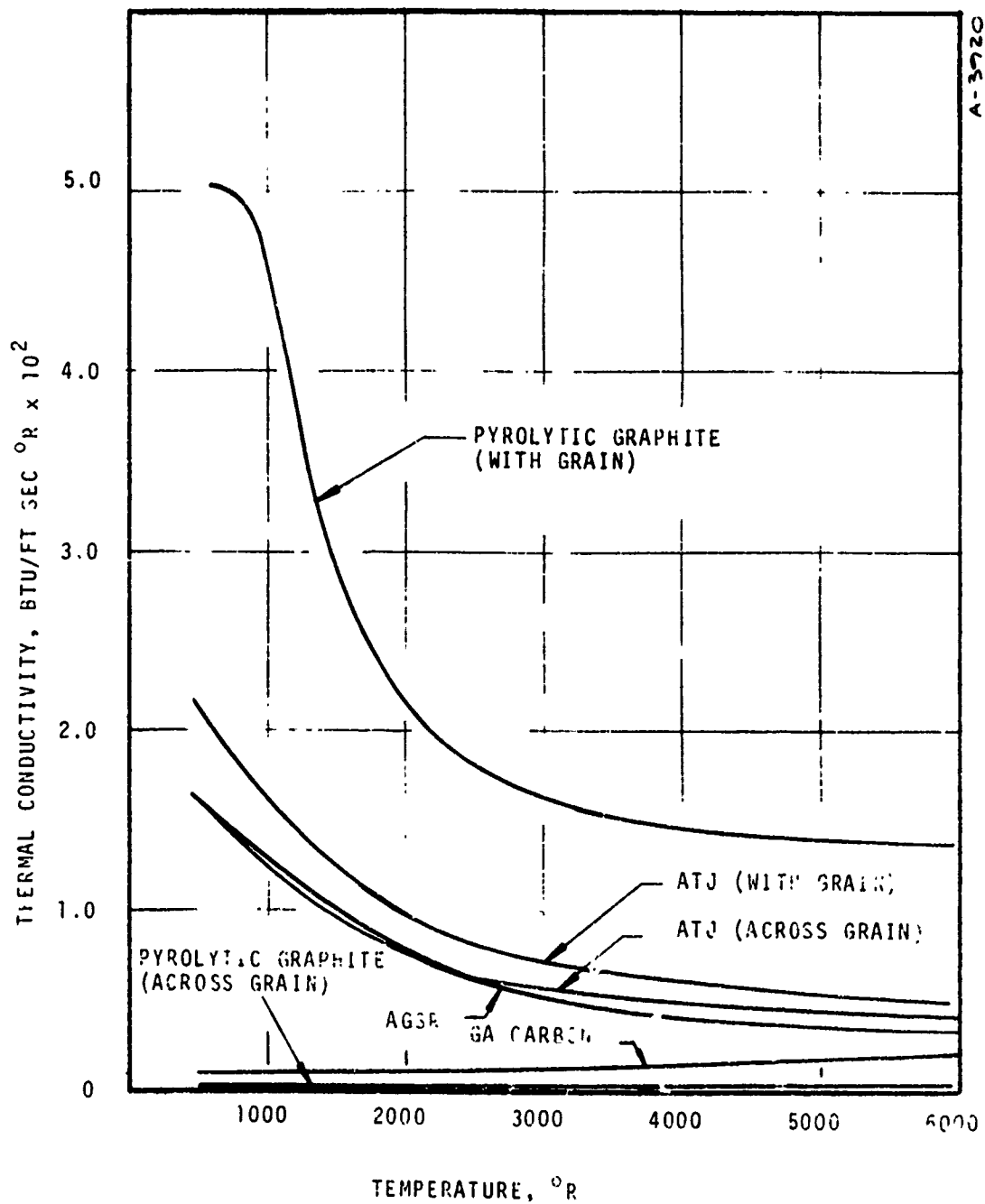


FIGURE 4-15
THERMAL CONDUCTIVITIES FOR PYROLYTIC GRAPHITE,
ATJ GRAPHITE, GA CARBON, AND AGSR GRAPHITE

TABLE 4-7

SPECIFIC HEAT AND DENSITIES FOR PYROLYTIC GRAPHITE,
ATJ GRAPHITE, AGSR GRAPHITE, AND GA CARBON

ATJ ($\rho = 108 \text{ lb/ft}^3$) and GA Carbon ($\rho = 96.6 \text{ lb/ft}^3$)		Pyrolytic Graphite ($\rho = 137.3 \text{ lb/ft}^3$)		AGSR Graphite ($\rho = 96.1 \text{ lb/ft}^3$)	
Temp (°R)	Specific Heat (Btu/lb°F)	Temp (°R)	Specific Heat (Btu/lb°F)	Temp (°F)	Specific Heat (Btu/lb°F)
492	.170	525	.240	500	.220
720	.250	760	.276	1000	.323
1080	.336	1060	.313	1500	.390
1800	.415	1850	.409	3000	.481
2160	.440	2190	.445	4000	.504
2520	.460	2650	.480	5000	.520
2880	.475	3060	.498	6000	.530
3240	.488	4460	.520		
3960	.505	7460	.520		
4680	.514				
5400	.524				

TABLE 4-8

THERMAL PROPERTIES USED FOR RPD 150 ASBESTOS PHENOLIC*
($\rho = 96.6 \text{ lb/ft}^3$)

Temp (°R)	Specific Heat (Btu/lb°F)	Thermal Conductivity (Btu/ft sec°R)
492	.170	$.825 \times 10^{-4}$
720	.250	$.825 \times 10^{-4}$
1080	.336	$.825 \times 10^{-4}$
1440	.385	$.850 \times 10^{-4}$
1800	.415	$.850 \times 10^{-4}$
2160	.440	$.870 \times 10^{-4}$
2520	.460	$.900 \times 10^{-4}$

* Since the ASThMA Program does not account for in-depth charring, the virgin material properties have been modified to take this into account.

4.3 COMPARISON OF COMPUTED AND MEASURED MATERIAL PERFORMANCE DATA

Based on the measured multiple pulse duty cycle operating conditions, one dimensional transient ablation and thermal response analyses were performed for both the upstream thermocoupled plug location (exit cone $A/A^* = 4.2$) and the throat plane of each of the five nozzles. For nozzle no. 8, a two-dimensional analysis was done for the graphite throat package and its asbestos phenolic backup material. Comparison of the results from the one-dimensional solution to those from the two-dimensional solution for this nozzle gave an accurate definition of

the differences between these two types of solutions. These differences at the back surface of the AGSR substrate were applied to the one-dimensional solutions for the other four nozzles in order to arrive at approximately two-dimensional solutions. The thermal performance predictions for the nozzle throat package and for the FM 5055A nozzle exit cone are compared to the measured material thermal performance in Sections 4.3.1 and 4.3.2, respectively.

4.3.1 Throat Package Response Analysis Results

A two-dimensional thermal response analysis including the effects of surface ablation was performed for the throat package of nozzle no. 8. This solution provided an accurate evaluation of the temperature field within the throat package for the entire four pulse duty cycle. The nodal layout for this ASTHMA 2-D analysis as well as the locations for the two thermocouples is shown in Figure 4-16. Part of the asbestos phenolic backup material is not included in

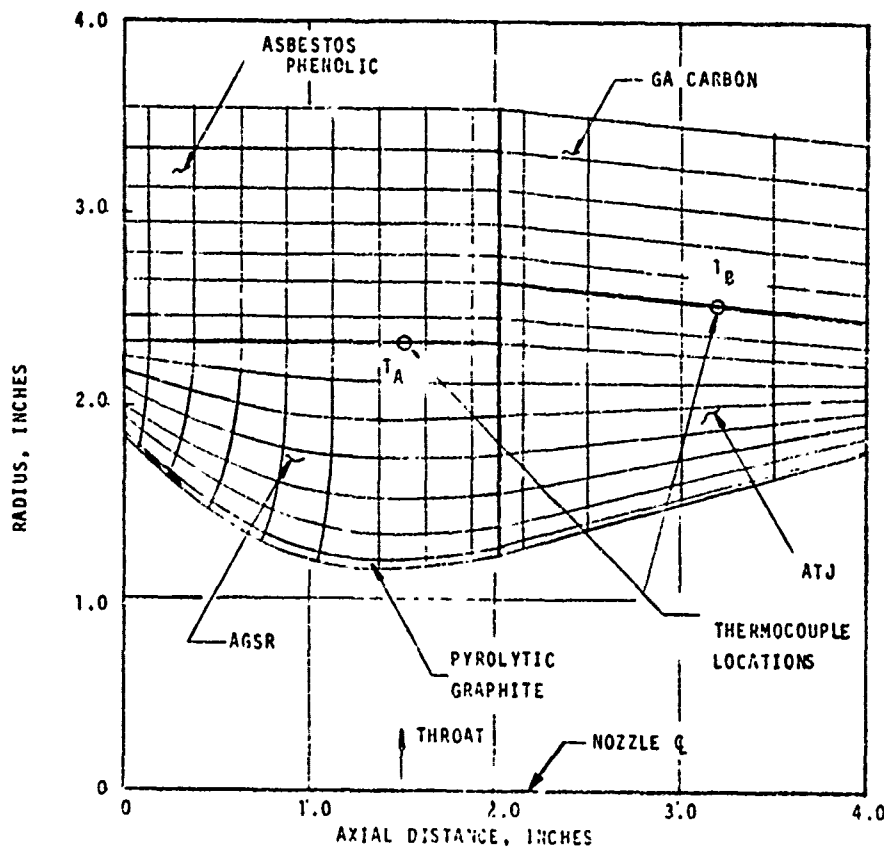


FIGURE 4-16 THROAT PACKAGE NODAL LAYOUT FOR 2-D ANALYSIS

the nodal grid as it does not influence the thermal response of the throat package. The surface thermochemistry maps shown previously in Figure 4-9 were defined for surface locations corresponding to grid system axial distances (see Figure 4-16) of 0.5, the throat, 1.5 and 2.5 inches.

To make maximum utilization of the 2-D analysis for nozzle no. 8, a 1-D analysis was performed at the nozzle throat plane using the CMA code. By comparing the surface recession and the surface and in-depth transient temperatures from both solutions, the adequacy of the 1-D analysis can be defined. Since the surface energy balance formulation in the CMA and ASTHMA codes are identical, the same throat surface response map could be utilized in each solution. The convective and radiative surface boundary conditions could also be specified identically so that the only difference between the CMA and ASTHMA solutions at the throat plane is the 2-D heat conduction effects. Since the materials, geometries, and overall heat flux levels are similar for all five nozzle firings, the differences in the temperatures predicted by the two types of solutions for nozzle no. 8 can be applied to the temperatures predicted by the 1-D throat analyses for nozzles no. 4, 5, 6, and 7 in order to obtain approximate 2-D predicted temperatures. By comparing these temperatures to the measured temperatures at the back wall of the throat insert, the relative accuracies of the two prediction procedures can be evaluated for each of the five duty cycles. Comparisons of computed one- and two-dimensional thermal response results are compared to the measured back wall temperature histories in Section 4.3.1.1. The throat plane surface recession calculations are compared to data in Section 4.3.1.2.

4.3.1.1 In-Depth Temperature Comparisons

The predicted transient temperatures using the ASTHMA 2-D analysis are compared in Figure 4-17 with the temperatures measured at the rear surface of the AGSR for nozzle no. 8. As shown by this figure, the predicted temperatures which take two-dimensional effects into account are in excellent agreement with the measured data as the difference between the measured and predicted 2-D temperatures is less than 100°F for the entire nozzle no. 8 duty cycle (4 pulses). Figure 4-18 shows the measured and predicted temperature histories for the thermocouple at the back wall of the ATJ throat retainer ring. Again, the temperatures predicted by the two dimensional analysis are in excellent agreement with the measured temperature as the maximum difference throughout all four pulses is less than 130°F.

The close agreement between the 2-D predicted and the measured temperature histories indicates that the overall energy content of the throat package has been correctly computed. Even though this energy content is the integrated effect of the surface convective and radiative heat fluxes during the entire duty

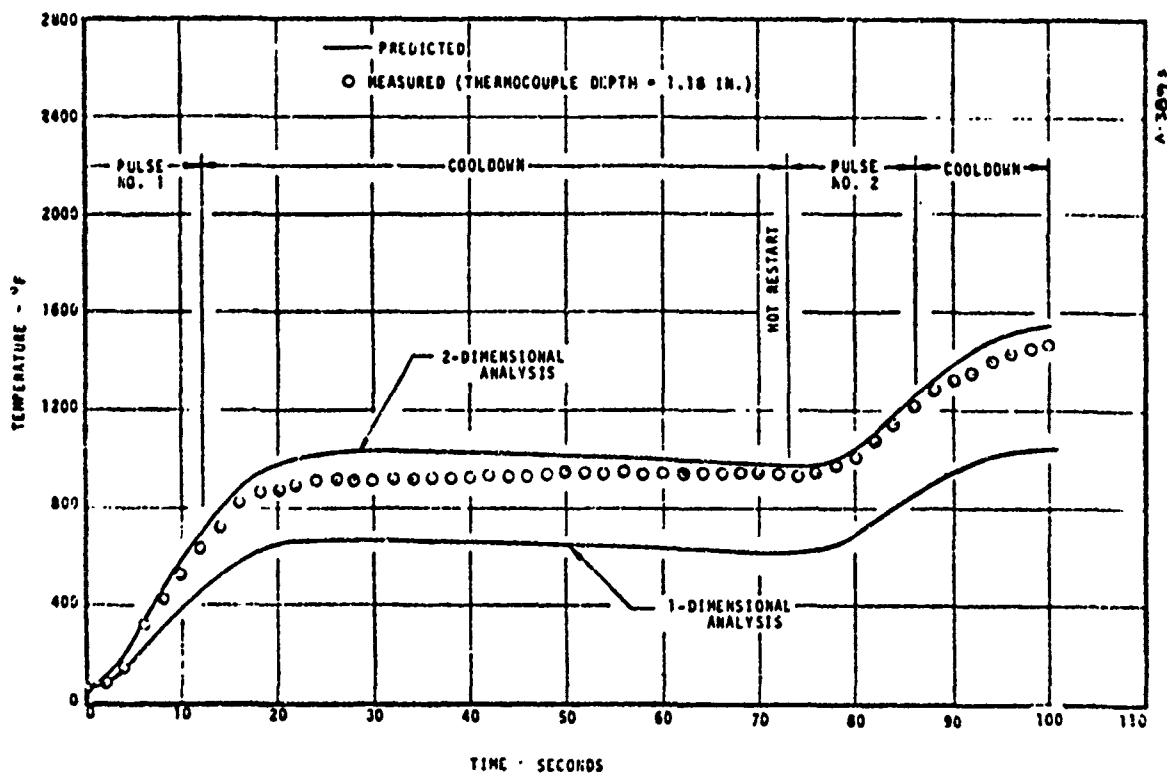


FIGURE 4-17 COMPARISON OF PREDICTED AND MEASURED IN-DEPTH TEMPERATURE HISTORIES AT THE THROAT NOZZLE NO. 8

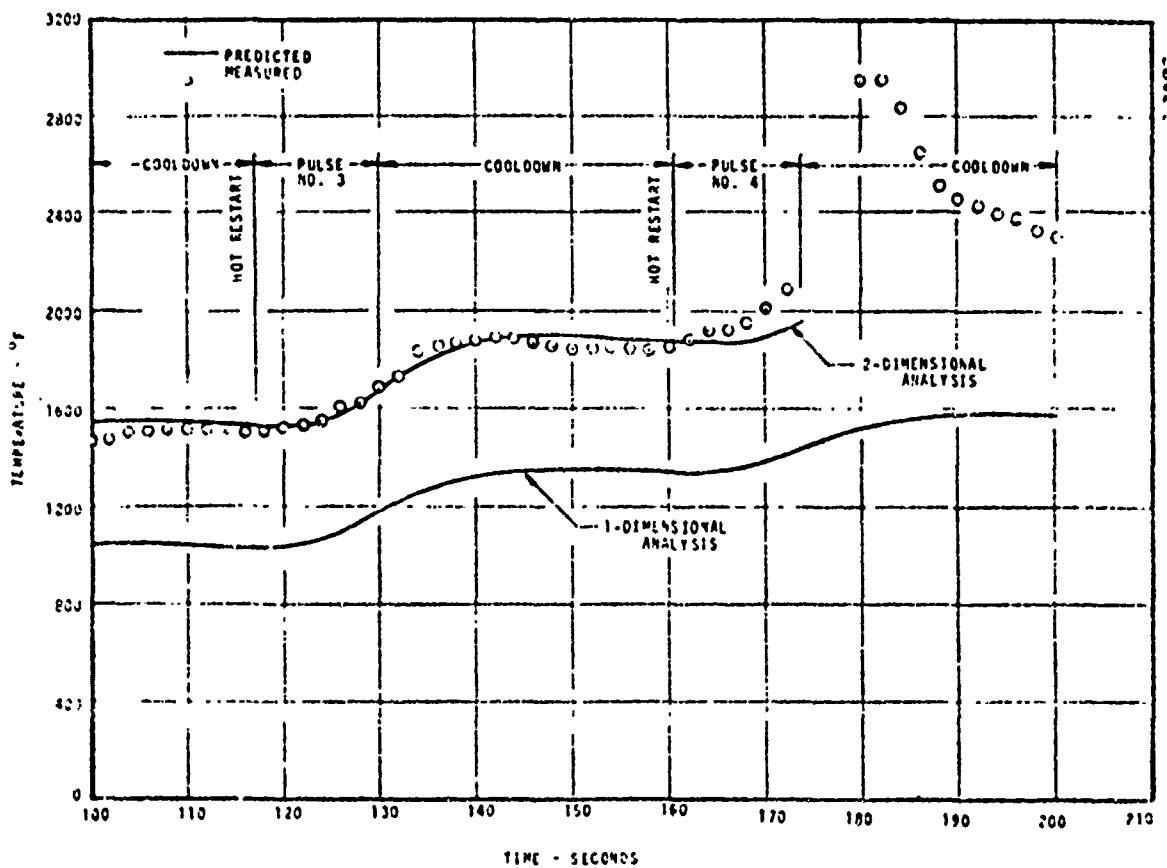


FIGURE 4-17 (CONCLUDED)

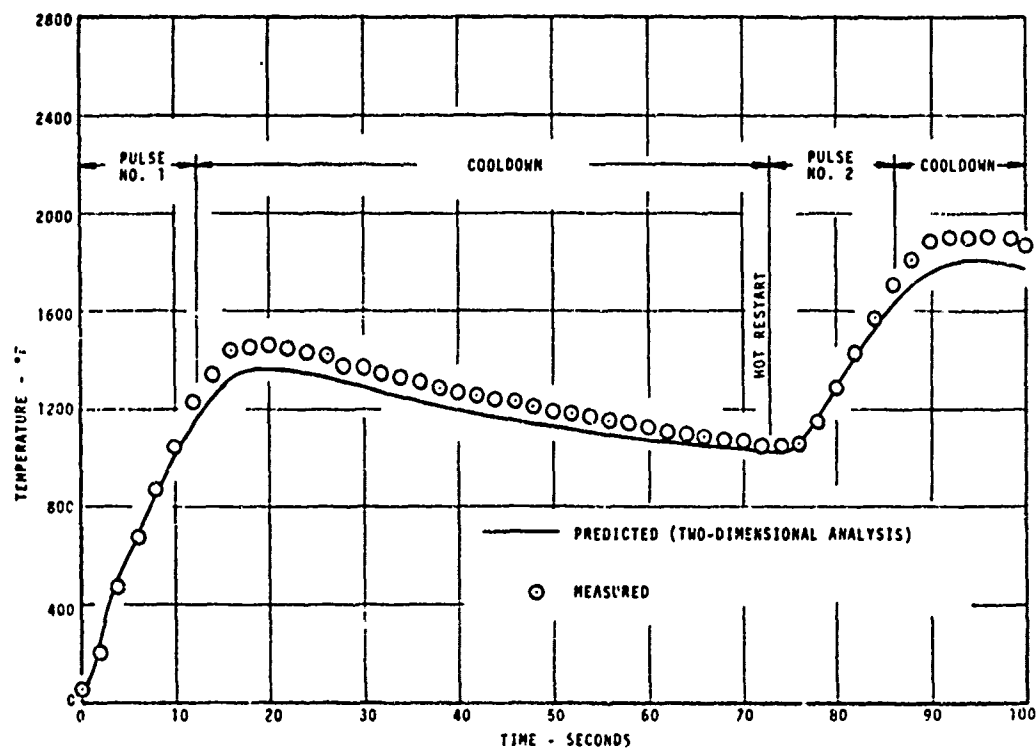


FIGURE 4-18 COMPARISON OF PREDICTED AND MEASURED IN-DEPTH TEMPERATURE HISTORIES AT THE A.T. BACKWALL NOZZLE NO. 8

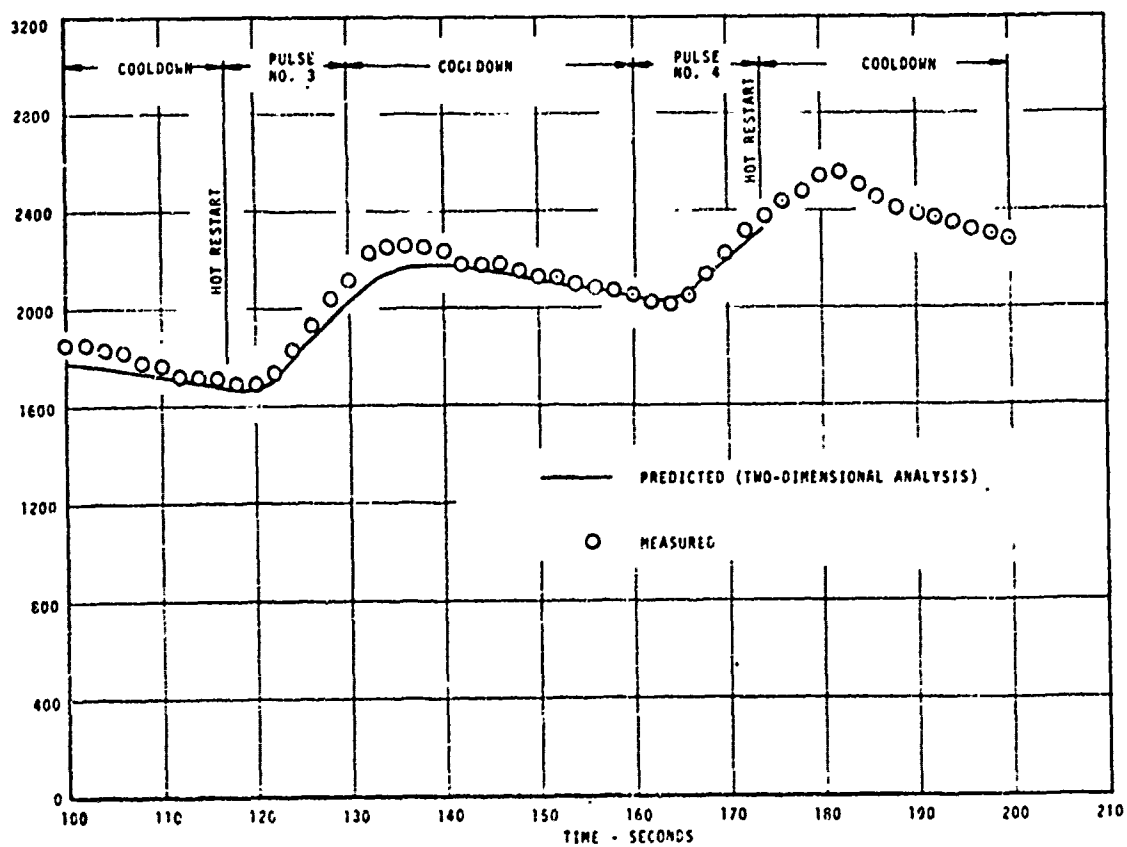


FIGURE 4-18 (CONCLUDED)

cycle, the agreement between the predicted and measured temperatures does substantiate the analysis procedures used to define the environmental boundary conditions at the nozzle surface.

The results of the one-dimensional CMA analysis for nozzle no. 8 are also shown in Figure 4-17. The one-dimensional predictions closely parallel the two-dimensional ASTHMA predictions but are consistently low by as much as 550°F. This result was expected because:

- The path of thermal energy transport in the 1-D analysis is radial and, thus, all of the heat must be conducted through the PG coating which has a thermal conductivity about 15 times smaller than for both the AGSR substrate and the ATJ throat retainer ring materials.
- The path of thermal energy transport in the 2-D analysis is both radial and axial and, thus, because of the lower thermal resistance of the ATJ throat retainer ring, heat enters this ring from the nozzle environment and is conducted axially into the AGSR substrate; this axial flow of heat causes the temperatures predicted by the 2-D analysis to be higher than those predicted by the 1-D analysis.

The remaining four nozzles (nozzles no. 4, 5, 6, and 7) were analyzed using only the one-dimensional CMA analysis. To estimate the expected two-dimensional analysis results for these nozzles, a simple model was formulated to account for the axial heat conduction. In this analysis, the amount of thermal energy which arrived at the throat thermocouple was assumed to come from two separate fluxes. One flux was that which penetrates the PG layer and the second flux is that which is conducted axially through the ATJ graphite. This second flux was computed in the two-dimensional analysis but not in the one-dimensional analysis. These heat fluxes were correlated with the temperature rise of the thermocouple at the backside of the AGSR at the nozzle throat plane. The temperature rise due to heat flux through the PG coated throat is predicted by the one-dimensional CMA analysis. The additional temperature rise resulting from the two-dimensional temperature prediction is a result of axial heat conduction. The temperature difference between the two prediction techniques at the backside of the AGSR are given in Figure 4-19 as a function of the local temperature predicted by the one-dimensional analysis. Using the correlation presented in this figure, the temperatures predicted by the CMA one-dimensional analysis were corrected to include two-dimensional heat conduction effects.

Figures 4-20 through 4-23 show the measured temperatures, the temperatures predicted by the one-dimensional analysis, and the estimated two-dimensional analysis temperatures at the backside of the AGSR for nozzles no. 4 through 7. These comparisons show that two-dimensional conduction effects are fairly well characterized by the temperature correction correlation presented in Figure 4-19.

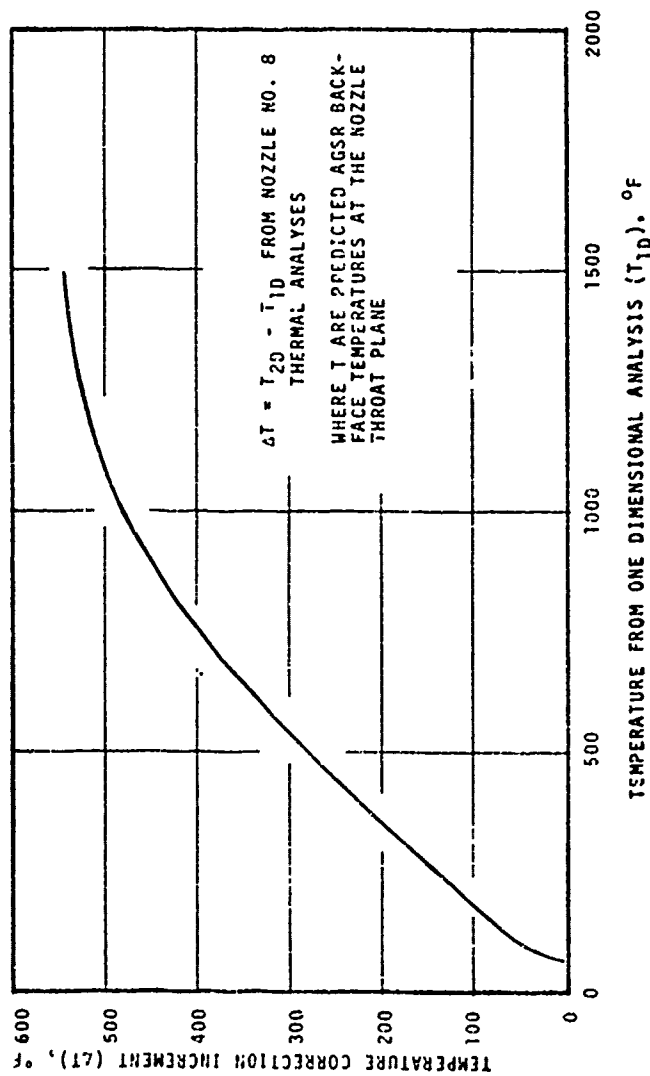


FIGURE 4-19 ONE-DIMENSIONAL ANALYSIS TEMPERATURE CORRECTION INCREMENT

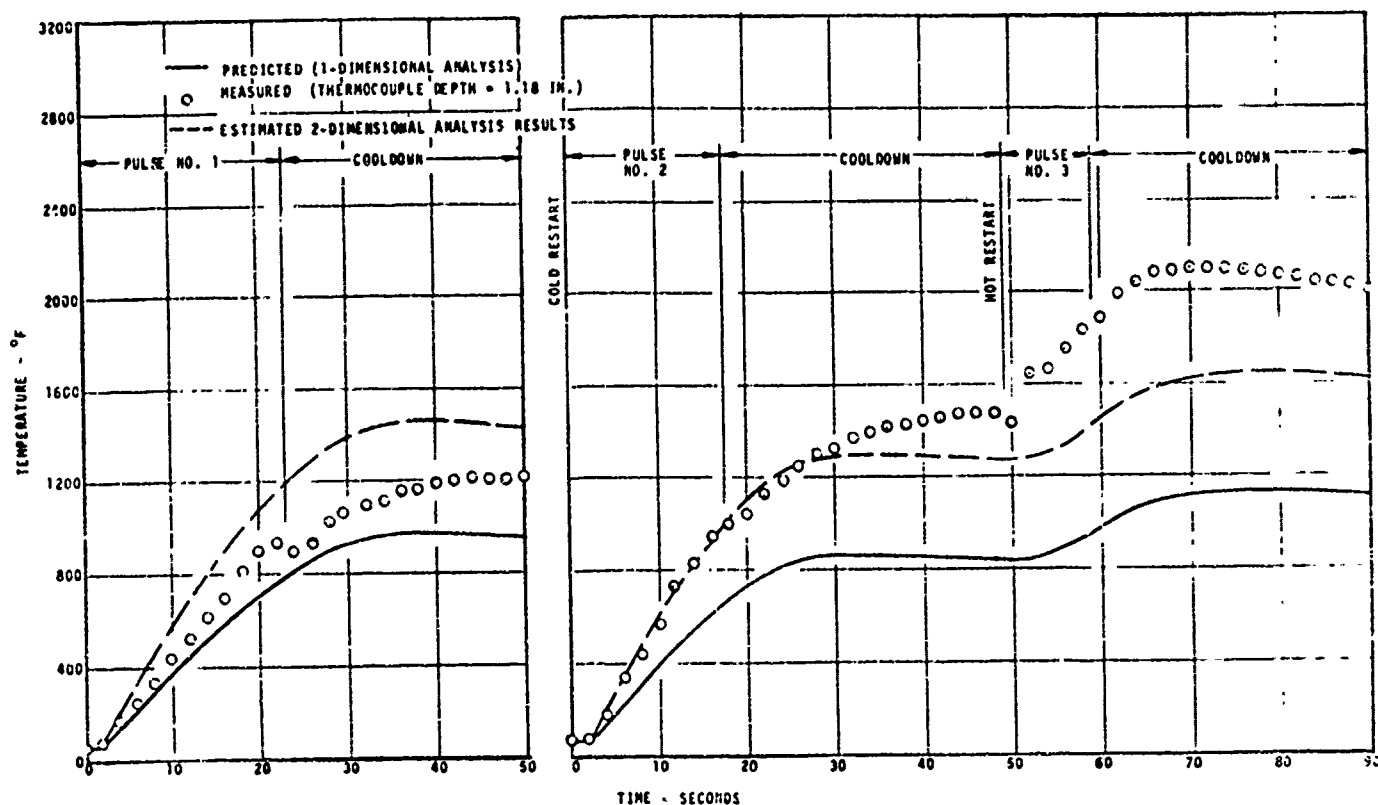


FIGURE 4-20 COMPARISON OF PREDICTED AND MEASURED IN-DEPTH TEMPERATURE HISTORIES AT THE THROAT - NOZZLE NO. 4

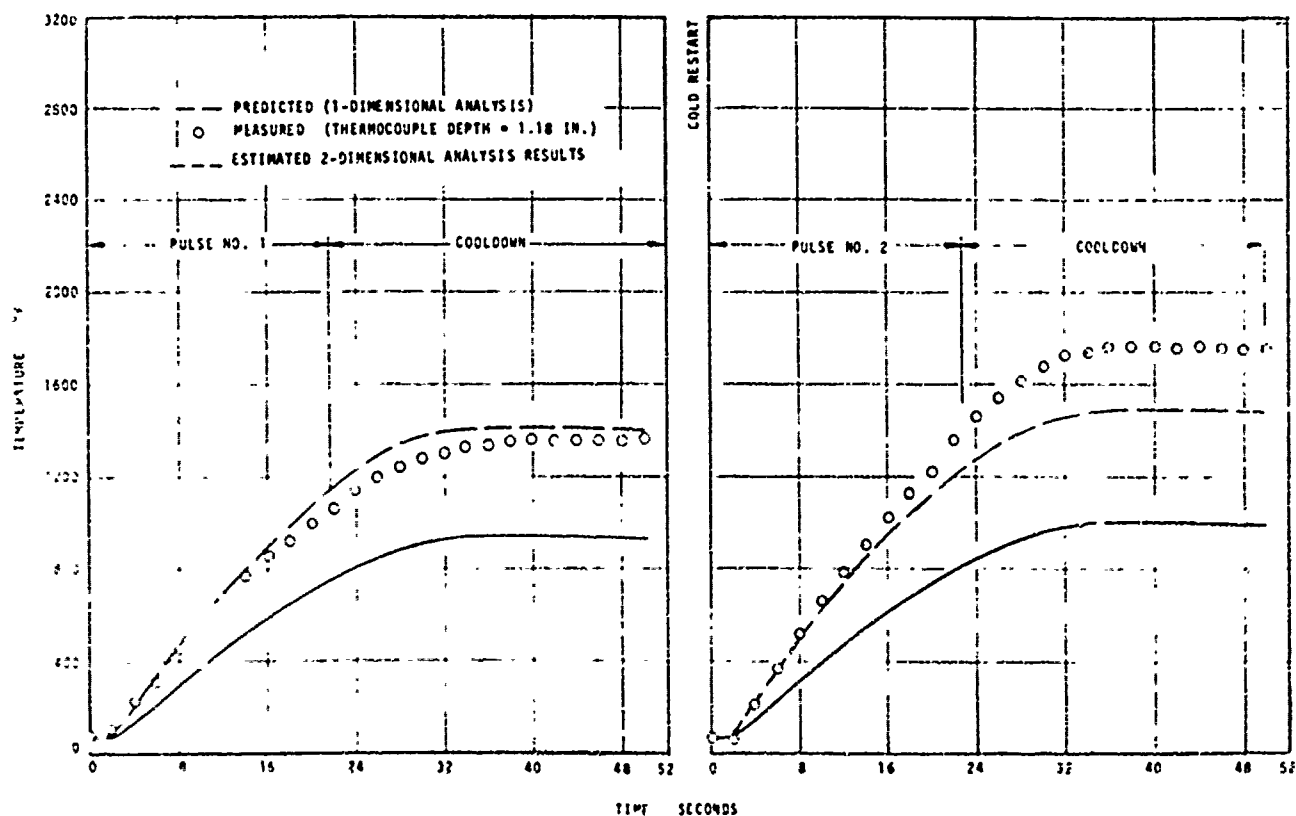


FIGURE 4-21 COMPARISON OF PREDICTED AND MEASURED IN-DEPTH TEMPERATURE HISTORIES AT THE THROAT - NOZZLE NO. 5

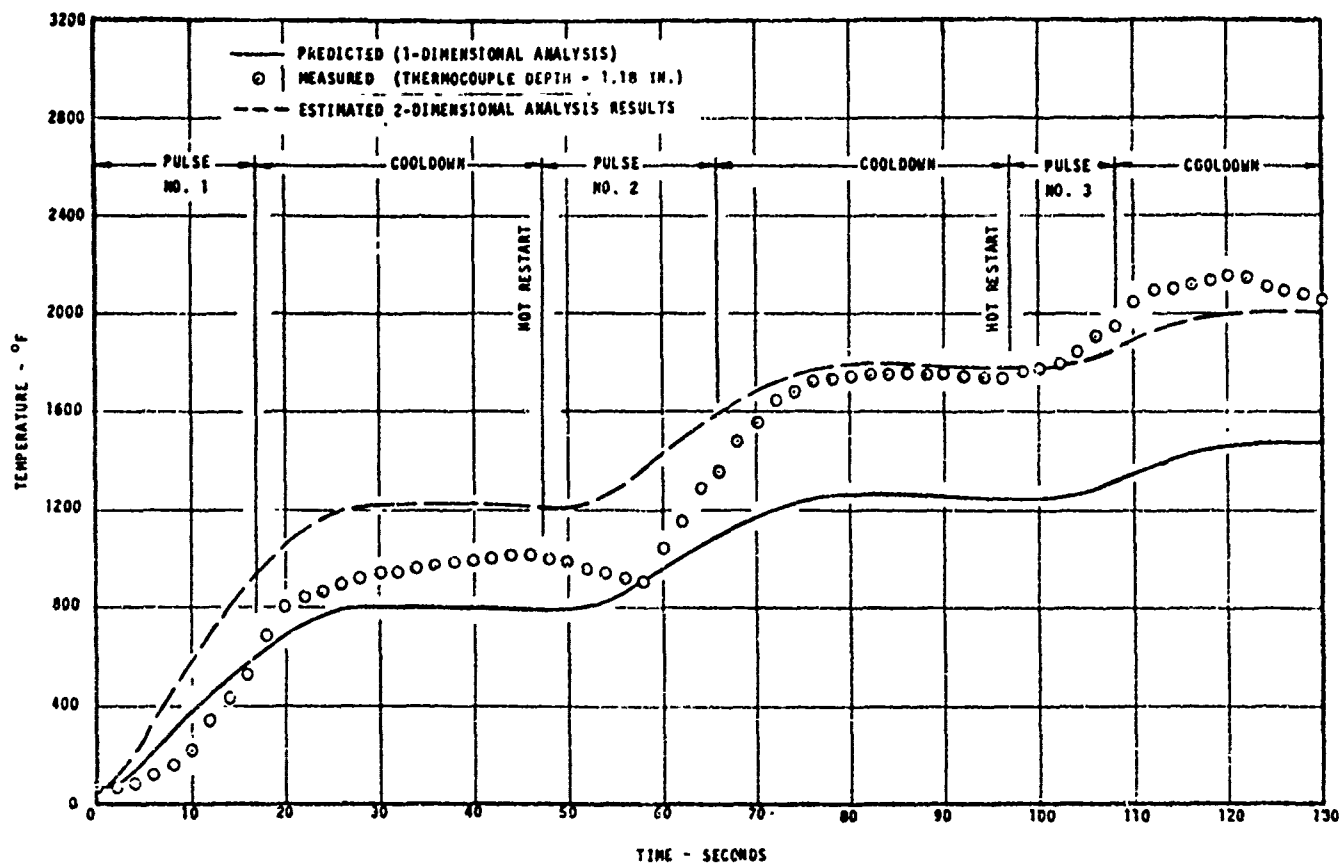


FIGURE 4-22 COMPARISON OF PREDICTED AND MEASURED IN-DEPTH TEMPERATURE HISTORIES AT THE THROAT - NOZZLE NO. 6

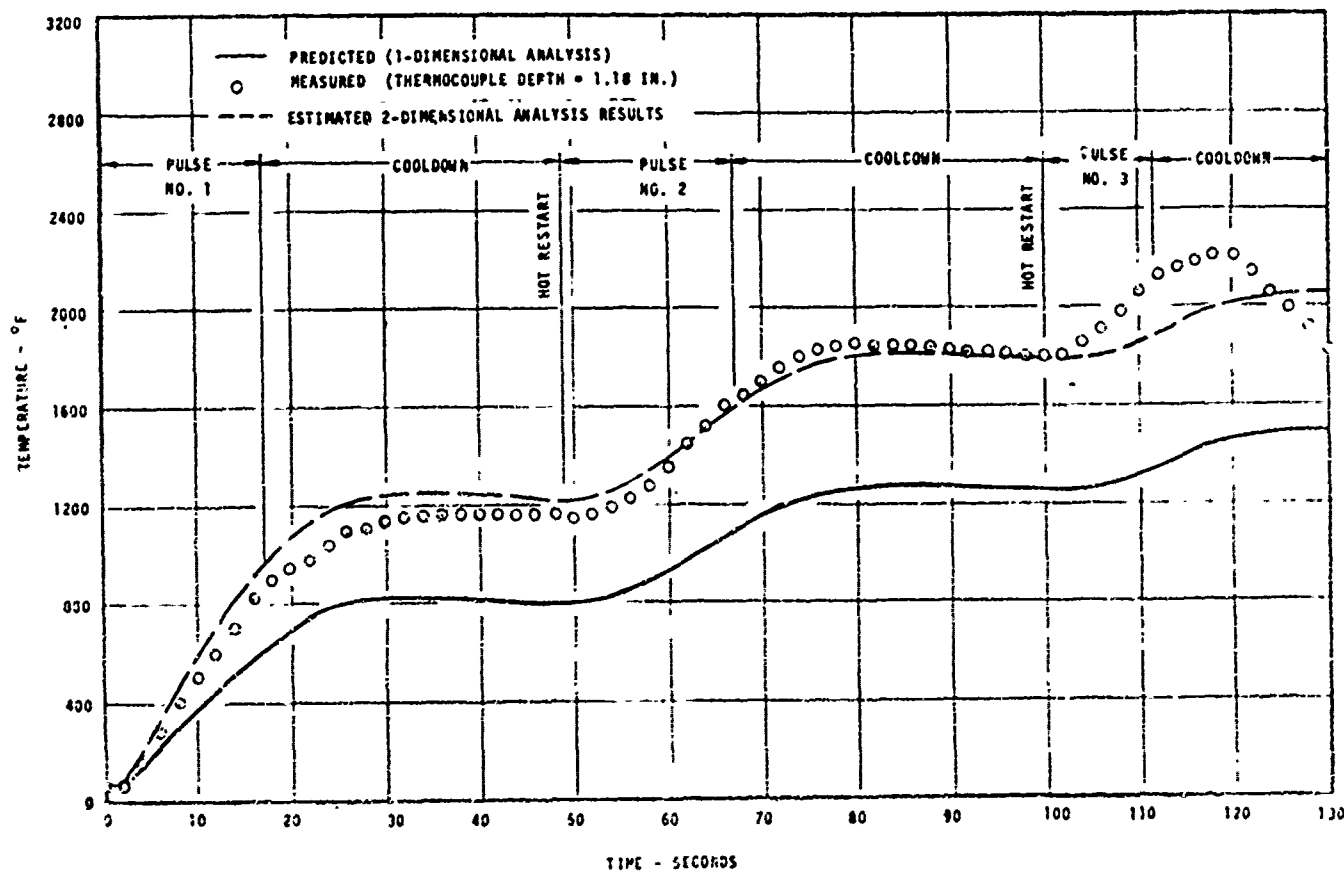


FIGURE 4-23 COMPARISON OF PREDICTED AND MEASURED IN-DEPTH TEMPERATURE HISTORIES AT THE THROAT - NOZZLE NO. 7

Furthermore, from the comparisons shown in Figures 4-17, 4-18, and 4-20 through 4-23, it is concluded that all of the firing and cooldown combinations could be accurately predicted by the 2-D analysis but that useful response information was obtained from the 1-D analyses. The primary disadvantage of the one-dimensional analysis is that it underpredicts the backside temperature and, thus, it is non-conservative in inferring bond line temperatures. In addition, the amount of discrepancy between the temperatures predicted by the two methods dictate that a two-dimensional analysis is required if a valid structural analysis is to be performed.

4.3.1.2 Evaluation of the Pyrolytic Graphite Layer Recession Calculations

As described in Section 4.2, the pyrolytic and ATJ graphite ablation rates during the multiple pulse firings were evaluated using the kinetically controlled graphite ablation model developed under Contract F04611-69-C-0081. A summary of the computed surface response of the pyrolytic graphite coated throat insert is given in Table 4-9 for each firing pulse. Also shown in this table are the average nozzle throat plane surface recession measurements, average throat recession rate values inferred from pressure data, and the predicted temperatures at the nozzle surface and at the front and rear faces of the AGSR substrate. For nozzle no. 8 both the one- and two-dimensional heat conduction results are shown. As pointed out in Section 4.3.1.1, the two-dimensional solution gave higher temperatures for the backwall of the AGSR substrate. However, the surface temperature and recession results were only slightly affected by the 2-D heat flow.

The average surface recession comparisons given in Table 4-9 indicate that for all five multiple pulse nozzles the predicted throat recession was substantially below the average of the post-test recession measurements. For nozzles 4, 6, 7, and 8, the PG throat liner was completely burned through in several places. Only the nozzle no. 5 throat liner which was exposed to only two pulses survived. The possible reasons for the difference between the predicted and measured surface recessions are

- The effect of nonuniform combustion product mixing on the local surface chemical reactions
- The possibility of pyrolytic graphite surface reaction kinetics changing because of the annealing effect of the first pulse heating cycle
- The kinetically controlled reaction rates and model may be inaccurate
- The difficulty in evaluating the heat transfer coefficient values in the boundary layer separation and reattachment region

Aspects of each of these possible explanations are described below.

TABLE 4-9
MULTIPLE PULSE NOZZLE THROAT RESPONSE SUMMARY

Nozzle	Pulse No.	Average Surface Temp	ACSR Substrate		Predicted Ave Surface Recession Rate (mils/sec)	Predicted Surface Recession (mils)	Measured Surface Recession (inches)	Recession Rate Inferred From Pressure Data (mils/sec)
			Maximum Frontside (*R)	Maximum Backside (*R)				
4	1	5330	1926	1404	0.14	3.3	---	2.0
	2	5310	1840	2195	0.14	5.8	---	2.1
	3	5300	2122	1569	0.12	7.0	0.037 ± 0.050	3.7
5	1	5340	1912	1375	0.15	3.2	---	1.9
	2	5320	2005	1433	0.14	6.4	0.016 ± 0.010	0.6
6	1	5330	1733	1240	0.15	2.5	---	1.5
	2	5350	2346	1696	0.15	5.2	---	2.6
	3	5340	2567	1910	0.14	6.8	0.035 ± 0.030	6.9
7	1	5330	1738	1255	0.15	2.6	---	2.3
	2	5350	2333	1711	0.15	5.4	---	2.3
	3	5345	2611	1939	0.14	7.0	0.036 ± 0.030	7.7
8	1	5320	1526	1113	0.14	1.8	---	2.3
	2	5340	2019	1485	0.14	3.6	---	2.5
	3	5350	2417	1785	0.14	5.5	---	2.5
	4	5350	2740	2030	0.14	7.4	0.38 ± 0.030	6.4
	1*	5340	1853	1498	0.15	1.8	---	2.3
	2*	5350	2511	2027	0.15	3.9	---	2.5
	3*	5380	2993	2383	0.15	5.9	---	2.5
	4*	5380	3302	---	0.15	7.9	0.38 ± 0.030	6.4

* ASTHMA 2-D ANALYSIS

As described in Section 3, there was evidence that the combustion products were not totally mixed (Figure 3-2). If the fraction of oxygen in the boundary layer were on the average higher than that in the total flow, measured recessions would be greater than the computed recession. The possibility that the kinetic response model developed under Contract F04611-69-C-0081 did not adequately characterize the ablation phenomena in the multiple pulse duty cycles also exists. For example, the effect of the pyrolytic graphite annealing during the first firing pulse and cooldown may have affected the kinetic response mechanisms during later pulses. Arc heater tests were run under the kinetic model development program (Contract F04611-69-C-0081) which indicated that annealed models tended to ablate slightly faster than "as deposited" models. Such conditioning of the PG coating would result in higher recession rates during the start pulses. The recession rates inferred from chamber pressure versus time data indicate that an annealing effect was probably not important. Although the quality of these recession rate data is low because the changes in pressure were small, the average throat recession rates were roughly constant until the probable burn through time, independent of the type of start up or the number of pulses. Alternately, it may be possible that the kinetic response model is not suited to the ANB 3066 simulator propellant environment. This is not likely, since the model has been shown to adequately characterize the response of pyrolytic graphite to several similar propellant formulations.

The most probable explanation for the large measured throat recessions is the severe heating caused by the disturbed flow field in the throat region. Boundary

layer reattachment in the vicinity of the throat plane could provide sufficient additional heat and mass transfer to explain the larger than computed recessions. In the multiple pulse nozzles the shape of the ablative part at the nozzle entrance most certainly caused a separated turbulent wake flow field in the throat region. Reattachment of such a flow would result in a very severe local heating condition. The analytical evaluation of the heat and mass transfer in such a flow situation was not attempted in this study. However, the simple flow model which was used for the computations described here gave a baseline, lower limit boundary layer solution. The throat package thermal response comparisons described in Section 4.3.1.1 demonstrated that the overall boundary layer solution was adequate. However, local perturbations such as increased heating at the reattachment point would not significantly affect the in-depth response of the nozzle throat insert.

4.3.2 Carbon Cloth Phenolic Exit Cone Response Analysis

One-dimensional transient heating and material ablation solutions were performed using the CMA code for the upstream ($A/A^* = 4.2$) thermocoupled plug location for each of the five multiple pulse nozzles. The 1-D analysis procedure accurately modeled the ablative response. Two CMA program options were alternately utilized to specify the heated surface boundary condition. For each simulator firing pulse, the radiative and convective surface heat fluxes were evaluated by demanding energy conservation at the ablating surface. These solutions accounted for the energy fluxes associated with each of the ablation phenomena depicted in Figure 4-1. For the cooldown periods between or after firing pulses, the convective heating option was not allowed and the surface radiative boundary condition was evaluated by a simplified surface energy balance.

The nodal system for the CMA analysis was the same for each of the five nozzles. This system is shown schematically in Figure 4-24. Also shown are the locations of the three in-depth thermocouples. The computed temperatures at these locations are compared to the response measurements in Section 4.3.2.1. Recession and char thickness calculations are compared to post test measurements in Section 4.3.2.2. Computed density profiles are related to the density profile measurements (Section 3) in Section 4.3.2.3.

4.3.2.1 In-Depth Temperature Histories

The computed surface and in-depth temperature histories for the five multiple pulse nozzles are compared to thermocoupled plug data in Figures 4-25 through 4-29. The general conclusion reached from these comparisons is that the analysis technique does a reasonable job computing the in-depth thermal response of the ablative materials. Differences between the response analysis results and the data are primarily attributable to:

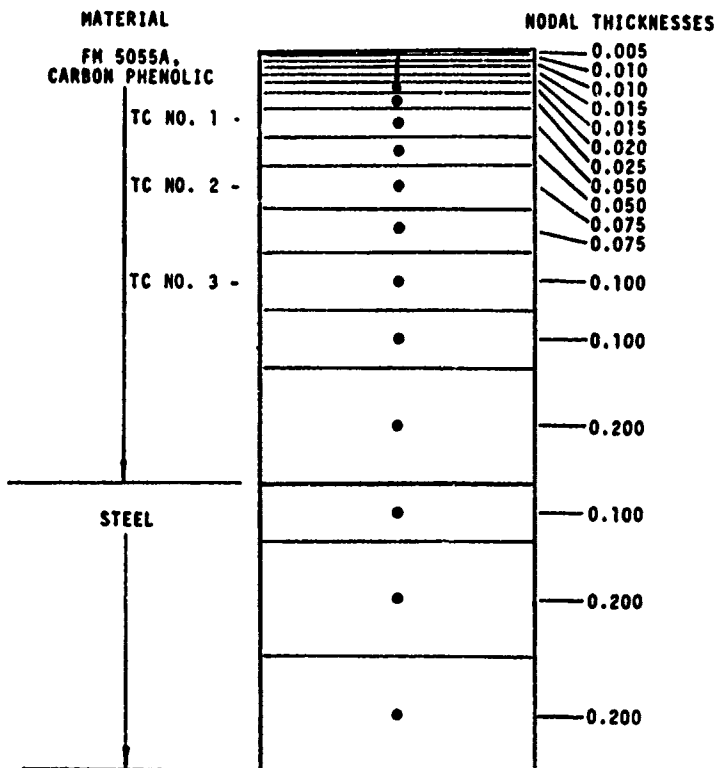


FIGURE 4-24 ONE-DIMENSIONAL NODAL GRID FOR EXIT CONE CARBON PHENOLIC THERMAL ANALYSIS

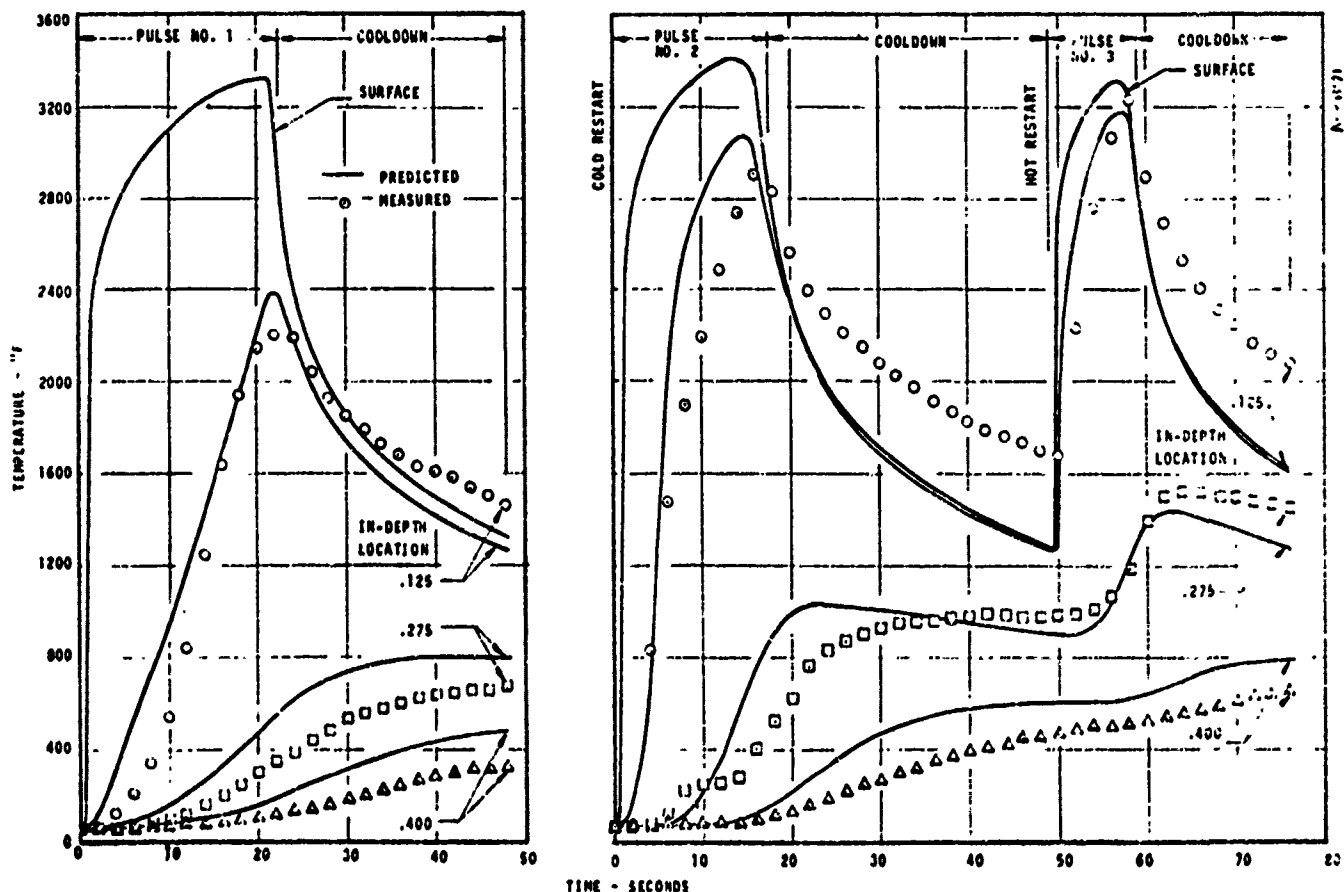


FIGURE 4-25 COMPARISON OF PREDICTED AND MEASURED IN-DEPTH TEMPERATURES FOR FM5055A CARBON CLOTH PHENOLIC AT AN AREA RATIO OF 4.2 - NOZZLE NO. 4

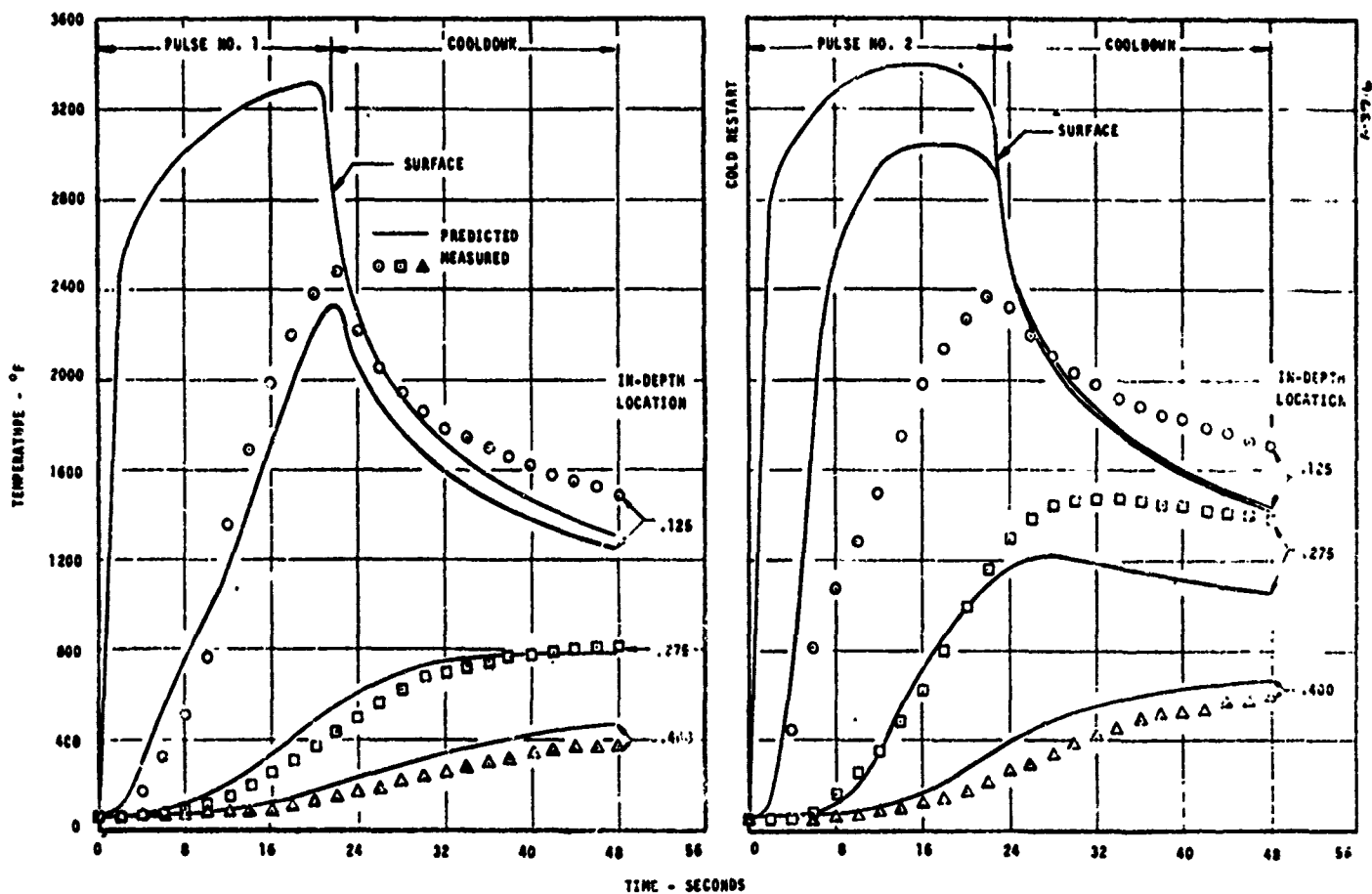


FIGURE 4-26 COMPARISON OF PREDICTED AND MEASURED IN-DEPTH TEMPERATURES FOR FMSOXA CARBON CLOTH PHENOLIC AT AN AREA RATIO OF 4.2 - NOZZLE NO. 5

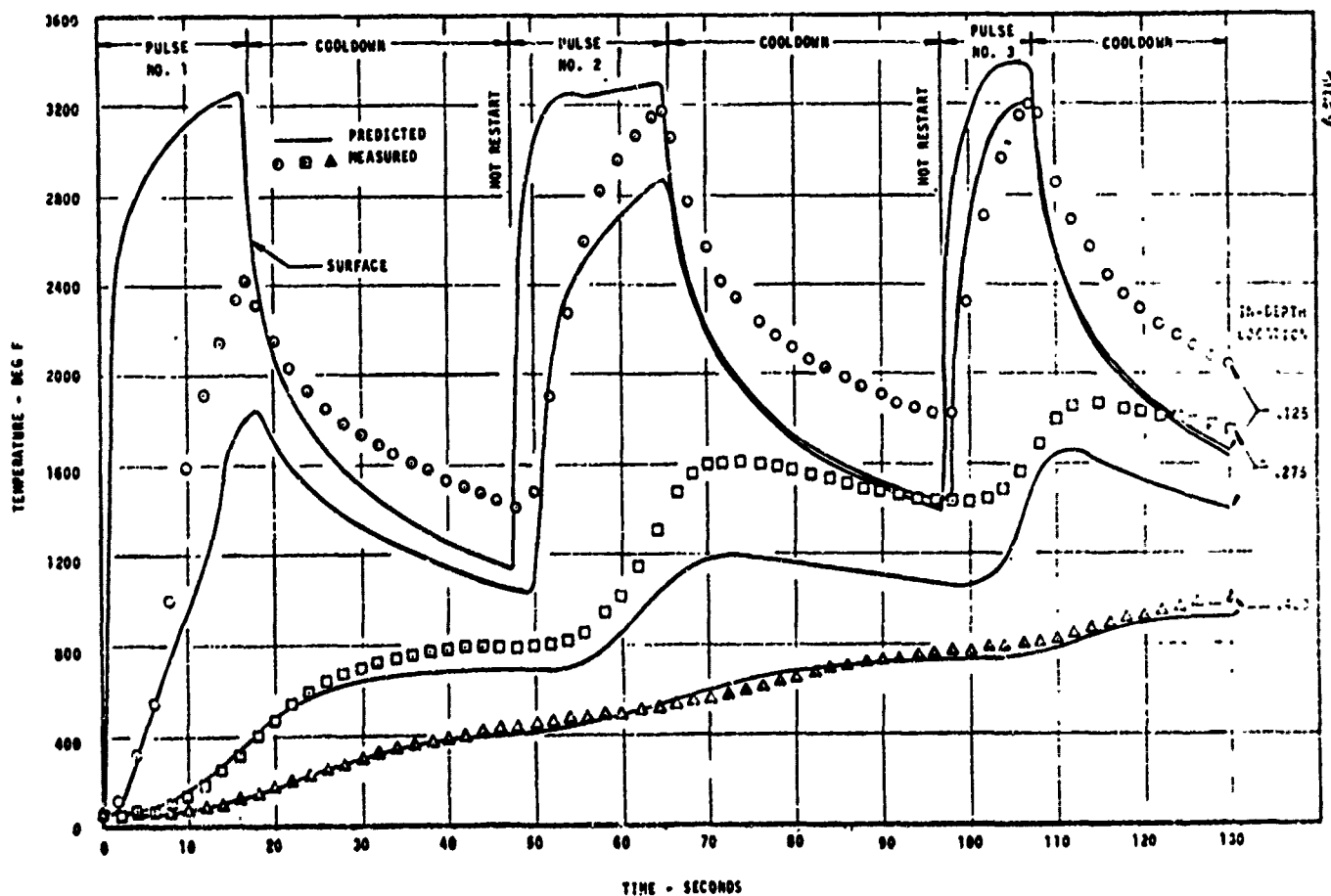


FIGURE 4-27 COMPARISON OF PREDICTED AND MEASURED IN-DEPTH TEMPERATURES FOR FMSOXA CARBON CLOTH PHENOLIC AT AN AREA RATIO OF 4.2 - NOZZLE NO. 6

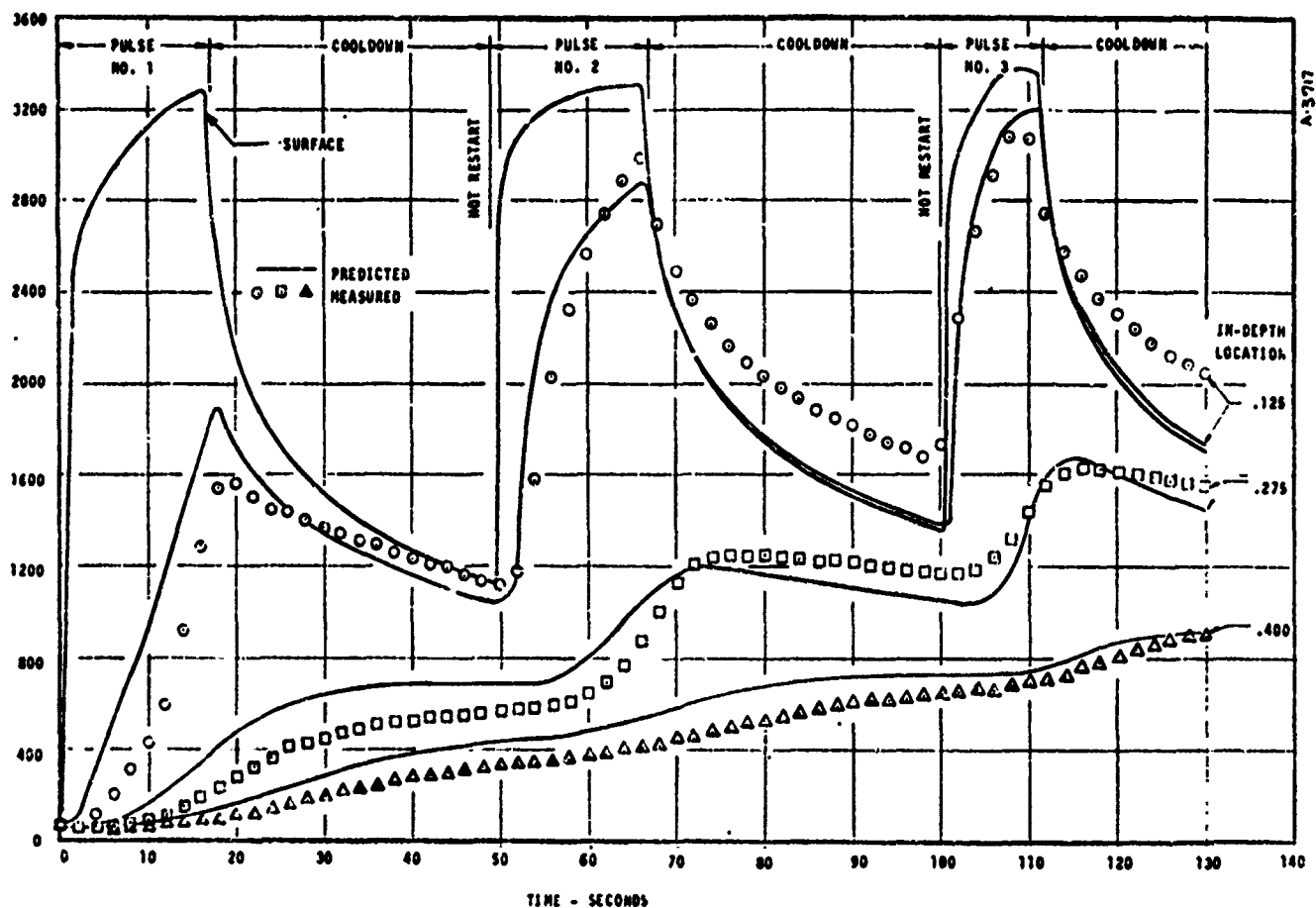


FIGURE 4-28 COMPARISON OF PREDICTED AND MEASURED IN-DEPTH TEMPERATURES FOR FMSOSA CARBON CLOTH PHENOLIC AT AN AREA RATIO OF 4.2 - NOZZLE NO. 7

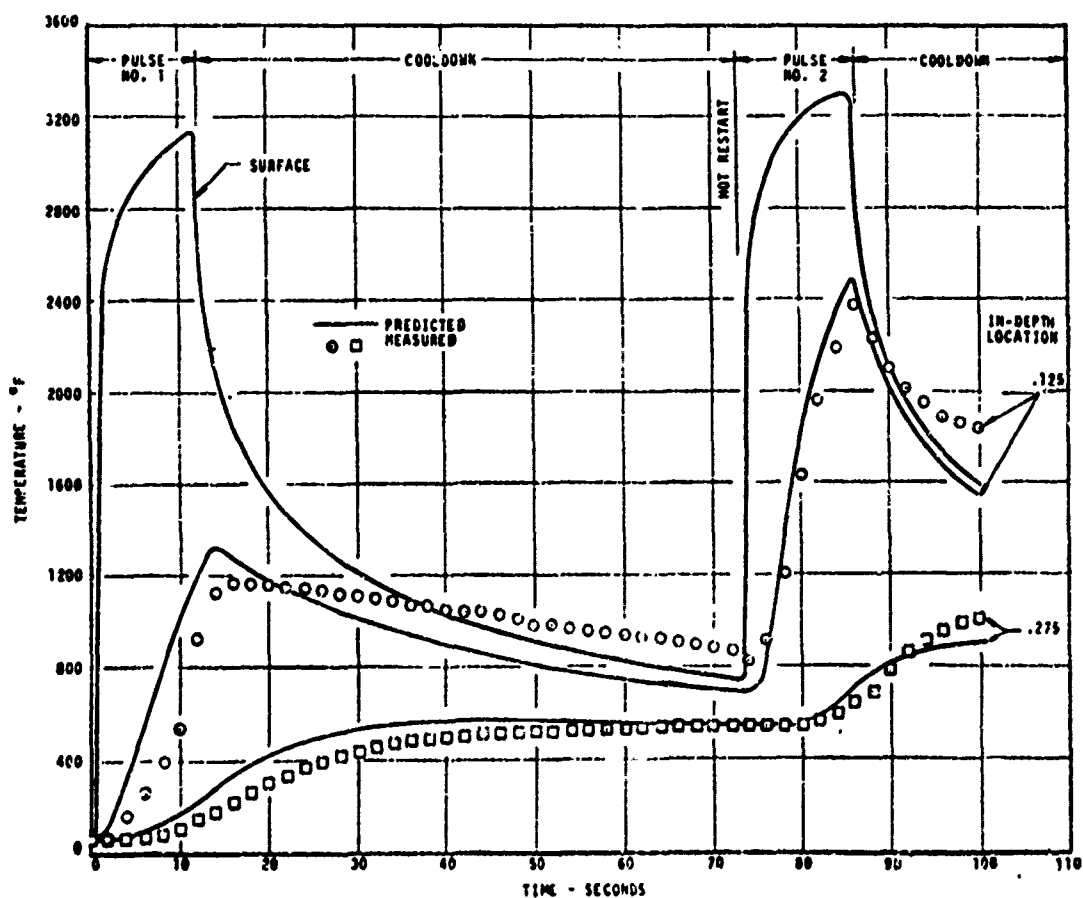


FIGURE 4-29 COMPARISON OF PREDICTED AND MEASURED IN-DEPTH TEMPERATURES FOR FMSOSA CARBON CLOTH PHENOLIC AT AN AREA RATIO OF 4.2 - NOZZLE NO. 8

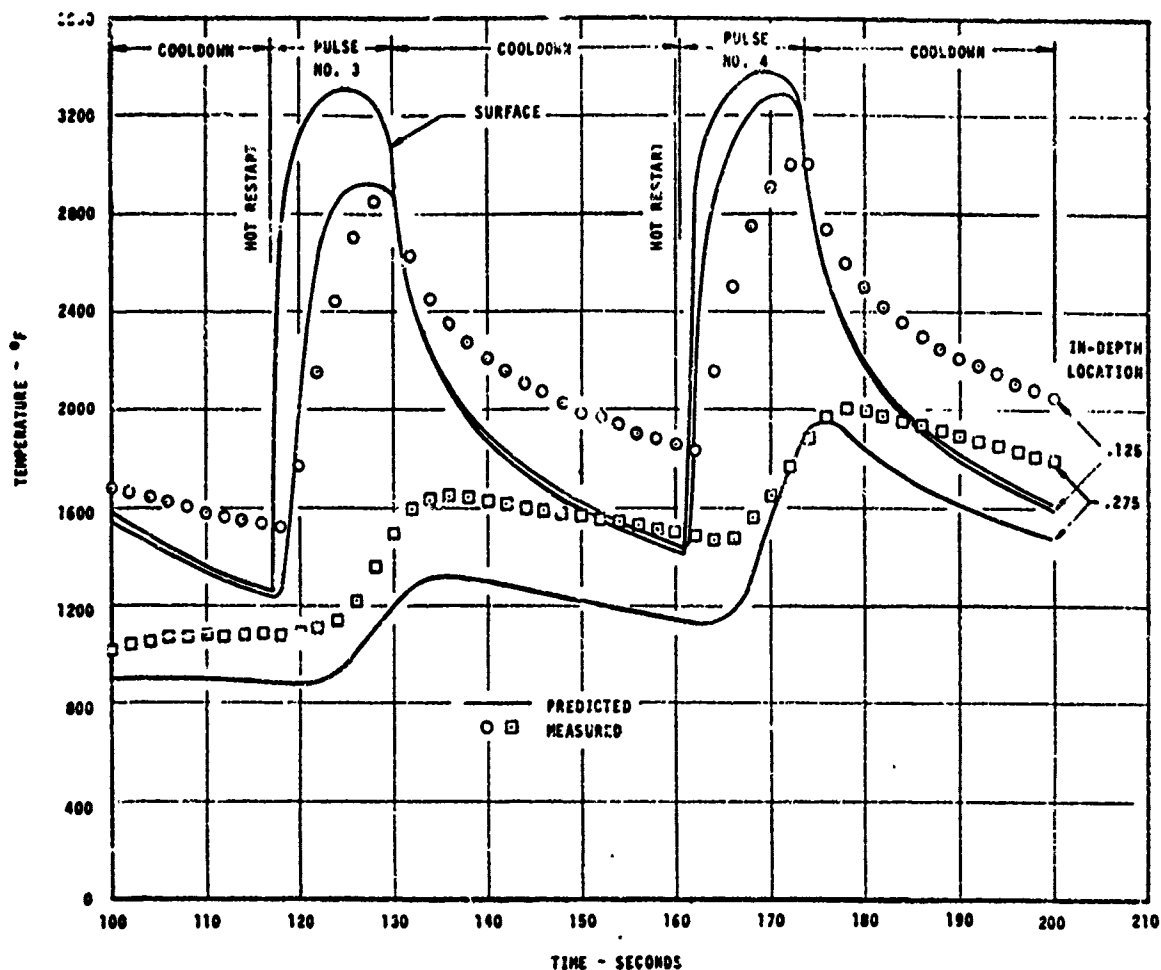


FIGURE 4-29 (CONCLUDED)

- uncertainties in material thermophysical properties
- the inability to model two-dimensional heat conduction or surface heat convection during cooldown

Factors which are of secondary importance in explaining these differences are

- uncertainties in thermocouple depths
- erroneous data due to thermocouple lag time
- effects of char swell on material response

An analysis of the sensitivity of computed in-depth temperatures to material property errors was described in Section 4.2 which showed that the property values used in the 1-D analysis were of sufficient accuracy to compute the proper response trends. However, uncertainties in material properties would result in an uncertainty band of at least $\pm 100^\circ\text{F}$ in the predicted temperatures.

Differences between the predicted and measured temperatures indicate that the material response was not well modeled during the cooldown phases of the duty cycles. This was apparent since calculated temperatures in the char layer

from TC no. 1 were well below the corresponding thermocouple data. There are two possible reasons for the computed results being low. One is that the surface boundary condition specification during the cooldown was incorrect. However, this explanation does not seem appropriate as the analysis of the temperature response sensitivity to the radiation interchange model (Section 4.2) indicated that the underprediction could not be explained by an error in the radiation model. This analysis showed that even with no net radiation energy loss from the surface, the measured temperatures at the TC no. 1 location were above the computed temperatures. Furthermore, it is possible but unlikely that during the nozzle cooldowns the simulator purge flow provided convective heating to the nozzle surface. The second and most reasonable explanation for the measured temperatures being higher than the 1-D solution is that heat is being conducted into the exit cone from the graphite throat package. This speculation is confirmed by the response comparisons for nozzles no. 4 and 5 (Figure 4-25 and 4-26). Each of these nozzles had cold restarts and the difference between the predicted and measured cooldown temperatures at the first thermocouple location (0.125 inches) was much smaller in the first pulse than the second. This is consistent with the realization that after the second pulse the char layer would be much thicker which would result in the net heat flux from the throat insert being much larger.

The heat conduction in the exit cone char layer is difficult to model analytically with the 1-D analysis procedure. A crude approximation could be made by allowing a source term to be specified for each node of the analysis grid. A more rigorous technique would be to use the 1-D charring solution for the firing pulse as the initial condition for a 2-D non-charring analysis of the cooldown. The 2-D grid would include the entire throat package and exit cone. The correct modeling of cooldown events is important only because of the hot restart duty cycle requirement. For hot restarts, the errors in the temperature field are maintained and subsequent errors become additive. For the multiple pulse duty cycles analyzed in this program, errors in computed in-depth temperature were no larger than 400°F.

The secondary factors described above may also have contributed to the differences between the computed in-depth temperature histories and the data. These sources of error are not peculiar to the multiple pulse duty cycles, and since they have been discussed in detail in Reference 8, only a brief summary of them is included here.

The uncertainty in thermocouple depth directly results in an uncertainty in the predicted temperatures. Since the thermocouple depths reported by the nozzle fabricator for the thermocoupled plugs were not obtained from post fabrication location measurements (e.g., from x-ray photographs), the uncertainty in thermocouple location was estimated to be ± 0.02 inches.

This uncertainty results in temperature differences of approximately $\pm 200^\circ\text{F}$. Another source of uncertainty between the measured and predicted temperatures is the thermocouple lag time. This lag often occurs during times of rapid temperature rise, particularly if the thermocouple junction is not in good contact with the ablative material. The other source of uncertainty is char swell which distorts the thermocouple depths and makes direct comparisons difficult. More is said about the char swell phenomenon in Section 4.3.2.3.

Despite the minor difficulties associated with the effects of material property uncertainties, 2-D heat conduction effects during cooldowns and inherent systematic measurement uncertainties, the predicted thermal responses of the thermocoupled plug at $A/A^* = 4.2$ agreed favorably with the temperature data. The principal conclusion to be drawn from the comparisons between the predicted and measured in-depth temperature histories was that the thermal response of an ablative material subjected to any multiple pulse duty cycle is well characterized by current analysis techniques.

4.3.2.2 Recession and Char Thickness Comparisons

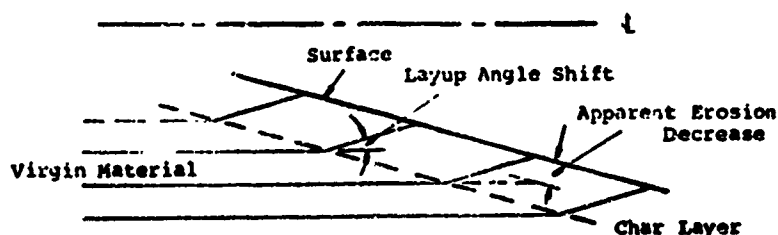
In Table 4-10 computed surface recession and char thickness results are compared to average measurements from the upstream ($A/A^* = 4.2$) thermocoupled plug

TABLE 4-10
COMPARISON OF PREDICTED AND MEASURED
PH 5055A CARBON CLOTH PHENOLIC THERMAL PERFORMANCE AT $A/A^* = 4.2$

Nozzle	Pulse No.	Nom. Surf. Temp.	Char Thickness (End of Cooldown)			Predicted Char Swell (inches)	Surface Recession		
			Measured (inches)	Predicted (No Char Swell) (inches)	Predicted (Including Char Swell) (inches)		Predicted Thermochem. (inches)	Net (inches)	Measured (inches)
4	1	3779	--	.184	.209	.025	.039	.014	--
	2	3867	--	.184	.209	.025	.083	.062	--
	3	3773	.31 \pm .04	.225	.255	.030	.117	.083	-.026 \pm .010
5	1	3777	--	.180	.204	.024	.030	.014	--
	2	3843	.26 \pm .04	.202	.228	.027	.097	.070	.016 \pm .025
6	1	3714	--	.156	.177	.021	.029	.008	--
	2	3740	--	.228	.259	.031	.074	.043	--
	3	3829	.37 \pm .06	.275	.312	.037	.183	.066	.006 \pm .025
7	1	3736	--	.157	.178	.021	.030	.009	--
	2	3764	--	.229	.260	.031	.074	.043	--
	3	3832	.34 \pm .04	.277	.314	.037	.184	.067	-.032 \pm .010
8	1	3570	--	.124	.141	.017	.020	.003	--
	2	3739	--	.192	.218	.026	.051	.025	--
	3	3773	--	.240	.273	.032	.083	.053	--
	4	3839	.40 \pm .04	.293	.333	.040	.117	.077	-.021 \pm .010

^aChar Swell = 0.135^a Predicted Char Thickness

location of the five multiple pulse nozzles. Because the material was a carbon cloth phenolic fabricated at a 0 degree layup angle with respect to the nozzle centerline, char swell phenomena had to be considered. Char swell apparently occurs because the pressure which is created during the resin depolymerization forces the distance between the cloth tape lamina to increase in the char layer. These forces are the most probable cause of the local delamination which occurred at several places in the exit cone. The appearances and typical locations of these delaminations were indicated in Figures 3-1 through 3-5. The following sketch shows how the char layer thickness is increased. Since this phenomenon is not modeled by



the CMA analysis procedure, computed results and data cannot be conveniently related without a char swell correction. In Reference 2 an empirical relation was defined so that the predicted thermochemical surface recession values could be corrected for char swell. This char swell correction relation modeled the observation that the char swell was directly related to the char thickness. The char swell was given by:

$$\delta_{\text{swell}} = k_s \tau_{\text{char}}$$

τ_{char} - the predicted char thickness in the absence of char swell

k_s - is a proportionality factor which is a function of the
a function of the material and the local layup angle

In Reference 2, the proportionality factor was found to be 0.135 for a MX 4926 carbon phenolic exit cone part with a layup angle relative to the exposed surface of 45 degrees. The 0.135 factor has been used to successfully describe the char swell amounts for a variety of ablative materials and layup angles (References 2, 4, and 5). For the FM 5055A carbon cloth phenolic material in the exit cone of the multiple pulse nozzles, the char thicknesses were computed using the 0.135 char swell factor, and they were on the average of 14 percent lower than the measured thicknesses. Predicted char thickness values with and without char swell are compared to data in Table 4-10. The computed surface recession with and without the char swell correction are also compared to measurements in this table.

The possible reasons for the inaccuracy of the char swell correction are that:

- The computed char thickness was low because the 2-D conduction along the char layer during cooldowns was not accounted for.
- The data used to define the 0.135 carbon swell factor were based on char swell thickness for layup angles (with respect to the nozzle surface) of 45 degrees whereas the layup angle for the nozzle exit cone being considered here is 15 degrees.

The first item above is the most significant because the char swell correlation factor was defined in Reference 2 based upon a predicted char layer thickness. Presumably, that baseline charring material ablation analysis was not complicated by 2-D heat conduction effects. The correlation is, therefore, dependent upon an accurate (no swell included) prediction of char thickness. If the 2-D conduction effect which was hypothesized in Section 4.3.2.1 had been taken into account in the analysis, the predicted char thickness and hence the computed char swell would have been larger.

The other item in the above list is a possible reason why the char swell correlation developed in Reference 2 may not be applicable to these multiple pulse duty cycle analyses. The major shortcoming of the correlation is that it does not include a layup angle dependence even though swell primarily occurs in the across-laminate direction. If such a dependence were incorporated in the correlation, it is probable that the proportionality factor would be larger than 0.135 for the FM 5055A, 15 degree layup material.

Despite the difficulties in evaluating the amount of char swell, the following conclusions about the analysis techniques and the material survivability in multiple pulse duty cycle applications can be made: 1) Predicted surface recessions from a design point of view are conservative, yet realistic; 2) char penetration calculations give results which are within the measurement uncertainties.

4.3.2.3 Density Profile Comparisons

The measured density profiles obtained from the shave and weigh and x-ray transmission techniques were presented in Figures 3-7 and 3-11, respectively. Also shown in Figure 3-7 are the predicted density profiles which were obtained from the one-dimensional CMA predictions presented in Section 4.3.2.1. In addition, the predicted density profile for MX 4926 thermal conductivities is shown in Figure 3-7i.

All the comparisons presented in Figure 3-7 between the predicted and measured profiles show that the thicknesses of the fully charred and of the pyrolysis zones are underpredicted. However, the predicted density profile when the MX 4926 thermal conductivities were used in the analysis is in better agreement with the measured profile than when the modified FM 5055A thermal conductivities were used. This difference in the predicted profiles was expected as the MX 4926 thermal conductivities are higher in the temperature range where the majority of the in-depth material degradation is occurring. Even though the uncertainties in the material thermal conductivity in the pyrolysis zone may be the reason for the discrepancy between the predicted and measured profiles, the primary reasons are believed to be

- axial heat conduction in the char layer from the nozzle insert to the exit cone analysis location during nozzle cooldown
- the char swell phenomenon which was evident in the surface recession and char thickness measurements presented in the previous section

The effect of the axial heat conduction would be to increase the thickness of the fully charred zone, and the effect of the char swell phenomenon would be to increase the thickness of the pyrolysis zone.

The measured densities in the fully charred and pyrolysis zones using the x-ray transmission technique are in poor agreement with those obtained using the shave and weigh technique. For example, the fully charred densities from Figure 3-11 is approximately 32 lbs/ft³ (≈ 0.5 gr/cm³) as compared to approximately 70 lbs/ft³ for those presented in Figure 3-7. However, the measured distance from the surface to the virgin material is the same using both techniques (0.45 inches from Figure 3-7j compared to 0.47 inches (12mm) from Figure 3-11). As explained in Section 3.2, the porosity of the sample in the fully charred and pyrolysis zones is the primary reason for the discrepancy in the measured densities. Future testing using the x-ray transmission technique should try to minimize the effect of the material porosity by using thicker samples.

SECTION 5

CONCLUSIONS AND RECOMMENDATIONS

The principal objectives of the study reported here were as follows:

- Obtain and report ablative response data for materials used in multiple pulse duty cycle rocket nozzles
- Verify the ability of current analysis techniques to predict the response of ablative materials in multiple pulse duty cycle applications

Both of these objectives were satisfied. Specific conclusions formed in the course of the program are as follows:

- The Philco-Ford TMSO-EM test facility successfully simulated the ANB-3066 propellant within a few percent, although flow field non-uniformities appeared to contribute to asymmetrical nozzle ablation.
- During each firing pulse, chamber pressure data, throat insert backwall temperature data, and thermocoupled plug temperature data were obtained.
- Net surface recessions, char thicknesses, density profiles, and X-ray transmission data were obtained from post-fire measurements of each of the five nozzles.
- Throat package backwall temperatures were accurately computed using a two-dimensional thermal analysis procedure (ARGEIBL, ACE, and ASTHMA computer codes).
- One-dimensional thermal analysis procedure (CMA code) was shown to be inadequate for evaluating in-depth temperatures of the PG coated throat insert, although predicted surface temperature and recession rate agreed favorably with two-dimensional results.
- PG coating recession rate was substantially underpredicted by the kinetically controlled surface response model developed under Air Force Contract F04611-69-C-0031; the underprediction is attributed to the inability of the boundary layer analysis procedure (ARGEIBL) to predict the severe heating at the point of boundary layer reattachment on the throat insert.

- One-dimensional (CMA code) in-depth temperature predictions for the FM 5055A carbon phenolic material at an exit cone area ratio of 4.2 were in general agreement with the thermocoupled plug data.
- Significant heat conduction from the graphite throat package along the carbon phenolic char layer occurred between firing pulses.
- Prediction of carbon phenolic recession at the exit cone area ratio of 4.2 was confounded by the char swell phenomenon, but agreement with data was obtained using a semi-empirical char swell correction relation.
- In light of the char swell phenomenon and uncertainties in measurement techniques, the predicted density profiles at the 4.2 area ratio agreed favorably with both the shave and weigh and the X-ray transmission measurements.
- X-ray diffraction measurements indicated the anticipated increase in graphite crystallization.

The general conclusion to be drawn from the efforts described in this report is that current analysis procedures are suitable for the evaluation of material response during multiple pulse duty cycles. No significantly different thermal events, other than increased significance of two-dimensional heat conduction, occur during multiple pulse firings. It can be concluded that material response phenomena are not strongly dependent on the type of duty cycle.

Specific recommendations relative to these multiple pulse duty cycle analyses are as follows:

- Post-fabrication X-ray photographs of thermocoupled plugs should be taken to accurately define thermocouple location relative to the exposed surface.
- Utilization of the separation producing lip in the throat inlet region should be evaluated; cold flow tests and/or boundary layer analyses should be performed to estimate the surface boundary conditions at the throat insert reattachment point.
- The evaluation of in-depth temperature distributions within graphite throat inserts, such as are necessary for thermostructural analyses, requires the consideration of two-dimensional conduction events.
- Consideration should be given to axial heat conduction at all locations in nozzles exposed to multiple pulse duty cycles.
- The purely theoretical evaluation of surface recession for exit cone char-ring ablator materials requires the development of a comprehensive char swell analysis capability.

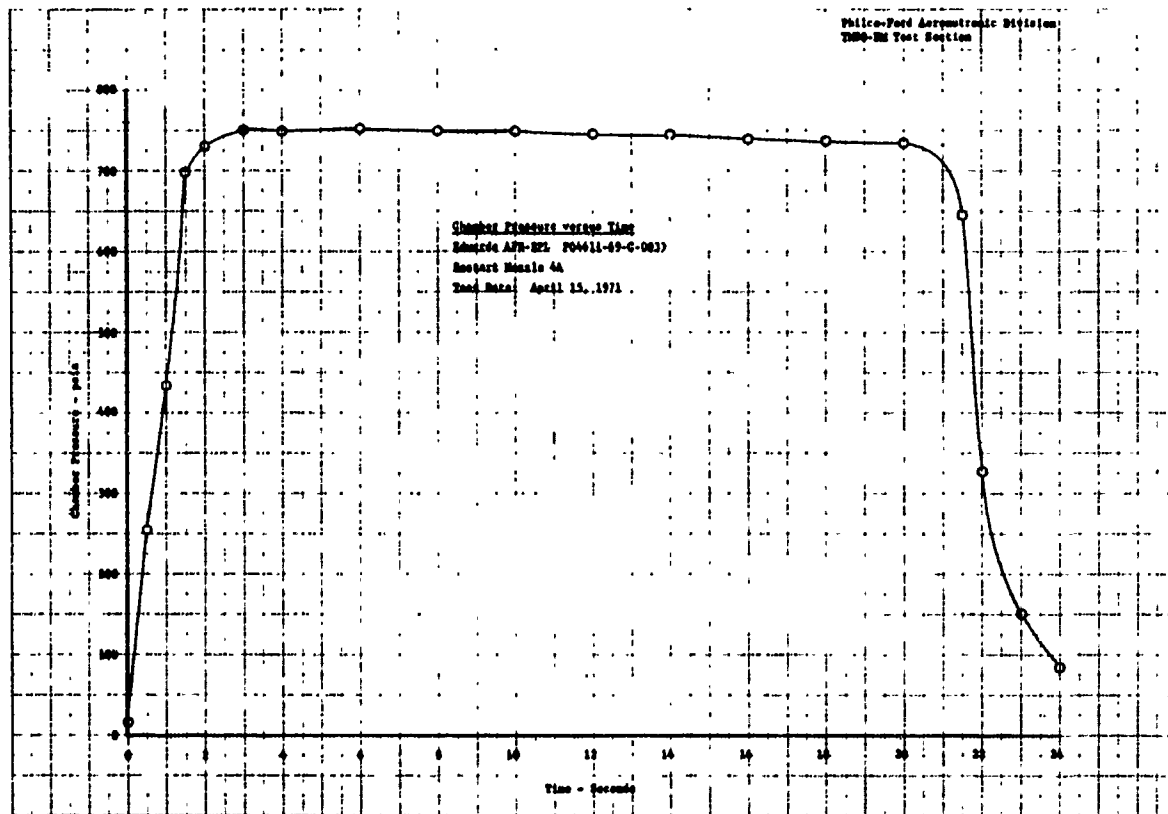
REFERENCES

1. Baker, D. L., Schaefer, J. W., and Wool, M. R., "Thermal Property and Ablative Response Characterization of Pyrolyzed Materials." Aerotherm Report No. 69-47, January, 1969.
2. Schaefer, J. W. and Dahm, T. J., "Studies of Ablative Material Performance for Large Solid Boosters." NASA CR-72080 (Aerotherm Report No. 66-2), December 15, 1966.
3. Schaefer, J. W., et al., "Studies of Ablative Material Performance for Solid Rocket Nozzle Applications." NASA CR-72429 (Aerotherm Report No. 68-30), March 1, 1968.
4. Baker, D. L., "Evaluation of Thermochemical Analysis Techniques, Thermochemical Screening, and Thermal Instrumentation Methods for High Pressure Solid Rocket Motors." (U) Aerotherm Report No. 69-52, August 15, 1969 (CONFIDENTIAL).
5. Baker, D. L., "Validation of Analytical Design Techniques for Solid Rocket Nozzles at High Chamber Pressures." (U) Aerotherm Final Report No. 71-31, May 3, 1970 (CONFIDENTIAL).
6. "Program Plan for Post-Test Evaluation of Nozzles Subjected to Multiple Pulse Duty Cycles." Contract No. FO4611-70-C-0019, dated March, 1970.
7. Wool, M. R. and Schaefer, J. W., "Sensitivity Analysis of PG Recession Predictability to Response Measurements." Aerotherm Report No. TM-70-6, October 1, 1970.
8. Baker, D. L., Wool, M. R., and Schaefer, J. W., "Development of Total and Radiative Heat Flux Measurement Systems for Rocket Nozzle Applications." AFRPL-TR-70-82 (Aerotherm Final Report No. 70-11), August, 1970.
9. Sparrow, E. M. and Cess, R. D., Radiation Heat Transfer. Brooks/Cole Publishing Company.
10. Youngman, B. P., "Determination of the Geometric View Factor From the Interior of a Cylinder of Incremental Height to a Disc." Aerotherm Informal Memo.
11. Clayton, W. A., Fabish, T. J., and Lagedrost, I. F., "Thermal Conductivity of Phenolic-Carbon Chars," AFML-TR-69-313, December 1969.

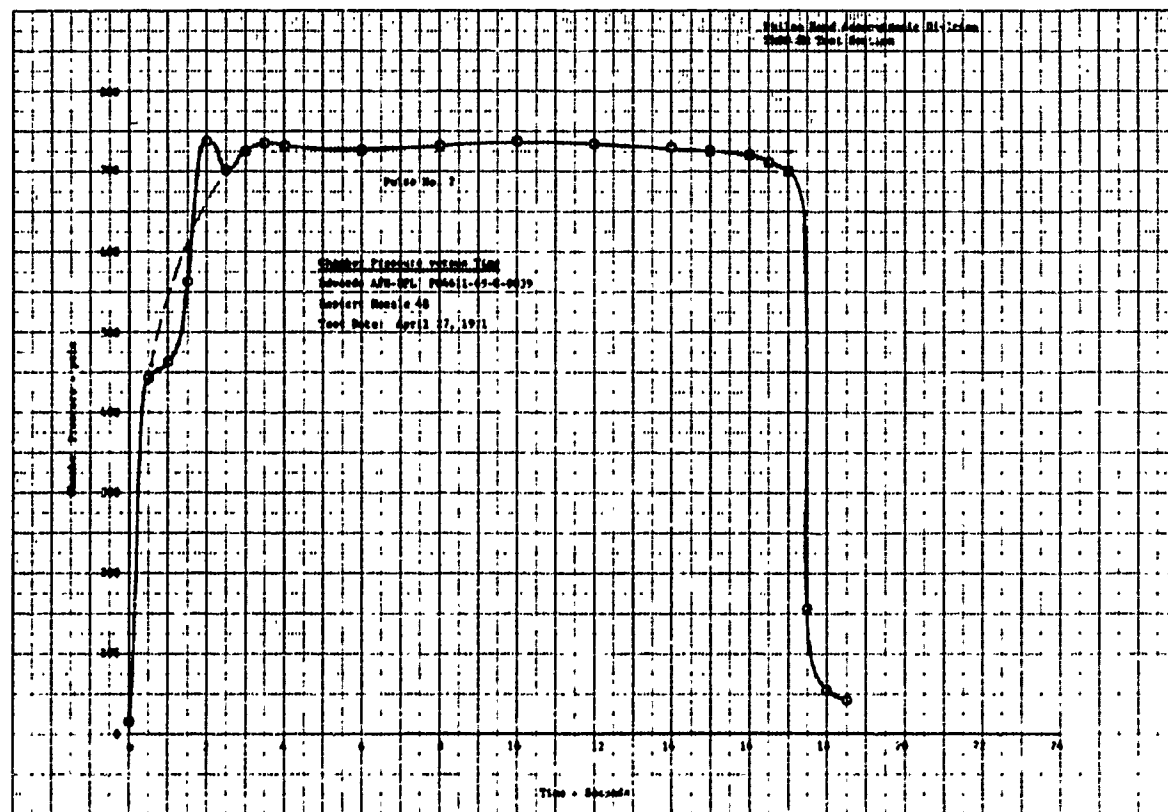
APPENDIX A

MEASURED CHAMBER PRESSURE HISTORIES

The five instrumented nozzles were tested by Aeronutronic in their solid rocket motor simulator under Air Force Contract F04611-69-C-0039. At the conclusion of this testing, the nozzles and the reduced data were delivered to Aerotherm for post-test analysis. The reduced data for the chamber pressure histories which were measured during the five multiple pulse data cycle tests are presented in this appendix in Figures A-1 through A-5. The test date is also shown on each figure. In some figures (for example, Figure A-1b), two curves are shown for the ignition transient. The solid curve represents the chamber pressure in the $O_2 - H_2$ start motor and was reported because the pressure port in the chamber experienced plugging as a result of ablation of the silica phenolic liner. The dashed line represents the estimated chamber pressure during ignition. As shown by this dashed line and by the solid line in Figure A-1a which was the measured chamber pressure (no plugging occurred), the chamber pressure ignition transient is a smoothly varying function. The oscillations recorded by the transducer in the start motor are a result of the transient flow rates which are caused by closing the valves to the start motor and by opening the valves in the fuel, oxygen, and nitrogen lines to the combustion chamber.

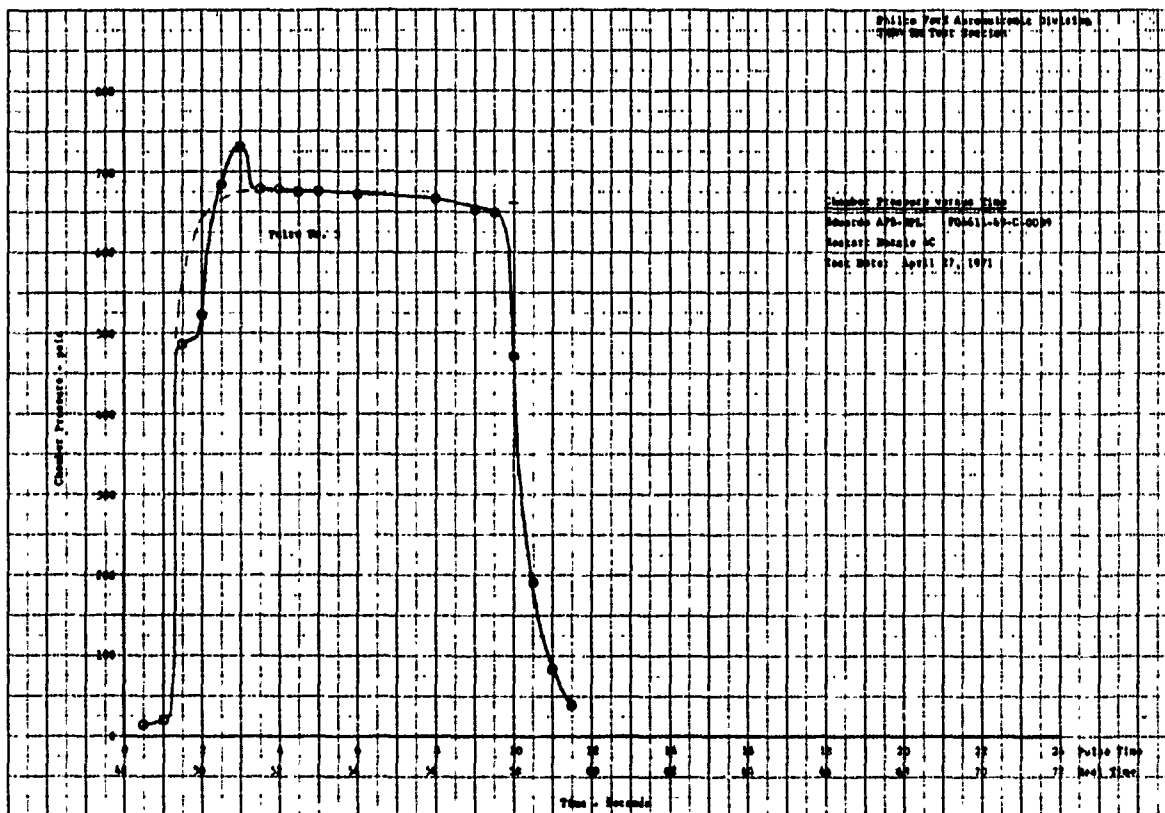


a) Pulse No. 1

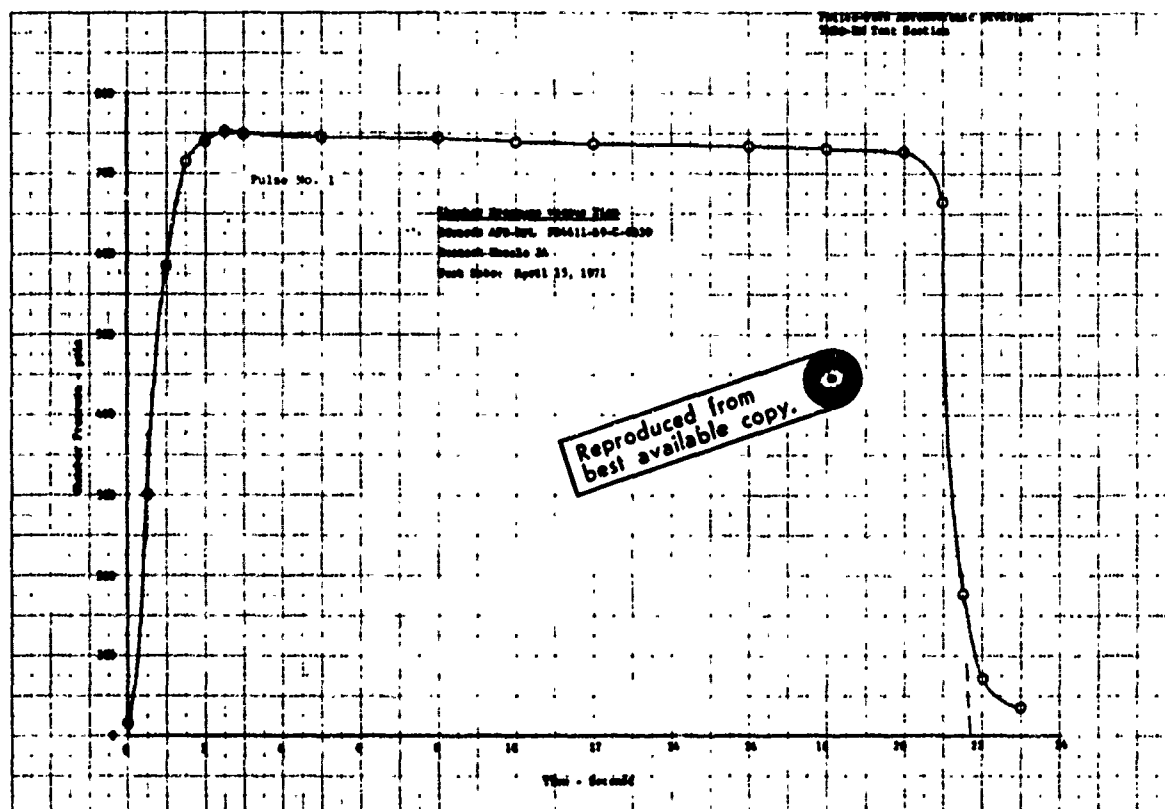


b) Pulse No. 2

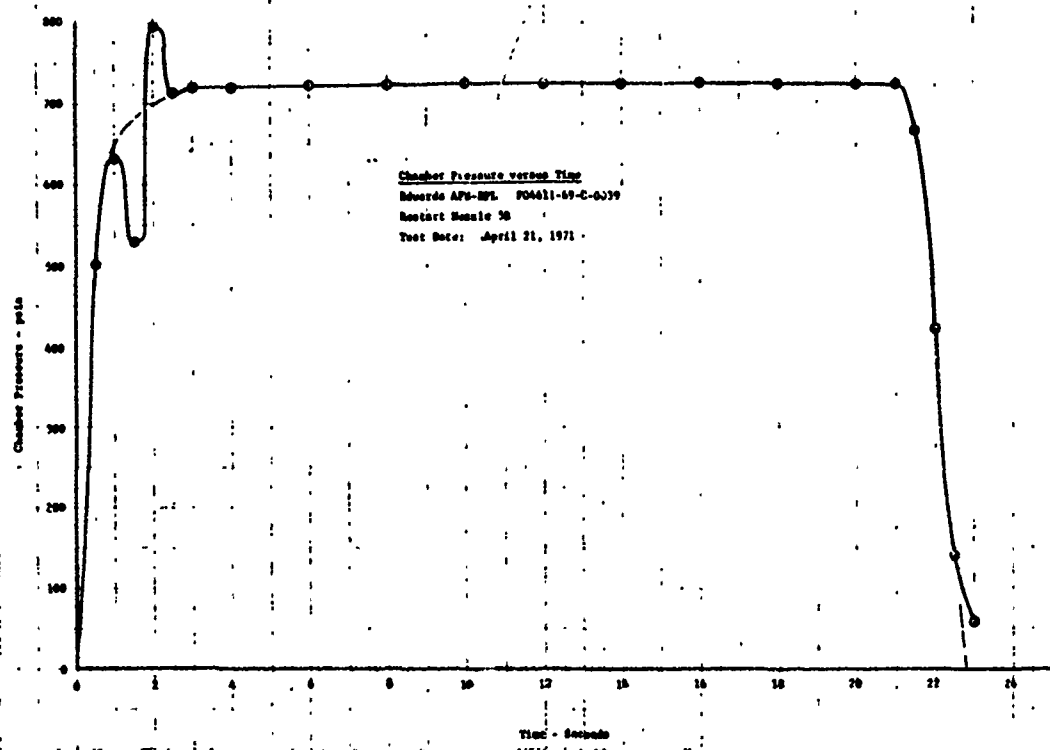
Figure A-1. Chamber Pressure Histories for Nozzle No. 4



c) Pulse No. 1
Figure A-1. (Concluded)



a) Pulse No. 1
Figure A-2. Chamber Pressure Histories for Hostile No. 5

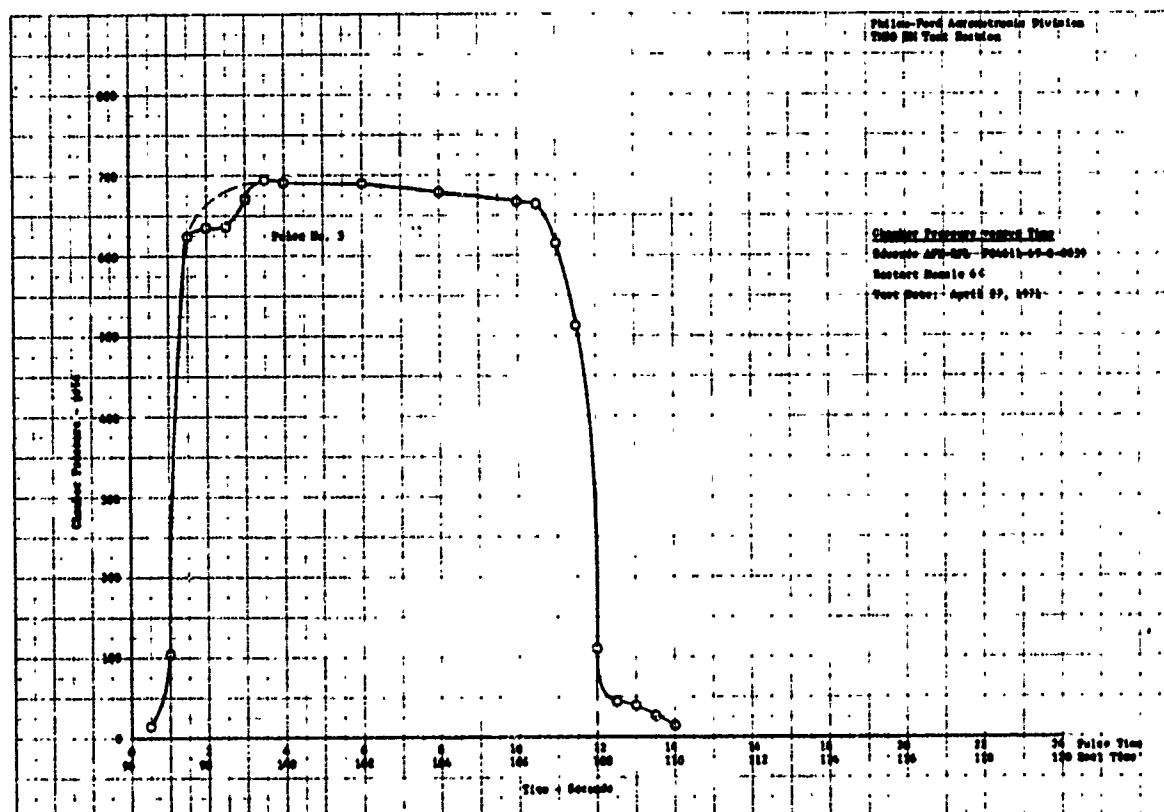
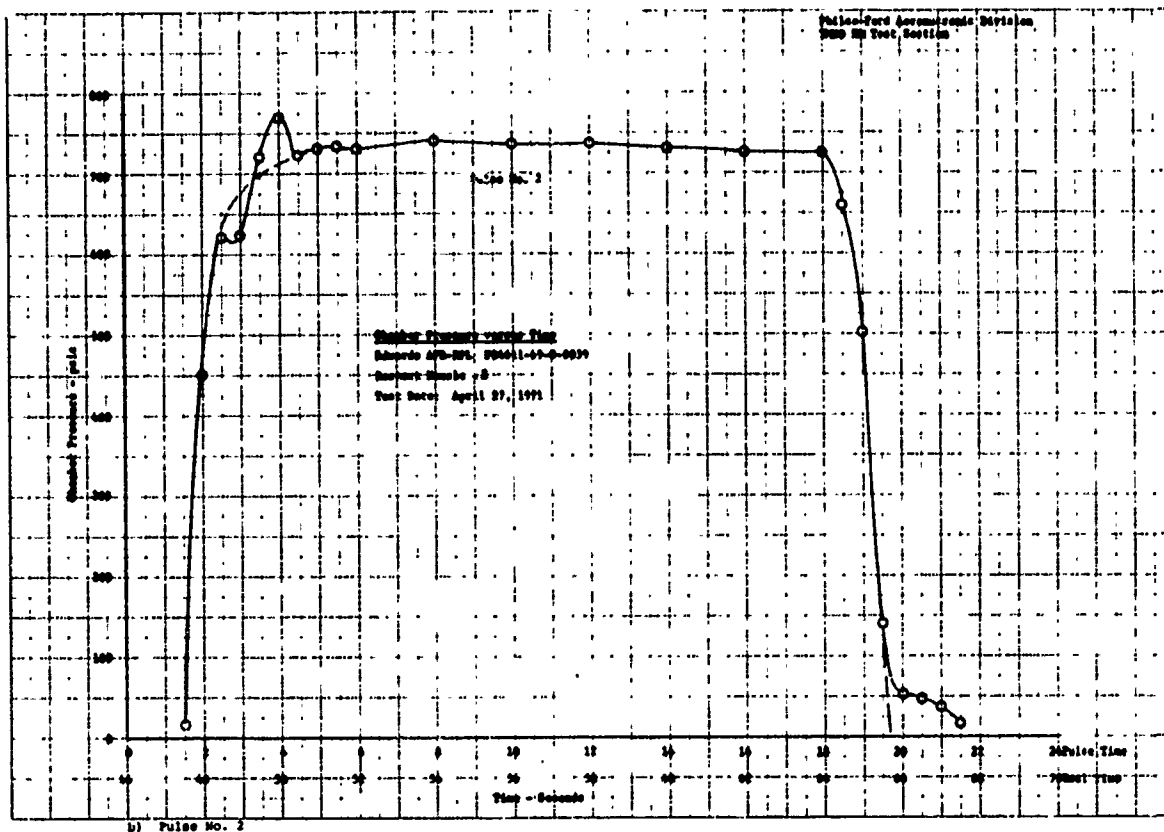


b) Pulse No. 2
 Figure A-2. (Concluded)



Reproduced from
 best available copy.

a) Pulse No. 1
 Figure A-3. Chamber Pressure Histories for Nozzle No. 6



c) Pulse No. 3
 Figure A-3. (Concluded)

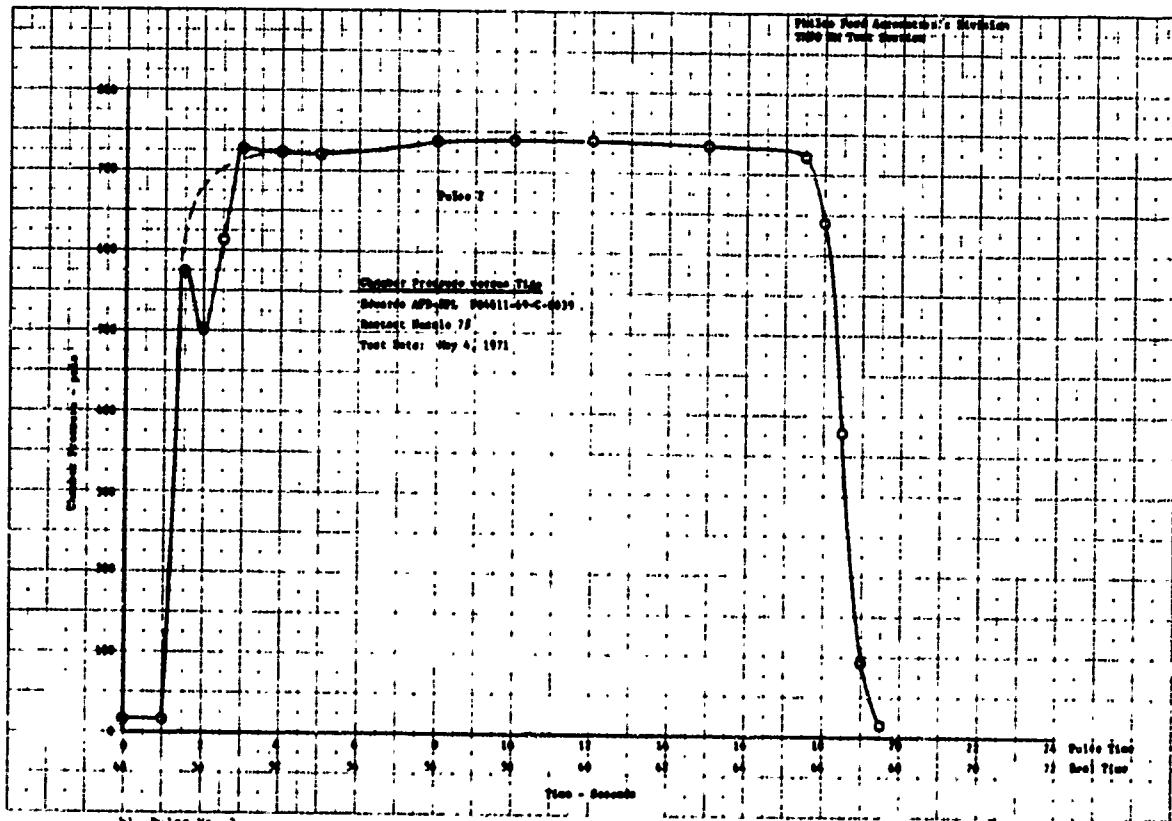
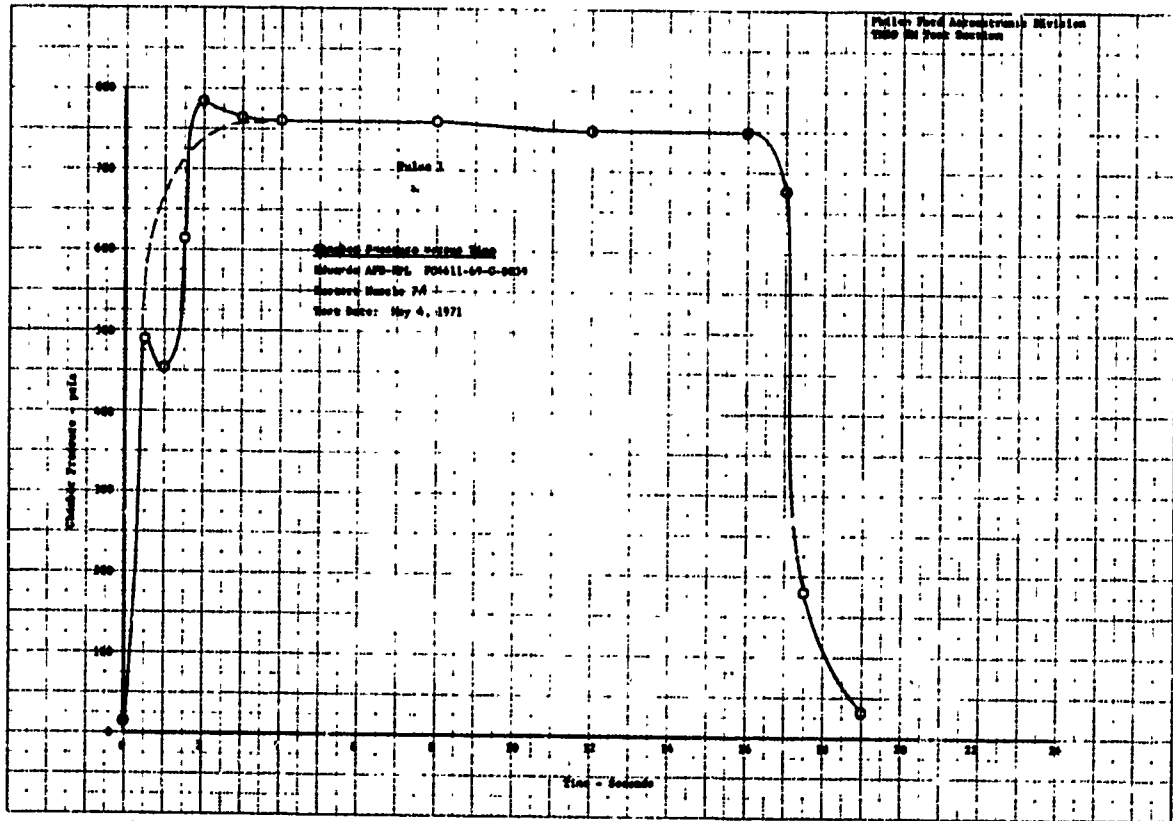
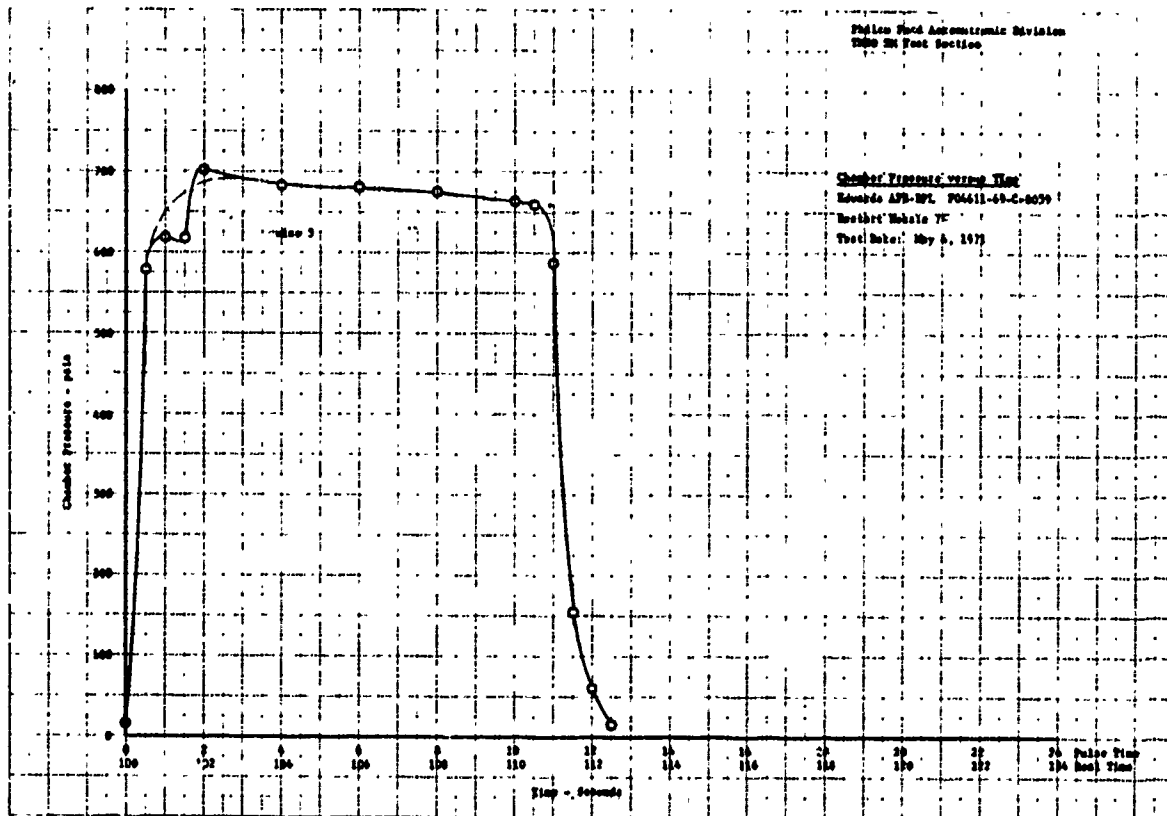
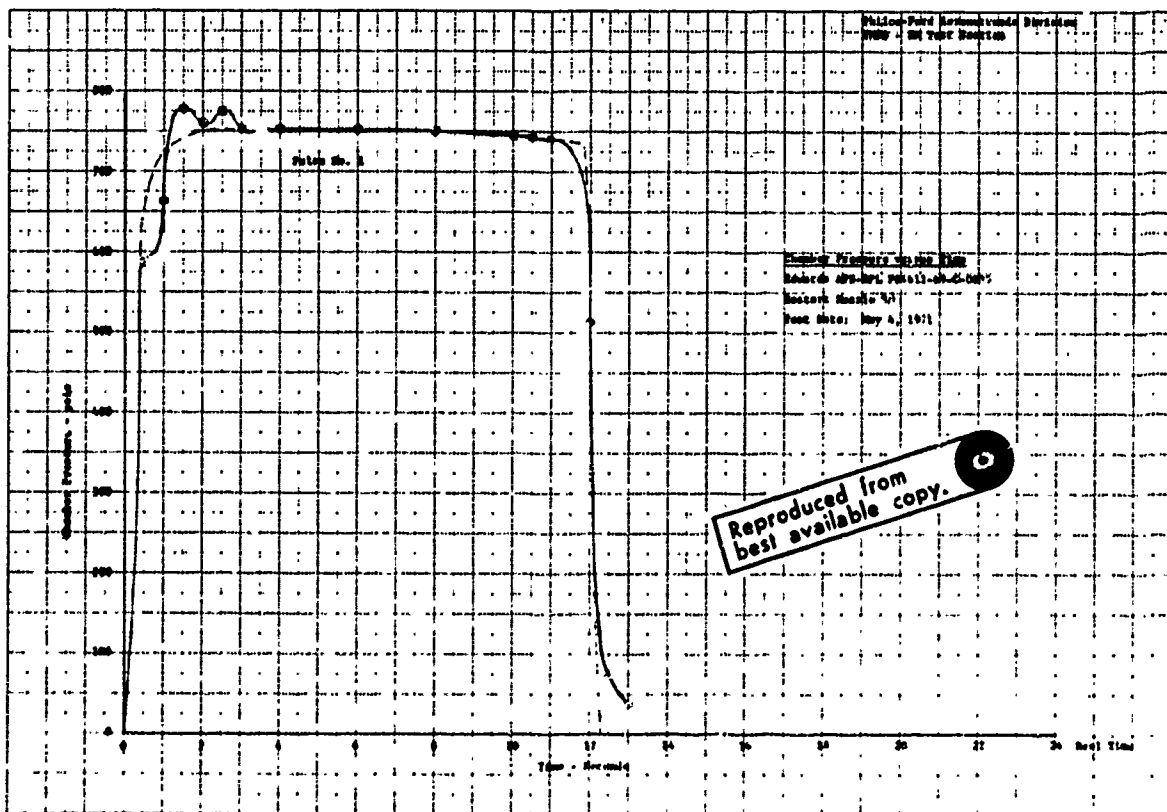


Figure A-6. Chamber Pressure Histories for Nozzle No. 7



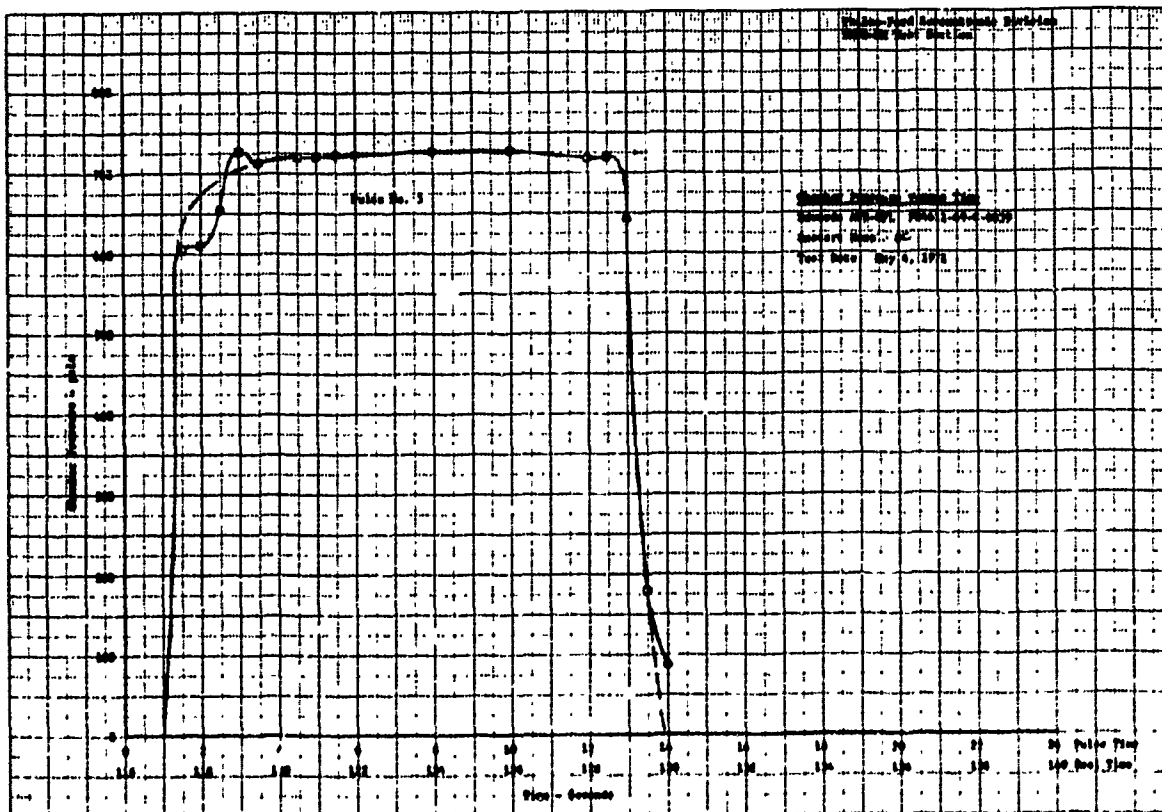
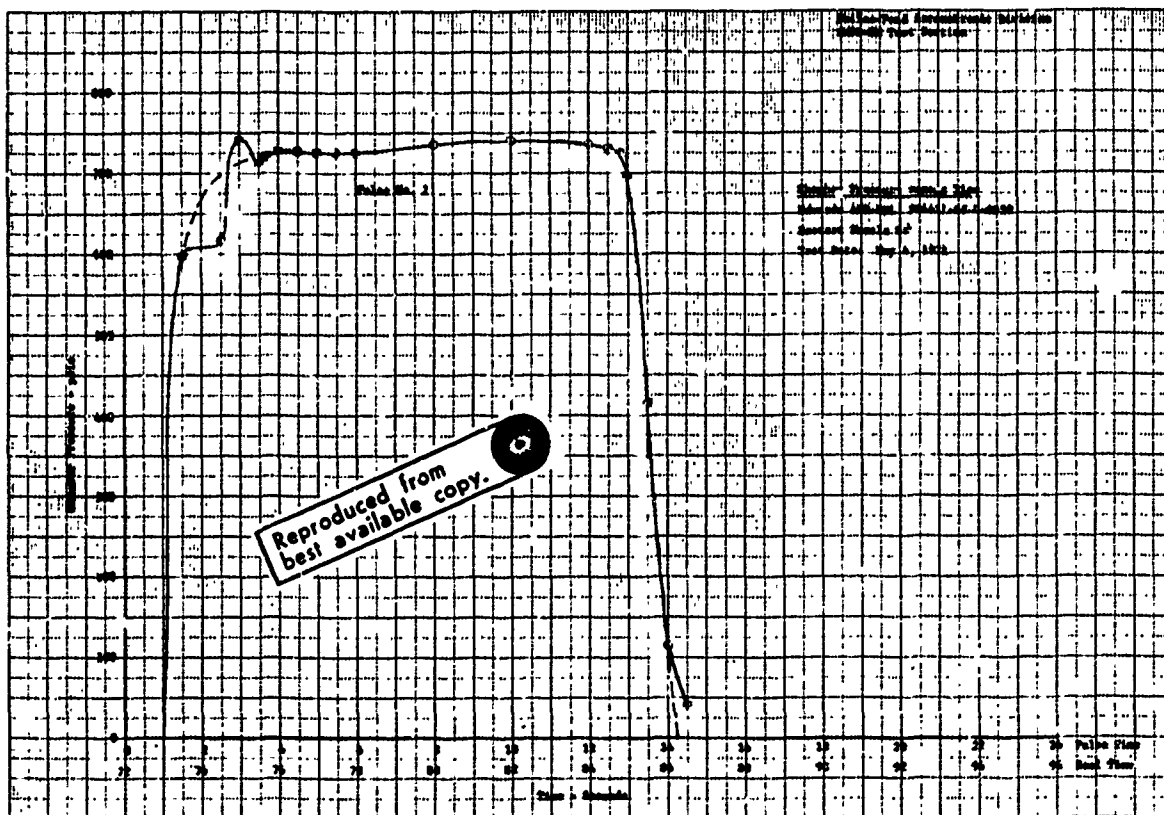
c) Pulse No. 3
Figure A-4. (Concluded)

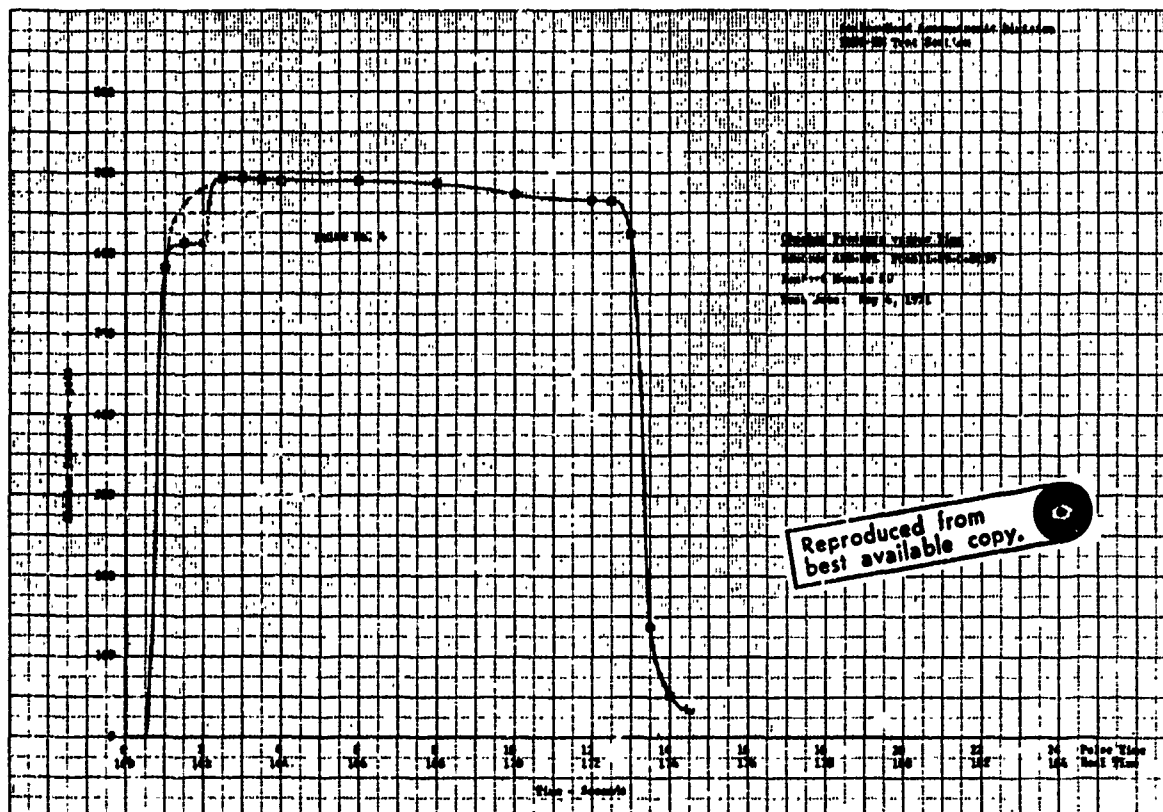


d) Pulse No. 1
Figure A-5. Chamber Pressure Distribution for S-220 No. 4

Reproduced from
best available copy.

6





d) Pulse No. 4
Figure A-5. (Concluded)

APPENDIX B

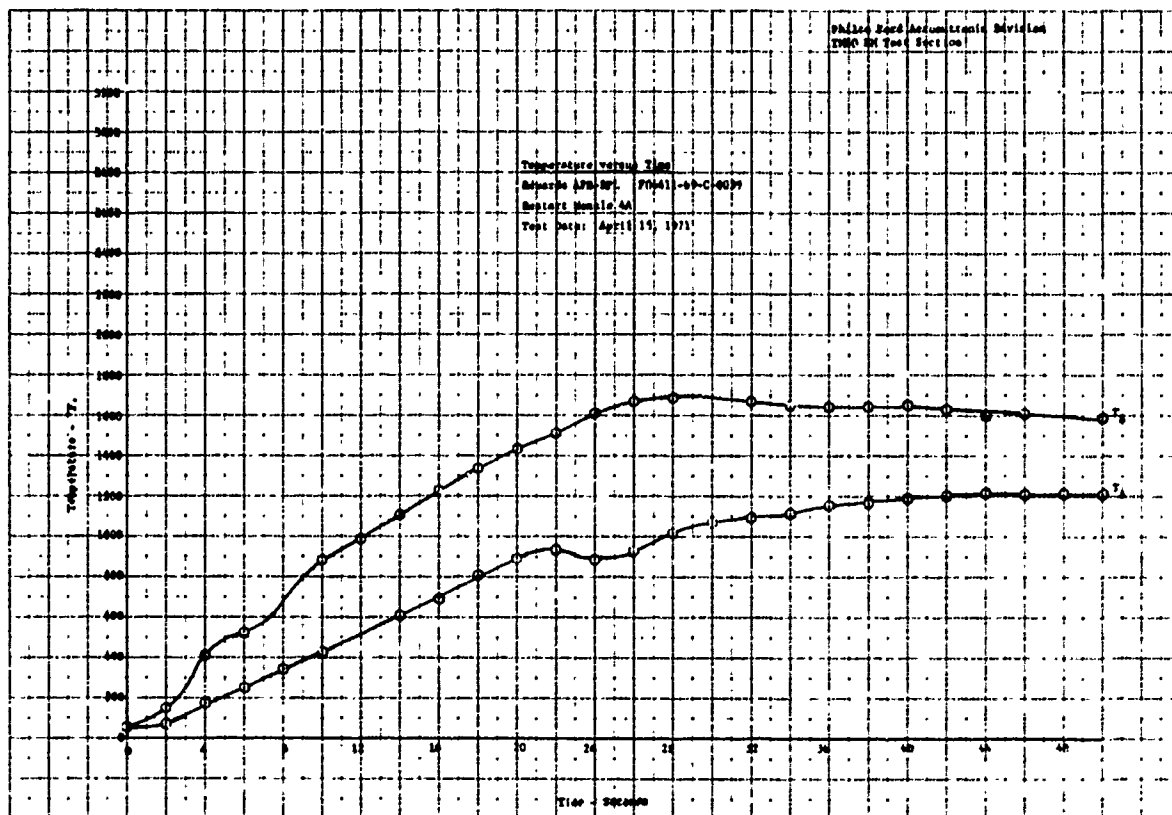
MEASURED TRANSIENT IN-DEPTH TEMPERATURE HISTORIES

As described in Section 2.2 and in Appendix A, the five thermocoupled nozzles were tested in the Aeronutronic solid rocket motor simulator and the reduced data delivered to Aerotherm at the conclusion of these tests. The measured temperatures for these tests at the locations shown in Figure 2-1 are presented in this appendix in Figures B-1 through B-5. In these figures, the curves are identified by $T_{\text{subscript}}$. The subscript "A" refers to temperatures at the backside of the AGSR graphite and the subscript "E" refers to temperatures at the backside of the ATJ graphite (refer Figure 2-1). The number subscripts denote the thermocoupled plug number which are correlated with the nozzle number using Table B-1. The number following the dash (i.e., the number one in T_{5-1}) refers to the thermocouple number in each plug. The number one refers to the thermocouple nearest the inside surface of the nozzle while the number three refers to the thermocouple farthest from the surface.

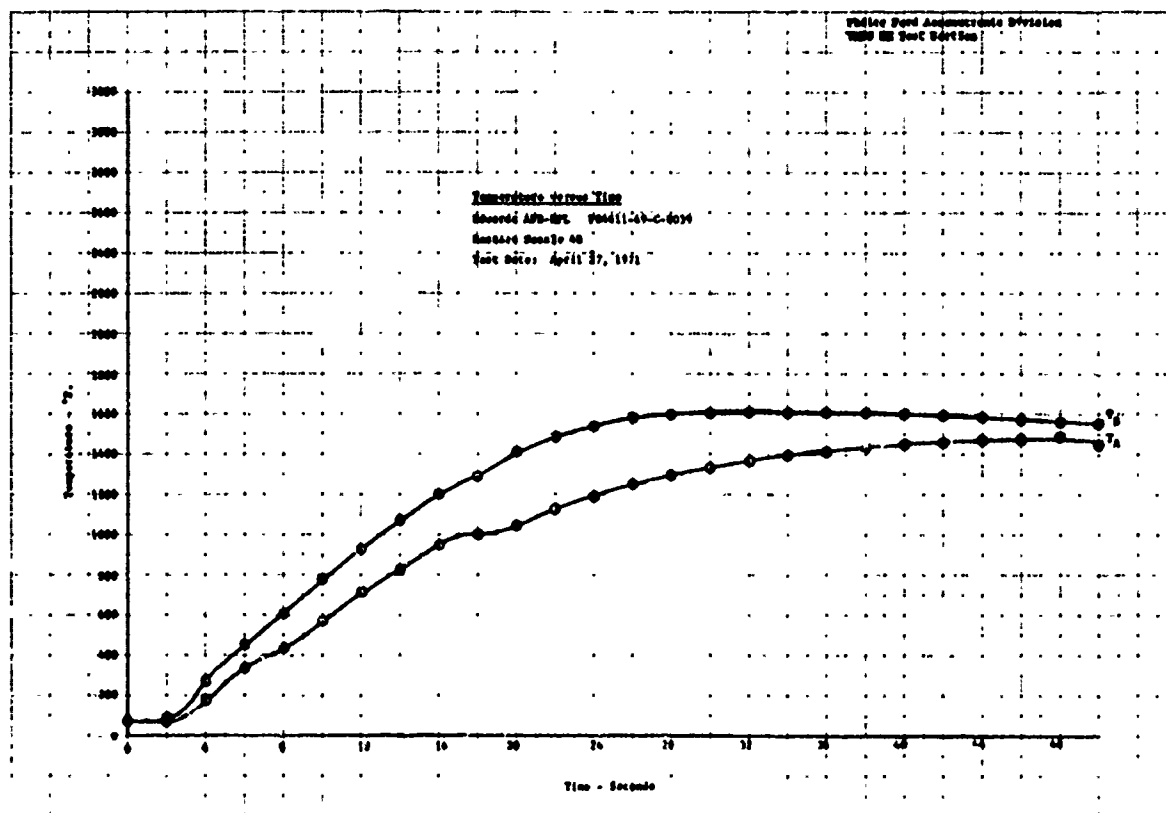
TABLE B-1

DEFINITION OF THERMOCOUPLED PLUG
NUMBERING SYSTEM AND THEIR INITIAL LOCATION

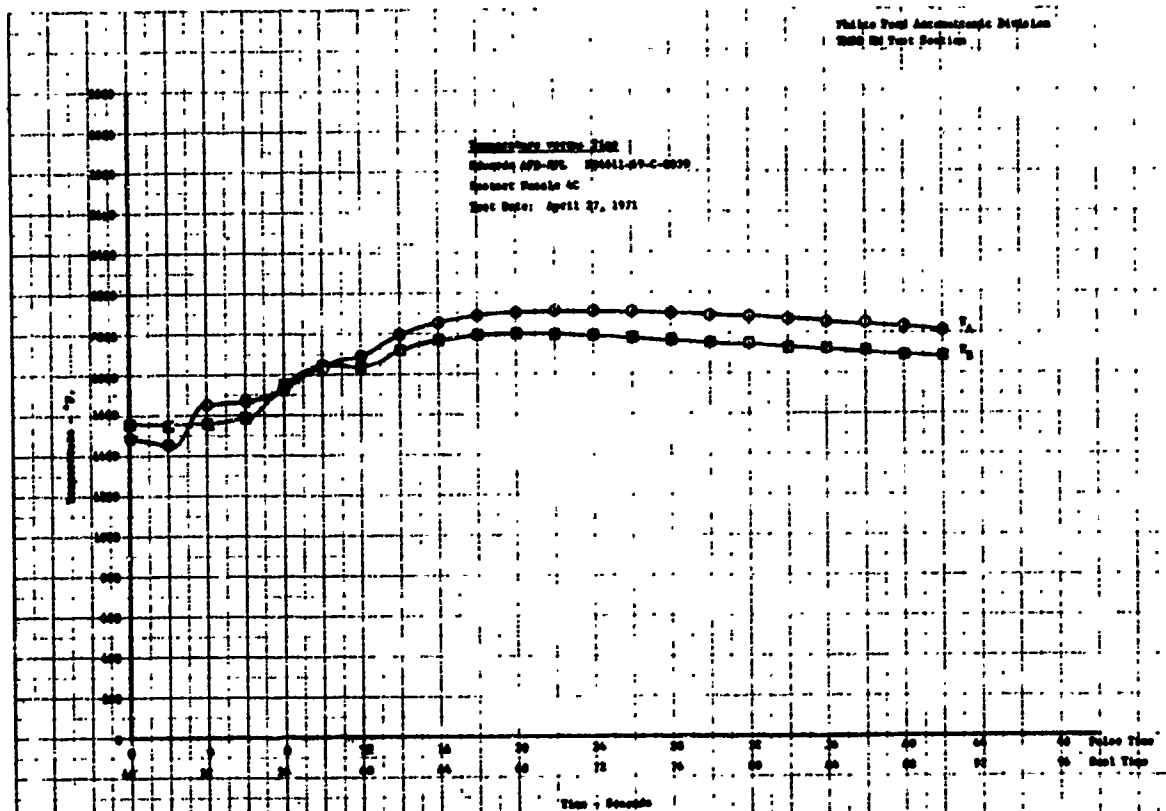
Nozzle No.	Thermocoupled Plug No.	Initial Area Ratio Location
4	5	4.29
	1	6.66
5	7	4.24
	3	6.63
6	709	4.26
	706	6.57
7	710	4.28
	707	6.62
8	711	4.29
	708	6.63



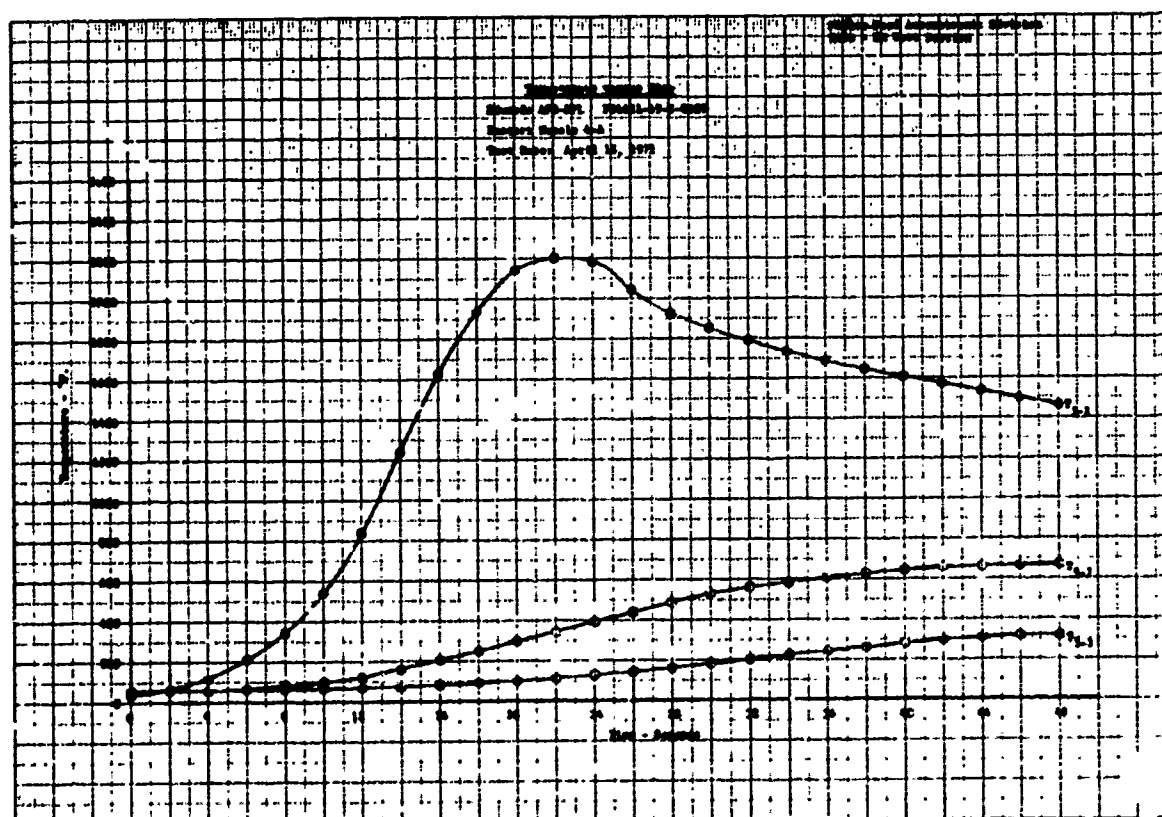
a) Pulse No. 1, Nozzle Throat Insert



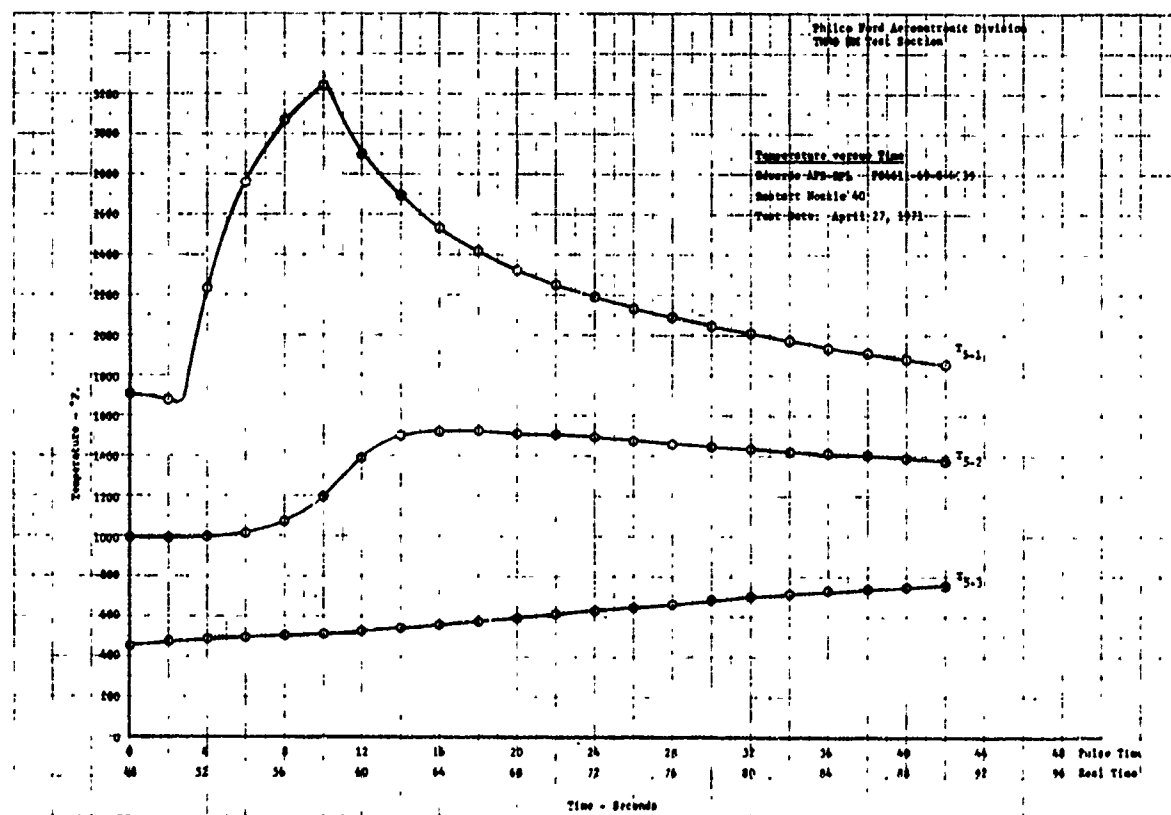
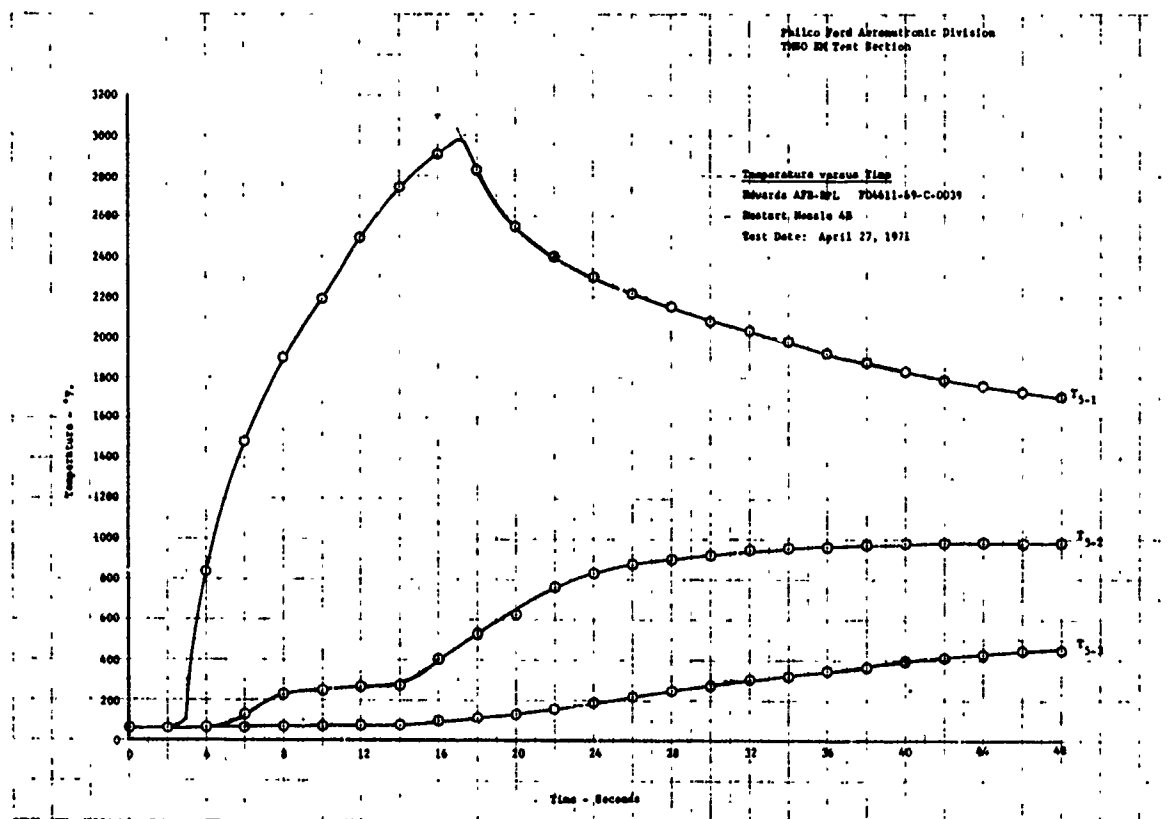
b) Pulse No. 2, Nozzle Throat Insert
 Figure B-1. Measured In-Depth Transient Temperatures for Nozzle No. 4

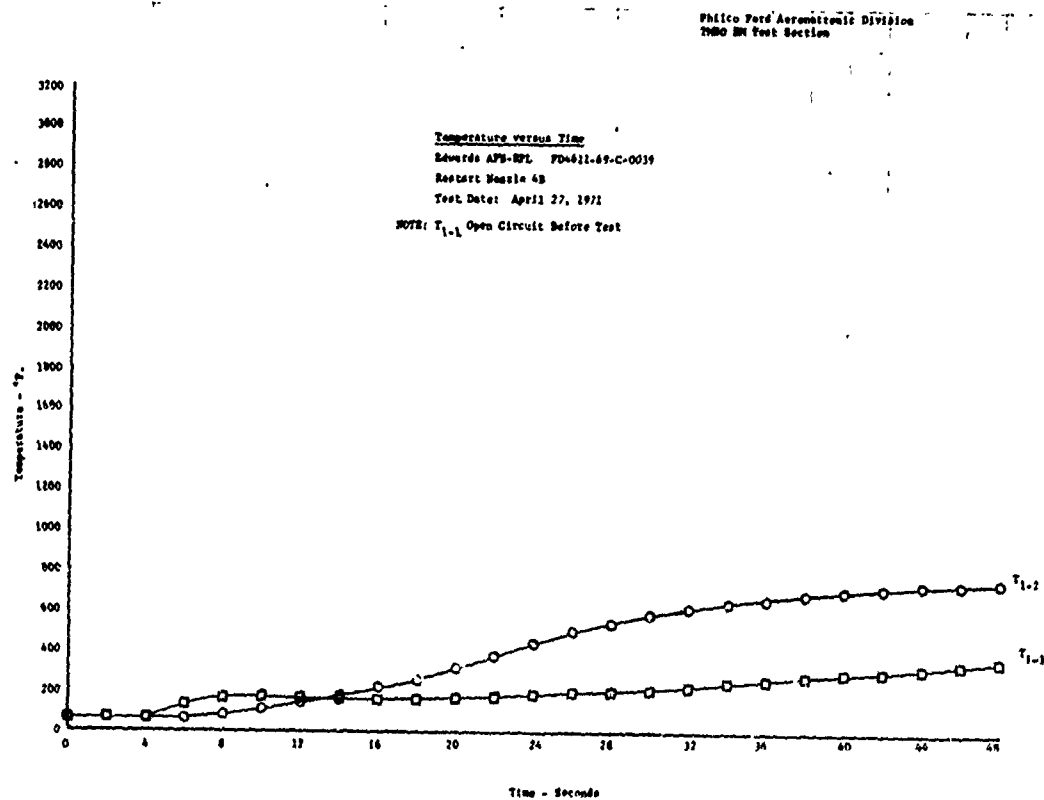
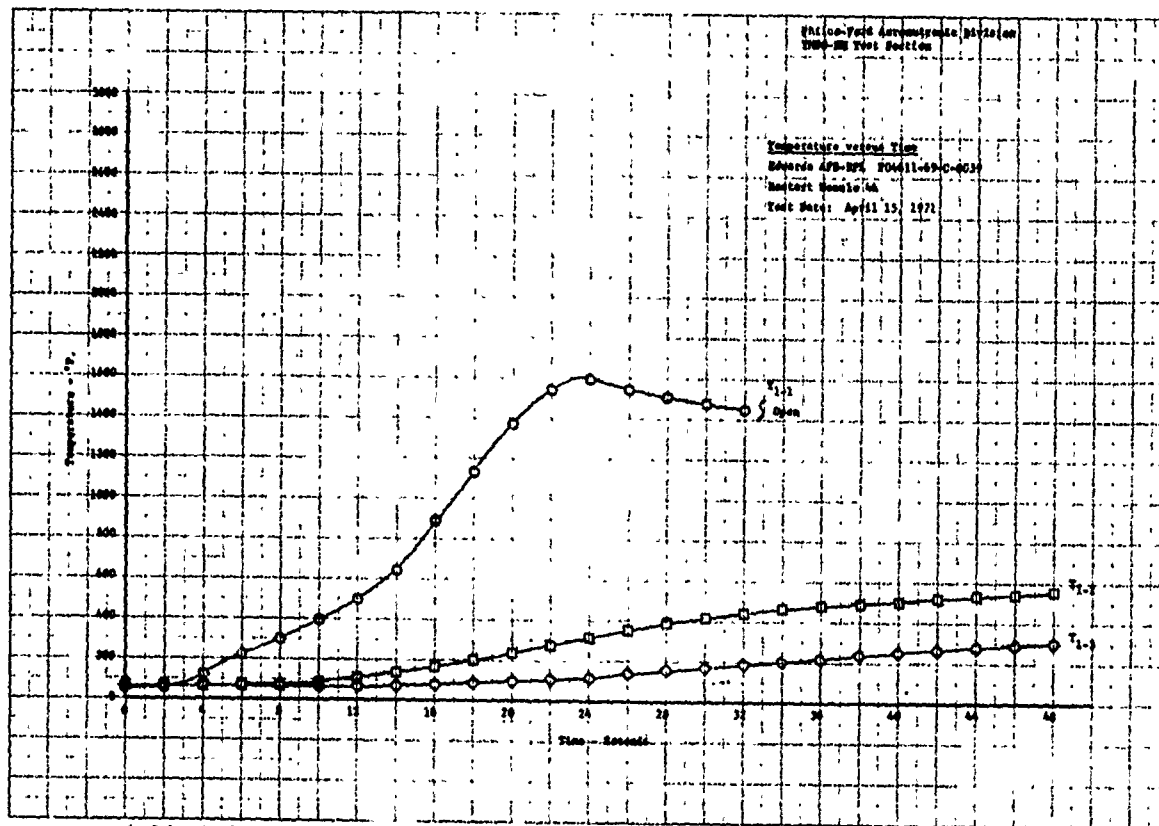


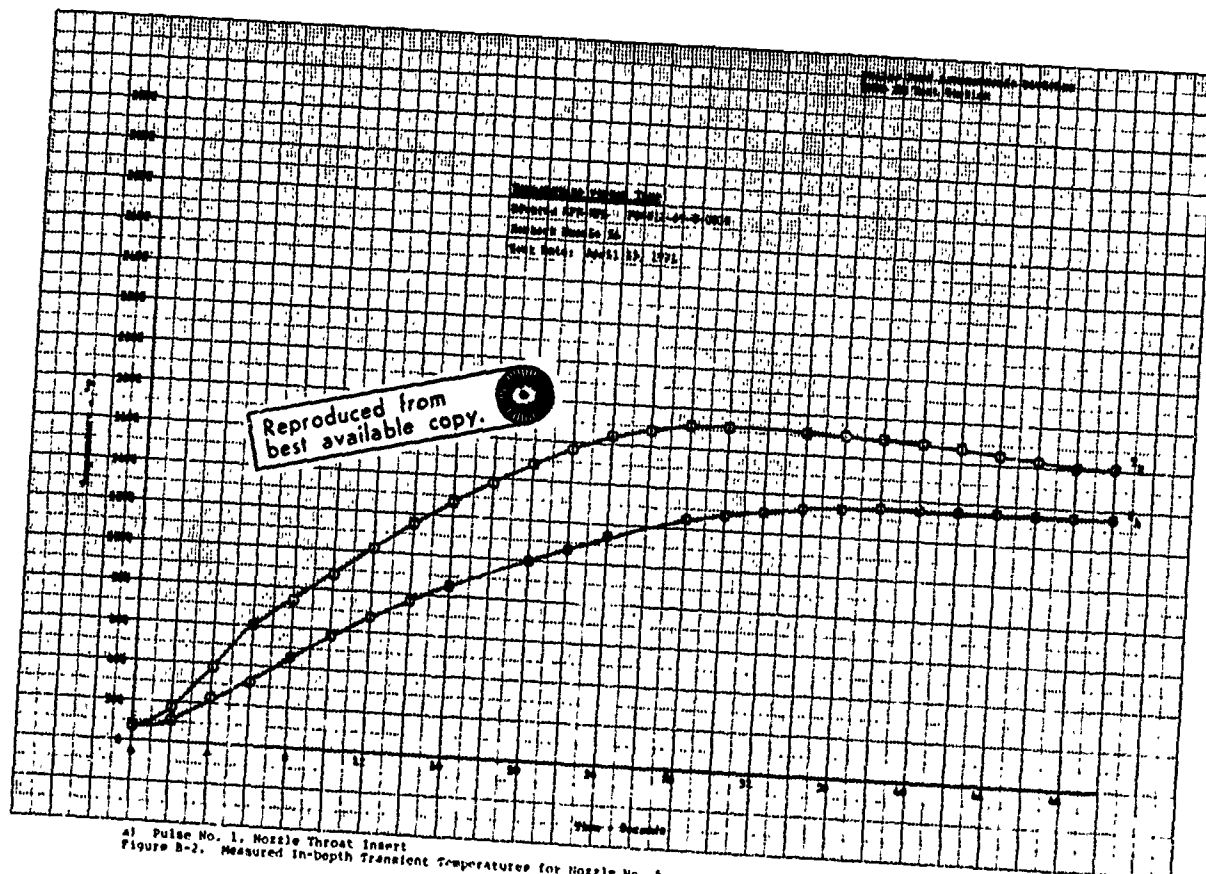
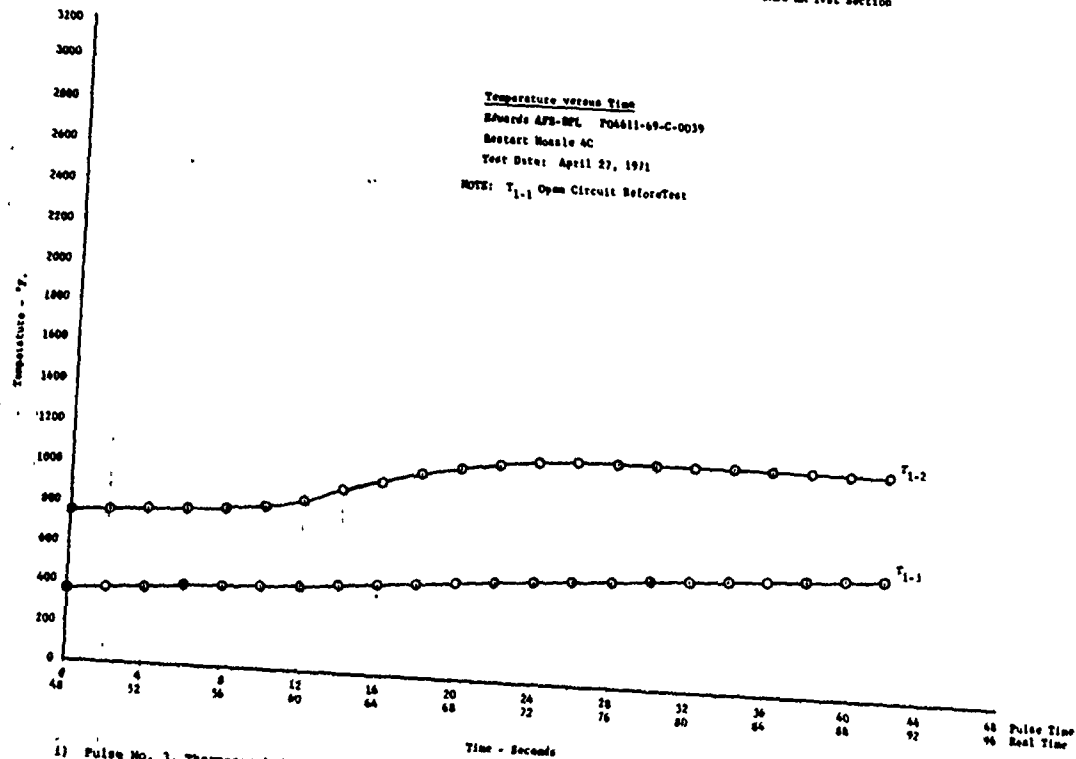
c) Pulse No. 3, Missile Threat Inert

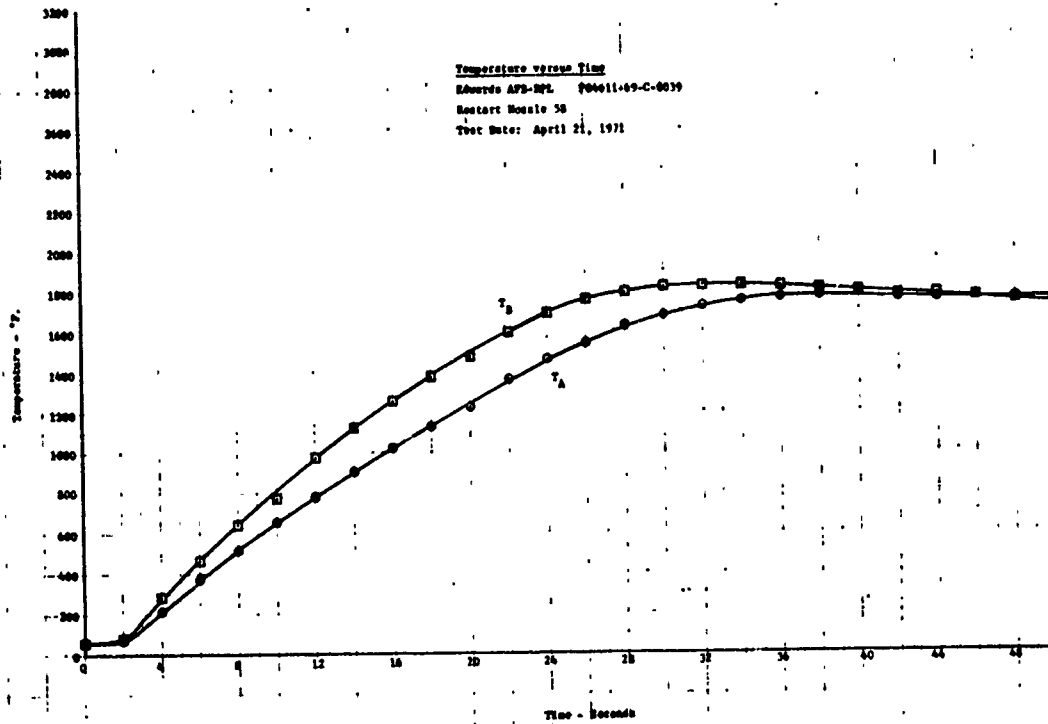


d) Pulse No. 1, Thermocoupled Flap at $A/A^* = 4.29$
Figure B-1. (Continued)

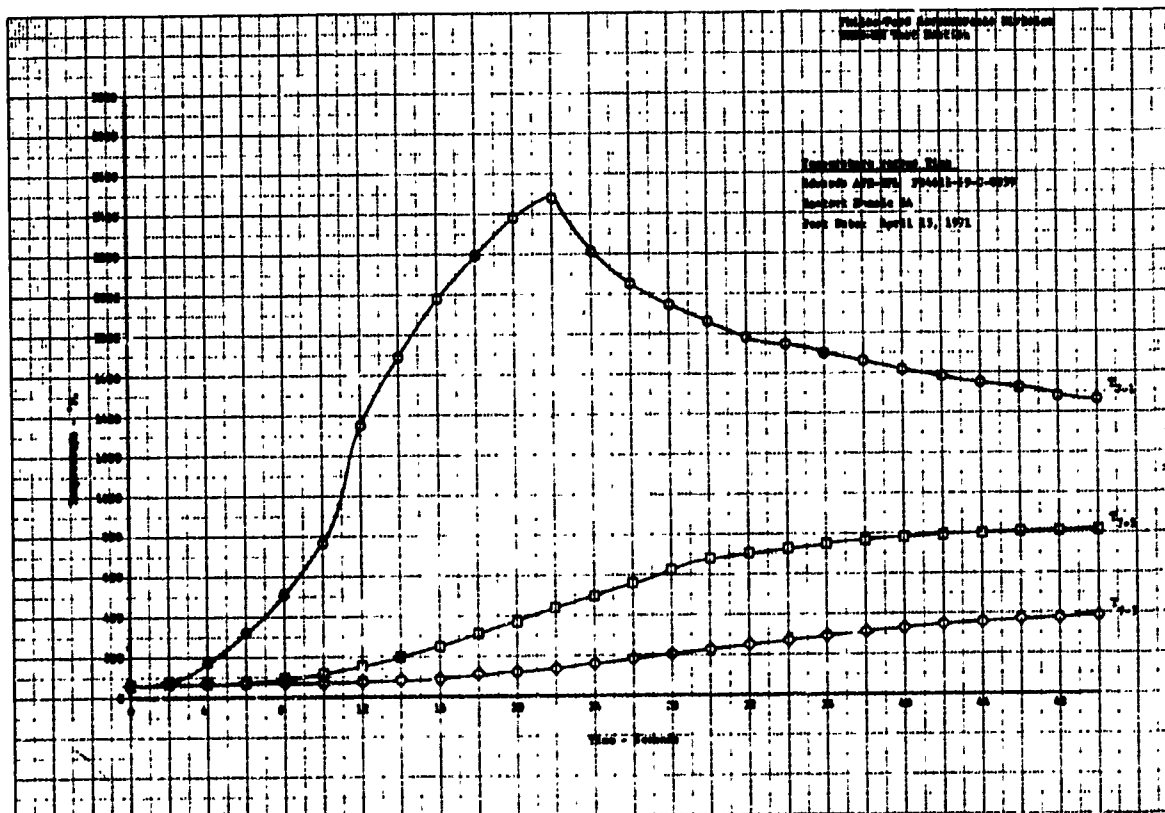




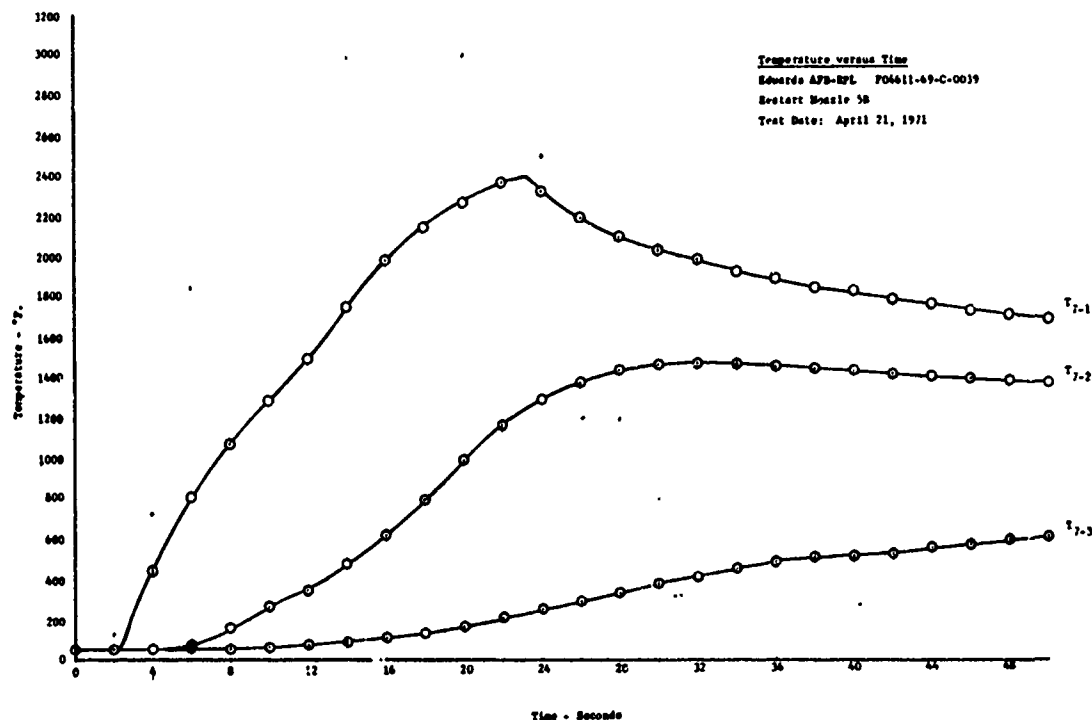




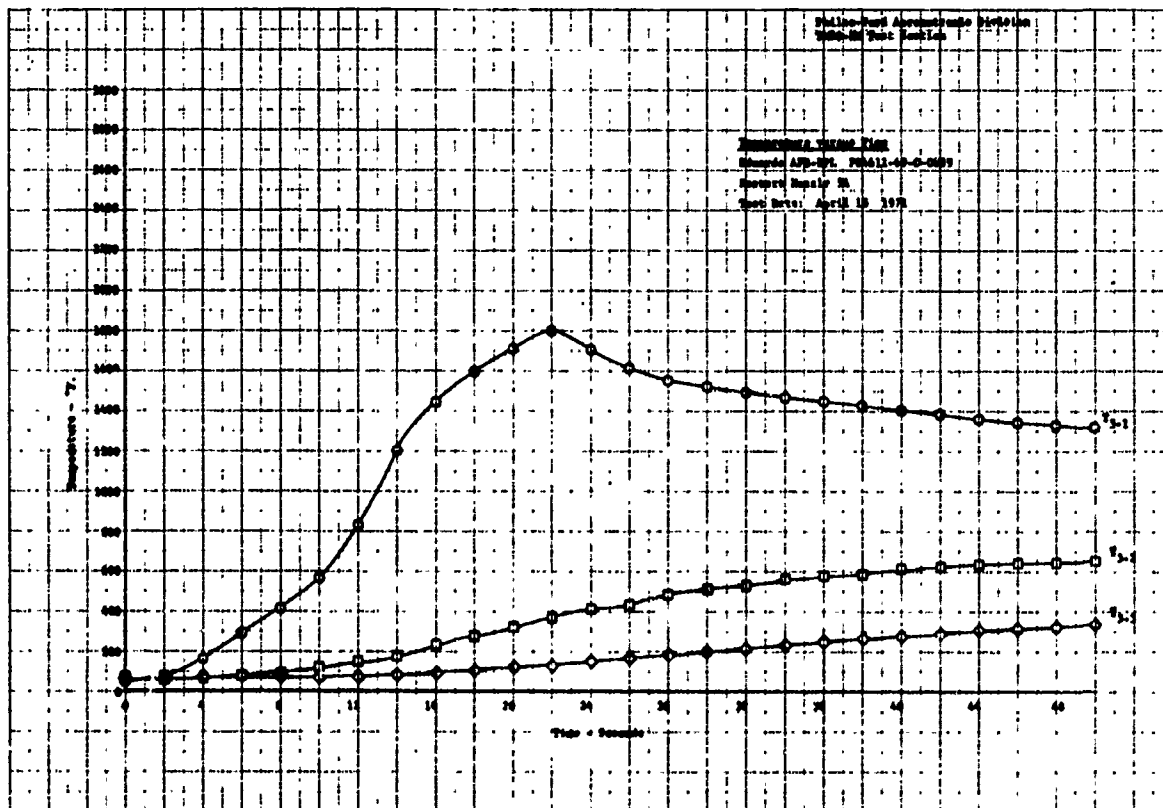
a) Pulse No. 2, Nozzle Throat Insert



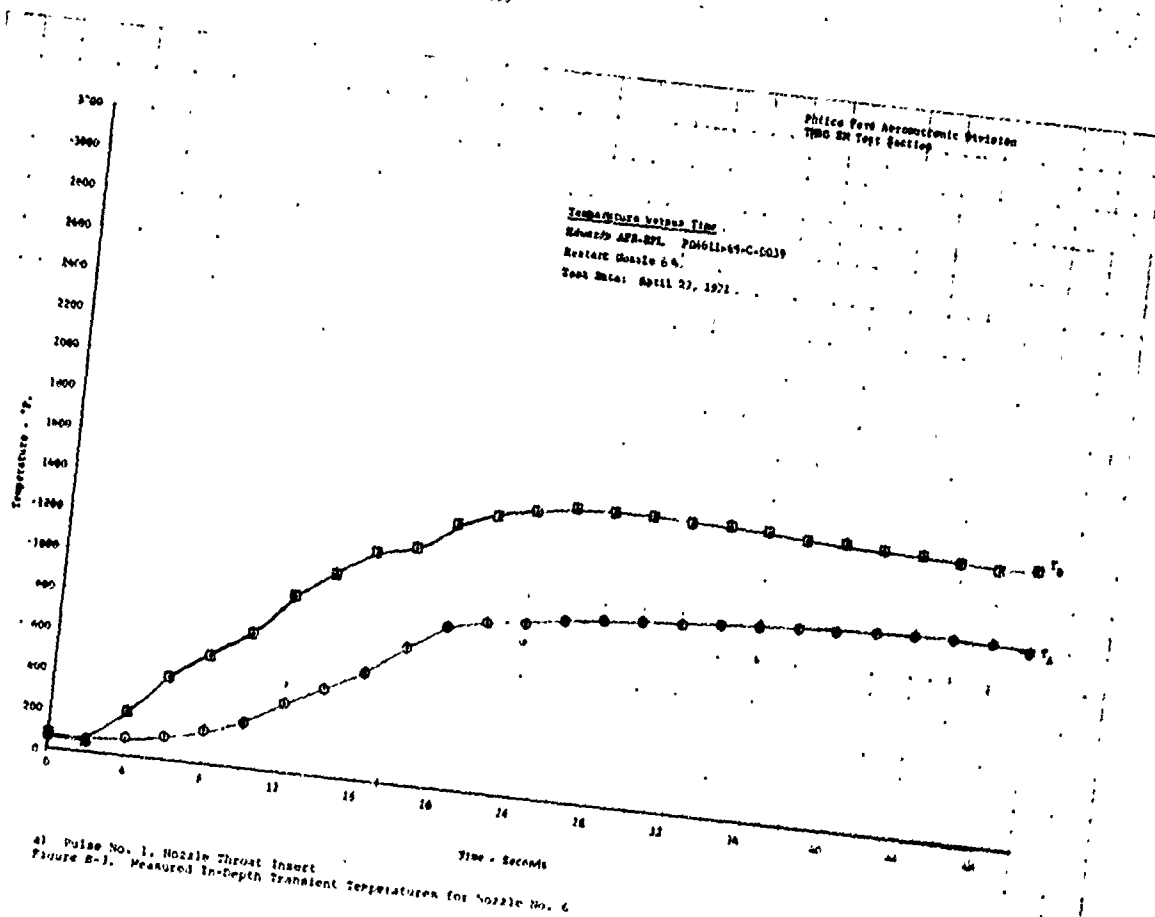
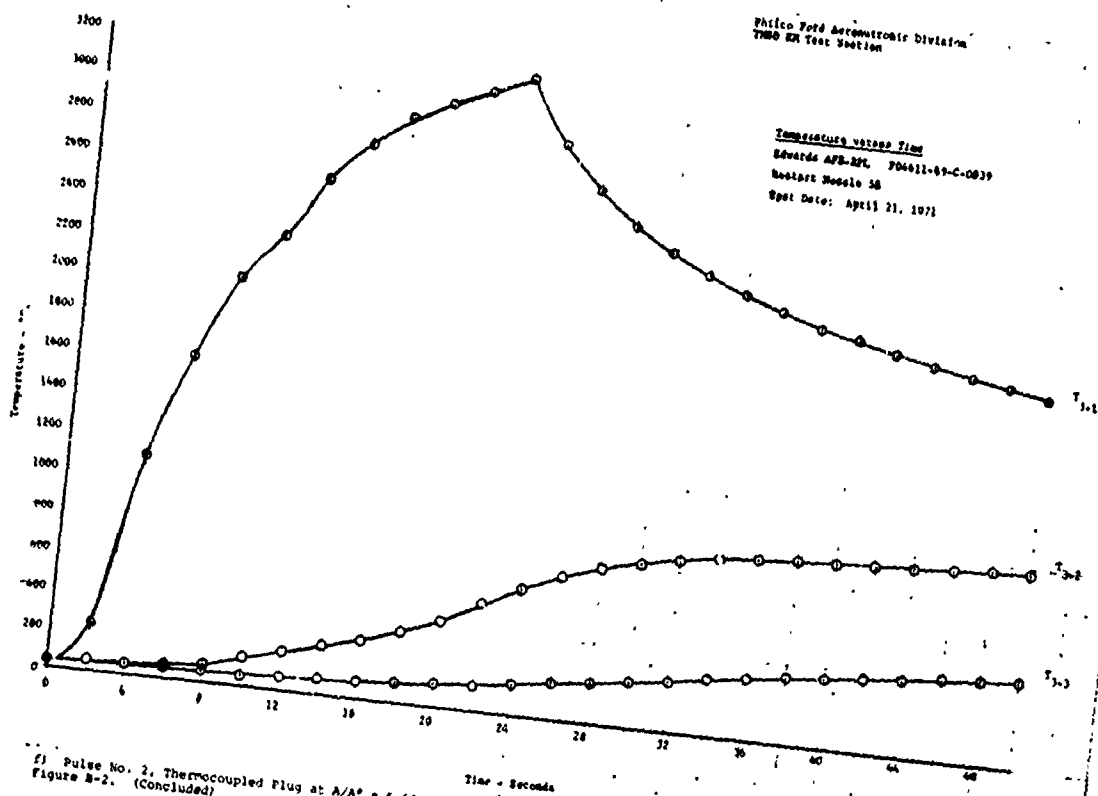
c) Pulse No. 1, Thermocoupled Plug at $A/A^* = 4.24$
 Figure B-2. (Continued)

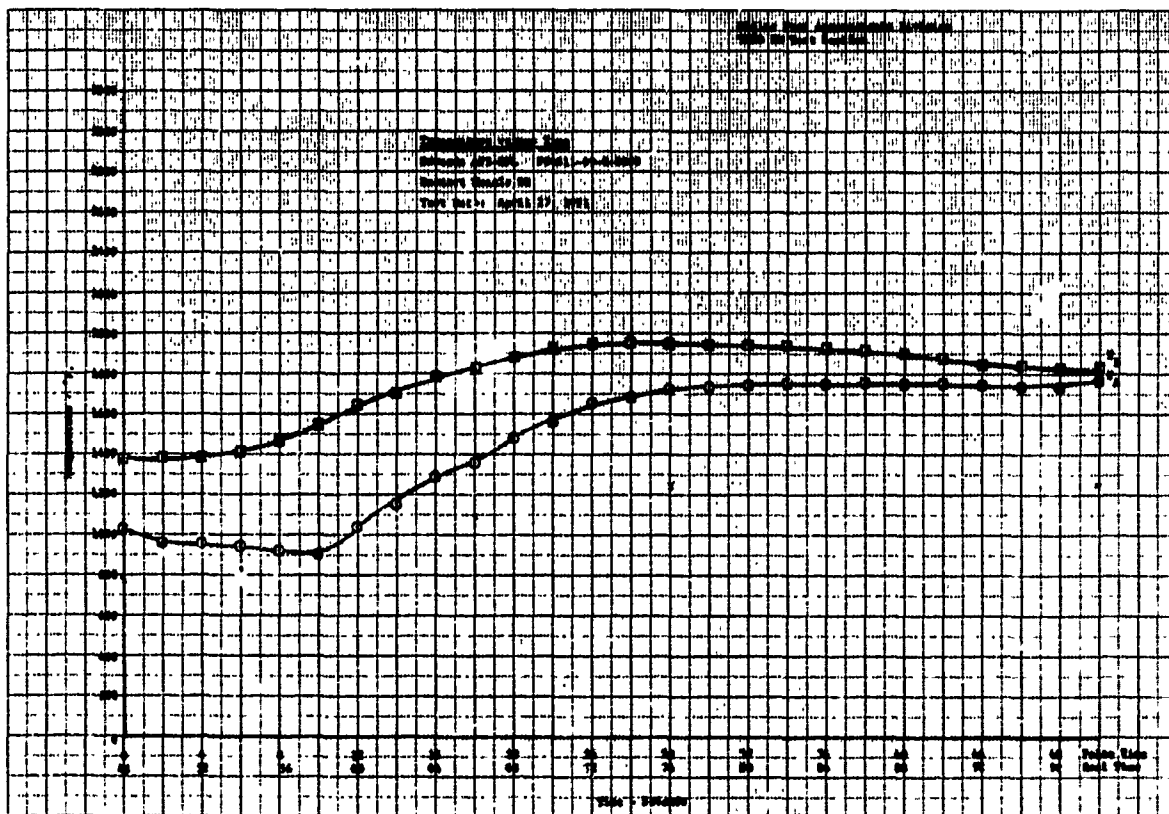


d) Pulse No. 2, Thermocoupled Plug at $A/A^* = 4.24$

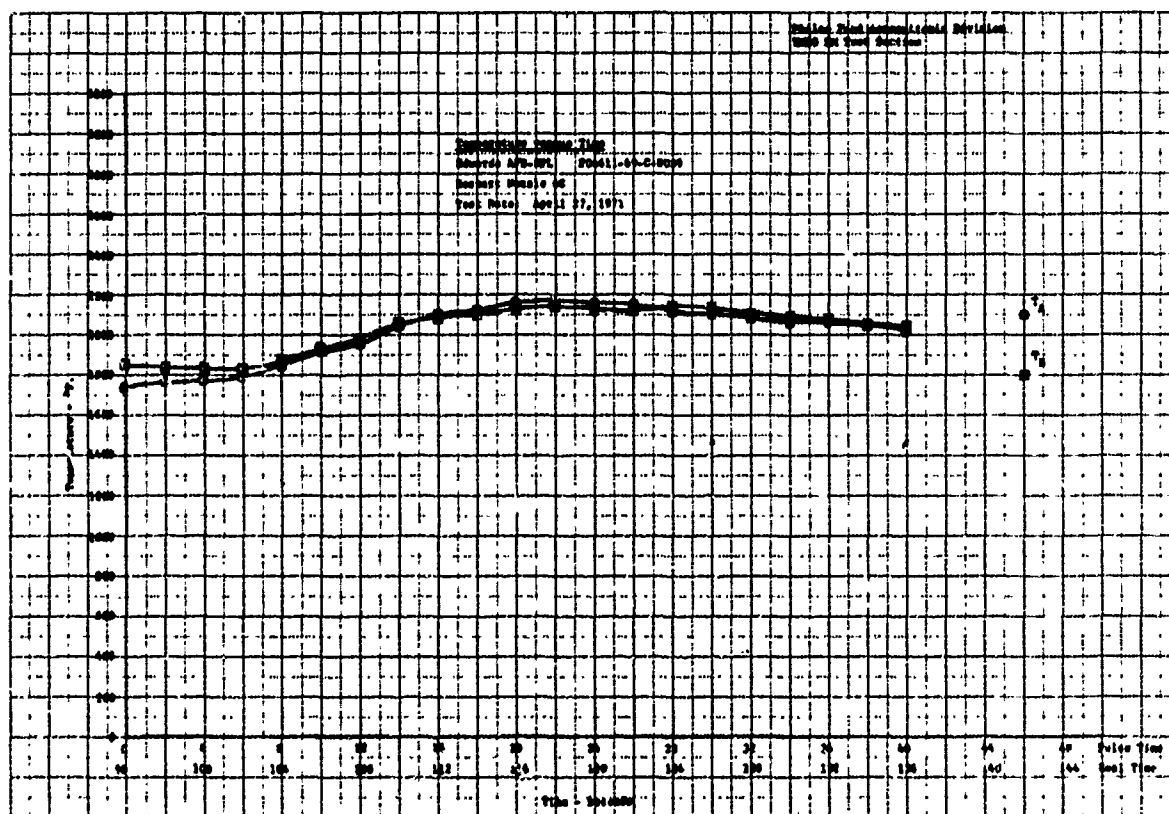


e) Pulse No. 1, Thermocoupled Plug at $A/A^* = 6.63$
Figure B-2. (Continued)



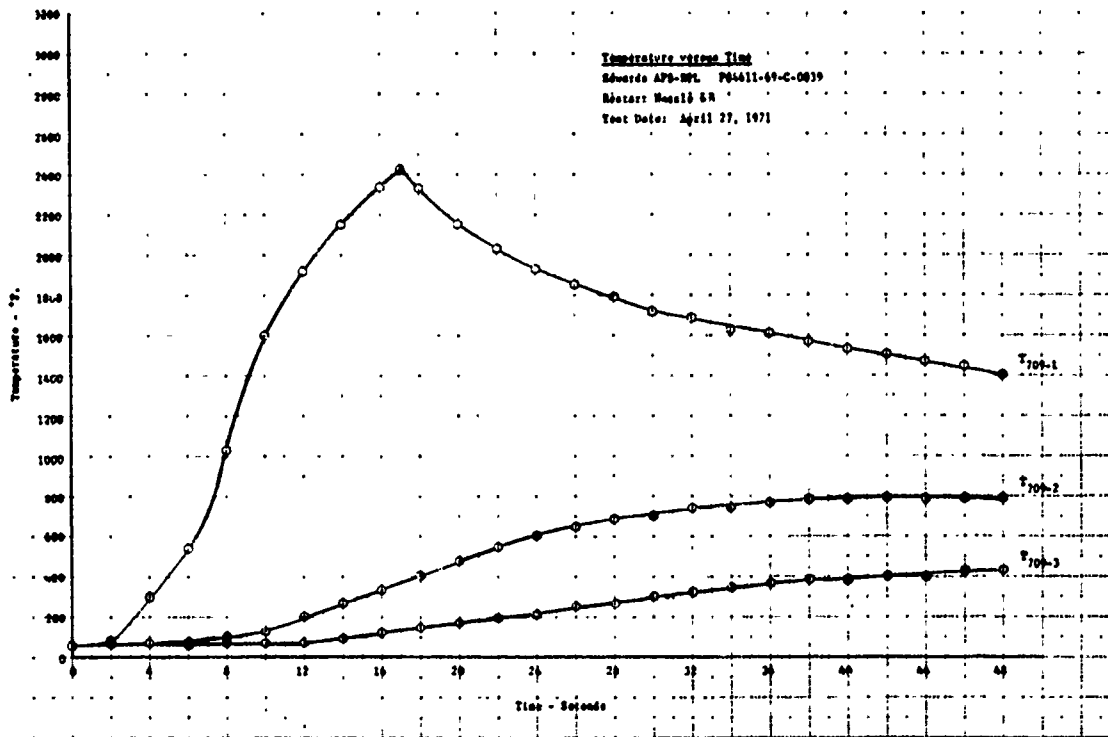


b) Pulse No. 2, Nozzle Throat Insert



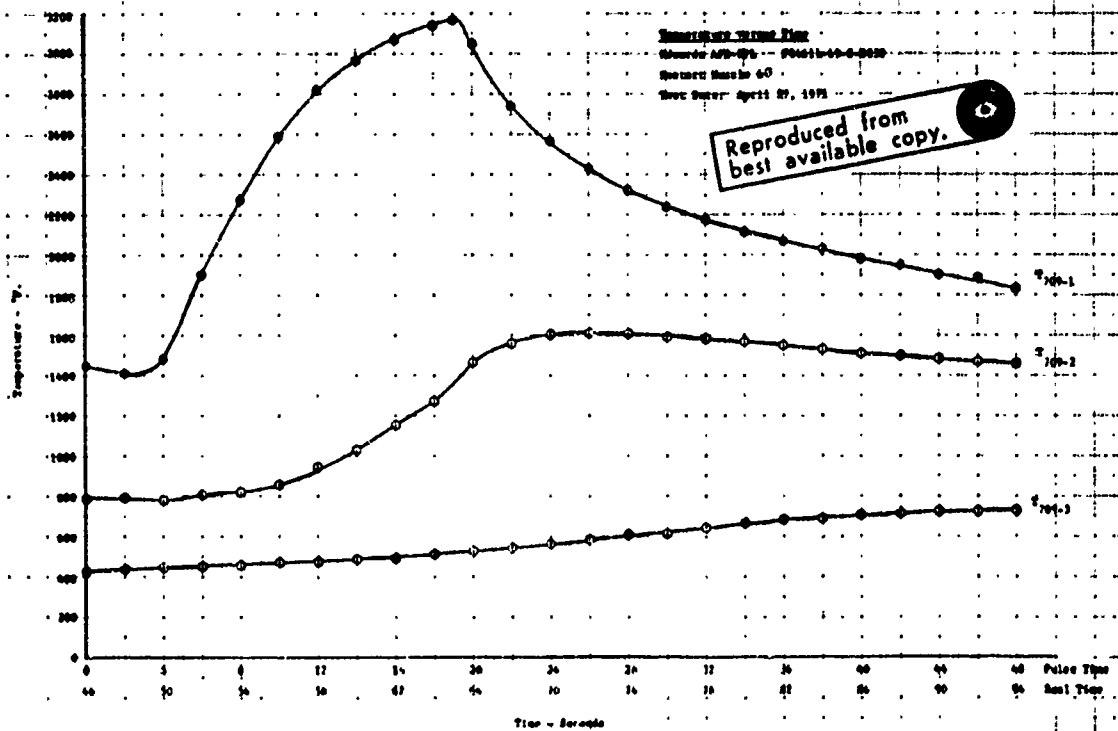
c) Pulse No. 1, Nozzle Throat Insert
Figure B-3. (Continued)

Philco Ford Aerodynamic Division
TMD 20 Test Section

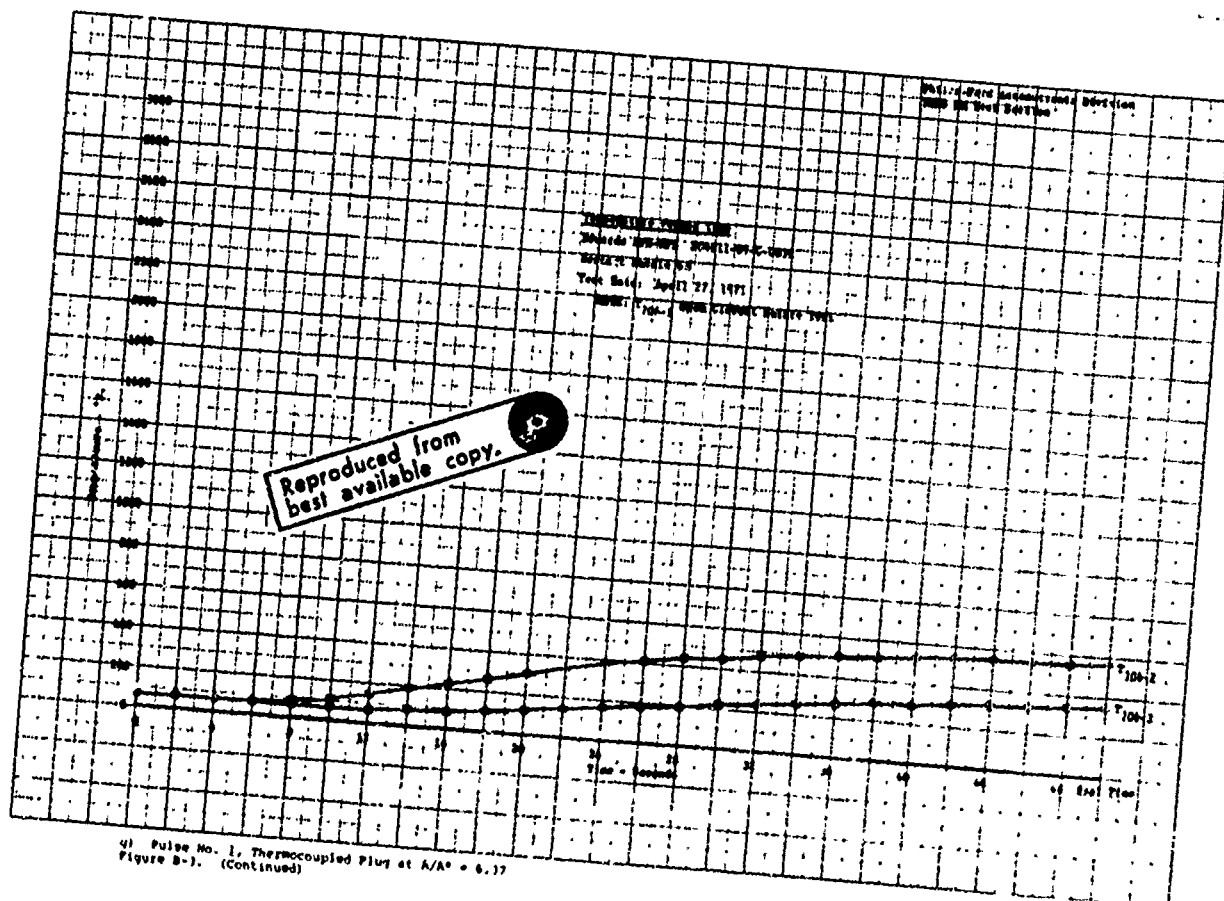
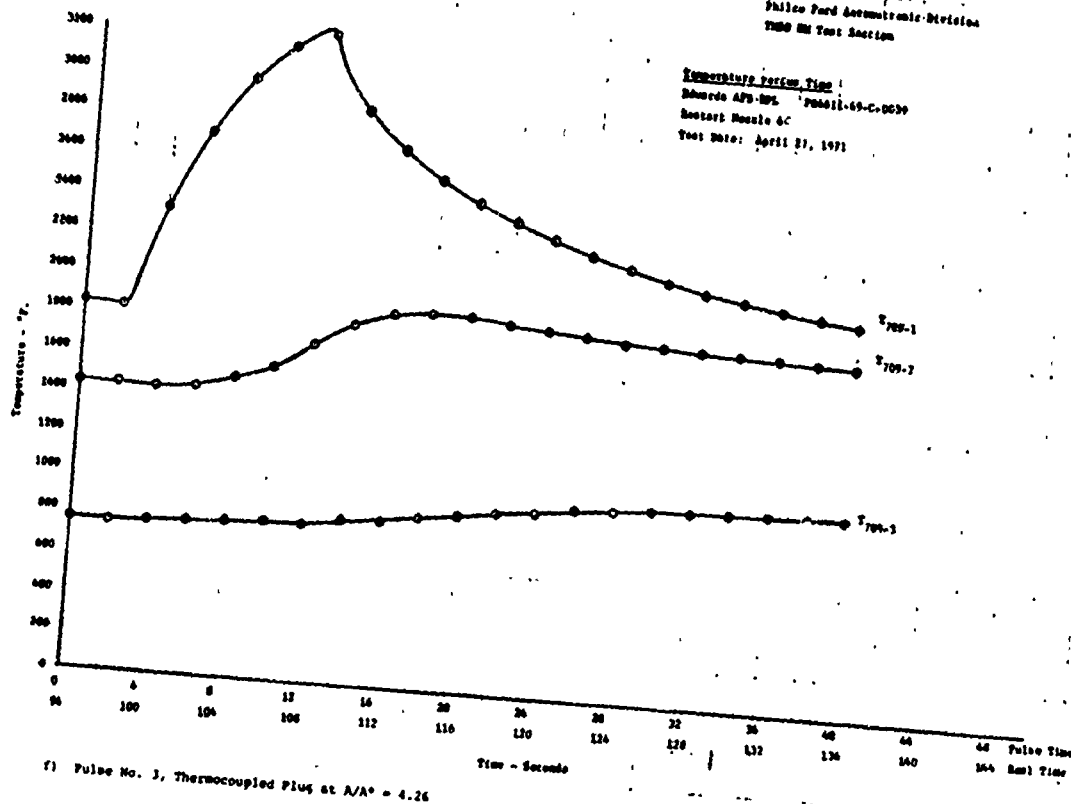


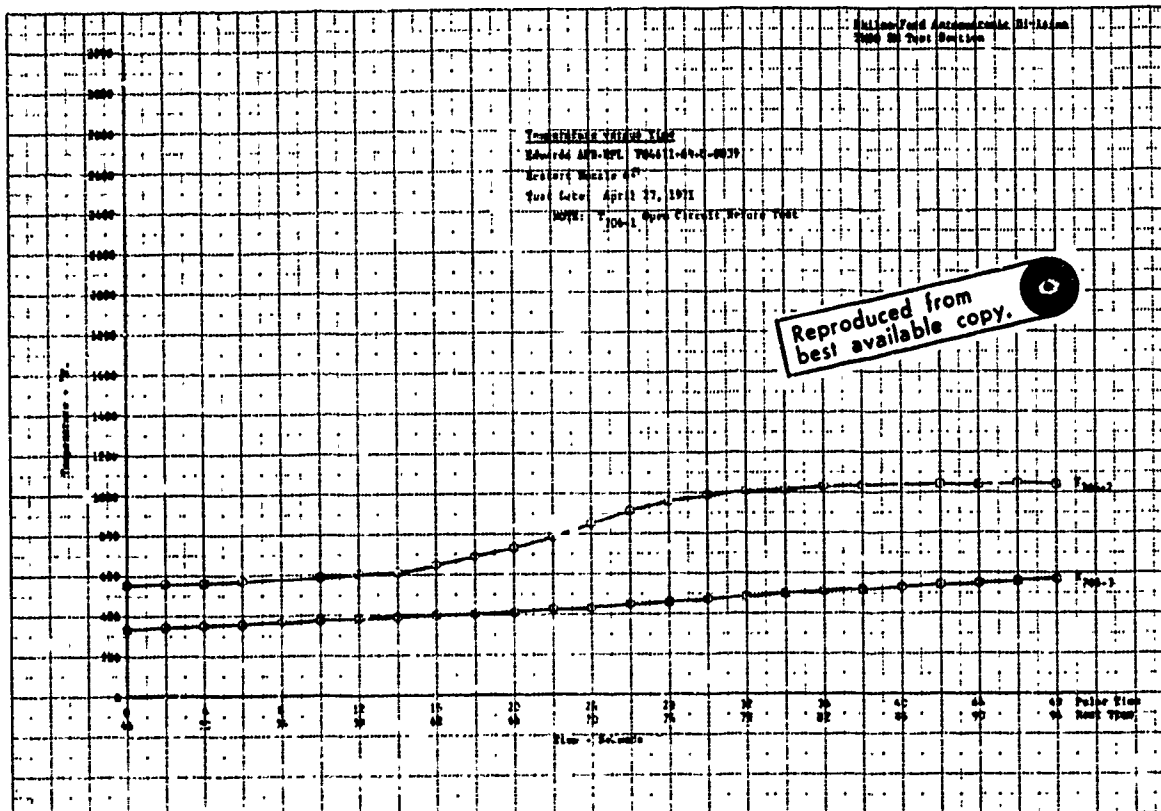
d) Pulse No. 1, Thermocoupled Fluj at $A/A^* = 4.26$

Philco Ford Aerodynamic Division
TMD 20 Test Section

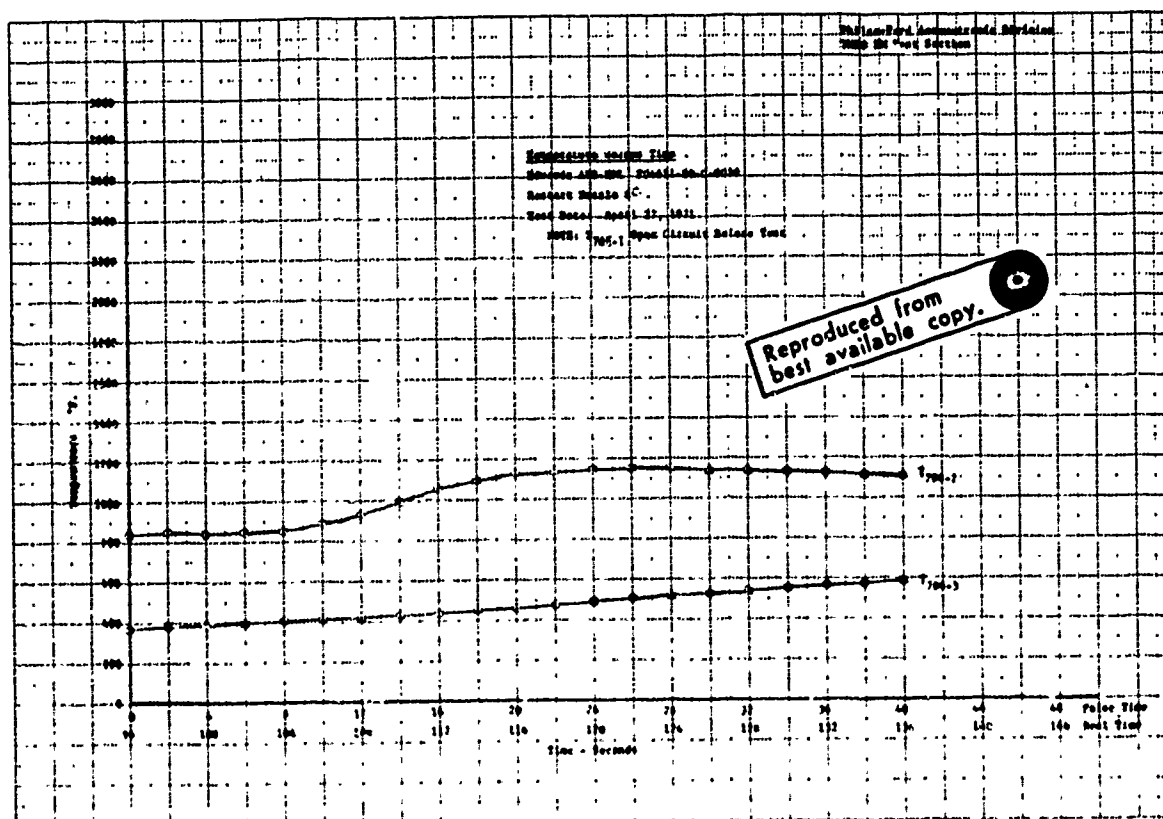


e) Pulse No. 2, Thermocoupled Fluj at $A/A^* = 4.26$
 Figure 10-1 (Continued)

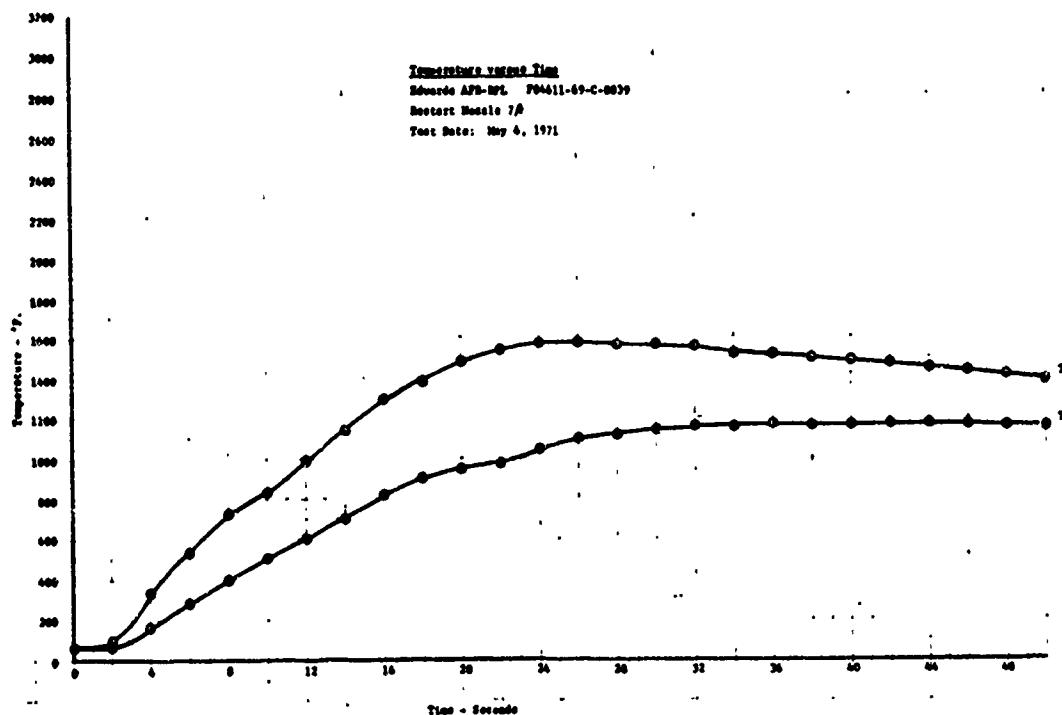




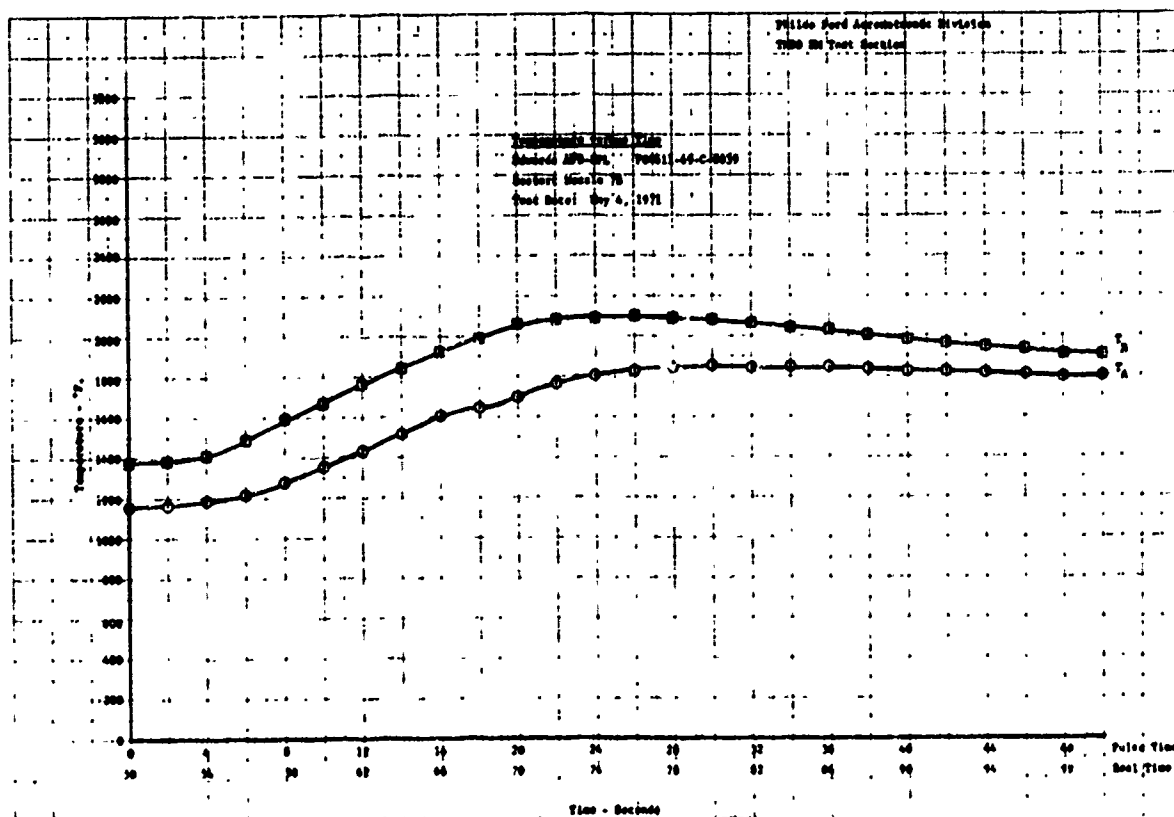
h) Pulse No. 2, Thermocoupled IL₁ at A/A* = 0.37



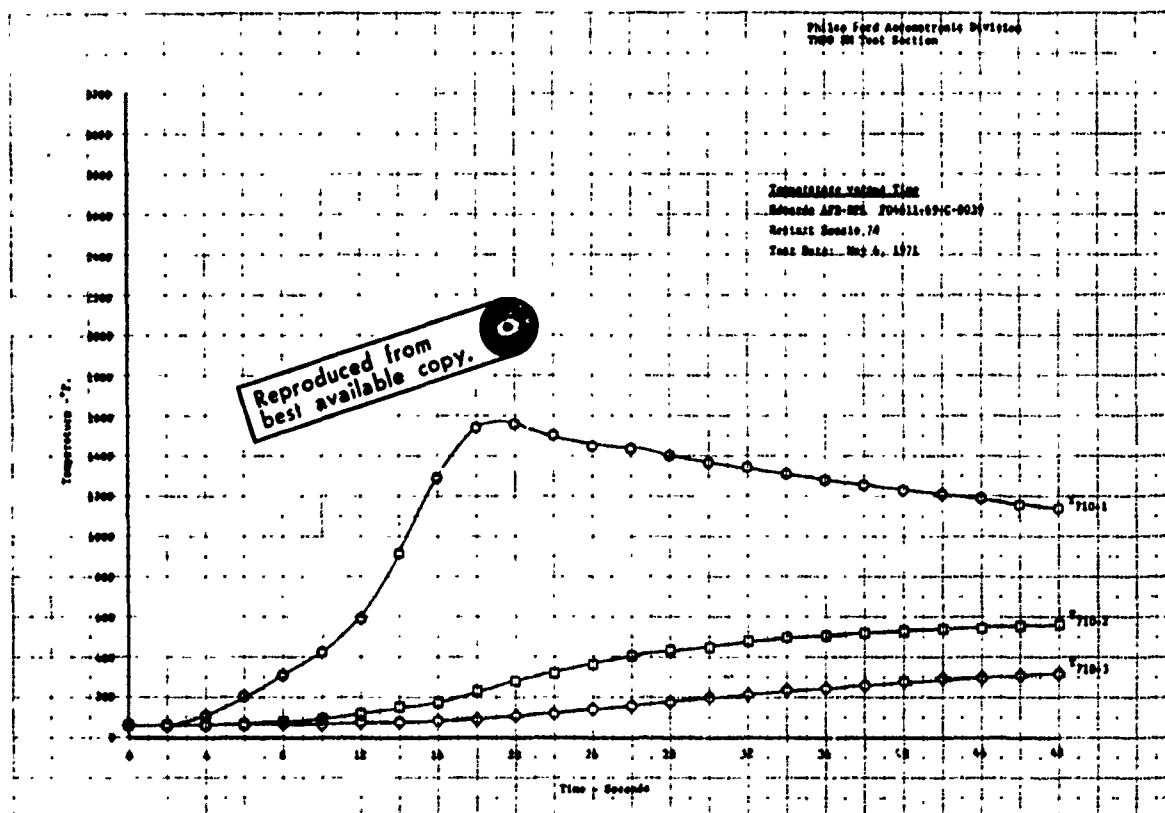
h) Pulse No. 3, Thermocoupled IL₁ at A/A* = 0.37
Pulse No. 3, IL₁ at A/A* = 0.37



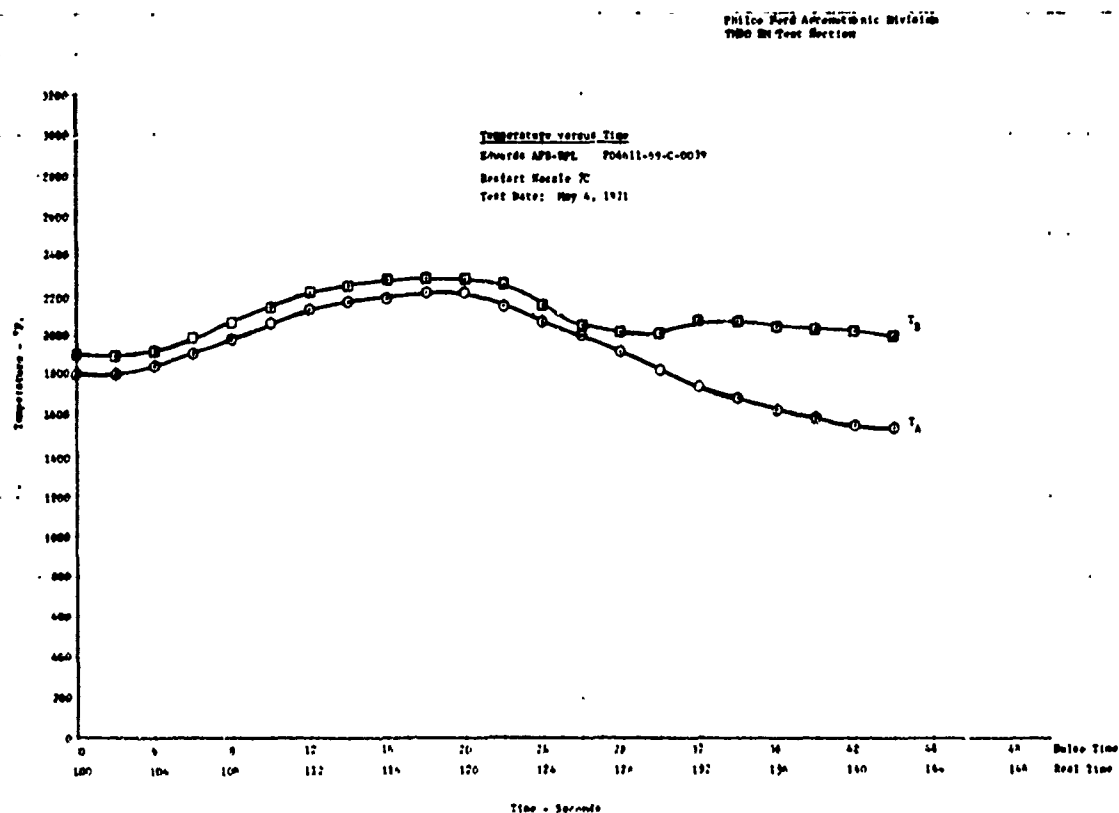
a) Pulse No. 1, Missile Throat Insert



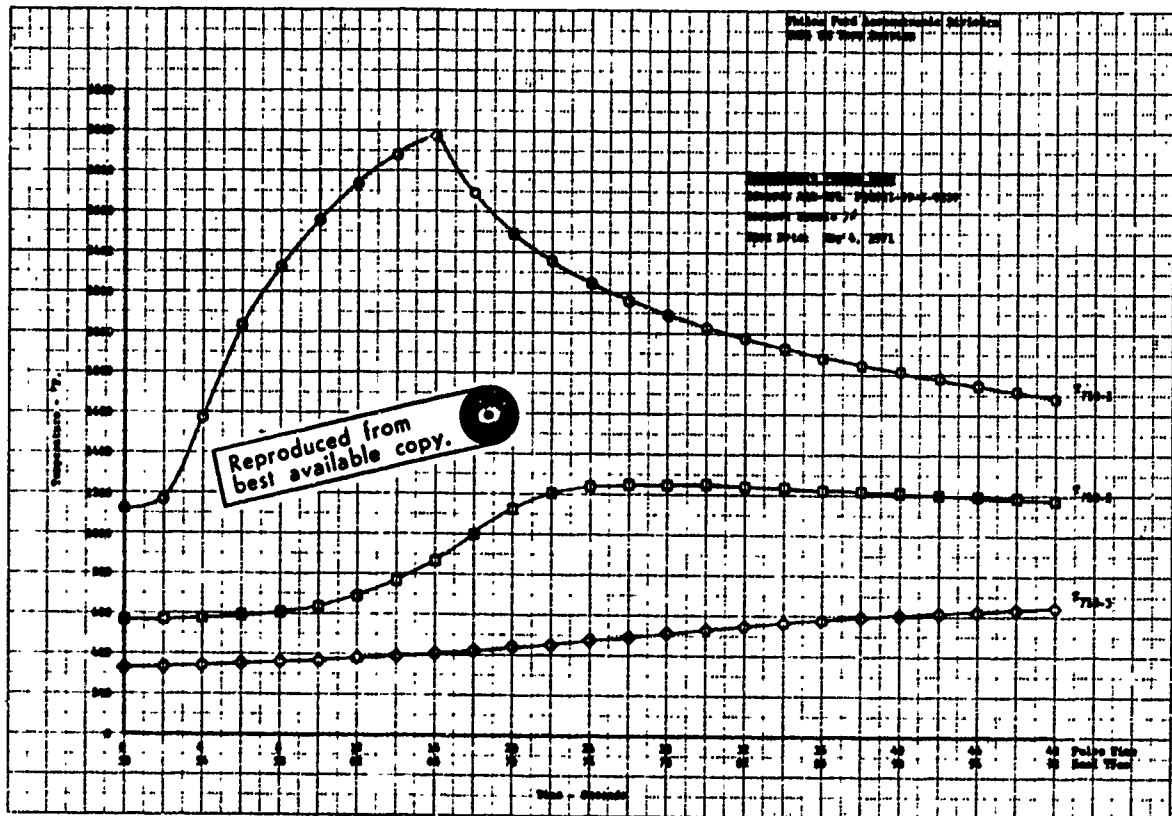
b) Pulse No. 2, Missile Throat Insert
Figure B-6. Measured In-Depth Transient Temperatures for No. 7A



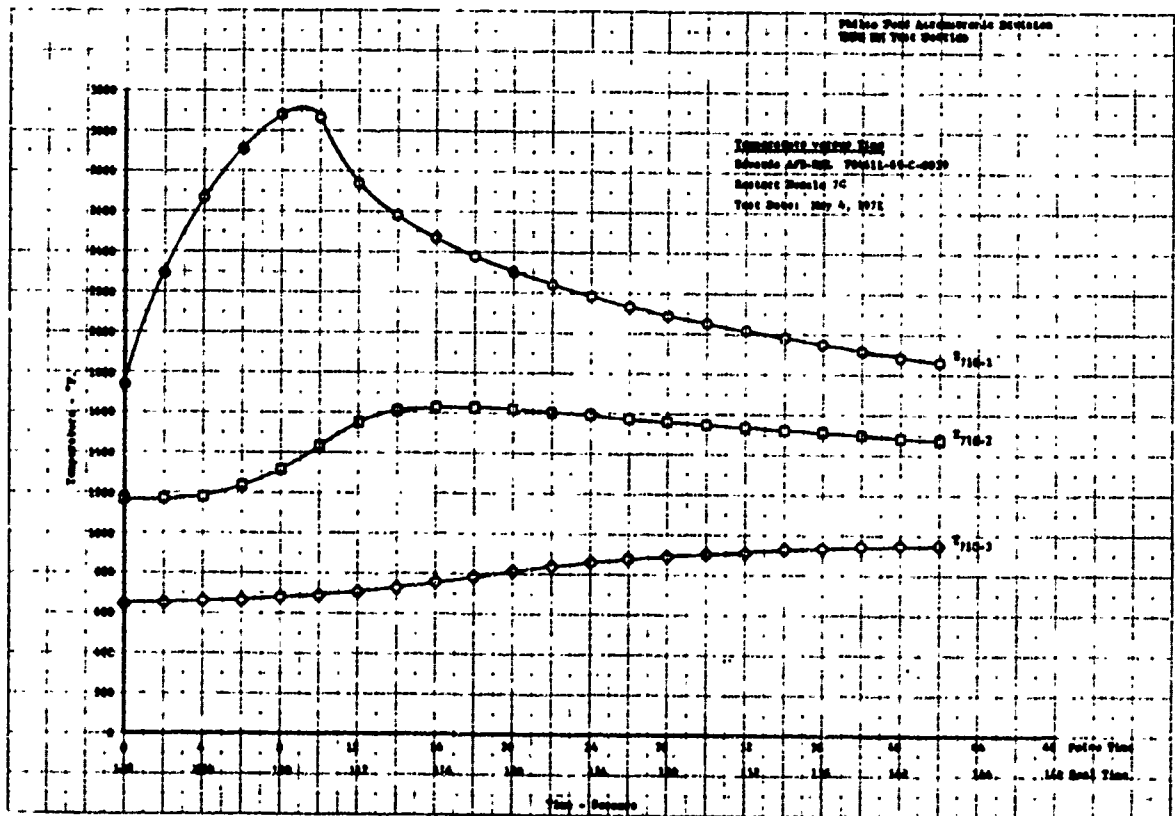
d) Pulse No. 1, Thermo-coupled Plug at A/A* = 4.78
Figure 8-4. (Continued)



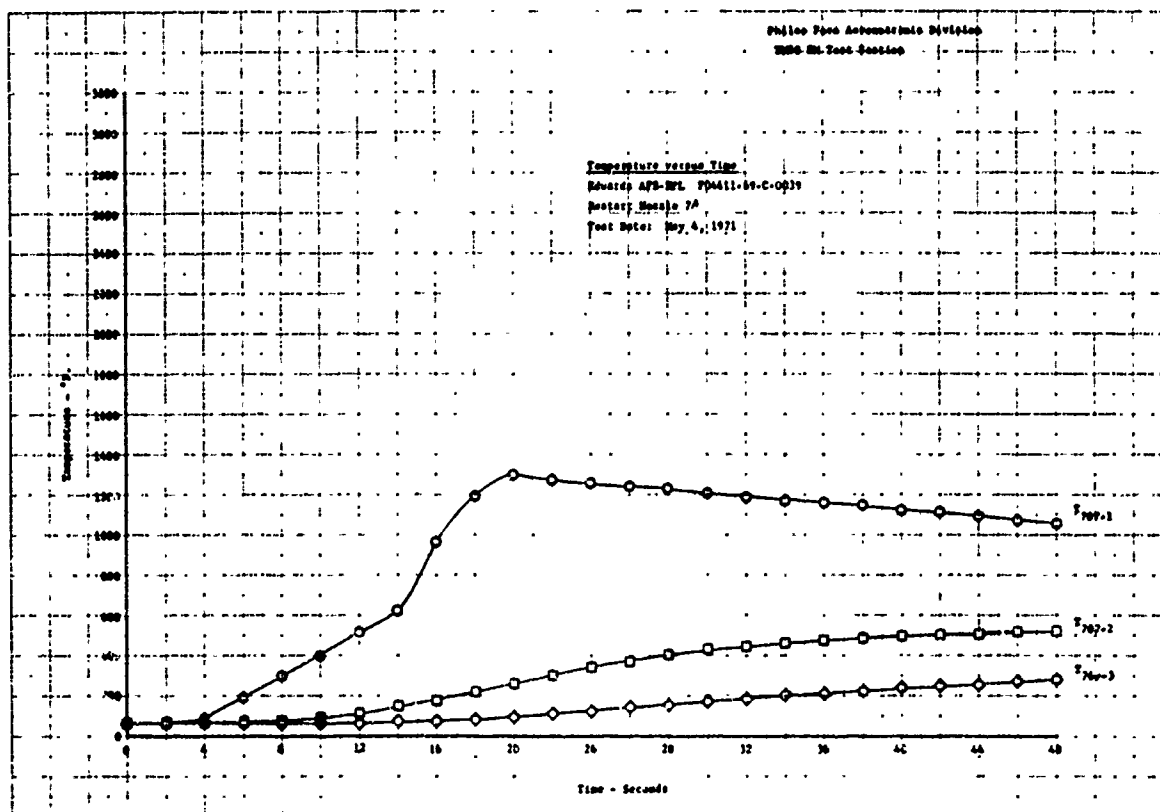
c) Pulse No. 1, Nozzle Throat Insert



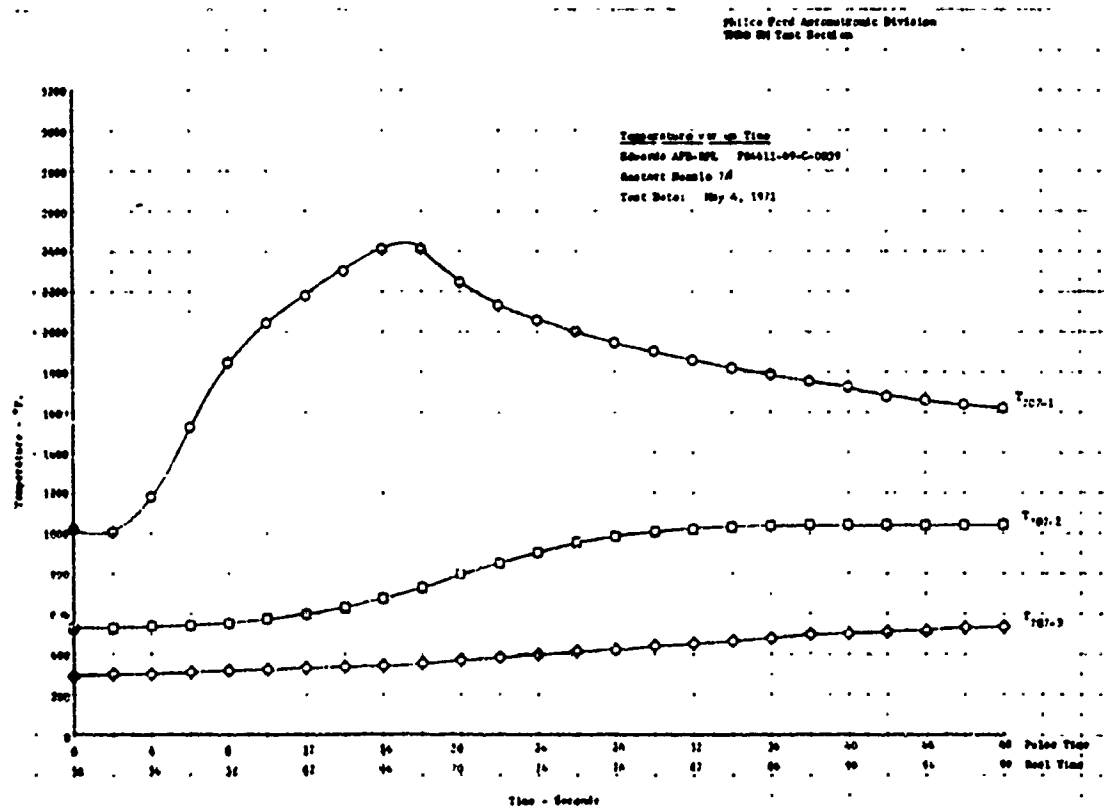
e) Pulse No. 2, Thermocoupled Plug at $A/A^* = 4.28$



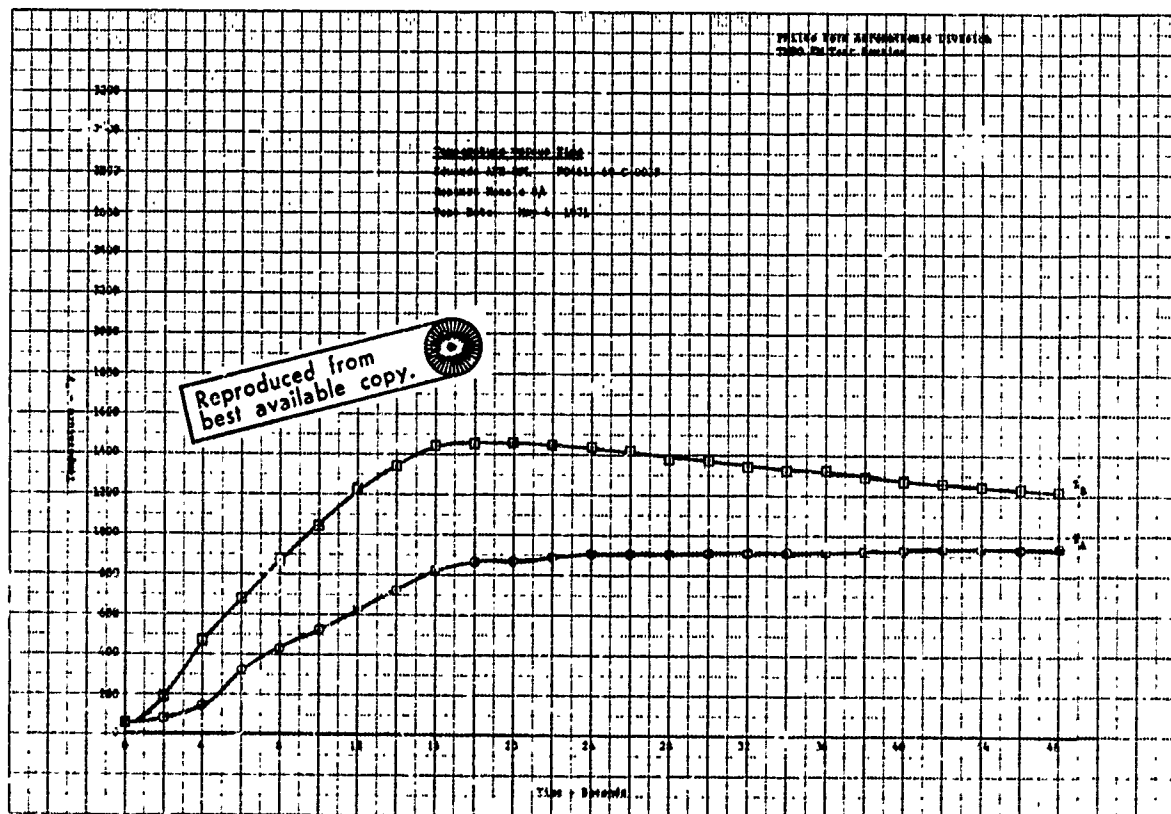
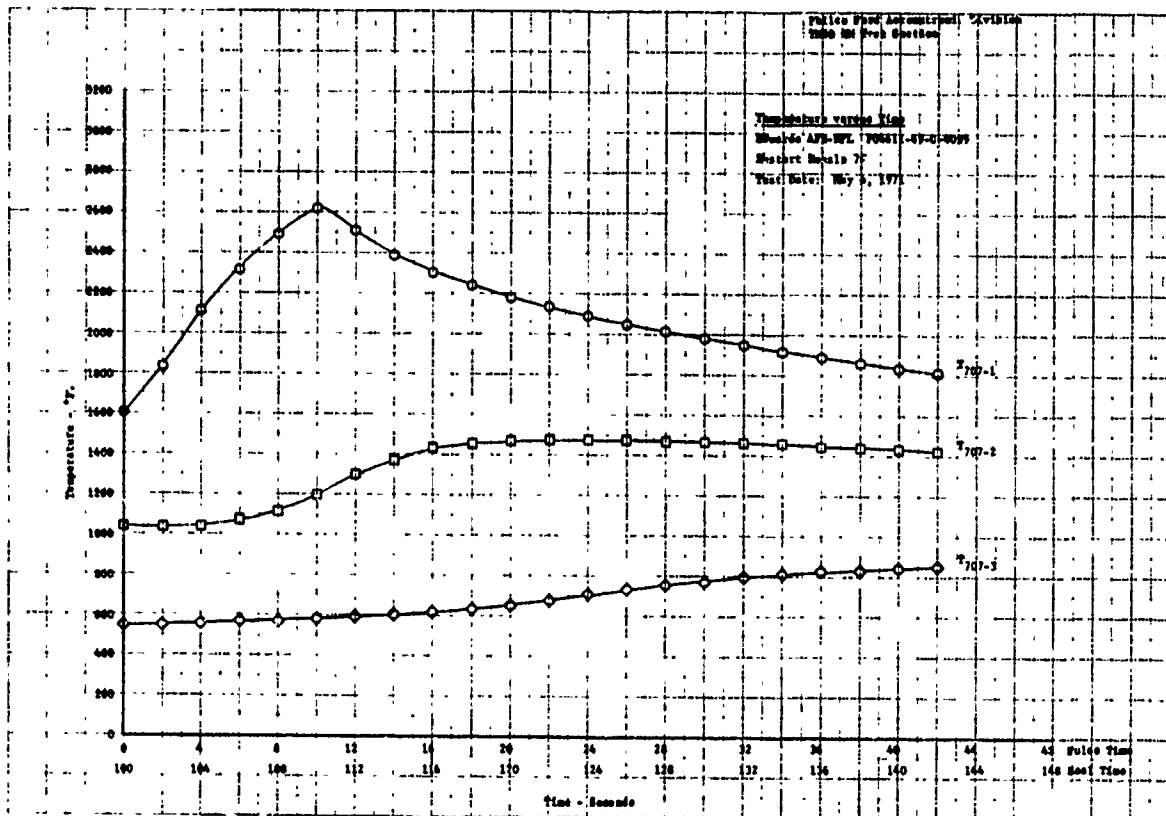
f) Pulse No. 3, Thermocoupled Plug at $A/A^* = 4.28$
Figure B-6. (Continued)

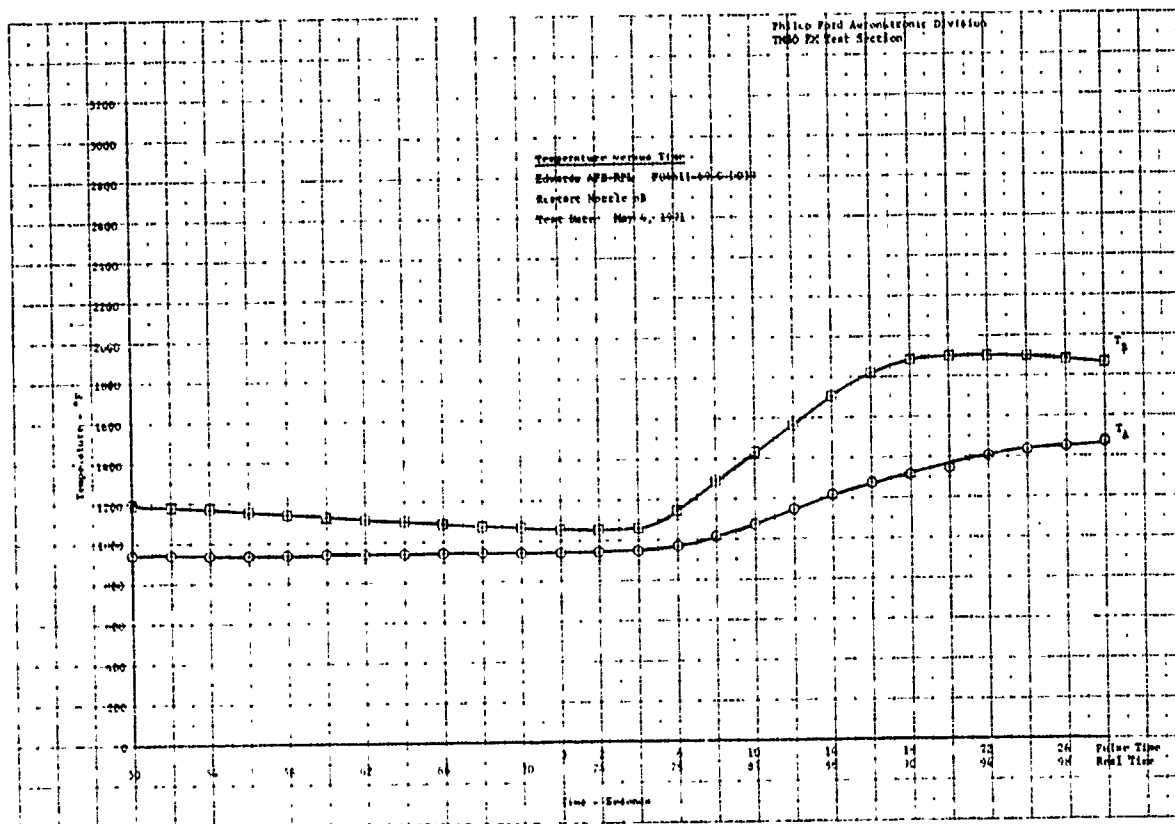


g1 Pulse No. 1, Thermocoupled Plug at A/A* = 6.62

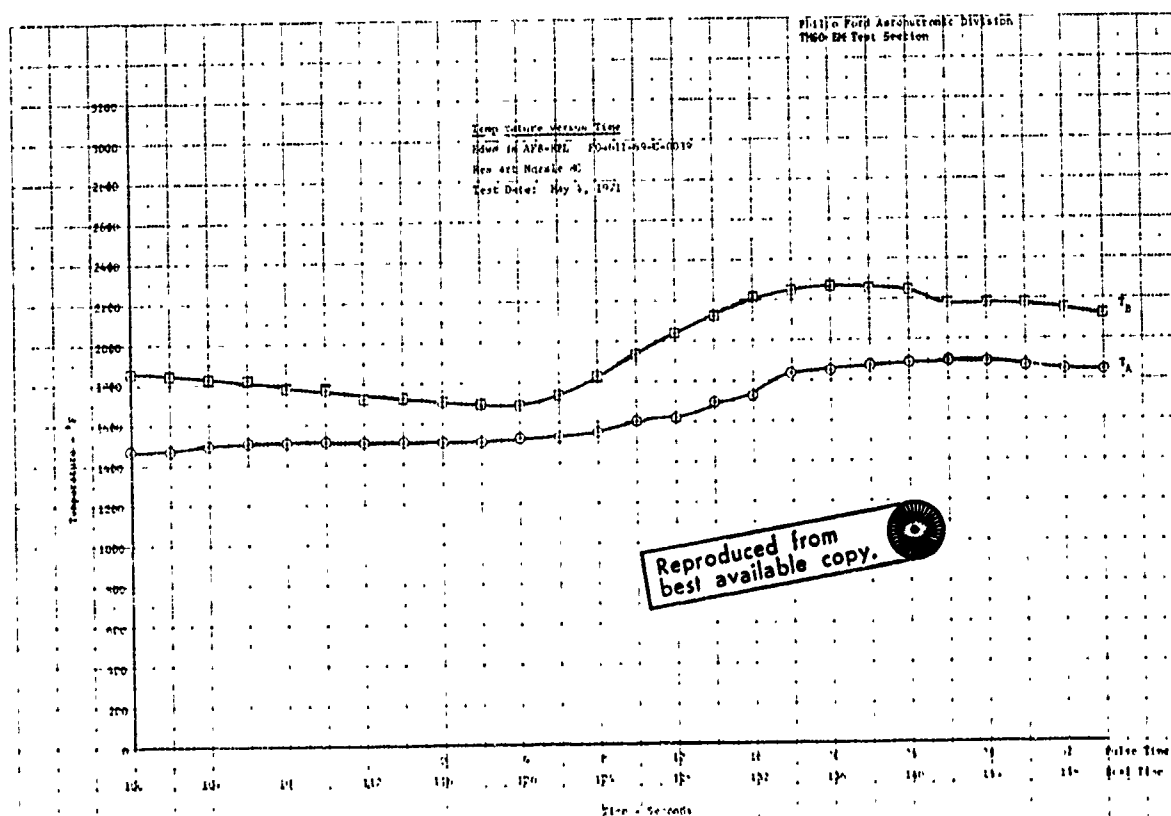


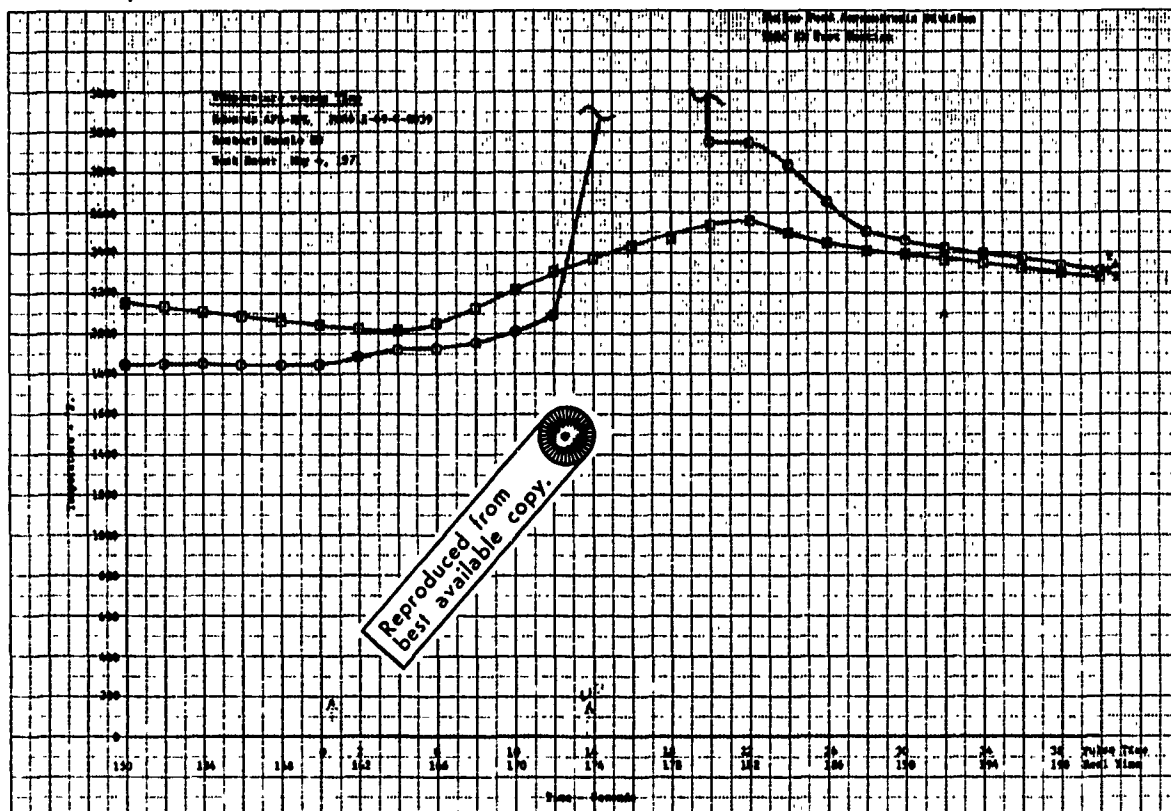
h1 Pulse No. 2, Thermocoupled Plug at A/A* = 6.62
 Figure B-2, (Continued)





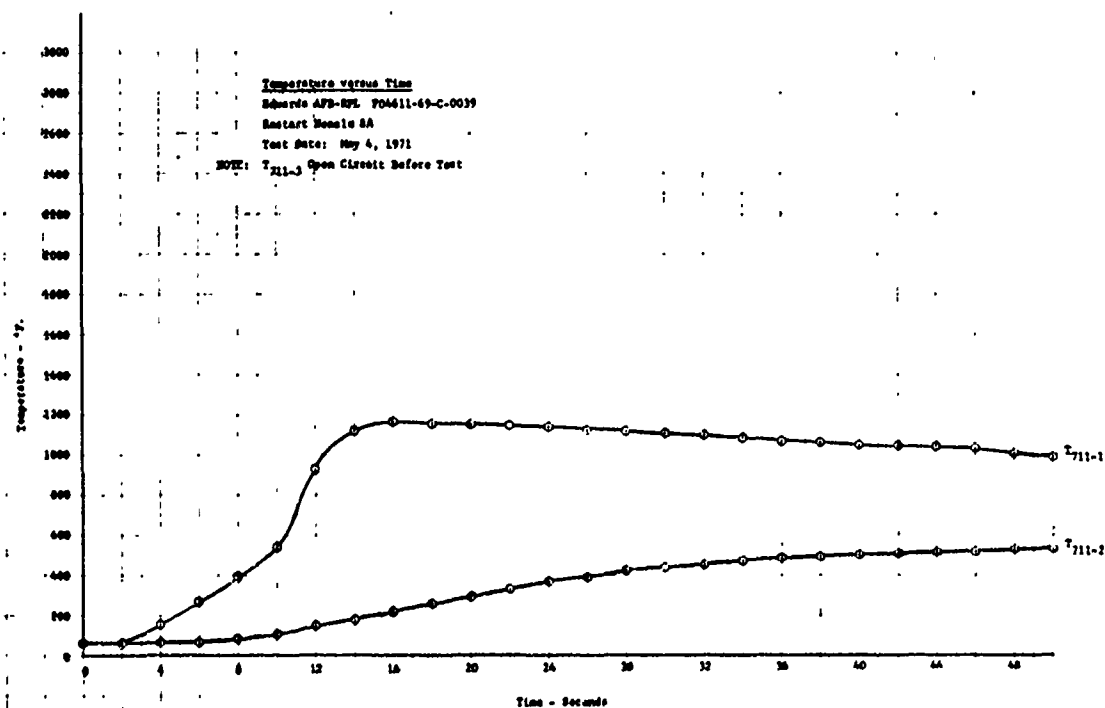
b) Pulse No. 2, Nozzle Throat Insert



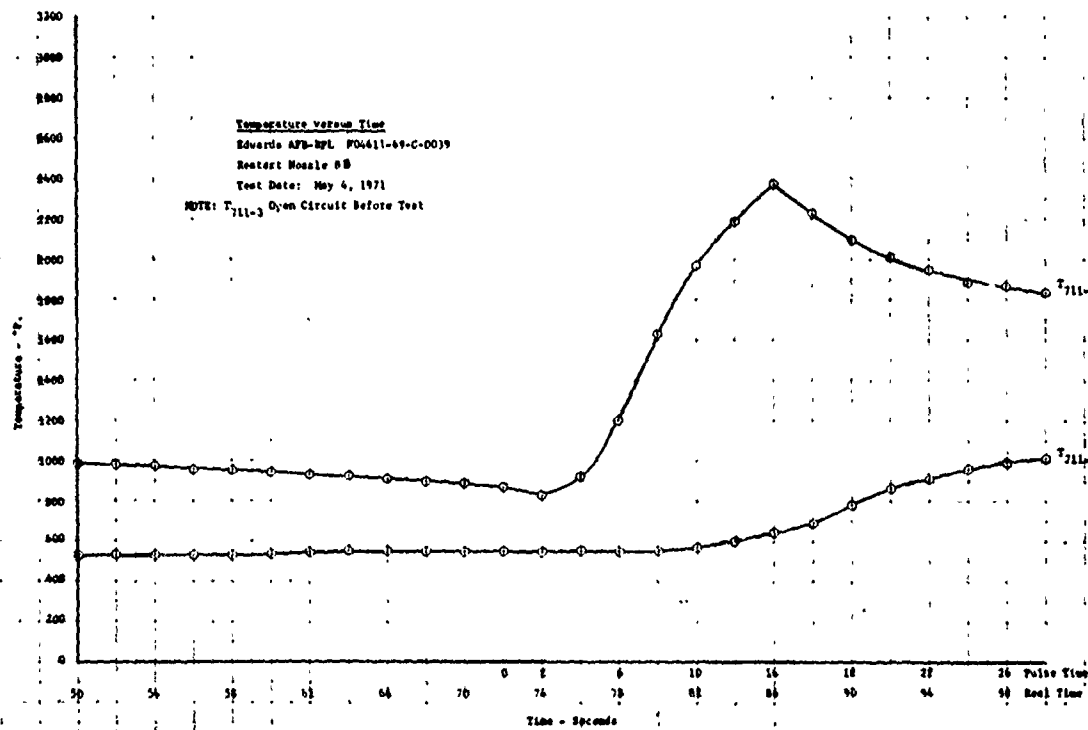


d) Pulse No. 4, Nozzle Throat Insert

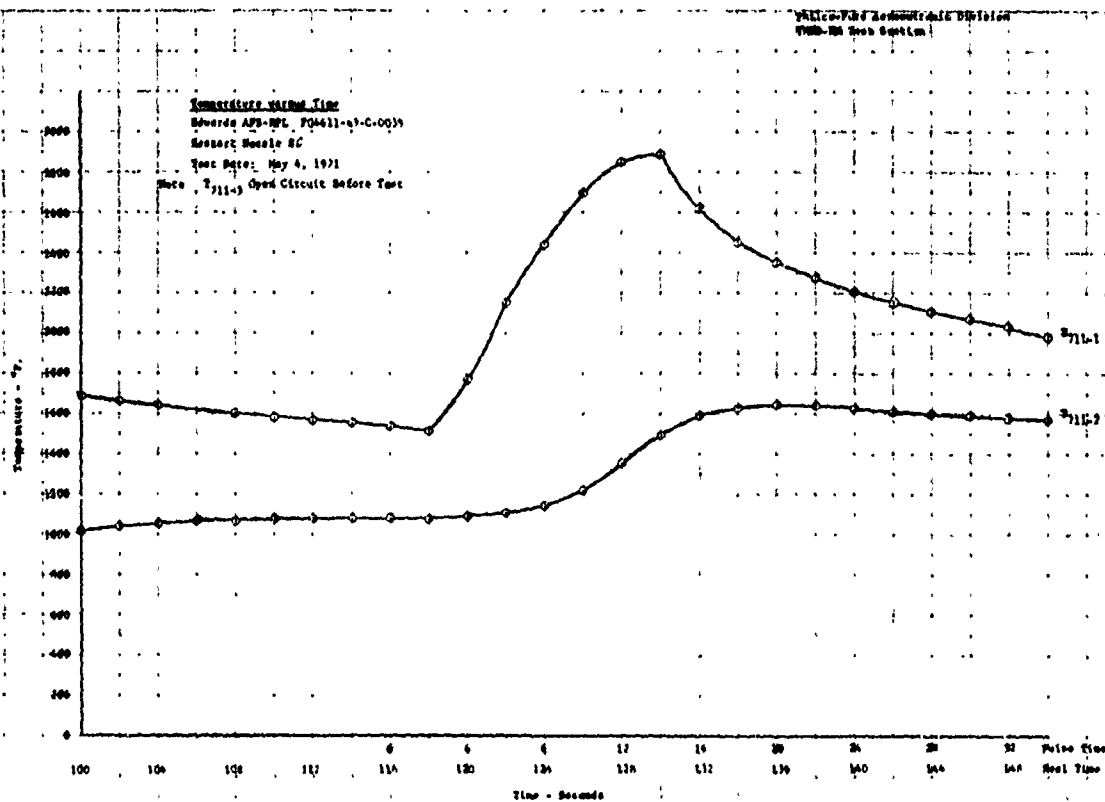
Philco-Ford Aeromagnetic Division
7700 BN Test Section



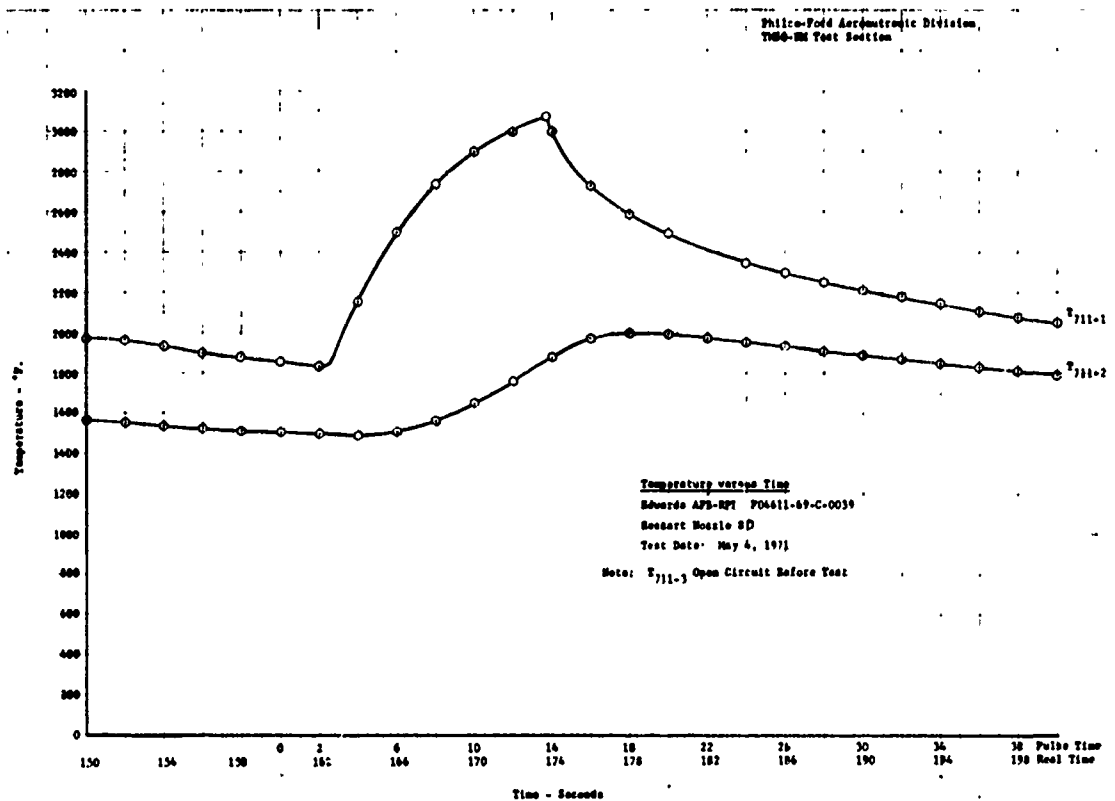
e) Pulse No. 1, Thermocoupled Plug at $A/A^* = 4.29$
Figure B-5. (Continued)



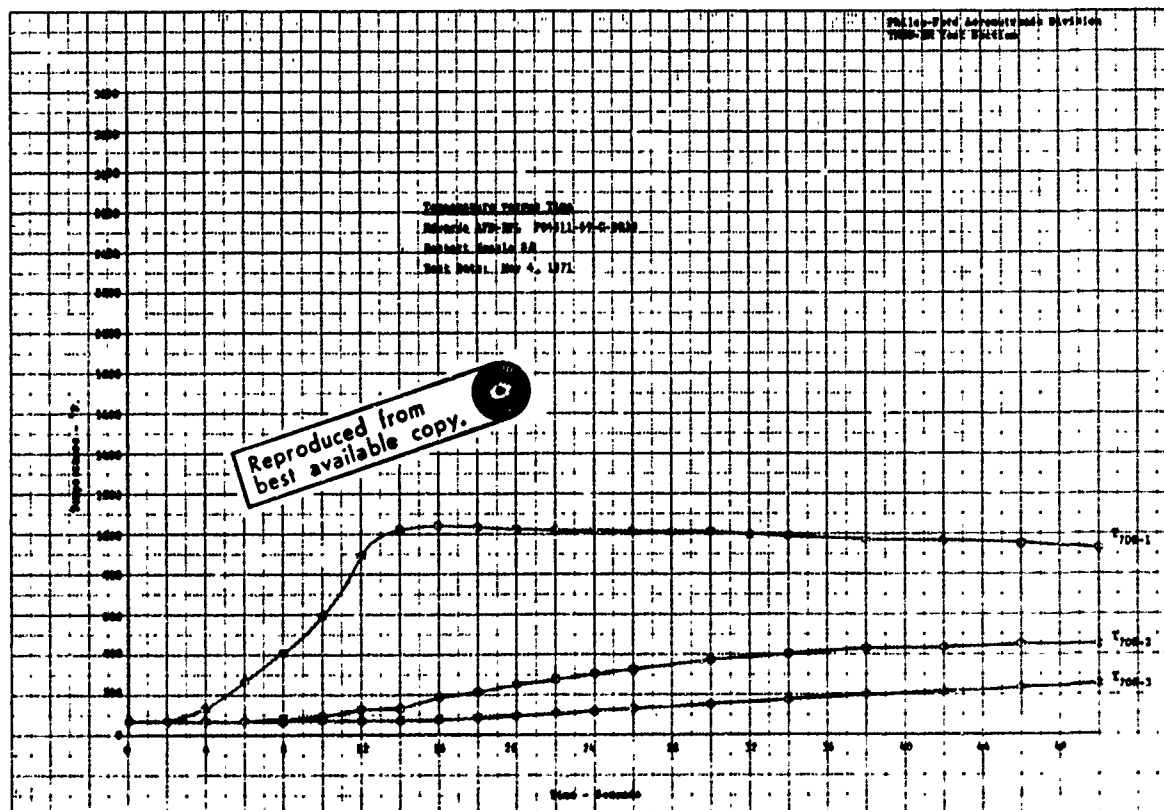
2) Pulse No. 2, Thermocoupled Plug at A/A* = 4.29



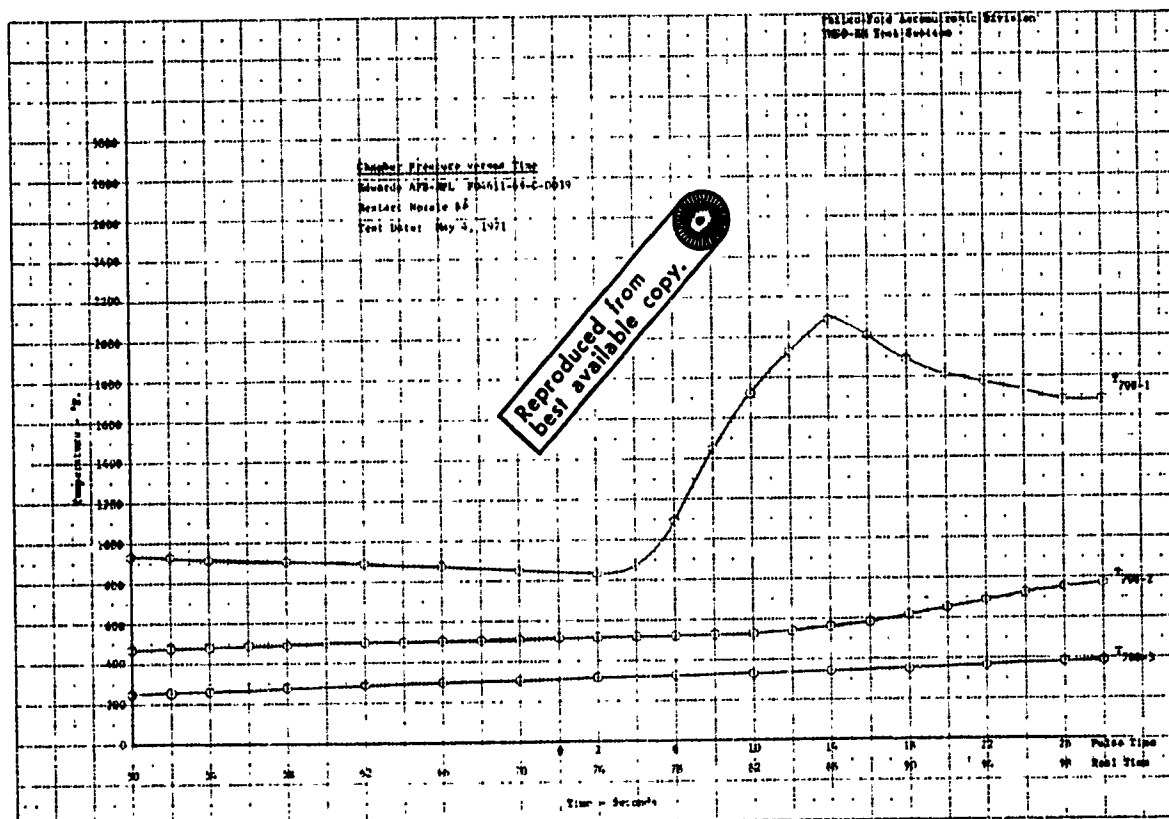
3) Pulse No. 3, Thermocoupled Plug at A/A* = 4.29
Figure B-5. (Continued)



h) Pulse No. 4, Thermocoupled Plug at $A/A^* = 4.29$

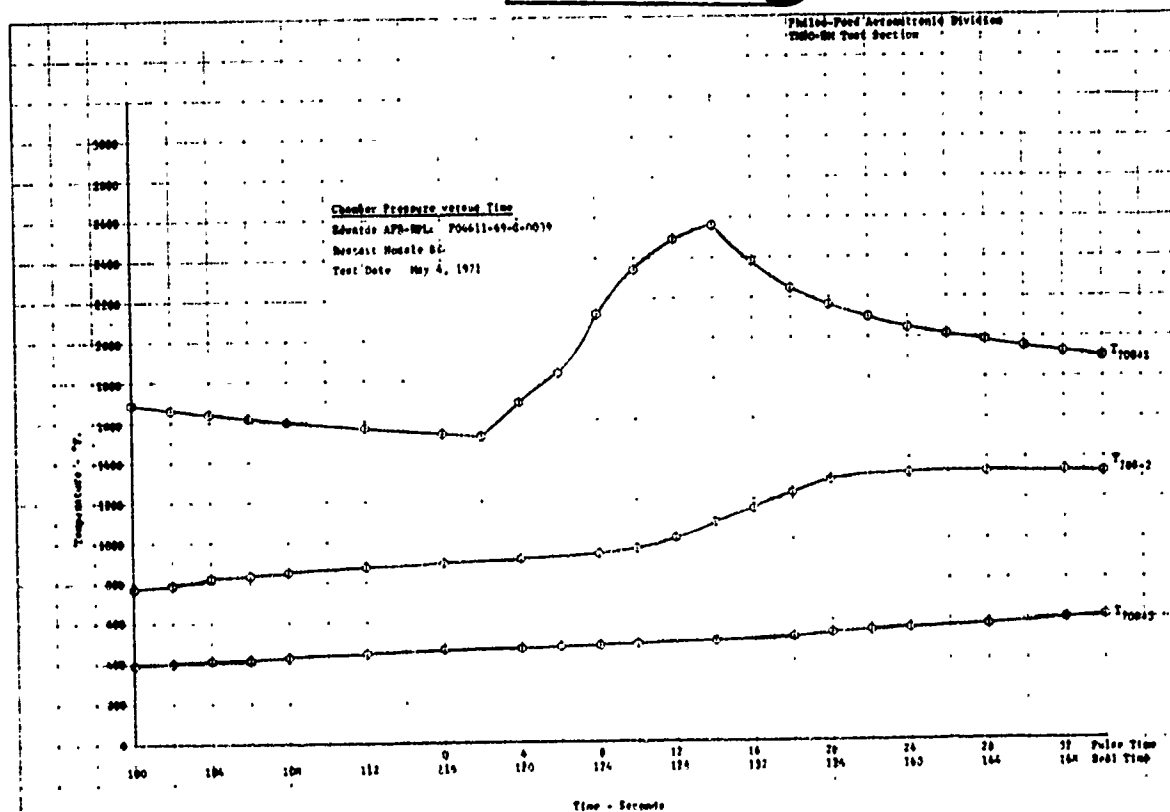


i) Pulse No. 1, Thermocoupled Plug at $A/A^* = 4.61$
Figure B-5. (Continued)

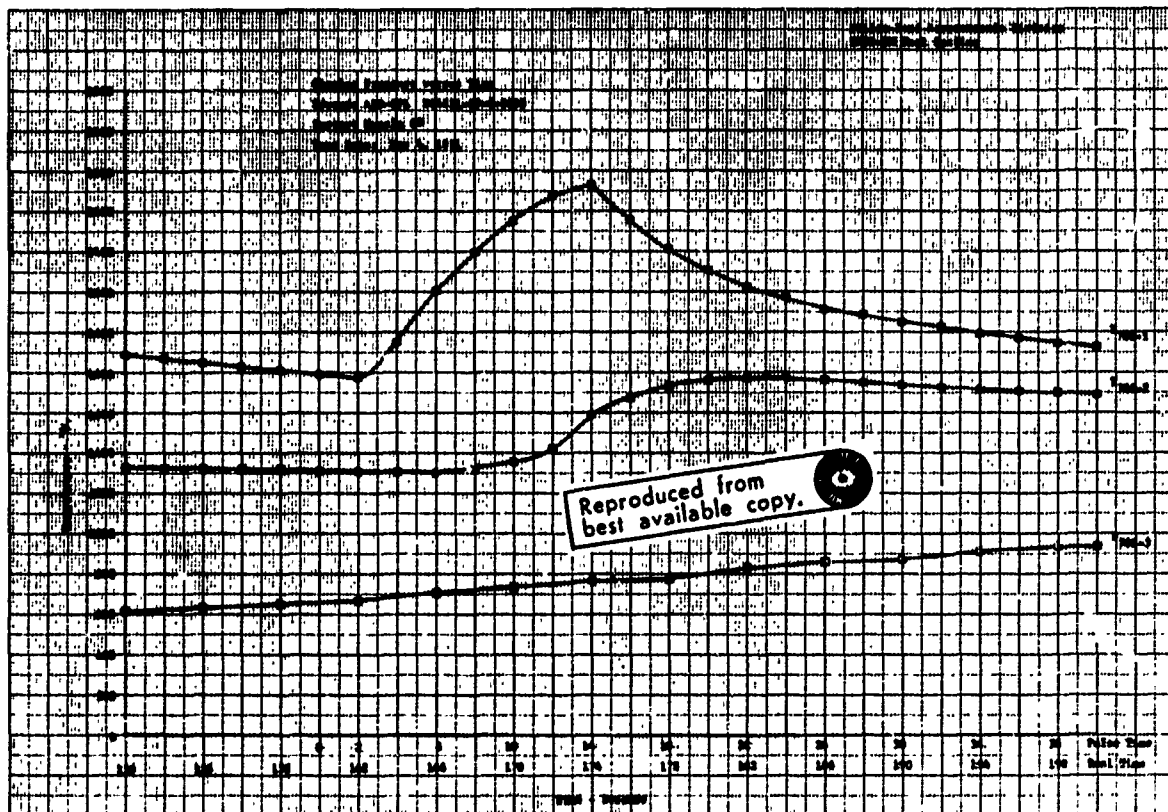


5) Pulse No. 2, Thermocoupled Flare at A² = 1.0

Reproduced from
best available copy.



6) Pulse No. 3, Thermocoupled Flare at A² = 1.0
 Figure B-5 is continued



1) Pulse No. 4, Thermocoupled Plug at $A/A^* = 0.63$
 Figure B-5. (Concluded)

APPENDIX C

DESCRIPTION OF AEROTHERM COMPUTER PROGRAMS

The following sections summarize the capabilities of the Aerotherm computer programs which were used in making the analytical predictions for this contract.

C.1 THERMOCHEMICAL STATE CODE (ACE)

C.1.1 General Capabilities

The ACE program solves for the equilibrium or kinetically controlled chemical composition for a variety of open or closed systems of arbitrary chemical composition. The ACE program is an outgrowth of the chemistry subroutines of the BLIMP program. The equations which are solved, the solution procedure which is utilized, and the program characteristics are described in Reference C-1 and are summarized in References C-4 and C-11.

The ACE program has the following major options:

A. Closed System Chemistry

- Evaluation of equilibrium (or kinetically controlled time dependent) chemical state for assigned pressure, elemental composition of up to three component mixtures, and either enthalpy, entropy, or temperature. Provision is made for readily carrying out isentropic expansion and compressions.
- Solution of normal and oblique shock relations to provide the state of the gases downstream of the shock and the isentropic stagnation state.

B. Open System Chemistry

- Calculation of surface mass balances to determine a relationship between normalized char recession rate, normalized pyrolysis gas rate, surface temperature, and pressure while considering either equilibrium between the char and gases adjacent to it or while considering selected rate-controlled surface reactions.

All of these options are formulated for completely general chemical systems. Consideration of any molecular, atomic, ionic, or condensed species requires only the inclusion of the basic thermodynamic data appropriate for

that species. These data are obtained, for example, from the JANAF Thermochemical Data Tables and include curve fit constants for entropy, specific heat, and heat of formation.

All options generate a complete state of the system, including molecular composition and thermodynamic and transport properties. The surface state option provides additional information as discussed below.

The surface state option of the ACE program contains a number of features which make it very powerful in the analysis of ablation data and thus enables the determination of the governing surface physicochemical phenomena. In the first place, one does not have to choose a priori the surface species. For example, in the case of the Apollo material, even if minor constituents are neglected, the char surface could be SiO_2^* , C^* , SiC^* , Si^* or Si_3N_4^* . The thermochemically controlling species will be discovered by ACE as part of the solution process. Secondly, it is possible to isolate species or component gas mixtures from the system or to consider rate-controlled surface reactions or surface-catalyzed homogeneous reactions. Thirdly, each condensed species can be assigned a fail temperature above which it cannot serve as the surface. This latter capability can be used to represent mechanical removal of a species or removal of a species above its melt temperature. A fourth major capability of the ACE program is that it permits consideration of unequal diffusion coefficients as well as unequal heat and mass-transfer coefficients through an application of the same approximation for binary diffusion coefficients utilized in the BLIMP program. A principal limitation of the ACE program is that the surface is considered to be homogeneous. To illustrate, the surface of the Apollo material would be predicted to be one of the species listed above, but not a mixture of two or more of these species.

The surface state options of the ACE program provide a char recession rate normalized by a mass-transfer coefficient, and other information needed to perform an energy balance on the surface of a charring ablating material, as a function of pyrolysis gas rate normalized by the same mass-transfer coefficient, surface temperature, and pressure. It thus does not by itself constitute an ablation prediction tool. In the first place, it is necessary to specify the mass-transfer coefficient and this cannot be done precisely without solving the boundary-layer equations. Secondly, the determination of surface temperature requires the solution of a surface energy balance. One procedure which is used for ablation predictions is to generate surface state solutions with the ACE program in the form of punched card output. This is then used as input to the CMA program (Option 1) which performs the surface energy balance; the operation of this coupled ablation prediction is discussed in Section C.3.1.

C.1.2 Examples of ACE Program Use

The ACE program receives daily use at Aerotherm, particularly for ablation computations. Almost all of the references to be cited during the discussions of the ablation codes also contain descriptions of uses of ACE. References C-3, C-4, C-6, C-8, C-9, C-10, C-11, C-12, and C-13-16 are of particular interest in this regard. Reference C-17 describes a materials screening task carried out entirely by ACE and covering a very wide range of materials and environments.

C.2 AEROTHERM REAL GAS ENERGY INTEGRAL BOUNDARY LAYER (ARGEIBL) COMPUTER PROGRAM

The ARGEIBL program calculates bulk transfer parameters for non-ablating laminar and/or turbulent boundary layers for axisymmetric or flat plate geometries using an energy integral method. The essence of this method is the assumption that the flat plate relationship between the local boundary layer energy thickness, δ , and the Stanton number, C_H , is valid also for flows with a streamwise pressure gradient. This assumption permits solution of the pressure gradient boundary layer energy integral equation for δ , and then employed again, permits calculation of the pressure gradient Stanton number, C_H , from δ . Appendix A of Ref. C-2 describes the theoretical background of ARGEIBL in some detail.

The ARGEIBL program can treat any real gas chemical system, provides for transition from laminar to turbulent flow, and permits axial variations in wall temperature and free stream properties. The thermodynamic and transport properties required for input to the program are generally obtained using the ACE program and the axial pressure gradient from a flow field analysis. Other required inputs include (1) boundary layer edge thermodynamic state over the surface, and (2) geometrical specification of the vehicle or body shape.

Output from the code includes boundary layer heat-transfer coefficient, and boundary layer thickness parameters (displacement and momentum) as a function of body location. The heat transfer coefficient distribution is a required input parameter to the heat conduction codes discussed subsequently. Boundary layer displacement thickness enables evaluation, in an iterative manner, of boundary layer edge entropy by considering the shock angle through which the "edge gas" has passed.¹

Reference C-3 has some descriptions of typical uses of the ARGEIBL code in ablation predictions.

¹ Experience with this technique at Aerotherm has shown near absolute convergence with only 1 iteration, i.e., a first guess and 1 more solution.

C.3 CHARRING MATERIAL ABLATION (CMA) PROGRAM

C.3.1 General Capabilities and Solution Procedure

The CMA program is a coded procedure for calculating the in-depth thermal response of a charring, ablating material. The basic physics included correspond to simple charring of the form

$$\text{plastic} \rightarrow \text{char} + \text{gas}$$

according to a three component Arrhenius rate law where

$$\rho = \Gamma(\rho_A + \rho_B) + (1-\Gamma) \rho_C \quad (C-1)$$

and

$$\left(\frac{\partial \rho}{\partial \theta} \right)_y = B_i \rho_{O_i} \left(\frac{\rho_i - \rho_{r_i}}{\rho_{O_i}} \right)^{\psi_i} \exp(-E_{a_i}/RT) \quad (C-2)$$

Usually components A and B represent constituents of the resin or plastic binder and Γ is the volume fraction of resin in the composite material, while component C represents a more refractory reinforcement. The program is often used for graphite and other non-charring materials; for such problems the decomposition reactions (C-2) are simply by-passed and the material treated as a single component ($\Gamma = 0$).

The program is an implicit, finite-difference computational procedure for computing the one-dimensional transient transport of thermal energy in a three-dimensional isotropic material which can ablate from a front surface and which can decompose in depth. Decomposition (pyrolysis) reactions are based on a three-component model. The program permits up to eight different backup materials of arbitrary thickness. The back wall of the composite material may transfer energy by convection and radiation.

The ablating surface boundary condition may take one of three forms:

OPTION 1 - Film coefficient model convection-radiation heating with coupled mass transfer, including the effects of unequal heat and mass transfer coefficients (non-unity Lewis Number) and unequal mass diffusion coefficients. Surface thermochemistry computations need not presume chemical equilibrium at the surface, as described in detail in Section C.1.1.

OPTION 2 - Specified surface temperature and surface recession rate.

OPTION 3 - Specified radiation view factor and incident radiation flux, as a function of time, for a stationary surface.

Any combination of the first three options may be used for a single computation. Option 3 is appropriate to cooldown after termination of convective heat input and is often useful in conjunction with Options 1 and 2.

The program permits the specification of a number of geometries, including plane, cylindrical or annular, and spherical. In the most general case, area may vary arbitrarily with depth.

The rear surface of the last node may be specified as insulated, or may experience convective and radiative heat transfer to a "reservoir" at a specified reservoir temperature if a rear surface convective coefficient and an emissivity are input.

Material properties such as thermal conductivity, specific heat, and emissivity are input as functions of temperature for virgin plastic and char. For partially decomposed material, the program performs an appropriate averaging on density to determine effective material properties.

The basic solution procedure is by a finite difference approach. For each time step, the decomposition relations are solved and then the in-depth energy fluxes constructed in general terms. These are then harmonized with a surface energy balance (if a surface energy balance option is being used) and the in-depth temperatures determined. New material property values are set up and the solution is ready for the next time increment.

The CMA program outputs instantaneous mass ablation rates and blowing parameters for char and pyrolysis gas, total integrated mass ablation of char and pyrolysis gas, total recession and recession rates of surface, of the char line, and of the pyrolysis line. It also outputs the surface energy flux terms, namely, the energy convected in, energy radiated in, energy reradiated out, chemical generation, and conduction away (q_{cond}). Further, it describes how the input energy of q_{cond} is "accommodated" or "partitioned" in the solid material. Part of the energy is consumed in decomposing the plastic, part is consumed in sensible enthalpy changes of the solid, and part is "picked up" by the pyrolysis gases as they pass through the char. Thermocouple and isotherm output can also be called for.

C.3.2 Some Surface Energy Balance Details

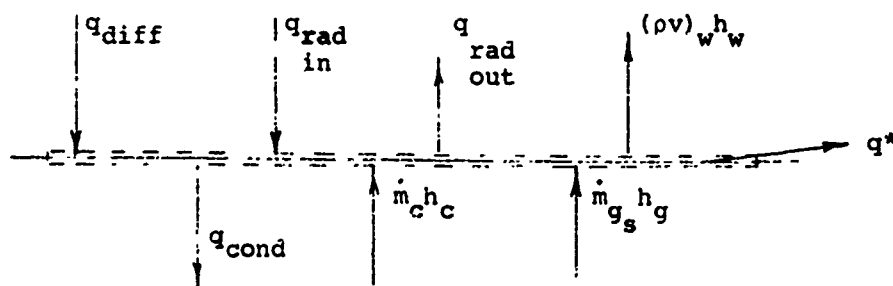
C.3.2.1 General Remarks

The most powerful and unusual feature of the CMA program is its general coupling to a thermochemical erosion energy balance at the exposed, heated surface. This coupling involves two aspects: the surface energy balance formulation itself, described in this section, and the chemical state pro-ram used to provide input information for the energy balance process, described in Section C.1.

C.3.2.1.1 Surface Energy Balance Procedure

In calculations under Option 1, the in-depth solution is coupled to a general film-coefficient boundary condition.

The following sketch shows the various energy fluxes of interest



Since the surface control volume is attached to the receding surface, there is an apparent flow of char material into the control volume and an associated energy flux $\dot{m}_c h_c$. In the case of a charring material, the pyrolysis gas flow into the control volume from below bringing an energy flux $\dot{m}_g h_g$. There is a diffusional energy flux in from the boundary layer; this is denoted q_{diff} . There is a convective energy flux away from the surface in the gross motion due to mass injection: $(pv)_w h_w$. An additional important gross motion energy flux is denoted $\sum \dot{m}_{r,l}^* h_l$ in the sketch; this term represents energy carried away in the removal, through mechanical action, of condensed phase materials. Other terms in the energy balance are the obvious radiation terms and conduction into the material.

In the course of the transient in-depth solution, which essentially provides the q_{cond} , it is necessary to evaluate all of the other surface energy balance flux terms. This in turn naturally requires some sort of surface thermochemical state solution. For this purpose it has proved expedient to prepare in advance, using suitable ablation thermochemistry codes, (such as the one described in Section C.1) a series of tables which

include all the surface mass transfer and chemical relations. The in-depth solution may then be coupled to the surface events through the surface energy balance. For example, when chemical equilibrium is achieved at the ablating surface, the development presented in Reference C-4 describes the means for obtaining the thermodynamic state of the gas at the ablating surface in terms of the pressure, and char and pyrolysis off-gas rates. In equation form,

$$\text{Thermodynamic state} = f(B'_g, B'_c, P) \quad (C-3)$$

where

$$B'_g = \frac{\dot{m}_g}{\rho_e u_e C_M} \quad (\text{normalized pyrolysis off-gas rate})$$

$$B'_c = \frac{\dot{m}_c}{\rho_e u_e C_M} \quad (\text{normalized char recession rate})$$

P = boundary layer edge pressure

The thermodynamic state includes definition of surface temperature and gas molecular composition. This, in turn, enables evaluation of the various quantities appearing in the boundary layer driving potential for heat and mass transfer (Reference C-4). Tables representing solutions to the functional relationship represented by Equation (A-3) are generated for a complete map covering the range of B'_g , B'_c , and P , of interest. These tables are generated by the ACE chemical state program described in Section C.1.

As an example of this procedure, suppose a table is prepared which, for a parametric array of dimensionless char erosion rates (B'_c), dimensionless pyrolysis off-gas rates (B'_g), and pressure, presents the relevant ablating surface temperature and requisite boundary layer composition and enthalpy quantities. During each time step in the course of the in-depth solution the program generates a pyrolysis gas rate B'_g and computes the rate at which energy is conducted into the material from the surface. With B'_g and the pressure known, the input parametric tables then serve to define that B'_c which yields temperature and enthalpy quantities which provide a balanced, harmonized set of energy fluxes at the surface.

It is worth noting that the coupling between one in-depth solution (performed by the CMA program) and the surface thermochemistry solution (performed by the ACE program) yields a very general and powerful ablation thermochemical data to be extended to many geometries and flow fields at

no additional cost, since the surface thermochemical solution quantities are normalized on the transfer coefficient. Secondly and more importantly, the ACE program is general enough in its thermochemical solution procedures to handle any combination of environment and ablator. Thus, the CMA plus ACE scheme can treat complex chemical systems as easily (from our standpoint) as the simple carbon-air system. In practice, these programs have been used with great success as heatshield and rocket nozzle design and analysis tools for a wide variety of materials (including graphite, carbon phenolic, graphite phenolic, silica phenolic, tungsten, tantalum, ice, and teflon) exposed to varied environments (including aluminized solid propellants; beryllium and solid propellants; liquid propellants such as H_2-O_2 , $N_2O_4-N_2H_4$ /UDMH, $OF_2-B_2H_6$, and flox-methane; various hybrid propellants; as well as air and numerous simple test gases such as Ar, He and N_2 . Furthermore, ACE will automatically discover the chemical nature of the exposed surface (it may be a non-obvious species containing elements from the environment as well as from the ablating material), and can account for any number of kinetically controlled heterogeneous reactions. These two features are very important ones for graphite ablation analysis. Graphites are sometimes "loaded" with "additives" to form erosion resistant coatings on the heated surface (as described, for example, in Reference A-5). ACE will predict the existence of these coatings and the resultant changes in erosion resistance. Kinetic control is occasionally of interest for graphite also. ACE will also include the effects of unequal mass diffusion coefficients for the various boundary layer species.

ACE can also automatically include simple melting of surface species, detecting surface species and allowing them to run off at their melting points, accounting for the energy events correctly in the process ($\sum m_{r_i}^* h_{f_i}$ in the sketch preceding). Thus one form of thermomechanical ablation (that occurring as a total loss of strength at a given temperature for a given species) is automatically accounted for in CMA through the ACE solution. Other forms of mechanical removal can be directly accounted for in CMA. This task is particularly simple for a non-charring material such as graphite since the mechanical failure rate does not in fact change the surface energy balance; the failing mass rate both enters and leaves the surface energy balance control volume at the same temperature. Thus the thermochemical corrosion rate can be determined in the usual manner and the surface temperature calculated in the process. Following this, the thermomechanical erosion rate can be determined using whatever procedure seems best (such as with empirical correlations) and the total recession rate determined as the sum of thermochemical and thermomechanical events.

C.3.3 Uses of the CMA Program

The CMA program has received extensive use in the Option 2 (assigned surface temperature and recession rate) mode to match in-depth thermocouple data and, in doing so, to discover in-depth properties such as thermal conductivity. References C-6 and C-7 provide examples of such use. The CMA program has also been very extensively used in its Option 1 mode as an ablation predictor; References C-3, C-6, C-8, C-9, C-10 provide a few descriptions of the many uses of the program.

C.4 THE AXI-SYMMETRIX TRANSIENT HEATING AND MATERIAL ABLATION ABLATION PROGRAM (ASTHMA)

C.4.1 Introduction

For strongly two dimensional ablation problems such as nose tips and certain rocket nozzles, 1-D calculations of the kind performed by the CMA program described above must be supplemented by two space dimension ablation calculations. The ASTHMA program is a suitable 2-D code for this purpose. It accounts only for non-charring materials such as graphite; otherwise it is as general in all respects as the CMA program described above. In particular, the code has the same very general thermochemical erosion boundary condition with appropriately general space dependent input of transfer coefficient, pressure, and boundary layer edge or recovery enthalpy so that 2-D thermochemical erosion may be realistically predicted. The following sections describe the ASTHMA code.

C.4.2 General Capabilities

The ASTHMA program computes the transient temperature response within a two-dimensional axisymmetric non-charring material. It accounts for two-dimensional surface recession, and allows for anisotropic in-depth thermal conduction. Input consists of geometry specification (in terms of finite difference grid), material properties tables, and heated surface boundary condition information as a function of time and surface location. The ASTHMA program has the same three boundary condition options as the CMA code described above:

OPTION 1 - Film coefficient model convection-radiation heating with coupled mass transfer, including the effects of unequal heat and mass transfer coefficients (non-unity Lewis number) and unequal mass diffusion coefficients. Surface thermochemistry computations need not presume chemical equilibrium at the surface.

OPTION 2 - Specified surface temperature and surface recession rate.

OPTION 3 - Specified radiation view factor and incident radiation flux, as functions of time, for a stationary surface.

Any combination of the first three options may be used during the problem history of any surface point.

Program output includes the history of the in-depth temperature field, the history of the surface point locations (recession and shape history) and surface temperatures, and the history of the local surface energy and mass fluxes.

C.4.3 The Surface Energy Balance

As in the case of the CMA program, the most powerful and unusual feature of ASTHMA is its general coupling to a thermochemical erosion energy balance at the heated surface. This energy balance is essentially the same as used in the CMA code; it is described in detail in Sections C.3.2 above. Here it will sufficient to emphasize that:

1. This procedure will treat any material exposed to any environment.
2. It accounts for unequal diffusion coefficients, non-unity Lewis number, departures from chemical equilibrium, and mechanical ablation.
3. The procedure will discover any chemical surface coatings naturally formed; this is important, for example, for loaded graphites.
4. Boundary condition input (recovery enthalpy, transfer coefficient, pressure, and radiation flux) may be made a function of surface location.

C.4.4 Uses of the ASTHMA Code

The ASTHMA code is described in References C-13 and C-14, where graphite rocket nozzle throat insert ablation studies are briefly described. Reference C-15 gives more detail on these studies. Reference C-16 describes numerous applications of ASTHMA to graphite nosetip ablation predictions.

REFERENCES

- C-1 Kendall, R. M.: A General Approach to the Thermochemical Solution of Mixed Equilibrium-Nonequilibrium, Homogeneous or Heterogeneous Systems. Aerotherm Corporation Report No. 66-7, Part V, March 14, 1967 (also NASA CR 1064).
- C-2 McCuen, P. A., Schaefer, J. W., Lundberg, R. E., and Kendall, R. M.: A Study of Solid-Propellant Rocket Motor Exposed Materials Behavior. Vidya Division, Itek Corporation, Palo Alto, California, AFRPL-65-33 (AD 462 331), February 26, 1965.
- C- ial
ain
- C-4 Kendall, R. M., Rindal, R. A., and Bartlett, E. P.: A Multicomponent Boundary Layer Chemically Coupled to an Ablating Surface. AIAA Journal, Vol. 5, No. 6, June 1967, pp. 1063-1071.
- C-5 Buckley, J. D.: Static, Subsonic, and Supersonic Oxidation of JT Graphite Composites. NASA TN D-4231, October 1967
- C-6 Rindal, R. A., Clark, K. J., Moyer, C. B., and Flood, D. T.: Experimental Analysis of Ablative Material Response in Liquid Propellant Rocket Engine, Aerotherm Corporation, Palo Alto, California, NASA CR-72301, September 1, 1967.
- C-7 Baker, D. L., Wool, M. R., and Schaefer, J. W.: A Dynamic Technique for Determining the Thermal Conductivity of Charring Materials, Eighth Conference on Thermal Conductivity, October 7-11, 1968, Thermophysical Properties Research Center, West Lafayette, Indiana.
- C-8 Spiegel, J. M., Wolf, F., and Zeh, D. W.: Simulation of Venus Atmospheric Entry by Earth Reentry, AIAA Paper No. 68-1148 (AIAA Entry Vehicle Systems and Technology Meeting, Williamsburg, Virginia, December 3-5, 1968).
- C-9 Bartlett, E. P., Anderson, L. W., and Curry, D. M.: An Evaluation of Ablation Mechanisms for the Apollo Heat Shield Material, Paper 69-98, AIAA Seventh Aerospace Sciences Meeting, New York, January 20-22, 1969.
- C-10 Moyer, C. B. and Rindal, R. A.: Finite Difference Solution for the In-Depth Response of Charring Materials Considering Surface Chemical and Energy Balances. Aerotherm Corporation Final Report 66-7, Part II, March 14, 1967 (also NASA CR-1061, June 1968).
- C-11 Kendall, R. M., et. al.: An Analysis of the Coupled Chemically Reacting Boundary Layer and Charring Ablator. Aerotherm Corporation Final Report No. 66-7, Part I, March 14, 1967 (also NASA CR 1060).
- C-12 Bartlett, E. P. and Anderson, L. W.: An Evaluation of Ablation Mechanisms for the Apollo Heat Shield Material. Aerotherm Corporation Final Report No. 68-38, Part II, October 15, 1968.

REFERENCES (Concluded)

- C-13 Moyer, C. B.: Axi-Symmetric Transient Heating and Material Ablative Program (ASTHMA), Description and User's Manual, Aerotherm Corporation, Mountain View, California, Report No. 68-27, January 15, 1968.
- C-14 Moyer, C. B.: Two Dimensional Transient Heating and Surface Thermochemistry Computer Programs, Atlantic Research Corporation, Alexandria, Virginia, AFRPL-TR-68-116, Vol. I, July 5, 1968.
- C-15
- C-16 Powars, C. A., Rindal, R. A., and Rodriguez, D. A.: A Detailed Thermal and Structural Analysis of Graphite Models Tested in Arc Heated Air. Aerotherm Corporation Final Report. Sandia Laboratories Contractor Report (to be published).
- C-17 Clark, K. J., Rindal, R. A., Inouye, L.M., and Kendall, R. M., Thermochemical Ablation of Rocket Nozzle Insert Materials, Aerotherm Corporation, Mountain View, California, NASA CR-66632, February 15, 1968.

UNCLASSIFIED

Security Classification

DOCUMENT CONTROL DATA - R & D

(Security classification of title, body of abstract and indexing annotation must be entered when the overall report is classified)

1. ORIGINATING ACTIVITY (Corporate author) Aerotherm Division of Acurex Corporation 485 Clyde Avenue Mountain View, California		2a. REPORT SECURITY CLASSIFICATION UNCLASSIFIED	
		2b. GROUP N/A	
3. REPORT TITLE Material Performance of Carbon Phenolic Ablators and Pyrolytic Graphite Coatings in Nozzles Subjected to Multiple Pulse Duty Cycles			
4. DESCRIPTIVE NOTES (Type of report and inclusive dates) Final Report			
5. AUTHOR(S) (First name, middle initial, last name) Mitchell R. Wool Duane L. Baker Andrew J. Murphy			
6. REPORT DATE October 1971		7a. TOTAL NO OF PAGES	7b. NO. OF REFS 28
8a. CONTRACT OR GRANT NO. F04611-70-C-0019		8b. ORIGINATOR'S REPORT NUMBER(S) Aerotherm Report No. 71-43	
b. PROJECT NO.		9a. OTHER REPORT NO(S) (Any other numbers that may be assigned to this report) AFRPL-TR-71-130	
c.			
d.			
<div style="border: 1px solid black; padding: 5px; width: fit-content; margin: 10px auto;"> THIS DOCUMENT APPROVED FOR PUBLICATION & UNLIMITED DISTRIBUTION </div>			
10. DISTRIBUTION STATEMENT This document is subject to special export controls and each transmittal to foreign governments or foreign nationals may be made only with prior approval of AFRPL (RFOR-STINFO), Edwards, California, 93522.			
11. SUPPLEMENTARY NOTES		12. SPONSORING MILITARY ACTIVITY Air Force Rocket Propulsion Laboratory Edwards Air Force Base, California	
13. ABSTRACT Measurements and analysis of the thermal and ablative response of five multiple pulse duty cycle rocket nozzles were performed. Nozzles were fired on a solid propellant simulator with a test stream composition, designated ANB-3066, which contained 16 percent aluminum. Nominal chamber pressure for each of the various firing pulses was 750 psia. Material temperature histories were recorded at several locations in each nozzle. Post-test measurements of surface recession, char penetration, and density versus depth, as well as thermocouple data are used for comparison with one and two-dimensional heat conduction and material ablation calculations. Agreement between prediction and data is favorable, although the analyses showed that two-dimensional heat conduction effects need be accounted for to obtain an accurate evaluation of the thermal response of multiple pulse duty cycle rocket nozzles. It is concluded that material decomposition and ablation phenomena are not strongly dependent on the type of duty cycle.			

DD FORM 1473

REPLACES DD FORM 1473, 1 JAN 68, WHICH IS OBSOLETE FOR ARMY USE.

UNCLASSIFIED

Security Classification

UNCLASSIFIED

Security Classification

14	KEY WORDS	LINK A		LINK B		LINK C	
		ROLE	WT	ROLE	WT	ROLE	WT
	Ablation Computer Codes Ablative Material Carbon Phenolic Heat Conduction Analyses Heterogeneous Chemical Kinetics In-depth Phenolic Depolymerization Pyrolytic Graphite Rocket Nozzle Thermal Response Solid Propellant Surface Thermochemistry Thermal Analysis Thermal Properties Thermocouple Data						

UNCLASSIFIED

Security Classification